FINAL THESIS upto 7 chapters new 18-11-2025.docx

Delhi Technological University

Document Details

Submission ID
trn:oid:::27535:121870663

Submission Date
Nov 18, 2025, 4:28 PM GMT+5:30

Download Date
Dec 14, 2025, 2:43 PM GMT+5:30

File Name
FINAL THESIS upto 7 chapters new 18-11-2025.docx

File Size
23.4 MB

210 Pages

51,038 Words

293,079 Characters

5% Overall Similarity

The combined total of all matches, including overlapping sources, for each database.

Filtered from the Report

- Bibliography
- Quoted Text
- Cited Text
- Small Matches (less than 14 words)

Exclusions

- 6 Excluded Sources

Match Groups

134 Not Cited or Quoted 5%
Matches with neither in-text citation nor quotation marks

0 Missing Quotations 0%
Matches that are still very similar to source material

0 Missing Citation 0%
Matches that have quotation marks, but no in-text citation

0 Cited and Quoted 0%
Matches with in-text citation present, but no quotation marks

Top Sources

3% Internet sources
4% Publications
2% Submitted works (Student Papers)

Integrity Flags

1 Integrity Flag for Review

Replaced Characters
19 suspect characters on 31 pages
Letters are swapped with similar characters from another alphabet.

Our system's algorithms look deeply at a document for any inconsistencies that would set it apart from a normal submission. If we notice something strange, we flag it for you to review.

A Flag is not necessarily an indicator of a problem. However, we'd recommend you focus your attention there for further review.

Match Groups

- **134** Not Cited or Quoted 5%
  Matches with neither in-text citation nor quotation marks
- **0** Missing Quotations 0%
  Matches that are still very similar to source material
- **0** Missing Citation 0%
  Matches that have quotation marks, but no in-text citation
- **0** Cited and Quoted 0%
  Matches with in-text citation present, but no quotation marks

Top Sources

3% Internet sources
4% Publications
2% Submitted works (Student Papers)

Top Sources

The sources with the highest number of matches within the submission. Overlapping sources will not be displayed.

1	Publication	Neha Bhatt, Mohan Singh Mehata. "WSe_2 quantum dots: A fluorescent probe for ... <1%
2	Internet	dspace.dtu.ac.in:8080 <1%
3	Submitted works	Sabanci Universitesi on 2024-12-25 <1%
4	Publication	Erkan Yılmaz, Emre Yavuz. "Use of transition metal dichalcogenides (TMDs) in ana... <1%
5	Publication	Neha Bhatt, Mohan Singh Mehata. "WSe_2 Quantum Dots: A Fluorescent Probe for ... <1%
6	Internet	libweb.kpfu.ru <1%
7	Publication	Rezvan Najafi, Mohammad Amjadi, Tooba Hallaj, Saeedeh Narimani. "A dual che... <1%
8	Publication	Vijay K. Singh, Himanshu Mishra, Rashid Ali, Sima Umrao et al. " In Situ Functional... <1%
9	Internet	ouci.dntb.gov.ua <1%
10	Publication	Mohan Singh Mehata, Aneesha. "Selectively probing ferric ions in aqueous envir... <1%

11 Submitted works
Delhi Technological University on 2020-04-30 <1%

12 Publication
Samarjit Pattnayak, Ugrabadi Sahoo, Shubhalaxmi Choudhury, Garudadhwaj Hot... <1%

13 Publication
Neda Azizi, Tooba Hallaj, Maryam Majidinia, Naser Samadi, Bita Azizzadeh. "WS2 ... <1%

14 Internet
dokumen.pub <1%

15 Internet
www.mrforum.com <1%

16 Publication
Priyanka Kashyap, Payal Sharma, Ritu Gohil, Dushyantsingh Rajpurohit, Divya Mis... <1%

17 Publication
Fei Li, Jie Gao, Yijun Li, Xiwen He, Langxing Chen, Yukui Zhang. "Selective and sen... <1%

18 Submitted works
Universidad Estadual Paulista on 2024-03-18 <1%

19 Submitted works
National Institute of Technology, Sri Nagar Jammu & Kashmir on 2025-07-15 <1%

20 Publication
Liliana Anchidin-Norocel, Gheorghe Gutt, Elena Tătăranu, Sonia Amariei. "Electro... <1%

21 Internet
orbilu.uni.lu <1%

22 Submitted works
Universidad Nacional de Colombia on 2023-09-22 <1%

23 Publication
Yongming Guo, Yixia Liu, Yubin Xiang. "Tungsten disulfide quantum dots: Synthe... <1%

24 Publication
Shi, Zhuojie | Wang, Lei. "Organic-Based Interface Materials for High-Efficiency a... <1%

25 Internet
epub.uni-regensburg.de <1%

26 Internet
iris.unibs.it <1%

27 Publication
Abdrabou, Moataz. "Innovative Techniques for Partially Upgrading Oil Sand Bitu... <1%

28 Publication
"Smart Nanosensors", Springer Science and Business Media LLC, 2025 <1%

29 Submitted works
National Sun Yat-sen University on 2024-12-14 <1%

30 Publication
Tahir, Muhammad Hassan. "Optical and Thermal Characterization of Vertically Co... <1%

31 Submitted works
Federal University of Technology on 2025-02-07 <1%

32 Publication
Wenxu Yin, Xin Liu, Xiaoyu Zhang, Xupeng Gao, Vicki L. Colvin, Yu Zhang, William ... <1%

33 Publication
Zhang, Yi. "Three dimensional atom probe tomography of nanoscale thin films, in... <1%

34 Internet
events.iist.ac.in <1%

35 Submitted works
Delhi Technological University on 2020-04-30 <1%

36 Submitted works
IIT Delhi on 2025-04-16 <1%

37 Submitted works
Indian School of Mines on 2019-08-29 <1%

38 Submitted works
Anna University on 2025-09-09 <1%

39 Submitted works
Delhi Technological University on 2019-09-20 <1%

40 Publication
Li, Yun. "Development of biocompatible polymer monoliths for the analysis of pro... <1%

41 Submitted works
North-Eastern Hill University, Shillong on 2024-01-18 <1%

42 Publication
Samiksha Shukla, Mohan Singh Mehata. "Selective picomolar detection of carcino... <1%

43 Publication
"Handbook of Graphene", Wiley, 2019 <1%

44 Submitted works
Anna University on 2025-03-10 <1%

45 Publication
Price, Sco. "A Model Catalyst Investigation of Mass-Selected Vanadium and Vanad... <1%

46 Publication
Vineet Sharma, Mohan Singh Mehata. "Rapid optical sensor for recognition of ex... <1%

47 Internet
iris.unipa.it <1%

48 Publication
Chaoliang Tan, Xiehong Cao, Xue-Jun Wu, Qiyuan He et al. "Recent Advances in Ul... <1%

49 Submitted works
OP Jindal University, Raigarh on 2024-03-21 <1%

50 Submitted works
Universidad de la Rioja on 2024-09-21 <1%

51 Internet
iris.uniroma1.it <1%

52 Submitted works
Banaras Hindu University on 2024-06-06 <1%

53 Publication
Mabowa, Mothepane Happy. "Towards the Development and Determination of Tr... <1%

54 Publication
Md. A. Rashed, M. Faisal, Farid A. Harraz, Mohammed Jalalah, Mabkhoot Alsaiari, ... <1%

55 Submitted works
University of Malaya on 2016-02-26 <1%

56 Internet
dspace.univ-eloued.dz <1%

57 Publication
Fellowes, Jonathan William Haddon. "The Bacterial Biogenic Synthesis of Magneti... <1%

58 Submitted works
Indian Institute of Science Education and Research on 2020-01-08 <1%

59 Submitted works
University of Iowa on 2022-08-25 <1%

60 Publication
"TMS 2022 151st Annual Meeting & Exhibition Supplemental Proceedings", Spring... <1%

61 Submitted works
Coventry University on 2023-08-16 <1%

62 Publication
Johnstone, Lucas R.. "Exploitation of Plasmonic Nanoparticles for Optical Enhance... <1%

63 Publication
Muhammad Tahir Waseem, Hafiz Muhammad Junaid, Hira Gul, Zulfiqar Ali Khan, ... <1%

64 Publication
Smith, Timothy J.. "Redox-Dependent Transformations in Molecular Self-Assembly... <1%

65 Submitted works
University of Hong Kong on 2025-05-29 <1%

66 Publication
Vineet Sharma, Mohan Singh Mehata. "Synthesis of Photoactivated Highly Fluore... <1%

67 Publication

Zhou, Xin. "Engineering Noble Metal Co-Catalysts on TiO 2 Nanostructures for En... <1%

TABLE OF CONTENTS

Chapter 1: Introduction 15
1.1. Historical Evolution: From Ancient Art to Modern Science 15
1.2. Nanoscience and Its Technological Impact 16
1.3 Classification of Nanomaterials 17
1.3.1. Classification by Constituents and Chemical Nature 17
1.3.2. Classification by dimension 18
1.4 Quantum Size Effects 21
1.4.1 Tunable electronic and optical properties 21
1.4.2 Enhanced surface effects 22
1.5 Two-Dimensional (2D) Nanomaterials: Emergence and Significance 22
1.5.1 Transition metal dichalcogenides 23
1.6 Scope and Overview of the Present Work 25
Chapter 2: Experimental Tools and Techniques 27
2.1 Synthesis of Nanomaterials 27
2.1.1 Top-Down Techniques 27
2.1.2 Bottom-Up Techniques 28
2.2 Characterization Techniques. 31
2.2.1 X-ray Diffraction (XRD) 32
2.2.2 Fourier Transform Infrared Spectroscopy (FT-IR) 35
2.2.3 High-Resolution Transmission Electron Microscopy (HR-TEM) 37
2.2.4 X-ray Photoelectron Spectroscopy (XPS) 38
2.2.5 UV/Vis/NIR Absorption Spectrophotometer 40
2.2.6 Photoluminescence (PL) Spectroscopy 42
2.2.7 Time-Correlated Single-Photon Counting (TCSPC) System 44
Chapter 3 In situ synthesis of WS_2 QDs for sensing of H_2O_2: Quenching and recovery of absorption and photoluminescence 46
3.1 Introduction 46
3.2 Experimental section 48
3.2.1. Chemicals and reagents 48
3.2.2. Synthesis 49
3.2.3. Chemical reactions involved 50
3.2.4. Characterization tools 50
3.3 Results and discussion 51

3.3.1. XRD and FTIR spectrum analysis 51
3.3.2 HR-TEM analysis 52
3.3.3. Optical properties of obtained WS2 QDs spectra 53
3.4. Hydrogen Peroxide Sensing 56
3.4.1. Effect of H2O2 on the absorption and PL of WS2 QDs 56
3.4.2. Effect of H_2O_2 on PL lifetime of WS_2 QDs 59
3.4.3. Restoring the PL of the sensing probe 61
3.4.4. Promising recovery mechanism 63
3.5. Conclusion 65
Chapter 4: Waterborne Explosives: A Rapid Detection Method using $MoSe_2$ Quantum Dots 66
4.1 Introduction 66
4.2. Experimental Sections 68
4.2.1. Materials 68
4.2.2. Synthesis method 68
4.2.3 Characterization Techniques: 69
4.3 Results and discussion 70
4.3.1. XRD analysis 70
4.3.2 FT-IR Spectrum analysis 70
4.3.3 Transmission electron microscopy (TEM) analysis 71
4.3.4. Optical properties of obtained MoSe2 QDs 72
4.3.5. 2,4,6-TNP explosive sensing 75
4.4. Conclusion 87
Chapter 5: Reusable fluorescent WS_2 QDs Sensor for Ultralow-Level Detection of Cr^{6+} in Real Water Samples 89
5.1 Introduction 89
5.2 Experimental section 91
5.2.1. Chemicals and reagents 91
5.2.2. Synthesis 91
5.2.3. Reaction Pathway 92
5.3 Results and discussion 93
5.3.1. XRD and FTIR study 93
5.3.2 HR-TEM analysis 94
5.3.3. Photophysical Performance and Properties of WS2 QDs 95
5.3.4. Photostability and Environmental stability of synthesized WS2 QDs under different conditions 100

5.4. Cr6+ sensing 101
5.4.1 Effect of Cr6+ on UV-vis Absorption and PL spectra of WS2 QDs 101
5.4.2 Effect of Cr6+ on PL Lifetime of WS2 QDs 105
5.4.3 XPS analysis after Cr6+ addition 108
5.4.4 Performance Analysis of EDTA as a General Chelator in Cr6+ Detection 110
5.4.5 Restoring the PL of sensing probe WS2 QDs using AA (ascorbic acid) . 111
5.4.6 Promising Mechanism of PL Quenching and Recovery of WS2 QDs upon Cr6+ Interaction 113
5.4.7 Application of WS2 QDs nanoprobe to quantify $Cr6^{+}$ in real samples ... 116
5.5. Conclusion 118
Chapter 6: Toward Real-World Vitamin B12 Diagnostics: WS_2 QDs as a Next-Generation PL Sensing Platform 119
6.1 Introduction 119
6.2 Experimental Section 122
6.2.1 Materials used 122
6.2.2 Synthesis 123
6.2.3 Reaction dynamics in WS_2 QDs formation 123
6.2.4 Analytical Techniques 124
6.3 Results and discussion 125
6.3.1 XRD and FT-IR analysis 125
6.3.2 HR-TEM analysis 126
6.3.3. UV-Vis absorption and PL spectra of obtained WS2 QDs 127
6.3.4 PL decay analysis 130
6.3.5 Stability Analysis of WS2 QDs Under Environmental Stressors 131
6.4. Vitamin B12 (Cbl) Sensing 132
6.4.1. Effect of Cbl on PL lifetime of WS2 QDs 134
6.4.2 Selective Detection of Cbl Using WS2 QDs: Interference and Anti-Interference Analysis with Other Analytes 137
6.3. Mechanism of Fluorescence Quenching Between WS2 QDs and Cbl 138
6.5. Conclusions 139
Chapter 7: A Spectroscopic Approach for Amoxicillin Sensing: Insights from UV-Vis and photoluminescence studies 140
7.1 INTRODUCTION 140
7.2. EXPERIMENTAL SECTION 143
7.2.1 Materials used 143

7.2.2 Synthesis 143
7.2.3 Optimised reaction pathway 145
7.2.4 Characterization techniques 146
7.3. RESULTS AND DISCUSSION 147
7.3.1 XRD analysis 147
7.3.2 High-resolution transmission electron microscopy (HRTEM) analysis 148
7.3.3 Optical Properties of WS_2 QDs 149
7.3.4 Systematic Assessment of the Optical and Environmental Stability of WS_2 QDs: 155
7.4. AMOXICILLIN (AMX) SENSING 157
7.4.1 Influence of Incubation Time on PL Response 157
7.4.2 FT-IR Characterization of WS2 QDs and Their Interaction with AMX 159
7.4.3 Impact of AMX on optical properties of WS2 QDs 160
7.4.4 Selectivity and sensitivity of AMX towards WS_2 probe 163
7.4.5 Impact of AMX on PL decay of WS_2 QDs 164
7.4.6 Proposed Photoluminescence Quenching Mechanism 167
7.5. Conclusion 168
Chapter 8: Conclusion, Future Scope of Work and Social Impact 170
8.1 Conclusion 170
8.2 Future Scope of Work 171
8.2.1 Surface Engineering and Doping 171
8.2.2 Development of Multi-Analyte and Ratiometric Sensors 171
8.2.3 Integration into Portable and On-Site Devices 171
8.2.4 Biological Applications and Toxicity Studies 172
8.2.5 Mechanistic and Theoretical Investigations 172
8.2.6 Environmental and Industrial Applications 172
8.2.7 Electrochemical and Photocatalytic Sensing 172
8.3 Society Impact 172
8.3.1 Environmental Benefits 173
8.3.2 Public Health and Safety 173
8.3.3 Economic and Technological Advancement 173
8.3.4 Sustainability and Green Chemistry 173
8.3.5 Real-World Applicability 174
References 175

LIST OF TABLES

Table 3.1 PL lifetime and pre-exponential factors of WS_2 QDs dispersed in water at 320 nm excitation. 56
Table 3.2 PL lifetime and pre-exponential factors of WS_2 QDs at the excitation wavelength of 320 nm and PL wavelength of 420 nm at different concentrations of H_2O_2. 61
Table 3.3 A comparison of different probes claimed for H2O2 detection. 64

Table 4.1 Parameters estimated from Stern−Volmer plots of PL intensity of $MoSe_2$ QDs at 410 nm with various NACs at fixed concentrations of 99 nM. 80
Table 4.2 PL lifetime and pre-exponential factors of $MoSe_2$ QDs at the excitation wavelength of 340 nm and PL wavelength of 410 nm at different concentrations of 2,4,6-TNP. 82
Table 4.3 Comparison of $MoSe_2$ QDs-based probe with the reported probes for 2,4,6-2,4,6-TNP sensing. 84
Table 4.4 Calculated LoD values with quenching percentage for $MoSe_2$ QDs in different water samples. 86

Table 5.1 Tri-exponential fitted PL lifetimes and pre-exponential factors of colloidal WS_2 QDs. 99
Table 5.2 Summary of reported Cr^{6+} detection probes and their analytical performance parameters. 104
Table 5. 3 PL lifetimes and pre-exponential parameters of WS_2 QDs dispersed in water excited with 320 nm and monitored at 410 nm for different concentrations of Cr^{6+}. 106
Table 5.4 Peak area, FWHM, and total organic contribution from different elements present in XPS analysis of WS_2 QDs/Cr^{6+} system. 114
Table 5.5 Calculated values of LoD with quenching percentage for WS_2 QDs in different water samples. 116
Table 5.6 Cr^{6+} detection in real water samples at different spiked concentrations (9.9, 33, 99, 330 and 594 nM) 117

Table 6. 1 PL lifetime and pre-exponential factors of WS_2 QDs dispersed in water at 320 nm excitation. 131
Table 6. 2 Comparative data of WS_2 QDs-based probe with prior investigated probes for the detection of Cbl. 134
Table 6. 3 PL lifetimes and pre-exponential parameters of WS_2 QDs dispersed in DI, excited with 320 nm and monitored at 410 nm for different concentrations of Cbl. 136

Table 7. 1 PL lifetime and pre-exponential factors of colloidal WS_2 QDs at λ_{ex} = 320 nm. 154
Table 7. 2 Comparative data of WS_2 QDs-based probe with prior investigated probes for the detection of AMX. 163
Table 7. 3 PL lifetime and pre-exponential factors of WS_2 QDs upon addition of different concentrations of AMX at λ_{ex} = 320 nm and λ_{em} = 380 nm. 167

LIST OF FIGURES

Fig. 1. 1 Schematic illustrating the D(E) as a function of energy for materials in different dimensions 19
Fig. 1. 2 Schematic represents how reducing the QD size leads to an increased energy band gap 21
Fig. 1. 3 Metal coordination's (a), stacking sequences (b), and top view (c) of WS2 structural unit cells (2H-trigonal prismatic, 1T-octahedral and 3R-distorted octahedron phase). 24

Fig. 2. 1 Illustration of top-down and bottom-up strategies for the synthesis of NPs. 27
Fig. 2. 2 Schematic representation of a typical hydrothermal experimental setup. ... 30
Fig. 2. 3 Schematic representation of Bragg's law of X-ray diffraction. 33
Fig. 2. 4 Schematic representation of an X-ray diffractometer. 34
Fig. 2. 5 Image of Bruker D8 Advance powder X-ray diffractometer. 35
Fig. 2. 6 Schematic representation of FTIR instrumentation. 36
Fig. 2. 7 Image of thermoscientific Nicolet Summit X FT-IR spectrometer. 37
Fig. 2. 8 Schematic representation of the principle of the HR-TEM system. 38
Fig. 2. 9 Schematic representation of the XPS system. 39
Fig. 2. 10 Ray diagram of UV/Vis/NIR absorption spectrophotometer. 41
Fig. 2. 11 Photograph of UV/Visible/NIR spectrometer, Lambda-750, Perkin Elmer. 42
Fig. 2. 12 Ray diagram of Photoluminescence spectrofluorometer. 43
Fig. 2. 13 Photograph of spectrofluorometer, Fluorolog-3, Horiba Jobin Yvon. 44
Fig. 2. 14 Schematic representation of the TCSPC system. 45
Fig. 2. 15 Image of DeltaFlex-01-DD TCSPC measurement unit. 45

Scheme 3.1 Trigonal prismatic (2H) WS_2 (a) and Octahedral (1T) WS_2 (b). 47
Scheme 3.2 Synthesis processes of colloidal WS_2 QDs using a single-step hydrothermal growth method. 50

Fig. 3.1 XRD pattern of the produced WS2 QDs thin film (a) and FT-IR spectrum of colloidal WS_2 QDs dispersed in water (b). 52
Fig. 3.2 HRTEM images (a-c) of WS_2 QDs with particle size distribution (d). 53
Fig. 3.3 Absorption spectrum of WS_2 QDs dispersed in water. Inset represents the color photographs under visible illumination and UV irradiation (~365 nm) (a), The overlapped absorption and PL spectra WS_2 QDs (b). PL spectra of WS_2 QDs at the different excitation wavelengths (b) and the normalized spectra (c). Fitted decay curves of WS_2 QDs at 320 nm excitation and various PL wavelengths along with instrumental response function (d). 54
Fig. 3.4 PL excitation spectra of WS_2 QDs obtained by monitoring PL at different wavelengths, which are shown in the figure. 55
Fig. 3.5 Absorption spectra of WS_2 QDs in the absence and presence of various (0.33 nM to 594 µM) H_2O_2 concentrations (a) PL spectra of WS_2 QDs in the absence and presence of various (0.33 nM to 594 µM) concentrations of H_2O_2 with 320 nm excitation (b) and inset of (a) shows the plot of (A_0–A) as a function of the

concentration of H_2O_2 over a range of 0 to 594 µM and (b) inset of represents the corresponding linear S-V plot and photographs under UV and visible illumination for H_2O_2 concentration of 0, 231, 495 and 594 µM (c). 58
Fig. 3.6 Selectivity of PL quenching in WS_2 QDs was examined by using various chemicals. Plots of the PL intensity (%) of WS_2 QDs in the presence of each of chemicals (ANI, BZ, BZA, BAL, TOL and H2O2) relative to the intensity in the absence of chemicals (Initial). The concentration of the chemical was 594 µM in every case. 59
Fig. 3.7 Fitted decay profiles of WS_2 QDs in the presence of various concentrations of H_2O_2 with 320 nm excitation and monitored at 420 nm. The inset shows the S-V plots of individual lifetimes. 61
Fig. 3.8 Bar diagram of relative PL intensity (%) of WS_2 QDs in the absence (initial) and presence of 594 µM H_2O_2 (quenched) along with the insets of recovered PL intensity (%) by adding sequentially and at 297 µM of 0.1 N HCl (recovered). Insets show the sequentially restored PL by adding HCl and at initial, quenched and recovered PL spectra of WS_2 QDs along with their photographs under UV irradiation (a), absorption spectra of WS_2 QDs observed in the absence (Initial, green line) and presence of 594 µM of H_2O_2 (Quenched, blue line). Absorption spectrum observed upon addition of 297 □M of 0.1 N HCl to the sample having H_2O_2 (594 □M) is also shown (Recovered, red line) (b). 62
Fig. 3.9 PL intensity of the developed fluorescent probe (QDs) upon successive addition of H_2O_2 (594 µM) and HCl (297 µM) up to nine cycles. The plot shows excellent cyclic stability for more than nine cycles. 63
Fig. 3.10 The pictorial representation of the conversion of W(IV) to W(VI). 64

Scheme 4.1 Schematic representation of the synthesis process of $MoSe_2$ QDs. 69

Fig. 4.1 XRD pattern of obtained $MoSe_2$ QDs thin film and JCPDS cards details (a), FT-IR spectrum of synthesised $MoSe_2$ QDs dispersed in water along with the band's identification. 70
Fig. 4.2 HR-TEM images of obtained $MoSe_2$ QDs at different magnifications (a-c) with particle size distribution (d). The inset of (a) shows the extended view of the calculated d-spacing. 72
Fig. 4.3 Absorption spectrum of synthesised $MoSe_2$ QDs with its 2^{nd} order derivative (blue solid line) and Gaussian bands g1, g2 and g3 used to reproduce the measured absorption. The inset represents the colour of the solution under white LED and UV irradiation (~365 nm) (a). PL spectra of synthesised $MoSe_2$ QDs with different excitations ranging from 270 to 450 nm (b) and normalized PL spectra at different excitations (c). 73
Fig. 4.4 Photoluminescence spectra of colloidal $MoSe_2$ QDs at different excitation wavelengths along with the Gaussian band used to reproduce the observed spectra (a), PL excitation (PLE) spectra of $MoSe_2$ QDs with variable emission wavelengths (varying from 400 to 500 nm). The inset represents the normalized PLE spectra (b). 74
Fig. 4.5 Plot of PL intensity at 410 nm of $MoSe_2$ QDs as a function of pH (2-13) (a), and corresponding PL plot (b). 75

Fig. 4.6 Absorption spectra of $MoSe_2$ QDs in the absence and presence of varying concentrations of 2,4,6-2,4,6-TNP (3.3 to 99 nM) along with the absorption of bare 2,4,6-2,4,6-TNP at a fixed concentration of 99 nM (a), Photoluminescence spectra of $MoSe_2$ QDs in the absence and presence of various concentrations (3.3 to 99 nM) of 2,4,6-TNP with 340 nm excitation. The inset represents the corresponding S-V plot (b). 77
Fig. 4.7 The bar graphs of PL intensity quenching (%) of $MoSe_2$ QDs with fixed concentration (99 nM) of different analytes (a) and with a fixed concentration of 2,4,6-2,4,6-TNP (99 nM) and different analyst (99 nM) representing the anti-interference effect (b). The pink bar shows the change in PL intensity (%) in the presence of various analytes, whereas the black bars of (a) and (b) represent the PL intensity in the absence of analytes. 78
Fig. 4.8 Stern Volmer (S-V) plot of all analytes with the varying concentrations ranging from 3.3 to 99 nM (a), Absorption spectra of different NACs at a fixed concentration of 99 nM alongwith 2,4,6-TNP (b), Photoluminescence spectra of $MoSe_2$ QDs: in the absence (black solid line), in the presence of 4-NT at a fixed concentration of 99 nM (red solid line), and with 2,4,6-TNP (blue solid line) under 290 nm excitation (c), sensing response time of the probe in the presence of 2,4,6-TNP (99 nM) in an aqueous medium is < 0.3 min. Plots of PL intensity at 410 nm as a function of time upon adding 2,4,6-TNP. The inset of represents the time response of the probe in about seconds (d). 79
Fig. 4.9 Fitted decay curves of $MoSe_2$ QDs with different concentrations of 2,4,6-TNP (3.3 to 99 nM) with 340 nm excitation and monitored at 410 nm. 81
Fig. 4.10 Spectral overlap of absorption spectrum of 2,4,6-TNP, PL and PL- excitation spectra of $MoSe_2$ QDs (a), S-V plots of $MoSe_2$ QDs with 2,4,6-TNP obtained in RA and FF detection modes (b). 83
Fig. 4.11 Photoluminescence intensity of $MoSe_2$ QDs at 410 nm monitored in the repeated interval up to 8 months, representing stability of QDs longer than 8 months (a), Photoluminescence intensity (%) of $MoSe_2$ QDs monitored at 410 nm under continuous UV lamp irradiation (365 nm) for 180 min, representing the photostability of QDs (b). 85
Fig. 4.12 Photoluminescence spectra of $MoSe_2$ QDs in Yamuna River (a), DTU lake (b), tap water (c) in the absence and presence of various concentrations (3.3 to 99 nM) of 2,4,6-TNP with 340 nm excitation. The insets represent the corresponding S-V plots. 86
Fig. 4.13 Percentage quenching of PL intensity (at 410 nm) of $MoSe_2$ QDs in different water samples. A comparative bar graph representing 2,4,6-TNP sensing in real samples, highlighting the efficiency of QDs as a sensor for explosive detection in real-world samples monitoring. 87

Scheme 5.1 Schematic representation of the one-step hydrothermal synthesis route for colloidal WS_2 QDs. 92

Fig. 5.1 XRD pattern of synthesised WS2 QDs deposited on thin film (a) and FT-IR spectrum of WS2 QDs dispersed in aqueous medium (b). 94

Fig. 5.2 HR-TEM visuals of obtained WS_2 QDs at various magnifications (a,b) and particle size distribution (c). The enlarged view of the image with computed d-spacing is displayed in the inset of (b). 95
Fig. 5.3 Absorption spectrum of synthesised WS_2 QDs overlaid with its 2^{nd} order derivative (red dotted line). The inset displays the visible colour representation under white LED illumination and UV irradiation (365 nm)..... 96
Fig. 5.4 Overlapped absorption, PL, and PLE spectra of colloidal WS_2 QDs (a). PL spectra of WS_2 QDs recorded at various excitation wavelengths (b) and normalized PL spectra to highlight PL shift and profile consistency (c). CIE 1931 chromaticity diagram representing the colour coordinates of WS_2 QDs emissions (d). 97
Fig. 5.5 PLE spectra of synthesised WS_2 QDs at different emission wavelengths along with deconvoluted Gaussian bands g1, g2, and g3 (a). TRPL decay curves of WS_2 QDs excited at 320 nm, recorded at different emission wavelengths, along with IRF (b) and residual plots corresponding to the fitted decay profiles along with the associated χ^2 values (c). 99
Fig. 5.6 Bar graphs showing the relative PL intensity (%) of WS_2 QDs under different conditions: pH-dependent PL stability (a), UV irradiation (λ=365 nm) indicating photobleaching resistance (b), temperature-dependent PL response representing thermal stability (c) and long-term shelf-life stability at RT (d). 101
Fig. 5.7 UV–vis absorption spectra of WS_2 QDs recorded in the absence and presence of Cr^{6+} ions over a concentration range of 0.66 to 660 nM. The insets displays the corresponding (A_0- A) plot as a function of Cr^{6+} concentration at 336 nm and enlarged characteristic peak (a) and the corresponding B-H plot between $1/\Delta A$ vs $1/[Cr^{6+}]$ (b) PL spectra at λex = 320 nm and corresponding S-V plot of WS_2 QDs recorded upon incremental addition of Cr^{6+} ions over the entire concentration range of 0.66 to 660 nM (c,d). The concentration gradient was obtained by serial dilution of 10^{-6}, 10^{-5}, and 10^{-4} M Cr^{6+} stock solutions, added in different volumes (µL) to a fixed WS_2 QDs dispersion. 103
Fig. 5.8 Fitted TRPL decay profiles of WS_2 QDs at 320 nm excitation and monitored at 410 nm emission, recorded in the absence and presence of Cr^{6+} (660 nM) concentration (a), S-V plots based on individual PL lifetimes of varying concentrations of Cr^{6+} ions (b). 106
Fig. 5.9 Bar diagrams showing the quenching (%) response of WS_2 QDs in the presence of different analytes at fixed concentrations of 660 nM (a). Quenching (%) of colloidal WS_2 QDs exposed at 660 nM concentration of Cr^{6+} along with other interfering analytes at the same concentrations (b), showing negligible interference effects. The yellow bars in both (a) and (b) represent control samples without any analytes, and the blue-green bars represent the presence of analytes. Corresponding visual images of the QDs under white LED and 365 nm UV illumination, depicting PL changes with different analytes at 660 nM concentration (c). 108
Fig. 5.10 High-resolution XPS spectra of WS_2 QDs/Cr^{6+} system: W 4f, (a) S 2p, (b) C 1s, (c) N 1s, (d) O 1s, (e) and Cr 2p (f). 110
Fig. 5.11 Effect of different EDTA concentrations (99, 198, 297, 396, 495, 594, and 660 nM) for Cr^{6+} detection (a), Effect of different ascorbic acid concentrations (165, 231, 297, 393, 429, 462, and 528 nM) for Cr^{6+} detection (b), S-V plot of WS_2 QDs constructed by plotting $FF0 - 1$ vs conc. of AA recorded upon incremental addition of AA concentrations (165, 231, 297, 393, 429, 462, and 528 nM)(c). 111

Fig. 5.12 High-resolution XPS spectra of Cr 2p in WS_2 Qds/Cr^{6+}/AA system (a) and cyclic PL response of the developed WS_2 QDs-based probe upon successive alternate additions of Cr^{6+} (660 nM) and AA (528 nM) over 18 cycles. The plot demonstrates excellent reversibility and stability of the PL signal. 112
Fig. 5.13 WS_2 QD-based paper strip assay showing PL quenching by Cr^{6+} and recovery with AA under 365 nm UV light. 113
Fig. 5.14 UV-vis spectra of different analytes at fixed concentration of 660 nM... 115
Fig. 5.15 PL spectra of WS_2 QDs in tap water (a) and Triveni Sangam water (b) recorded upon incremental addition of Cr^{6+} ions over a concentration range of 0.66 to 660 nM. The insets present the corresponding S-V plots. 116

Scheme 6. 1 The molecular structure of vitamin B12 (Cbl) featuring a corrin ring with a centrally bound cobalt ion, surrounded by four nitrogen atoms from pyrrole groups. 119
Scheme 6. 2 Facile single-step hydrothermal preparation of water-soluble WS_2 QDs. 123

Fig 6. 1 XRD pattern of WS_2 QDs thin film exhibiting characteristic diffraction peaks indicative of crystalline phase (a), FT-IR spectrum of colloidal WS_2 QDs dispersed in water showing vibrational modes corresponding to surface functional groups (b). 125
Fig 6. 2 HR-TEM images of WS_2 QDs at various magnifications (a-c) with particle size distribution (d). Inset of (a) shows an enlarged image with measured d-spacing. 127
Fig 6. 3 Absorption spectrum of colloidal WS_2 QDs. Inset represents the color photographs under visible illumination and UV irradiation (~365 nm) (a), PL spectra (b), normalized PL spectra (c) at different excitations ranging from 270 nm to 420 nm and CIE 1931 plot with blue emission (d) of the synthesised WS_2 QDs. 129
Fig 6. 4 Fitted PL decay curves for WS_2 QDs at different emission wavelengths at λ_{ex} = 320 nm, along with IRF and their corresponding residuals and χ^2 values. 131
Fig 6. 5 Bar graphs showing relative PL intensity of WS_2 QDs with 3h of continuous UV irradiation (λ=365 nm) (a), across a range of pH from 3 to 11 (b) and over a period of 6 months (c), indicating excellent stability. 132
Fig 6. 6 Absorption spectra and PL spectra (λ_{ex} = 320 nm) of WS_2 QDs in the presence of different concentrations of Cbl ranging from 0.33 to 565 nM (a,b). Inset of (b) represents the corresponding S-V plot. 133
Fig 6. 7 Fitted PL Decay curves at λ_{ex}=320 nm of WS_2 QDs in the absence and presence of the lowest concentration 0.33 nM and the highest concentration of 565 nM of Cbl, along with their respective residual profiles and χ^2 values. 136
Fig 6. 8 Bar diagrams showing the quenching (%) response of WS_2 QDs in the absence of different analytes at fixed concentrations of 565 nM (a). Quenching (%) of colloidal WS_2 QDs exposed at 565 nM concentration of Cbl, along with other interfering analytes at the same concentrations 565 nM (b), showing negligible interference effects. The cyan bars in both (a) and (b) represent control samples without any analytes, and the magenta bars represent the presence of analytes. 137

Scheme 7. 1 Chemical structure of amoxicillin (AMX) 140
Scheme 7.2 Schematic illustration of modified hydrothermal synthesis of water-soluble WS_2 QDs..... 145

Fig 7. 1 XRD structure of synthesised WS_2 QDs deposited on a thin film…….148
Fig 7.2 HR-TEM image of the obtained WS_2 QDs at different magnifications (a,b), with particle size distribution (c). 149
Fig 7. 3 Absorption spectrum of WS_2 QDs with inset representing the visible color under normal LED light and UV light (a), PL spectra (b), normalized PL spectra (c) at different excitations ranging from 280 nm to 400 nm and CIE 1931 plot with blue cyan emission (d) of the synthesised WS_2 QDs..... 151
Fig 7. 4 PL (a) and PLE (b) spectra of WS_2 QDs, along with Gaussian bands used and simulated (Sim) spectra. Fitted PL decay transients for WS_2 QDs at various emission wavelengths at an excitation wavelength of 320 nm, along with IRF and their corresponding residuals (c). 153
Fig 7. 5 Relative PL intensity of WS_2 QDs across a range of pH from 3 to 12 (a), with 6 h of UV irradiation (λ=365 nm) (b) change in temperature from 0 to 100 ℃ (c), and over a period of 8 months (d), indicating excellent stability..... 156
Fig 7. 6 Quenching (%) of WS_2 QDs as a function of incubation time, in the presence of a fixed amount of AMX (607 nM). 158
Fig 7. 7 FT-IR spectra of WS_2 QDs, AMX and WS_2 QDs/AMX dispersed in DI. 159
Fig 7. 8 Absorption spectra and PL spectra (λ_{ex} = 320 nm) of WS_2 QDs in the presence of different concentrations of AMX ranging from 0.33 nM to 607 nM (a, b), and an Inset of (b) corresponding S-V plot. Bar diagrams showing the relative quenching response of WS_2 QDs in the presence of different analytes at fixed concentrations of 607 nM (c), and the same concentration of AMX (607 nM) along with other interfering analytes (d), showing negligible interference effects. The blue-cyan bars in both (a) and (b) represent control samples without any analytes, and the magenta bars represent the presence of analytes. 162
Fig 7. 9 Fitted PL Decay profiles of WS_2 QDs in the absence and presence of AMX, along with their respective residual profiles and χ^2 values at λ_{ex} = 320 nm and λ_{em} = 380 nm..... 166

LIST OF SYMBOLS

LIST OF ABBREVIATIONS

NS	Nanoscience
NPs	Nanoparticles
NT	Nanotechnology
NMs	Nanomaterials
nm	Nanometer
CNTs	Carbon nanotubes
QDs	Carbon quantum dots
PL	Photoluminescence
DOS	Density of states
3D	Three-dimensional
2D	two dimensions
1D	one-dimensional
0D	zero-dimensional
QY	quantum yield
TMDs	transition metal dichalcogenides
CVD	chemical vapor deposition
WS_2	Tungsten disulfide
$MoSe_2$	molybdenum diselenide
H_2O_2	hydrogen peroxide
AMX	amoxicillin
XRD	X-ray diffraction
HR-TEM	high-resolution transmission electron microscopy
XPS	X-ray photoelectron spectroscopy
FT-IR	Fourier transform infrared spectroscopy
TCSPC	time-correlated single photon counting
FWHM	full width at half maximum
SAED	selected area electron diffraction
CCD	charge-coupled device

22

E_k	kinetic energy
E_b	binding energy
A	absorbance
PMT	photomultiplier tube
TRPL	time-resolved Photoluminescence
PLE	photoluminescence excitation
TAC	Time-to-Amplitude Converter
IRF	Instrument Response Function
SPR	surface plasmon resonance
DI	deionised
TOL	toluene
BZA	benzoic acid
BZ	benzene
ANI	aniline
BAL	benzaldehyde
GQDs	Graphene quantum dots
NACs	nitroaromatic compounds
DNT	2,4-dinitrotoluene
TNT	2,4,6-trinitrotoluene
TNP	2,4,6-trinitrobenzene
DNB	1,3-dinitrobenzene
2-NT	2-nitrotoluene
4-NT	4-nitrotoluene
BzCOOH	benzoic acid
BzCHO	benzaldehyde
ANI	aniline
ACN	acetonitrile
UP	ultrapure
RT	room temperature
PLE	photoluminescence excitation
OD	Optical density
S-V	Stern-Volmer Plot
LoD	detection limit
PET	photoinduced electron transfer
FRET	Forster resonance energy transfer
RA	right angle
FF	front face
Cr	Chromium
AA	ascorbic acid
PTEE	polytetrafluoroethylene
H_2S	hydrogen sulfide
NH_3	ammonia gas
d-spacing	interplanar spacing
EDTA	ethylenediaminetetraacetic acid
MRLs	maximum residual limits

TC	tetracycline
DOX	doxycycline
NOR	norfloxacin
AMP	ampicillin
UA	uric acid
Fru	fructose
Glu	glucose
DA	Dopamine
Suc	sucrose
Chol	cholesterol
CDH	Central Drug House
S	Sulfur
H_2S	chalcogen hydride gas
RBC	red blood cell
EL	electroluminescent
7AI	7-azaindole
6HQ	6-hydroxyquinoline
Vit K	vitamin K
DA	Dopamine
IFE	INNER-FILTER EFFECT

LIST OF NOMENCLATURE

Chapter 1: Introduction

1.1. Historical Evolution: From Ancient Art to Modern Science

Nanoscience (NS) has its origins much further back in time than most people think. NMs were unknowingly utilised by ancient craftsmen. The 4th-century Lycurgus Cup obtains its dichroic colour from gold and silver nanoparticles (NPs), and stained-glass windows manufactured in the Middle Ages acquired their vivid colours through the application of metal oxide NPs [1,2]. In the 19th century, Michael Faraday conducted pioneering experiments with colloidal gold that laid the groundwork for NS. Working in the basement laboratory of the Royal Institution in the 1850s, Faraday discovered that gold could be divided into particles so small they were invisible to any microscope of his day. He observed that solutions containing these fine gold particles showed a distinctive red colouration, which varied depending on the particle size- a phenomenon he explored through careful optical experimentation. Faraday prepared pure colloidal gold samples using chemical reduction, and famously noted that the colour changes were not due to a chemical compound, but rather to the size-dependent interaction of light with suspended particles. This work culminated in his 1857 Bakerian Lecture, in which he described the remarkable optical properties of 'activated gold' and outlined what we now recognise as the Faraday-Tyndall effect, where the scattering of light by colloidal particles produces visible colored cones. Faraday's systematic study of ruby-glass fluids not only demonstrated the key principle that nanoscale dimensions govern material properties but also established experimental routes and theoretical insight that would inspire future generations of researchers in NS and nanotechnology (NT) [3–5].

NS got its start in the modern era with Richard Feynman's landmark 1959 lecture, "There's Plenty of Room at the Bottom". In this visionary talk, Feynman proposed the idea that it should be possible to manipulate and arrange individual atoms and molecules, opening a new frontier for the engineering of materials and devices at the atomic scale. Although his proposals seemed futuristic at the time, Feynman's insights anticipated many of the core approaches now fundamental to NT, such as atomic-scale fabrication, molecular machines, and data storage on unprecedentedly small scales [6–

8]. The term "nanotechnology" was later introduced by Norio Taniguchi in 1974, who formally defined it as the meticulous engineering of materials and devices with nanometre-scale precision, further establishing the conceptual framework that would guide technological advances in this field. Both Feynman's foresight and Taniguchi's definition continue to shape research directions in NS and NT today [9].

Building on Feynman's foundational vision, the field of NS rapidly advanced with the invention of high-resolution characterisation tools such as the scanning tunnelling microscope and atomic force microscope in the 1980 [10,11]. These tools enabled the direct visualisation and handling of materials at the atomic level, thus facilitating the production and research of a wide range of nanomaterials (NMs).

1.2. Nanoscience and Its Technological Impact

NS and NT have transformed the way materials are understood and engineered by shifting attention from bulk properties to phenomena that emerge at the nanometer (nm) scale. When at least one dimension of a material becomes comparable to characteristic physical lengths (electron mean free path, exciton Bohr radius, phonon wavelengths), quantum confinement, surface-to-volume ratio effects, and altered defect physics produce electronic, optical, and chemical behaviours that are distinct from the bulk. These size-dependent changes enable novel functionalities– for example, tunable band gaps, enhanced catalytic activity, strong light-matter interactions, and altered mechanical properties–which can be exploited across electronics, photonics, energy conversion, and sensing technologies [12].

The drive toward NMs arose from the realisation that traditional bulk materials could not meet the demands of next-generation technologies. As device miniaturisation progressed, especially in electronics and medicine, scientists needed materials with tunable properties, high sensitivity, and multifunctionality. NMs–engineered at the atomic or molecular level–offered solutions: they could be designed for specific optical, electrical, or catalytic behaviours, and their high surface area [13] made them ideal for sensing and catalysis [7,12,14].

Unlike bulk counterparts, NMs exhibit emergent properties due to their quantum confinement and large surface-to-volume ratio, which enable enhanced adsorption,

faster response rates, and increased reactivity–traits crucial for high-performance applications ranging from biosensors to energy storage and targeted therapeutics [12,15]. The ability to tailor the structure, composition, and surface chemistry of NMs has opened pathways for multifunctional systems that can respond dynamically to external stimuli, highlighting their pivotal role in transforming modern technology [16,17].

1.3 Classification of Nanomaterials

NMs can be distinguished by their dimensionality, chemical composition, morphology, and physicochemical properties. This multi-level classification is crucial for understanding how their structure influences their applications in sensing, electronics, catalysis, and medicine.

1.3.1. Classification by Constituents and Chemical Nature

1.3.1.1 Carbon-based NMs: Carbon-based NMs, such as carbon nanotubes (CNTs), Fullerenes, graphene, and carbon quantum dots (QDs), are the next generation of materials that find their application in the field of electronics due to their excellent electrical properties, and in the field of multifunctional materials. The atomically thin nature of graphene, with its high carrier mobility and flexibility, makes it a suitable material for electronics. In contrast, CNTs can be utilised in mechanical applications due to their high tensile strength and in thermal applications due to their high thermal conductivity. Besides, Fullerenes and Carbon QDs show excellent optical properties and are biocompatible; therefore, they are used in sensing, energy, and the biomedicine fields [18,19].

1.3.1.2 Metal-based NMs: Metal-based NMs, such as gold, silver, platinum, and iron oxide

NPs are valued for their plasmonic, magnetic, and catalytic properties. Gold and silver NPs show strong localised surface plasmon resonance, enhancing their use in biosensing and imaging. Platinum NPs are highly efficient catalysts, and iron oxide nanoparticles are widely used for magnetic resonance imaging and targeted drug delivery [20–23].

1.3.1.3 Semiconductor NMs: Semiconductor NMs include silicon NPs, CdSe QDs, and TMD QDs. The materials are engineered to exhibit variable bandgaps and display unique optical/electronic properties. One of the size-dependent photoluminescence (PL) properties of QDs is exploited for the application of optoelectronic devices and bioimaging. TMD QDs offer strong excitonic effects and high charge carrier mobility [24,25].

1. **Polymeric NMs:** Polymeric NMs, such as dendrimers, micelles, and nanogels, offer

excellent biocompatibility and versatility in drug delivery. Dendrimers have highly branched structures for targeted therapy, while micelles and nanogels can encapsulate drugs for controlled release. Their tunable surface chemistry and responsiveness to stimuli make them suitable for advanced biomedical applications [26–28].

2. **Lipid-based NMs:** Lipid-based NMs, such as liposomes and solid lipid NPs, are used

broadly in the medical field and the pharmaceutical industry because they are compatible with the human body and can release drugs in a controlled way. Liposomes carry water-loving as well as water-hating drugs, thus making the drugs more effective and less toxic [29,30]. Solid lipid NPs further enhance stability and targeted delivery. Recently, lipid NPs have gained significant importance in the fields of vaccine and gene therapy, owing to their efficient encapsulation, protection of payloads, and minimal toxicity [31,32].

1.3.2. Classification by dimension

NMs are classified by the number of dimensions in which electrons are confined to the nanoscale (1–100 nm). This dimensionality not only determines their physical form but also fundamentally alters their electronic properties, especially the density of states (DOS)– the number of available electronic states at each energy level.

D(E), which represents the number of available electronic states per unit energy, arises significantly with the dimensionality of a material and is a key factor governing its optical and electronic behaviour (Fig. 1.1). In three-dimensional (3D) bulk materials, the D(E) increases smoothly with the square root of energy ($D_{3D}(E) \propto E^{1/2}$), leading

to continuous energy bands. When the dimensionality is reduced to two dimensions (2D), as in atomically thin layers, the D(E) becomes step-like, remaining constant within each sub-band and resulting in sharper optical transitions ($D_{2D}(E) \propto E^0$). In one-dimensional (1D) systems such as nanowires or nanotubes, the D(E) exhibits a series of singularities (Van Hove singularities) due to QC along two directions ($D_{1D}(E) \propto E^{-1/2}$), while in zero-dimensional (0D) systems like QDs, the energy levels become fully discrete, like atomic orbitals ($D_{0D}(E) \propto \sum \delta(E - E_i)$). This progressive confinement from 3D to 0D not only modifies the DOS but also enhances excitonic effects, alters carrier dynamics, and leads to tunable bandgaps–all of which are crucial in designing nanoscale optoelectronic and photonic devices.

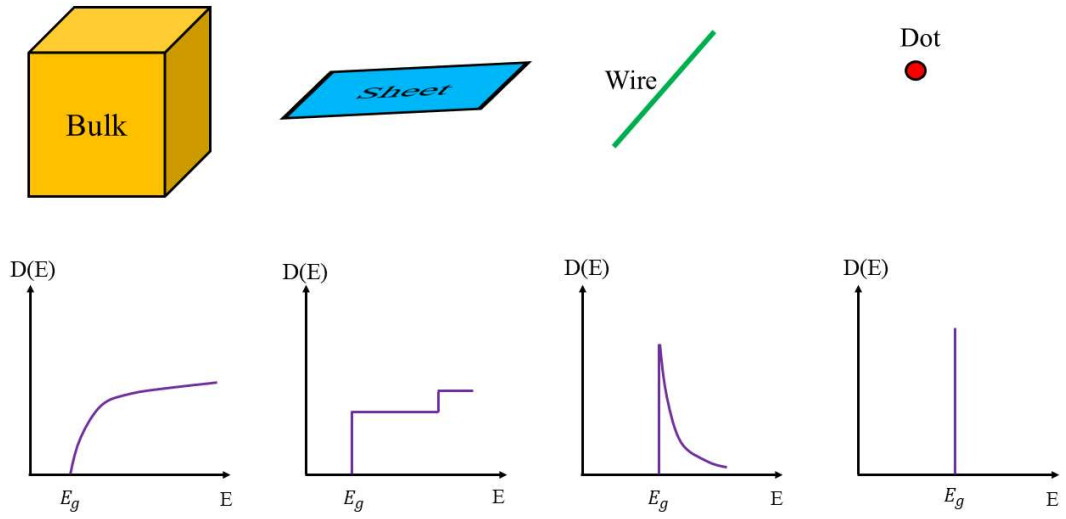

Fig. 1. 1 Schematic illustrating the D(E) as a function of energy for materials in different dimensions

1.3.2.1 Zero-Dimensional (0D) nanomaterials

Zero-dimensional (0D) NMs are characterized by QC in all three spatial dimensions (x, y, and z), such that charge carriers are restricted within a region comparable to or smaller than their exciton Bohr radius. This means that electrons are restricted in every direction, resulting in discrete, quantised energy levels– a phenomenon known as QC. Common examples include QDs, NPs, and fullerenes. These materials often exhibit spherical or quasi-spherical shapes and possess a high surface-to-volume ratio, which enhances their chemical reactivity and provides many active sites per unit mass [33]. The unique optical and electronic properties of 0D NMs, such as size-dependent PL

and high quantum yield (QY), make them highly valuable for applications in bioimaging, sensing, and optoelectronics [34,35].

1.3.2.2 One-Dimensional (1D) nanomaterials

1D NMs exhibit QC in two spatial dimensions, while charge carriers are free to move along one direction. This anisotropic confinement gives rise to unique electronic and optical properties, such as Van Hove singularities in the DOS. Common examples include nanowires, nanotubes, and nanorods, which typically appear as needle-like or wire-like forms [36,37]. In 1D NMs, electrons may move without restriction along the elongated axis but are limited in the other two directions, which leads to the step-like DOS and the extraordinary transport properties. These materials may be in the form of crystals or a glassy state, metals, ceramics, or polymers, and can be either the main agents or those absorbed in other media. Their high aspect ratio and efficient charge transport make them ideal for applications in nanoelectronics, sensors, and energy storage [38,39].

1.3.2.3 Two-Dimensional (2D) nanomaterials

2D NMs are confined in only one spatial dimension, with their thickness reduced to a few atomic layers, while charge carriers remain free to move in the other two directions. Such materials exhibit step-like DOS and strong QC and surface effects. This results in sheet-like or plate-like structures, such as nanosheets, nanofilms, and layered materials like transition metal dichalcogenides (TMDs) are prominent examples of 2D NMs [40,41]. In these materials, electrons are confined in the thickness direction but are free to move in the plane, leading to a constant DOS within each sub-band. The large surface area and tunable electronic properties of 2D NMs make them highly attractive for sensing, catalysis, and flexible electronics [42,43].

1.3.2.4 Three-Dimensional (3D) nanomaterials

3D NMs lack QC, as their dimensions extend beyond the nanoscale in all three directions. They exhibit a continuous DOS like that of bulk materials, but may still show enhanced surface reactivity when composed of nanosized grains or particles. Some of these are nanocubes, nanonetworks, and bulk nanocomposites. In 3D NMs,

the electrons are free to move, and the DOS is continuous, like in bulk materials. Such materials may retain the properties of their nanoscale components and thus, they can be mechanically stronger, more catalytically active, and multifunctional [44,45]. 3D NMs find extensive applications in the field of structural materials, as porous materials, and as the supports for catalysis and adsorption [14,46].

1.4 Quantum Size Effects

At the nanoscale, materials exhibit properties that deviate markedly from their bulk counterparts due to QC. When the dimensions of a material approach the de Broglie wavelength of electrons, the motion of charge carriers becomes restricted, resulting in discrete energy levels rather than continuous bands. This phenomenon, known as the quantum size effect, leads to several notable changes [34,47].

1.4.1 Tunable electronic and optical properties

As the particle size decreases, the QC effect causes an increase in the band gap energy, which results in a noticeable blue shift in the absorption and emission spectra of NMs, as represented by Fig. 1.2. This size-dependent tunability of electronic and optical properties is central to the design of nanoscale devices and sensors [48].

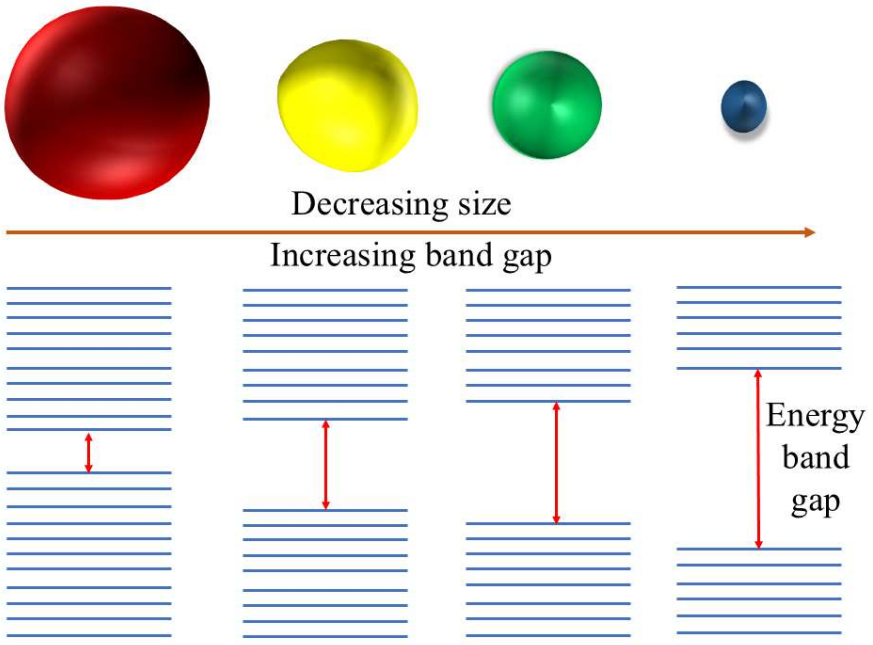

Fig. 1. 2 Schematic represents how reducing the QD size leads to an increased energy band gap

1.4.2 Enhanced surface effects

The surface-to-volume ratio rises sharply, so a larger fraction of atoms are at or near the surface, increasing chemical reactivity and altering thermal and mechanical properties [48,49].

1.5 Two-Dimensional (2D) Nanomaterials: Emergence and Significance

Graphene, a single layer of carbon atoms arranged in a 2D honeycomb lattice, marked the beginning of a new era in materials science following its successful isolation in 2004 by Geim and Novoselov. Its extraordinary physical properties—such as high carrier mobility (~2×10^5 cm^2 V^{-1} s^{-1}), excellent thermal conductivity (~5000 W m^{-1} K^{-1}), mechanical strength (Young's modulus ~1 TPa), and optical transparency (~97.7%)—established it as a model 2D material and triggered immense research activity worldwide [50]. The linear dispersion relation near the Dirac points yields massless Dirac fermion behaviour, which gives graphene its unique electronic and transport characteristics. Owing to these exceptional features, graphene was initially envisioned as a potential material for next-generation electronic, photonic, and energy devices. However, despite its outstanding properties, graphene also exhibits fundamental limitations that restrict its applicability in semiconductor-based technologies. The most critical drawback is the absence of an intrinsic band gap, resulting in a semi metallic nature with a zero-band gap. This makes it extremely difficult to achieve a high on/off current ratio in graphene-based field-effect transistors, a requirement for logic switching applications. Various approaches, such as chemical functionalization, doping, substrate-induced band gap opening, and QC in graphene nanoribbons, have been attempted to overcome this issue, but these often degrade carrier mobility and compromise structural integrity. Additionally, graphene's chemical inertness and lack of out-of-plane bonding hinder its interaction with many molecules, limiting its use in chemical sensing and catalysis without surface modification. The absence of strong light absorption near the band edge also restricts its efficiency in optoelectronic devices such as photodetectors and solar cells. Moreover, the large-scale synthesis of defect-free, monolayer graphene with uniform thickness remains challenging, as methods such as chemical vapor deposition (CVD)

or chemical exfoliation often produce multilayered or defect-rich films. Thus, while graphene has revolutionised research on 2D materials, these inherent limitations have motivated the exploration of alternative layered materials that possess tunable band gaps, rich chemistry, and diverse functionalities. In this context, TMDs have emerged as promising candidates, combining the advantages of a 2D morphology with semiconducting behaviour and versatile optoelectronic properties.

1.5.1 Transition metal dichalcogenides

TMDs represent an important class of layered 2D materials with the general chemical formula MX_2, where M is a transition metal such as molybdenum (Mo) or tungsten (W), and X is a chalcogen such as sulfur (S), selenium (Se), or tellurium (Te). Each monolayer consists of a hexagonally packed plane of metal atoms sandwiched between two planes of chalcogen atoms, forming a stable X–M–X structure. Fig. 1.3 represents the stacking sequence and structural unit cells of 2H-trigonal prismatic, 1T-octahedral, and 3R-distorted octahedron phase. Adjacent layers are held together by weak van der Waals forces, allowing them to be mechanically or chemically exfoliated into monolayers or few-layer nanosheets. The intrinsic semiconducting nature of many TMDs, along with their thickness-dependent electronic properties, distinguishes them from graphene, which is gapless. Several TMDs undergo a transition from an indirect band gap in bulk to a direct band gap in the monolayer, resulting in significantly enhanced optical absorption, strong PL, and pronounced excitonic effects. Beyond electronic and optical properties, TMDs also exhibit versatile chemical reactivity, layer-dependent mechanical strength, and tunable catalytic activity. These characteristics make TMDs promising candidates for applications in optoelectronics, catalysis, sensing, energy storage, and flexible electronics. The vast compositional and structural diversity within TMDs enable researchers to tailor their properties for specific applications by controlling layer number, phase, morphology, and defect density, establishing them as a central focus of contemporary 2D materials research.

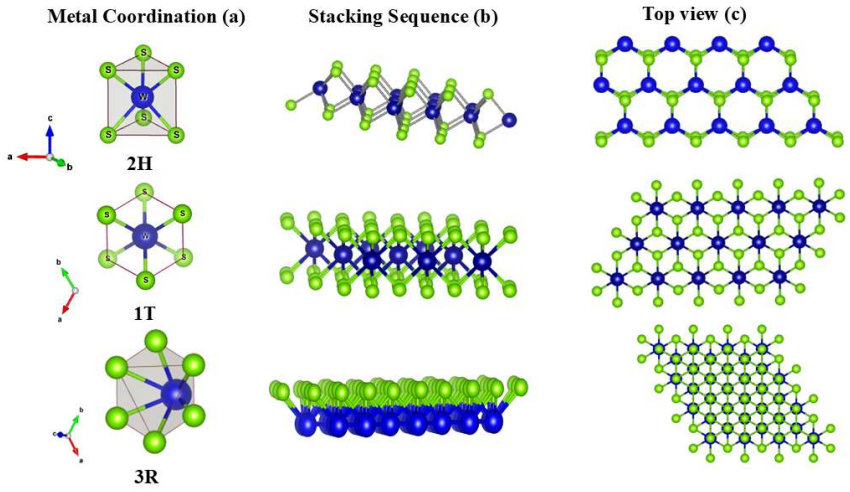

Fig. 1. 3 Metal coordination's (a), stacking sequences (b), and top view (c) of WS2 structural unit cells (2H-trigonal prismatic, 1T-octahedral and 3R-distorted octahedron phase).

TMDs such as Tungsten disulfide (WS_2) and molybdenum diselenide ($MoSe_2$) share a layered crystal structure, where each monolayer consists of a plane of transition metal atoms (W or Mo) sandwiched between two planes of chalcogen atoms (S or Se), forming an X–M–X configuration. These monolayers are held together by strong covalent bonds within the plane and weak van der Waals forces between the planes, enabling easy exfoliation into 2D sheets. Both WS_2 and $MoSe_2$ typically crystallise in the stable 2H phase, which belongs to the hexagonal space group P63/mmc (No. 194) [51]. In this structure, the metal atoms (W or Mo) exhibit trigonal prismatic coordination, while the chalcogen atoms (S or Se) are arranged above and below the metal plane, resulting in a sandwich-like geometry. The lattice parameters are similar for both materials, with $MoSe_2$ having a lattice constant of approximately a =3.28 Å, c =12.92 Å, and WS_2 with a =3.24 Å, c =12.32 Å, [52]. The interlayer spacing is slightly larger in $MoSe_2$ due to the larger atomic radius of selenium compared to sulfur [53].

At the monolayer level, both materials maintain hexagonal symmetry and a thickness of about 0.7 nm [51,52]. The weak interlayer vander Waals interactions allow for the isolation of single or few-layer nanosheets, which is crucial for exploring their unique 2D properties. Stacking of these monolayers in the bulk leads to indirect bandgap semiconducting behaviour, while monolayer forms often display a direct bandgap, making them attractive for optoelectronic applications [51,54]. WS_2 and $MoSe_2$, two

prominent members of TMDs, exhibit remarkable electronic, optical, and catalytic properties that make them highly suitable for sensing and energy applications. Both materials are semiconducting with thickness-dependent direct bandgaps, approximately 2.0 eV for monolayer WS_2 and around 1.5 eV for monolayer $MoSe_2$, which enables efficient absorption and emission in the visible light spectrum [51].

QDs derived from WS_2 and $MoSe_2$ represent a class of 0D NMs that exhibit pronounced quantum confinement effects, resulting in discrete energy levels and size-dependent optical and electronic properties. These QDs are typically synthesised via bottom-up methods, such as hydrothermal, solvothermal, or ultrasonication-assisted reactions, which allow for precise control over particle size, crystallinity, and surface chemistry. Recent advances have enabled the production of WS_2 and $MoSe_2$ QDs with high crystallinity, narrow size distributions, and stable PL, making them attractive for integration into sensor platforms with enhanced sensitivity and selectivity. For example, hydrothermally synthesised WS_2 QDs have demonstrated stable fluorescence and water solubility, and their PL can be selectively quenched by analytes such as Fe^{3+}, enabling their use as sensitive probes for chemical and biological sensing [67]. WS_2 and $MoSe_2$ QDs display strong PL, with emission wavelengths tunable by adjusting the particle size. This tunability arises from the quantum size effect, where reducing the QD diameter increases the bandgap, leading to a blue shift in emission. The QDs also exhibit high surface-to-volume ratios, providing abundant active sites for chemical interactions, which is advantageous for sensing and catalytic applications [55,56]. Similarly, $MoSe_2$ QDs produced via hydrothermal or liquid-phase exfoliation methods have shown tunable PL and efficient charge separation, which are beneficial for photocatalytic and optoelectronic applications [51,57].

1.6 Scope and Overview of the Present Work

The present thesis focuses on the synthesis, characterization, and application of TMDs NSs, particularly WS_2 and $MoSe_2$ QDs, as multifunctional photoluminescent materials for chemical and biological sensing. Motivated by the unique optical tunability, high surface reactivity, and QC effects of TMD QDs, this research explores their potential as efficient fluorescent probes for detecting environmentally and biologically significant analytes. The work is structured around a systematic investigation of the

synthesis–structure–property relationships of these QDs and their sensing behaviour toward diverse targets. The synthesised WS_2 and $MoSe_2$ QDs are characterized using various spectroscopic and microscopic techniques to understand their size, morphology, optical transitions, and defect states. Subsequently, their PL responses are utilised for the selective and sensitive detection of hydrogen peroxide (H_2O_2), 2,4,6-trinitrophenol (2,4,6-TNP), hexavalent chromium ions (Cr^{6+}), and the antibiotic amoxycillin (AMX), as well as Vitamin B12 (Cbl), among other substances. The underlying quenching mechanisms, including inner filter effect, charge transfer, and dynamic quenching, are analysed in detail to elucidate the interaction pathways between the QDs and analytes. Overall, the thesis aims to establish a comprehensive understanding of how compositional variation, surface chemistry, and excitation-dependent emission in WS_2 and $MoSe_2$ QDs can be exploited for real-world sensing applications.

Chapter 2: Experimental Tools and Techniques

2.1 Synthesis of Nanomaterials

The fabrication of NMs can be categorised into two main processes: top-down and bottom-up, as illustrated in Fig. 2.1. One method alone cannot overcome all NSs' challenges; thus, hybrid approaches combining the advantages of both methods are being developed.

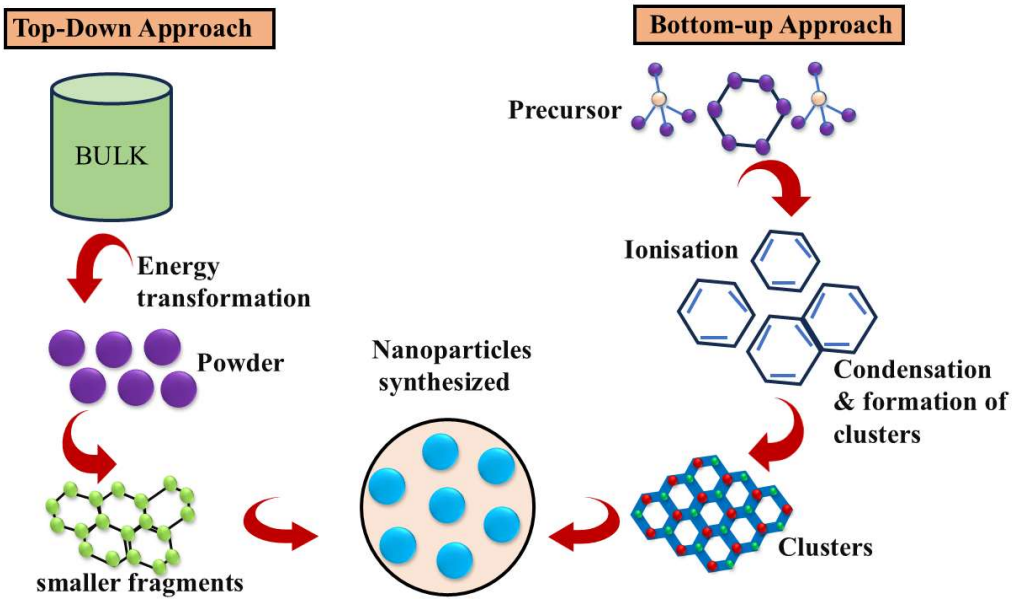

Fig. 2. 1 Illustration of top-down and bottom-up strategies for the synthesis of NPs.

2.1.1 Top-Down Techniques

Top-down methods start with bulk materials and break them down into nanoscale structures through physical or chemical processes. These are typically subtractive techniques, where the original material is reduced in size:

2.1.1.1 ***Mechanical Grinding (Ball Milling):*** Bulk materials are mechanically ground to a powder of a small particle size. NPs are commonly produced by ball milling in

various industrial processes due to their ease of scalability and straightforwardness; however, they can still cause the generation of defects and a wide size distribution.

2.1.1.2 ***Lithography:*** This technique uses light, electrons, or ions to pattern materials at the nanoscale. Photolithography and electron-beam lithography are essential for fabricating nanoarchitectures in microelectronics and nanodevices.

2.1.1.3 ***Etching:*** Chemical or plasma etching selectively removes material to create nanoscale features. It is often combined with lithography for precise patterning.

2.1.1.4 ***Erosion:*** Physical or chemical erosion processes, such as laser ablation or ion beam milling, are used to sculpt NSs from bulk materials.

Top-down approaches can be effective for generating vast amounts of NMs and for involving NSs in existing devices. However, these methods may still have some drawbacks, such as defects, high prices, and a smaller extent of atomic-scale feature control [58,59].

2.1.2 Bottom-Up Techniques

Bottom-up methods construct nanomaterials atom by atom or molecule by molecule, starting from gaseous or liquid precursors. These additive techniques allow for fine control of the material's composition and structure:

28

2.1.2.1 ***Sol-Gel Method:*** Involves the transition of a system from a liquid 'sol' (colloidal suspension) to a solid 'gel' phase. It is widely used for synthesising metal oxide NPs and thin films.

2.1.2.2 ***Chemical Vapour Deposition:*** Gaseous reactants are deposited onto a substrate, where they react to form thin films or NSs. CVD is crucial for producing high-purity, uniform NMs, including 2D materials like TMDs [25].

2.1.2.3 ***Physical Vapour Deposition:*** The material is first vaporised and then condensed into a thin layer on a substrate. The method is used for creating nanoscale metals, semiconductors, and composites [60].

2.1.2.4 ***Electrochemical Deposition:*** NMs are synthesised by electrochemical reactions at electrodes, allowing for controlled growth of NSs such as nanowires and coatings.

2.1.2.5 ***Atomic Layer Deposition:*** Thin films are fabricated one layer at a time through alternating exposure to precursor gases, providing the materials with control for both thickness and composition at the atomic scale.

2.1.2.6 ***Hot Injection Method*****:** This method is an extensively used bottom-up technique for synthesising NMs, especially QDs and other colloidal nanocrystals. Essentially, a cold precursor solution is quickly injected into a hot solvent that contains surfactants or stabilising agents, usually at temperatures exceeding 150°C. This sudden injection creates a high level of supersaturation, which imparts the nucleation of NPs immediately followed by a controlled growth phase. One of the primary benefits of this method is the ability to isolate the nucleation and growth phases of the process. Despite its strengths, this method can be challenging to scale up due to the need for rapid and uniform mixing, as well as precise temperature control. Furthermore, the method is also very sensitive to slight changes in the concentration of the reactants and the injection rate, which can yield different results each time the experiment is repeated [61–63].

2.1.2.7 ***Hydrothermal Synthesis:*** Hydrothermal synthesis is a solution-based technique that enables the formation of NMs under elevated temperature and pressure in a sealed vessel known as an autoclave. This method is inspired by natural geological processes and is particularly effective for producing crystalline phases that are difficult or impossible to obtain by conventional high-temperature methods [45,64,65].

Working Mechanism of Hydrothermal Method

The process begins by dissolving precursor materials in water or another solvent, generally with the addition of mineralizers to enhance solubility. The solution is transferred to a Teflon-lined or steel autoclave, which is then sealed and heated to temperatures typically above 100°C, generating high vapour pressure inside the vessel. The high temperature and pressure increase the solubility and reactivity of the precursors, thereby facilitating nucleation and crystal growth. Depending on the

synthesis strategy, a temperature gradient may be maintained within the autoclave, allowing the nutrient to dissolve at the hotter end and crystallise at the cooler end, or the entire vessel may be cooled gradually to induce supersaturation and crystallisation. Fig. 2.2 represents the Schematic of a typical hydrothermal synthesis vessel, showing the Teflon cup containing water and solid reagents, enclosed by a stainless-steel shell and lid, with a bursting disc for pressure control.

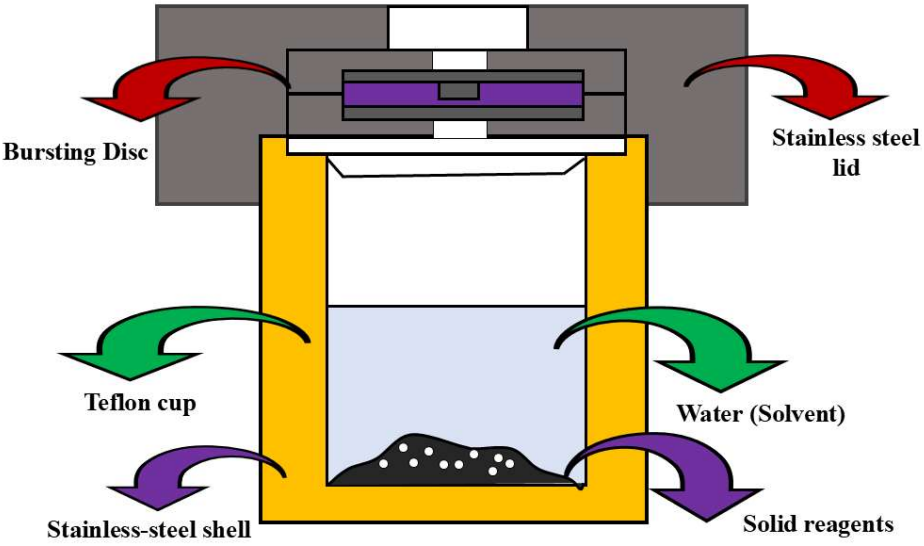

Fig. 2. 2 Schematic representation of a typical hydrothermal experimental setup.

Key Parameters and Control

65

The morphology, size, and crystallinity of the final NMs can be quantitatively controlled by adjusting the synthesis parameters, including temperature, pressure, pH, reaction time, and precursor concentration. For example, lower temperatures and shorter reaction times favour the formation of kinetically stable phases, while higher temperatures and longer durations promote thermodynamically stable products. The use of mineralizers (e.g., NaOH, KOH) can further influence the solubility and growth kinetics, enabling the synthesis of diverse NSs such as rods, sheets, spheres, and hollow particles [66,67].

Advantages of Hydrothermal Synthesis

1. ***Versatility:*** *Capable of producing a wide range of NMs, including oxides, chalcogenides, and complex structures.*

2. ***Morphology and Size Control:*** *Fine-tuning of synthesis conditions allows for precise control over particle shape and size.*

3. ***High Purity and Crystallinity:*** *The method yields highly crystalline products with fewer defects, which is essential for advanced applications.*

4. ***Eco-Friendly:*** *Often uses water as the solvent and requires lower energy input compared to other methods.*

5. ***Access to Unique Phases:*** *Enables the synthesis of materials that are unstable or have high vapour pressure near their melting points.*

For TMDs such as MoS_2, WS_2 and $MoSe_2$, hydrothermal synthesis is especially advantageous. It allows for the controlled growth of uniform nanosheets and QDs with tailored properties, which are critical for high-performance sensing applications. The ability to adjust reaction conditions enables the optimisation of the surface area, crystallinity, and defect density of TMD NMs, directly impacting their sensitivity and selectivity in chemical and biological sensors [68–70].

2.2 Characterization Techniques

After synthesizing NMs, it is essential to carefully characterise them to understand their structure and properties. Characterization techniques help reveal important details such as particle size, shape, crystal structure, chemical composition, and optical behaviour. These methods allow researchers to see how the materials are built at the atomic level and to measure how they interact with light and other substances. This chapter presents the experimental procedures and advanced characterisation techniques employed throughout the thesis to analyse the synthesised NMs. A comprehensive approach was adopted to ensure accurate determination of structural, morphological, compositional, and optical properties, which are crucial for understanding the behaviour and performance of NPs in various applications.

Structural and compositional information was obtained using X-ray diffraction (XRD), high-resolution transmission electron microscopy (HR-TEM), and X-ray

photoelectron spectroscopy (XPS). Functional groups and molecular interactions were identified by Fourier transform infrared spectroscopy (FT-IR). Optical properties, including absorption and emission behaviour, were studied using UV-visible spectroscopy and PL measurements. PL lifetimes and excited-state dynamics were further explored with time-correlated single photon counting (TCSPC).

Together, these techniques offer a comprehensive toolkit for probing the structure, composition, and optical properties of NMs. The following sections present ray diagrams and concise descriptions of each characterization method, detailing their working principles, instrumentation and operational features to facilitate a deeper understanding of the experimental approaches used in this thesis.

2.2.1 X-ray Diffraction (XRD)

X-ray diffraction is a fundamental and widely used technique for characterizing the crystal structure, phase composition and lattice parameters of crystalline materials, including NMs. The technique is non-destructive and requires minimal sample preparation, making it ideal for routine analysis of powders, thin films, and bulk samples.

The method is based on the interaction of monochromatic X-rays with the periodic atomic planes in a crystal. When a finely ground, homogenized sample is irradiated with X-rays, the atoms in the crystal lattice scatter the incident rays. Constructive interference occurs at specific angles, producing a diffraction pattern that is characteristic of the material's atomic arrangement [71].

The principle underlying XRD is Bragg's law (Fig. 2.3), which relates the wavelength of the X-rays (λ), the interplanar spacing (d), and the angle of incidence (θ) as follows:

$$2dSin\theta = n\lambda \quad (2.1)$$

Where n is an integer representing the order of reflection. When the Bragg condition is satisfied, the diffracted X-rays reinforce each other, resulting in detectable peaks in the diffraction pattern. By scanning the sample over a range of 2θ angles, all possible diffraction directions are sampled due to the random orientation of crystallites in a

powder specimen. Each material exhibits a unique set of d-spacings, allowing for phase identification by comparison with standard reference patterns.

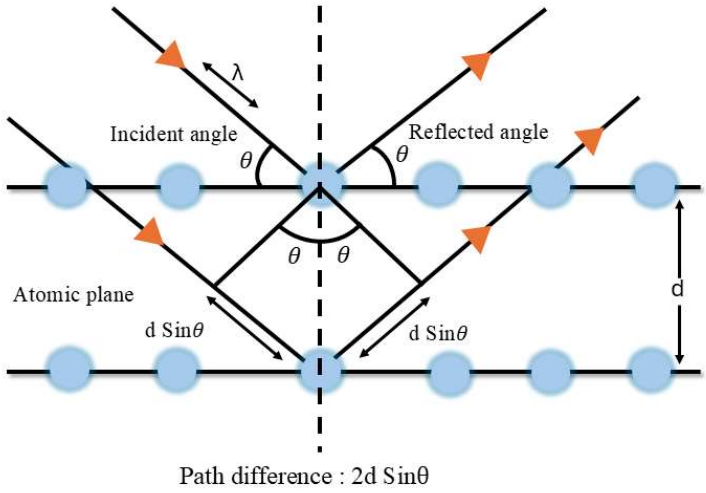

Fig. 2. 3 Schematic representation of Bragg's law of X-ray diffraction.

A typical X-ray diffractometer consists of an X-ray tube (commonly with a copper target for CuK_{α} radiation, λ=1.5418 Å), a sample holder and a detector mounted on a goniometer. The X-ray tube generates X-rays by accelerating electrons toward a metal target, resulting in the production of characteristic X-ray lines. The monochromatic X-rays are collimated and directed onto the sample and the diffracted rays are detected as the sample and detector rotate through preset angles. The resulting diffraction pattern is recorded as intensity versus 2θ and the positions and intensities of the peaks provide information about the crystal structure, unit cell dimensions, and crystallite size. The schematic representation of X-ray diffractometer is shown in Fig. 2.4.

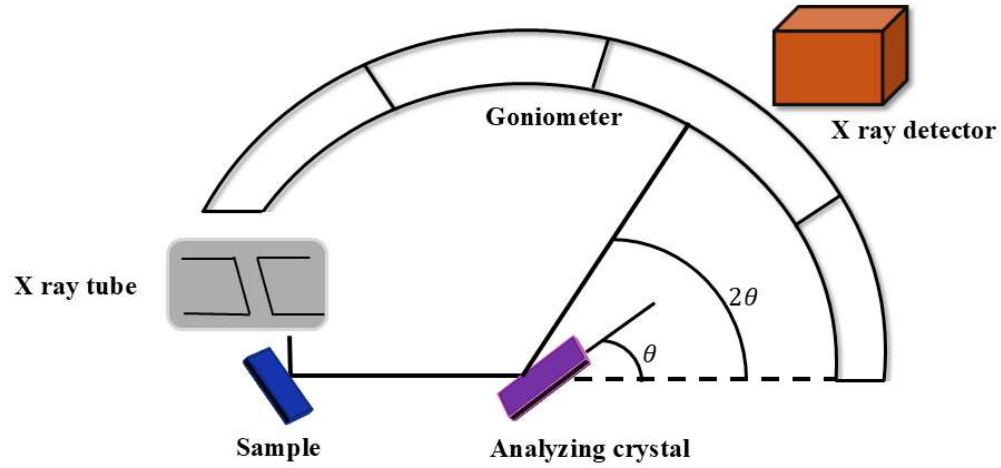

Fig. 2. 4 Schematic representation of an X-ray diffractometer.

XRD is especially valuable for NMs, as it can reveal not only phase composition and crystallinity but also estimate average crystallite size through peak broadening analysis. This is achieved using the Scherrer equation, which relates the crystallite size (D) to the wavelength of the X-ray radiation (λ), the full width at half maximum (FWHM, β) of diffraction peaks, and the Bragg angle (θ):

61

$$D = \frac{K\lambda}{\beta_{1/2}\cos\theta} \tag{2.2}$$

Here, K is a dimensionless shape factor dependent on the crystallite geometry, typically~ 0.9. The broadening of diffraction peaks, after correction for instrumental contributions, arises primarily from the finite size of coherently diffracting crystalline domains. Smaller crystallites result in broader peaks, allowing this formula to provide an approximate average size. It is important to note that the Scherrer equation estimates the size of crystal domains, which may differ from particle size, especially when particles are aggregates of multiple crystallites [72].

XRD measurements in this thesis were carried out in reflection mode using a Bruker D8 Advance powder X-ray diffractometer (Fig. 2.5) operated at 45 kV with Cu Kα radiation (λ = 1.546 Å).

Fig. 2. 5 Image of Bruker D8 Advance powder X-ray diffractometer.

2.2.2 Fourier Transform Infrared Spectroscopy (FT-IR)

FT-IR is a crucial analytical technique used to identify and characterize materials based on their molecular vibrations. In FT-IR, infrared radiation passes through a sample, where specific frequencies are absorbed by the material, depending on its molecular structure, while the remaining radiation is transmitted. The resulting unique spectrum reflects the vibrational modes of the functional groups present in the material, which acts as a molecular fingerprint. Unlike traditional dispersive spectroscopy, FT-IR employs an interferometer to simultaneously measure all infrared frequencies, significantly reducing scan times from minutes to seconds. The collected interferogram, containing combined frequency information, is converted to a frequency spectrum through Fourier transformation by the instrument's computer system (Fig. 2.6).

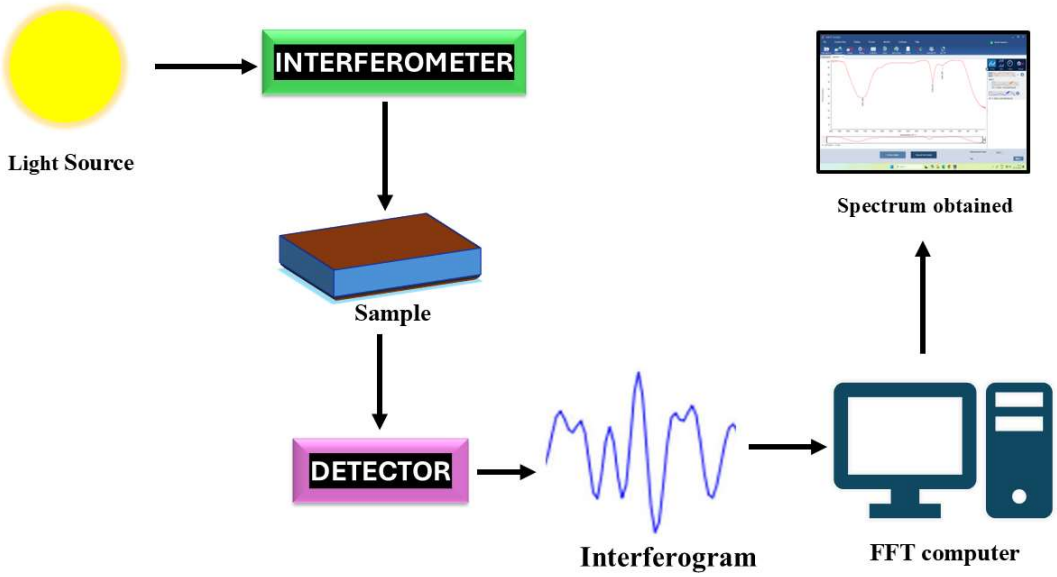

Fig. 2. 6 Schematic representation of FTIR instrumentation.

FT-IR spectrometry offers several instrumental advantages. It offers high scan speed (Fellgett advantage), high sensitivity due to greater optical throughput (Jacquinot advantage) and precise wavelength calibration using a He–Ne laser (Connes advantage). The instrument also features mechanical simplicity, ensuring stability and reliability during routine analyses [73,74].

FT-IR measurements in this thesis were performed using two different spectrometers: a Perkin Elmer, Two-spectrum FT-IR spectrometer, and a thermoscientific Nicolet Summit X FT-IR spectrometer. Both instruments operated in the wavenumber range of 400-4000 cm^{-1} (Fig. 2.7).

Fig. 2. 7 Image of thermoscientific Nicolet Summit X FT-IR spectrometer.

2.2.3 High-Resolution Transmission Electron Microscopy (HR-TEM)

HR-TEM is a powerful analytical technique used to study the morphology, size, lattice structure and crystallinity of NMs at the atomic scale. It provides information in both real and reciprocal space through imaging and selected area electron diffraction (SAED) patterns, respectively.

It operates by transmitting a highly focused beam of high-energy electrons (typically several hundreds of kV) through an ultra-thin specimen. The electrons interact with the sample's atomic planes, producing an interference pattern that forms a magnified image revealing lattice fringes and structural defects at the atomic scale.

The electron beam is generated by a thermionic or field emission gun and focused by electromagnetic lenses into a monochromatic beam before passing through the specimen. Transmitted electrons are further magnified using objective and projector lenses and then collected by detectors such as a charge-coupled device (CCD) camera or phosphor screen. Contrast in HR-TEM images arises from variations in sample thickness and density, with denser regions appearing darker due to greater electron scattering. HR-TEM enables the direct visualisation of lattice fringes and atomic arrangements, allowing for the determination of interplanar spacing (d-spacing) and confirmation of the crystalline nature of the sample through SAED patterns [75]. It is

widely employed for analyzing lattice defects, dislocations, grain boundaries, stacking faults, and other structural features of NMs.

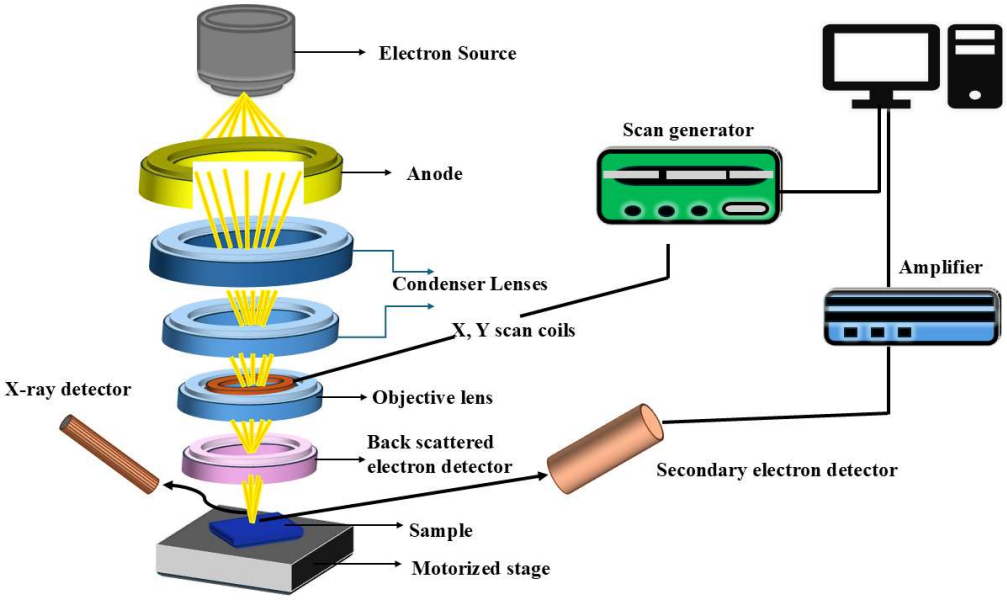

Fig. 2. 8 Schematic representation of the principle of the HR-TEM system.

HR-TEM analysis in this study was performed using the Thermo Scientific TALOS system, operated at an accelerating voltage of 200 kV, which enables high-resolution imaging critical for detailed structural characterization.

2.2.4 X-ray Photoelectron Spectroscopy (XPS)

XPS is a quantitative, surface-sensitive technique used to determine elemental composition, chemical states, and electronic environments within the top 1–10 nm of a material's surface. This enables precise identification and quantification of surface atoms, as well as insight into chemical bonding, oxidation state, and sample homogeneity.

The technique is based on the photoelectric effect, in which a material is irradiated with monochromatic X-rays, causing the emission of core-level electrons. The kinetic energy (E_k) of these emitted photoelectrons is measured and related to their binding energy (E_b) by the Einstein equation:

$$E_b = h\nu - E_k - \Phi \quad (2.3)$$

where $h\nu$ is the photon energy of the incident X-rays, and Φ is the work function of the spectrometer. Each element has a characteristic set of binding energies, which allows identification and analysis of the chemical state and electronic environment of atoms in the sample.

A typical XPS system is composed of three essential components: an X-ray source, an electron energy analyzer, and an ultra-high-vacuum chamber. The X-ray source provides monochromatic radiation, commonly Al K_α (1486.6 eV) or Mg K_α (1253.6 eV), which excites the core-level electrons of the sample atoms. The emitted photoelectrons are then analyzed by a hemispherical electron energy analyzer, which precisely measures their kinetic energy, enabling the determination of the corresponding binding energies. To ensure accurate measurements and minimize contamination or scattering of photoelectrons, the entire system operates under ultra-high vacuum conditions, typically around 10^{-9} mbar. In addition to these primary components, the system may include an electron or ion gun for in situ surface cleaning, as well as detectors for photoelectron counting and signal amplification. A schematic representation of the working principle of the XPS setup used in this study is illustrated in Fig. 2.9.

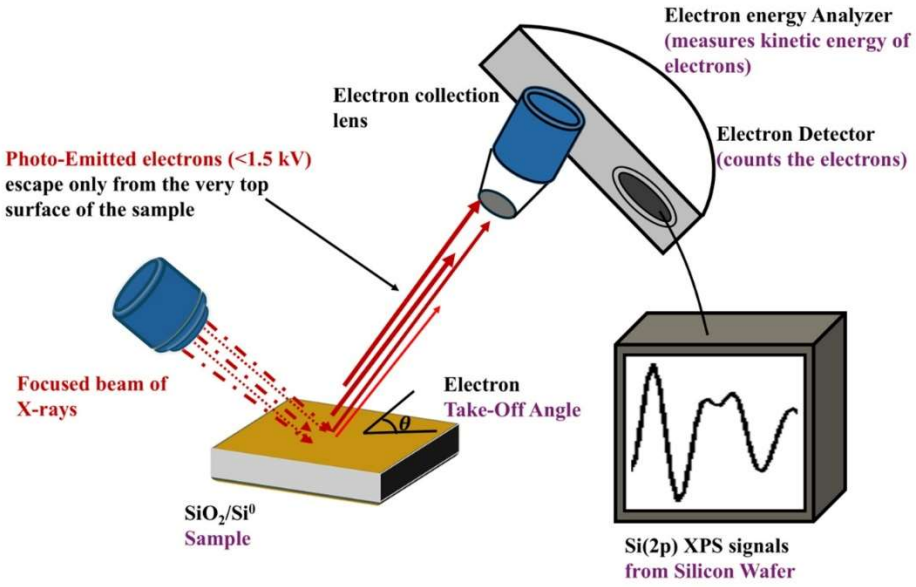

Fig. 2. 9 Schematic representation of the XPS system.

XPS analysis in this thesis was performed using a PHOIBOS 150 hemispherical analyser (SPECS system) with a monochromatic Al K_α source ($h\nu$ = 1486.6 eV) under an ultra-high vacuum (base pressure ~1 × 10^{-9} mbar). Spectra calibration was referenced to the C 1s peak of adventitious carbon at 284.8 eV, ensuring consistency across samples. Data analysis and peak deconvolution were performed in OriginLab using a Gaussian–Lorentzian fitting routine with linear background subtraction to resolve contributions from elements and their corresponding chemical states.

2.2.5 UV/Vis/NIR Absorption Spectrophotometer

Absorption spectroscopy is a fundamental optical characterization technique used to investigate the electronic and optical properties of semiconductor nanocrystals, thin films and bulk insulating materials. These materials exhibit distinct optical bandgaps and absorption occurs when incident photons possess sufficient energy to excite electrons from the valence band to the conduction band. The resulting absorption spectra provide valuable information about electronic transitions, excitonic features and the optical bandgap energy of the material.

Ultraviolet to near-infrared (UV/Vis/NIR) radiation is commonly employed to study these transitions, as it effectively covers the energy range relevant to most semiconductors. In this measurement, the sample is exposed to a beam of light and photons are absorbed by the electrons, while part of the light is transmitted. The spectrophotometer records the intensity of transmitted light (I) relative to the incident light intensity (I_0), generating a spectrum of absorbance (A) as a function of wavelength. The relationship follows the Beer–Lambert law, expressed as:

$$A = log\frac{I_0}{I} = \varepsilon cl \tag{2.4}$$

where A is absorbance, I_0 and I are incident and transmitted intensities, ε is the molar extinction coefficient, I is the path length and c is the concentration of absorbing species.

The UV/Vis/NIR spectrophotometer typically employs a deuterium lamp for UV and a tungsten halogen lamp for Vis/NIR, covering a wide spectral range from 190 to 3200 nm. The incident light beam is dispersed into its constituent wavelengths by a

diffraction grating or prism. The separated light is then divided into two beams using a half-mirror device, with one beam passing through a reference cuvette and the other through the sample cuvette. The system detects the transmitted intensities and computes absorbance using a ratio-recording method, ensuring high precision and baseline stability [76]. Fig. 2.10 demonstrates the ray diagram of instrumentation of UV/Vis/NIR spectrophotometer.

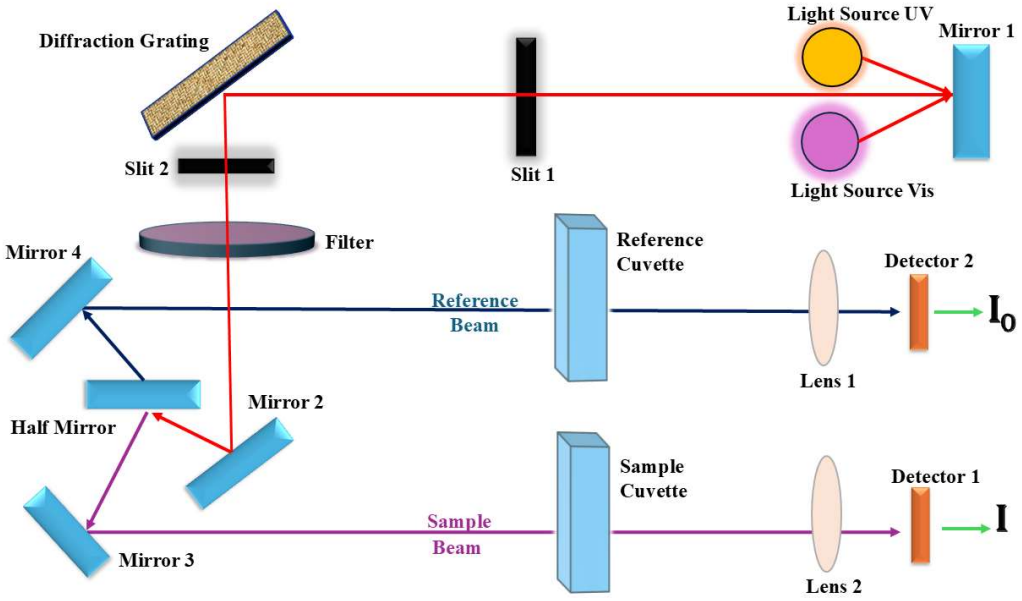

Fig. 2. 10 Ray diagram of UV/Vis/NIR absorption spectrophotometer.

This technique enables rapid, non-destructive analysis with minimal sample preparation, allowing for the reliable quantification of bandgaps and other parameters.

Absorption spectra measurements in this thesis were performed using a PerkinElmer Lambda-750 spectrophotometer (Fig. 2.11), which covers wavelengths from 190 to 3200 nm, equipped with automated electronics for precise data collection.

Fig. 2. 11 Photograph of UV/Visible/NIR spectrometer, Lambda-750, Perkin Elmer.

2.2.6 Photoluminescence (PL) Spectroscopy

PL spectroscopy is a powerful, non-destructive technique for probing the optical and electronic properties of NMs and semiconductors. In a typical PL spectrofluorometer setup, monochromatic light from a stable excitation source irradiates the specimen, initiating photon absorption. The emitted luminescence is then collected through a system of lenses and monochromators, dispersed according to wavelength and detected by a photomultiplier tube (PMT). The recorded signal is processed electronically and displayed as a spectrum of emission intensity versus wavelength, revealing the radiative recombination processes occurring within the material [77,78]. Fig. 2.12 shows the schematic ray diagram of the spectrofluorometer.

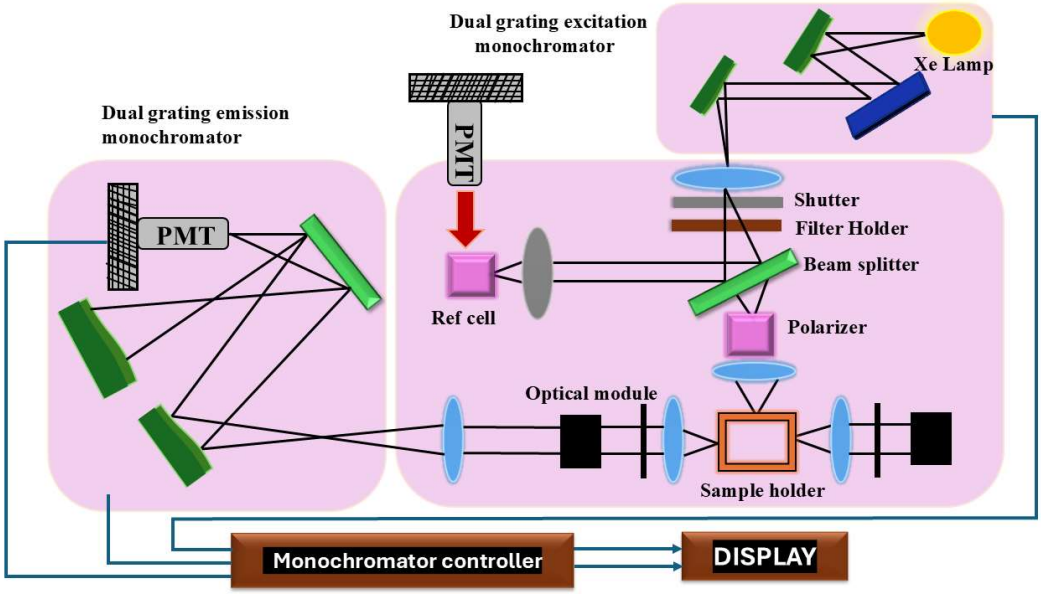

Fig. 2. 12 Ray diagram of Photoluminescence spectrofluorometer.

PL can be studied in both steady-state and time-resolved (TRPL) modes to distinguish radiative mechanisms, quenching and recombination dynamics. In steady-state PL, the emission intensity is recorded as a function of wavelength at a fixed excitation wavelength, whereas in photoluminescence excitation (PLE) spectroscopy, the emission wavelength is held constant and excitation intensity is varied to identify energy-specific transitions.

PL spectra in this thesis were recorded using two spectrofluorometers: a Horiba Scientific Fluorolog-3 spectrofluorometer (Fig. 2.13), equipped with double monochromators for high spectral resolution, a Hamamatsu R928P photomultiplier tube (PMT), and a 450 W xenon lamp and a customized JASCO spectrofluorometer (FP-8500). Measurements were typically performed at room temperature with tunable excitation and emission settings. The instrument configuration enables the precise determination of luminescence properties, which are crucial for optoelectronic and sensing applications.

Fig. 2. 13 Photograph of spectrofluorometer, Fluorolog-3, Horiba Jobin Yvon.

2.2.7 Time-Correlated Single-Photon Counting (TCSPC) System

TCSPC is a highly sensitive and precise optical characterization technique used for measuring PL lifetimes in the nanosecond and sub-nanosecond time domains. It operates on the principle of recording the time interval between the excitation of a fluorophore by a pulsed light source and the subsequent emission of a single photon. This time correlation enables the construction of a PL decay profile, providing crucial insights into radiative and non-radiative recombination processes within the material [79].

In a typical TCSPC setup, the specimen is excited using a pulsed laser or flash lamp of defined wavelength. Each excitation event generates PL photons that are detected by a PMT or a single-photon detector. The time difference between the excitation pulse and the detected photon is measured using a Time-to-Amplitude Converter (TAC). The TAC linearly charges a timing capacitor upon receiving a 'start' signal from the excitation pulse and stops charging when a 'stop' signal from the emitted photon is received, generating an output pulse whose amplitude corresponds to the time interval between the two events. These amplitudes are converted into a histogram of photon counts versus time channels, representing the PL decay curve of the sample, as represented in Fig. 2.14.

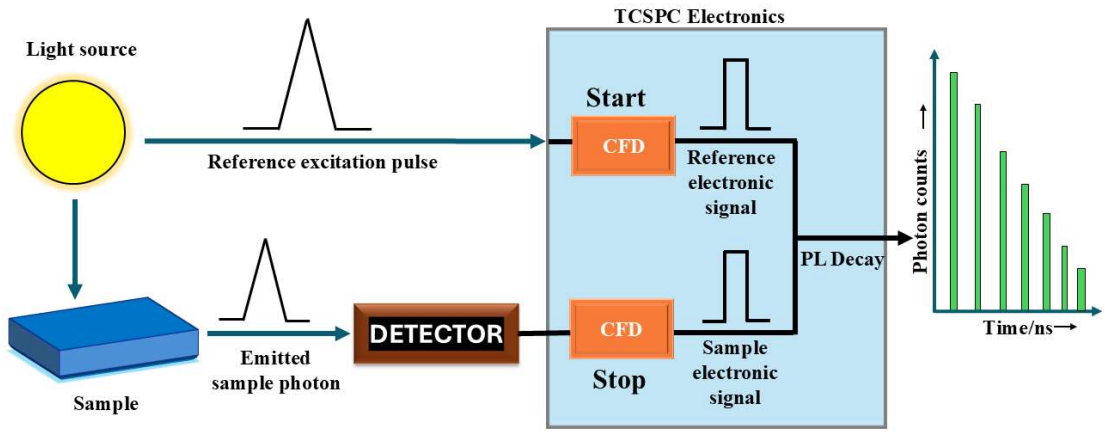

Fig. 2. 14 Schematic representation of the TCSPC system.

To ensure accurate lifetime determination, the Instrument Response Function (IRF)– which represents the temporal profile of the excitation pulse– is also recorded. The IRF is typically obtained by measuring the scattered light from a non-fluorescent reference material, such as LUDOX solution, through Stokes or Rayleigh scattering at the excitation wavelength. The measured decay curve is then deconvoluted with the IRF to yield precise lifetime values.

PL lifetime measurements in this thesis were carried out using a Horiba Jobin Yvon DeltaFlex-01-DD system equipped with a 320 nm DeltaDiode laser and a PPD.850 detector (Fig. 2.14). Data analysis and fitting were performed using the instrument's software, employing least-squares algorithms to extract accurate lifetimes.

Fig. 2. 15 Image of DeltaFlex-01-DD TCSPC measurement unit.

Chapter 3 In situ synthesis of WS_2 QDs for sensing of H_2O_2: Quenching and recovery of absorption and photoluminescence

3.1 Introduction

Due to their layered structure, diverse physical properties, and prospective uses in nanoelectronics and optoelectronics devices, transition metal dichalcogenides (TMDs) materials have piqued the interest of the scientific community [25]. Usually, TMDs are optically active materials due to their metallic or semiconducting characteristics, which depend on their structure. Especially, group-VI TMDs, such as WS_2, MoS_2 and WSe_2, exhibit semiconductor characteristics with a direct band gap [24,80], providing tunability in the band gap, high mobility, and vast surface area [81]. Moreover, TMDs have the standard formula MX_2 (M = Mo, W; X= S, Se, Te) composed of a transition metal atomic layer stacked between two chalcogen atom layers, depending on atomic stacking configurations. MX_2 can form two crystal structures, i.e., a trigonal prismatic (2H) phase and an octahedral (1T) phase (Scheme 3.1).

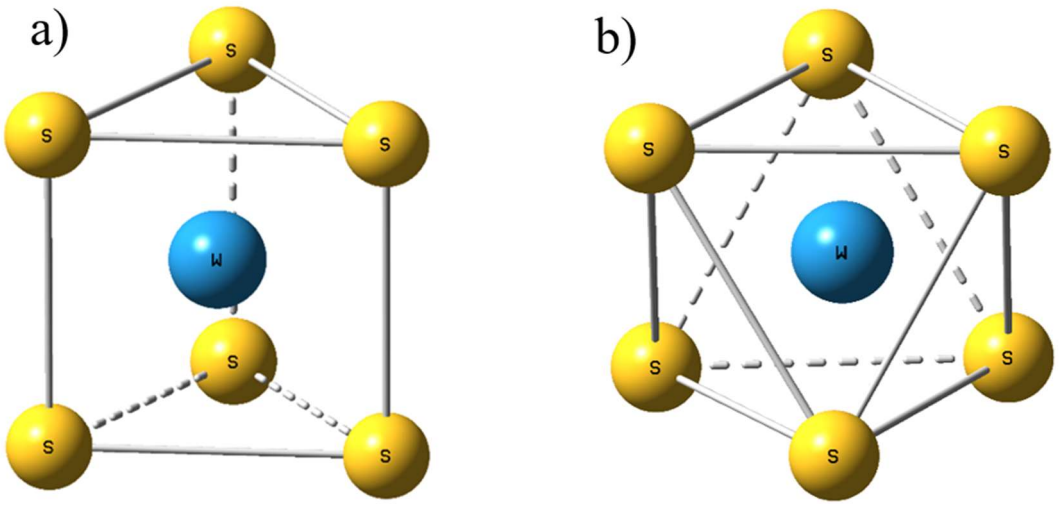

Scheme 3.1 *Trigonal prismatic (2H) WS_2 (a) and Octahedral (1T) WS_2 (b).*

Semiconductor TMDs quantum dots (QDs) such as WS_2, MoS_2, etc., with their unique properties such as strong fluorescence, high stability, low toxicity, and large surface area [17,82], allow them to be used in a variety of applications such as chemo and biosensors, energy harvesting and memory devices [82–84]. Due to their high photostability, they are also applicable in biomedical research such as gene delivery [24], drug delivery [19], diagnosis [17,82] and bio-imaging [85]. High quantum yield of photoluminescence (PL), broad absorption bandwidth and high photostability make them superior as PL probes to be used in sensing applications [86–88]. The advantage of QDs includes a narrow PL band, high quantum efficiency, active chemical sites for conjugation and high photostability [89,90].

An outstanding achievement has been obtained with some semiconducting TMDs such as MoS_2, $MoSe_2$, and WSe_2. WS_2 has also gained great attention due to its potential and sensing applications [91]. WS_2 consists of a crystal structure with the analogue of MoS_2; both Mo and W belong to the same column of the dichalcogenide family. WS_2 comprises S-W-S single layers through weak bonds, each of which comprises S atoms that contain two hexagonal planes. The intercalated hexagonal plane of W atoms binds with S atoms in a 2H configuration [92]. Each layer has a thickness of ~6 Å due to weak out-of-plane and strong in-plane covalent bonding in the presence of van der Waals forces, making it suitable for various applications such as optoelectronics, sensors, energy storage, catalysis, treatment, and bioimaging [64]. Reducing the layered structure from 2-D to 0-D leads to the formation of WS_2 QDs, resulting in strong blue PL under UV irradiation. Strong emission can be easily seen with the naked eye [11,29]. The formation of fluorescent WS_2 QDs leads to new physical and optical properties due to edge effects and strong quantum confinement [16,64]. WS_2 QDs have numerous active sites and a large surface-to-volume ratio, which extends beyond their monolayer 2D structures, enabling them to serve in photocatalysis-based applications [64,93,94]. The study of WS_2 QDs as a sensing probe is still in its early stage compared to other fluorescent materials, such as carbon QDs or semiconductor QDs [63,95,96], and it is interesting to study the fluorescent properties of WS_2 QDs as a probe [80,97].

Nowadays, the development of cost-effective, quickly responsive, and portable chemical sensors for detecting hazardous gases and explosives is in high demand due to the necessity for monitoring the ecological balance on Earth to protect human lives [65,98]. Hydrogen peroxide (H_2O_2) is a simple chemical compound, but it is essential in various fields such as mining, clinical, food manufacturing, and pharmaceutical applications. Excess H_2O_2 consumption harms the immune system. If the concentration of H_2O_2 exceeds a certain level, live cells will suffer from oxidative stress and substantial damage [99–101]. A higher elevation in the level of H_2O_2 generation also leads to various major diseases such as cancer, congestive heart failure, chest pains, and Alzheimer's disease. Therefore, detection of H_2O_2 is very important to maintain therapeutic interventions and for the proper etiology of diseases. Numerous tech niques were used to detect H_2O_2, such as spectrophotometry, chemiluminescence, fluorimetry, chemical titration, chromatography, etc [100–103]. To detect H_2O_2 concentration, electronic and optical methods may also be used. In electrochemical detection, electrons are generated through the catalytic reaction of H_2O_2, which is subsequently utilised as a current signal [41]. In the optical mode of detection, we have two types of signal-based studies: one utilises fluorescence signals, and the other employs surface plasmon resonance (SPR) [104]. Methods based on luminescent probes may be much more useful due to their high sensitivity, quick response, cost-effectiveness, and good selectivity [105].

In the present study, therefore, fluorescent WS_2 QDs have been synthesized in situ and examined whether these QDs can be used as an efficient sensing probe for H_2O_2 detection in an aqueous medium. Spectroscopic measurements confirmed the "turn OFF ON" mechanism with cyclic stability of the probe in the presence of H_2O_2. Naked eyes can also see the visible colorimetric response. It is shown that PL is quenched by ~98 % with H_2O_2 and that the quenched PL recovers entirely by adding a suitable amount of 0.1N of HCl.

3.2 Experimental section

3.2.1. Chemicals and reagents

Commercially available precursors and solvents having analytical purity were used in synthesis without further purification. Sodium tungstate dihydrate ($Na_2WO_4.2H_2O$, 96

%), H_2O_2, toluene, benzoic acid, benzene, aniline, benzaldehyde and HCl were procured from Thermo Fisher Scientific India Pvt. Ltd. L-cysteine ($HSCH_2CHNH_2COOH$, 98 %) was procured from Sigma Aldrich. For all experiments of H_2O_2 sensing, deionised (DI) water with a resistivity of 18.2MΩ·cm was used as a solvent.

3.2.2. Synthesis

WS_2 QDs were synthesised using the previously reported single-step and facile hydrothermal method with minor modifications [29]. Briefly, sodium tungstate and L-cysteine were dissolved into an aqueous medium simultaneously with a molar ratio of 1:2. The pH value of the solution was adjusted with a pH meter to be ~ 11.0 (basic) by using 0.1N NaOH solution with continuous stirring at 565 rpm at 30 ºC. After swirling for half an hour, the solution was sonicated for 20 min. Finally, the prepared solution was placed into a 100 mL stainless steel autoclave and vessel lined with Teflon. The hydrothermal vessel was kept for 36 h in the oven preheated to 200 ºC. After cooling down naturally, the vessel was taken out and the yellow-colored solution was centrifuged to get desired WS_2 QDs. Any additional capping, stabilising agent, or post-synthesis process was not necessary for the present synthesis. L-cysteine provides stability to the as-synthesised WS_2 QDs due to its photoresist property, making this method more attractive and straightforward. The systematic synthesis process for WS_2 QDs is illustrated in Scheme 3.2. The reaction that occurs during the synthesis is discussed in the next section.

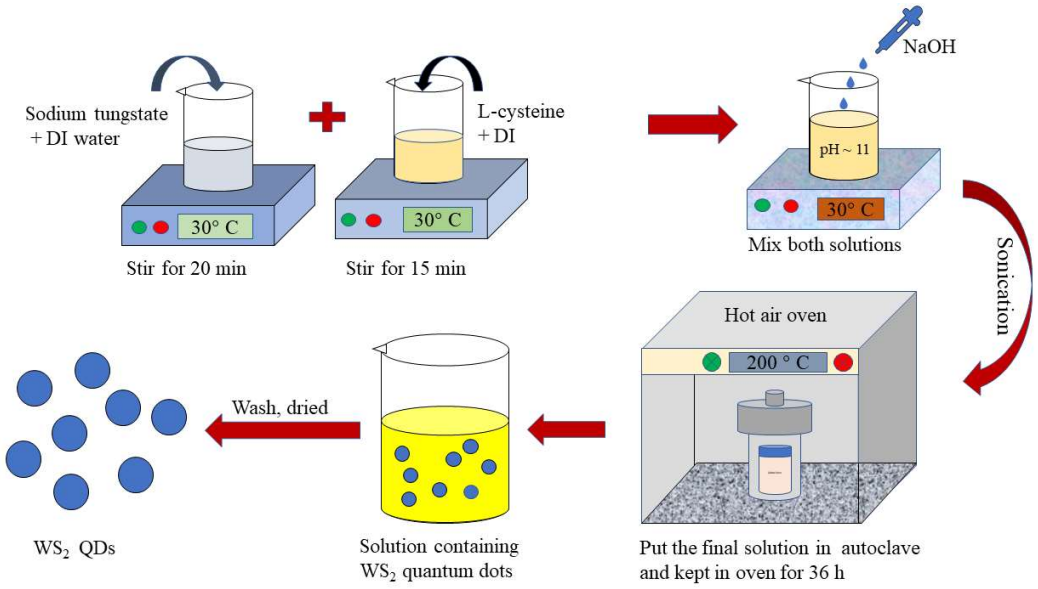

Scheme 3.2 *Synthesis processes of colloidal WS_2 QDs using a single-step hydrothermal growth method.*

3.2.3. Chemical reactions involved

L-cysteine interacts with DI water to form the simplest alpha-keto acids, i.e., pyruvic acid, having carboxylic acid and ketone functional groups, giving the emission of chalcogen hydride gas, which has the typical unpleasant stench of rotten eggs [64].

$$HSCH_2CHNH_2COOH + H_2O \rightarrow CH_3COCOOH + NH_3 + H_2S \uparrow$$

Tungstate reacts with the produced halide gas and pyruvic acid, resulting in the production of WS_2 QDs colloidal solution.

$$4\,WO_4^{2-} + 9\,H_2S + 6\,CH_3COCOOH \rightarrow 4WS_2 + SO_4^{2-} + 6CH_3COCOO^- + 12\,H_2O$$

3.2.4. Characterization tools

UV-visible absorption and PL spectroscopies are commonly used techniques to identify and detect chemically active species due to its high response even to small samples. The double beam UV/VIS/NIR spectrometer (Lambda 750, Perkin Elmer, USA) was used to measure steady-state absorption spectra. PL and PL-excitation spectra were recorded with Fluorolog-3 (Horiba Jobin Yvon). PL decay profiles were measured using a time-correlated single-photon counting (TCSPC) setup (DeltaFlex-01-DD, Horiba Jobin Yvon IBH Ltd), equipped with a detector (PPD 850) and a Delta Diode of 320 nm with a repetition rate of 4 MHz. The instrument response function (IRF) was captured by the Ludox scatterer. A transparent quartz cuvette cell, 1 cm in

length, was used for the measurements. Moreover, the experiments were carried out with WS_2 QDs upon adding various concentrations of H_2O_2 ranging from 0.33 nM to 594 µM. High-resolution transmission electron microscopic (HR-TEM) images were captured using TALOS thermo-scientific instruments with an accelerating voltage of 200 kV. Fourier transform infrared (FTIR) spectra in the range of 400 to 4000 cm^{-1} were obtained using FTIR spectrometers (Perkin Elmer).

3.3 Results and discussion

3.3.1. XRD and FTIR spectrum analysis

When TMDs changed from bulk to QDs, there was no clear evidence in the XRD pattern [106]. In most samples, there was no discernible signature in XRD patterns when the particle size was very small due to the creation of quantum dots [107]. Further, it was reported that there was no peak or signal in the XRD pattern of WS_2/MoS_2 [108]. In the present case, WS_2 QDs showed a hump corresponding to the (004) plane at $2\theta = 30°$, as shown in Fig. 3.1(a), and it matches well with the reported WS_2 QDs [106]. Figure 3.1(b) represents the FT-IR spectrum of the WS_2 QDs. The band at around 1045 cm^{-1} can be assigned to the C-O stretching vibration of hydroxyl groups [109]. The band at 1637 cm^{-1} represents the N-H out-of-plane and/or N-H_2 bending vibrations of the amide group [64]. The bands at 419 cm^{-1} and 2115 cm^{-1} are assigned to the W-S vibration and N=C stretching vibration, respectively [64,84]. The hydrophilic groups (-OH and -COOH) are considered to occupy the surface of the produced QDs. These groups contribute to the excellent water dispersibility of QDs, which significantly expands their sensing applications in aqueous environments, as exemplified by carbon dots [86].

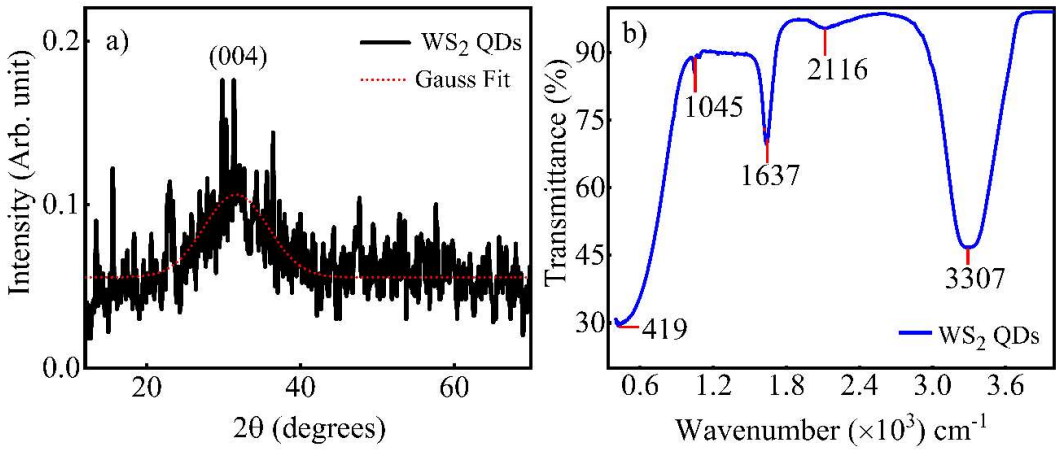

Fig. 3.1 *XRD pattern of the produced WS2 QDs thin film (a) and FT-IR spectrum of colloidal WS_2 QDs dispersed in water (b).*

3.3.2 HR-TEM analysis

The HR-TEM images of the synthesised WS_2 QDs at different magnifications are shown in Fig. 3.2. The HR-TEM images in Fig. 3.2(a,b) show that WS_2 QDs have a spherical, homogeneously distributed configuration with small aggregation of particles, whose size ranges from 2 to 5 nm. The ordered and paralleled lattice fringes demonstrate the crystalline nature of WS_2 QDs (Fig. 3.2a). The estimated crystal lattice *d* spacing of 0.2 nm corresponds to the (100) plane of WS_2 crystal, as shown in the inset of Fig. 3.2(a). The Gaussian distribution over the particles yields an average size of 4.5 nm as shown in Fig. 3.2(d). A narrow distribution of particles is helpful for further applications.

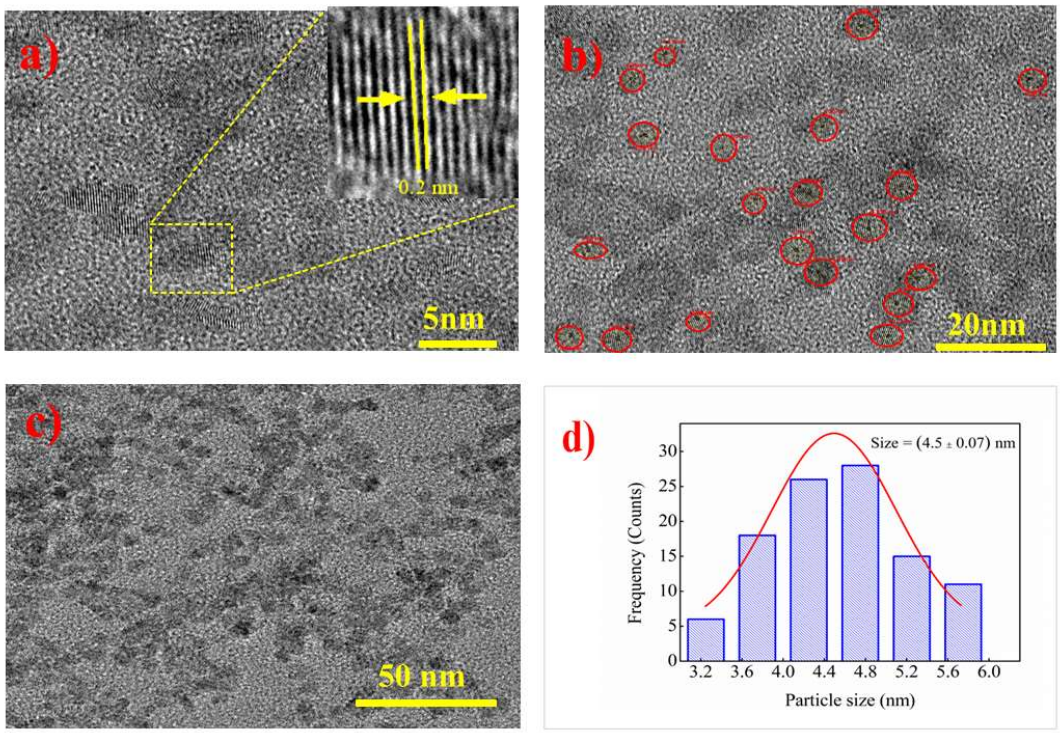

Fig. 3.2 *HRTEM images (a-c) of WS_2 QDs with particle size distribution (d).*

3.3.3. Optical properties of obtained WS2 QDs spectra

The absorption spectrum of colloidal WS_2 QDs dispersed in water is shown in Fig. 3.3(a), where the inset shows color images of WS_2 QDs observed under white light irradiation and UV light irradiation, respectively. The absorption spectrum shows intense bands at 334, 274 and 242 nm, along with a hump at 390 nm**.** The strong band at 334 nm corresponds to an excitonic absorption band caused by direct gap transitions at the K point in the Brillouin zone [106]. The band at 274 nm is caused by the optical transitions from the valance band to the conduction band, whereas the bands at 242 nm and 390 nm are considered to be caused by the absorption of surface-adsorbed functional groups such as sulphate or hydroxyl ions [64,108]. Figure 3.3(b) represents the PL spectra of WS_2 QDs observed at ambient temperature with different excitation wavelengths in the range of 280-450 nm. When the excitation wavelength (λ_{ex}) was shifted from 280 to 310 nm, the PL intensity increased, whereas the intensity decreased when λ_{ex} was shifted from 320 to 450 nm. With a shift of $\lambda_{ex}$from 280 to 400 nm, a gradual red shift of the PL peak was observed, as shown in Fig. 3.3(c). The maximum

shift of the PL peak was about 110 nm. At 310 nm excitation, the maximum PL intensity was observed at 415 nm with a full width at half maximum (FWHM) of 90 nm. The obtained FWHM and the excitation-dependent PL spectra indicate the possibility of numerous potential transition paths due to a considerable number of surface defects [110], as in the case of carbon nanodots [111]. The excitation-dependent PL spectra demonstrate polydispersity and/or inhomogeneous distribution of WS_2 QDs, which is understood in terms of carriers that may be produced and fall into localized states upon photoirradiation [88]. The carriers recombine radiatively or scatter into lower-energy localized states. Carriers having high excitation energy may recombine at highly localized states before the relaxation to the lowest state. If carrier relaxation in high localized states is slow, photons having high energy may be emitted [112], resulting in the excitation-wavelength dependent PL spectra [113].

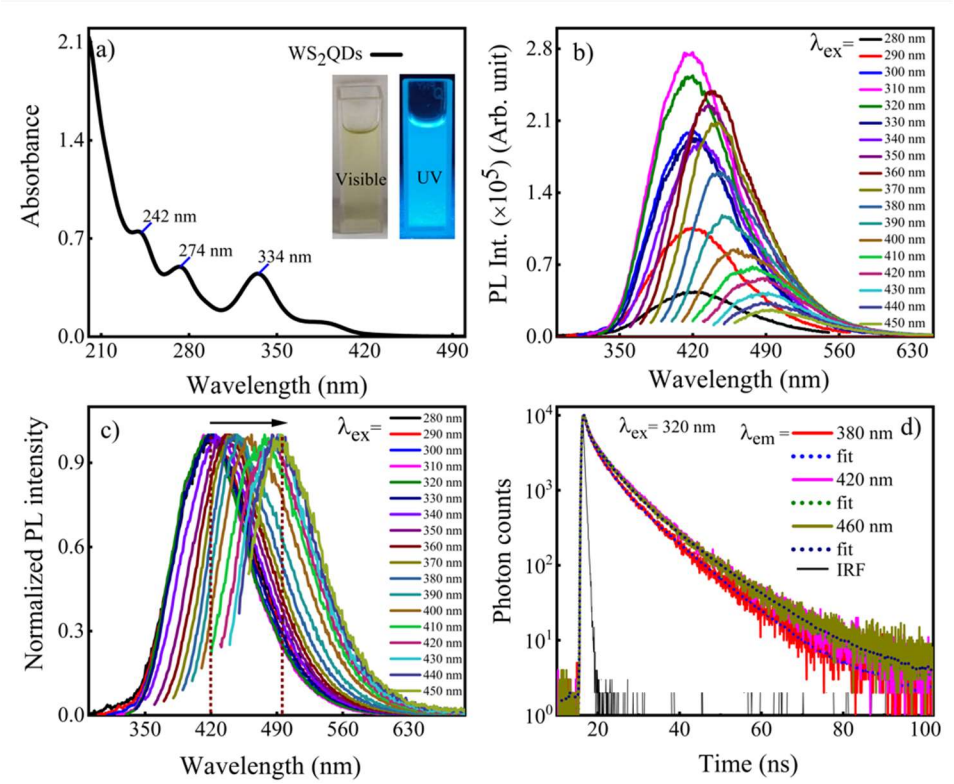

Fig. 3.3 *Absorption spectrum of WS_2 QDs dispersed in water. Inset represents the color photographs under visible illumination and UV irradiation (~365 nm) (a), The overlapped absorption and PL spectra WS_2 QDs (b). PL spectra of WS_2 QDs at the different excitation wavelengths (b) and the normalized spectra (c). Fitted decay curves of WS_2 QDs at 320 nm excitation and various PL wavelengths along with instrumental response function (d).*

Furthermore, PL excitation spectra were also observed by monitoring the emission at different wavelengths, as shown in Fig. 3.4. The PL excitation spectra are nearly independent of the monitoring wavelength, and a prominent band was observed at around 305 nm. It is also true that the PL band at around 360 nm showed a small blue shift with decreasing the monitoring wavelength.

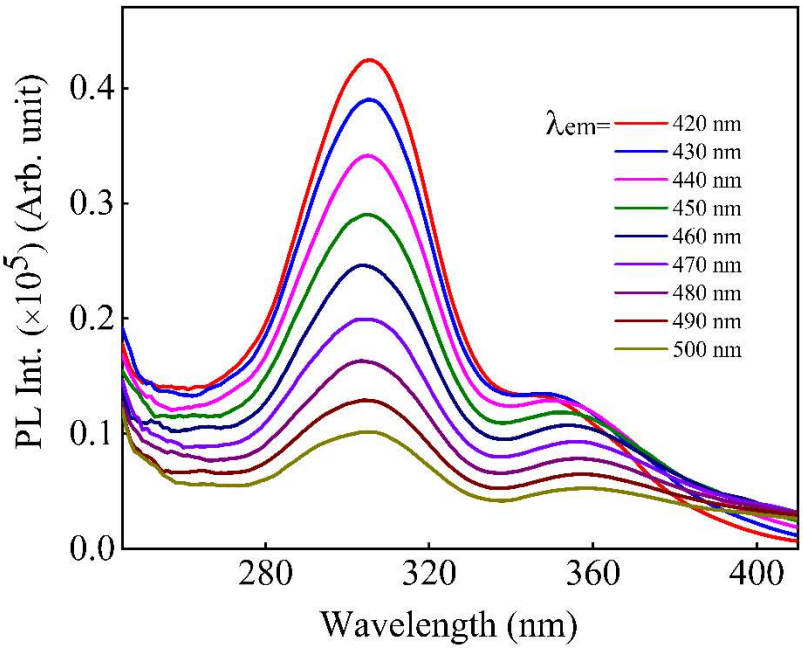

Fig. 3.4 *PL excitation spectra of WS_2 QDs obtained by monitoring PL at different wavelengths, which are shown in the figure.*

To estimate the quantum yield (QY) of fluorescence of WS_2 QDs, quinine sulfate, which has a QY of 54 %, has been used as a reference [114] , based on Eq. (3.1) [115].

$$QY_{sam} = QY_{ref} \times \frac{Area_{sam}}{Area_{ref}} \times \frac{Abs_{ref}}{Abs_{sam}} \times \left(\frac{\eta_{sam}}{\eta_{ref}}\right)^2 \quad (3.1)$$

where QY_{ref} and QY_{sam} are the quantum yield of quinine sulphate and WS_2 QDs, respectively. "Abs" indicates the absorbance, and the "area" represents the integrated areas of PL spectra. 'η' is the refractive index of the solvents employed for QDs and reference, namely distilled water and sulfuric acid. The QY estimated from the above equation was 8 %, which is higher than the reported QY for WS_2 QDs [64,91].

PL decay profiles of WS_2 QDs were measured with 320 nm excitation by monitoring the PL at 380, 420 and 460 nm. The decay profiles could be fitted by using a tri-exponential function, i.e., with Eq. (3.2).

$$I(t) = \alpha_1 \exp(-t/\tau_1) + \alpha_2 \exp(-t/\tau_2) + \alpha_3 \exp(-t/\tau_3) \quad (3.2)$$

where α_i and τ_i represent the pre-exponential factor and lifetime of i-th component. The results are summarized in Table 3.1, and typical fitted decay profiles are shown in Fig. 3.3(d).

PL at 380 nm shows that α_i of the fastest decaying component, which gives a lifetime of 0.36 ± 0.09 ns, was 0.69, and that α_i of the slowest decaying component, which gives a lifetime of 9.37 ± 0.07 ns, was only 0.10. As the monitoring wavelength became longer from 380 to 460 nm, the lifetime of all the decaying components became longer. In the results, the average lifetime (τ_{av}) calculated with $\tau_{av} = \frac{\sum \alpha_i \tau_i^2}{\sum \alpha_i \tau_i}$ became longer with increasing the monitoring PL wavelength (see Table 1). The monitoring wavelength dependence of the PL lifetime may be caused by the presence of multiple emitting states arising from different surface states.

Table 3.1 *PL lifetime and pre-exponential factors of WS_2 QDs dispersed in water at 320 nm excitation.*

λ_{ex} (nm)	λ_{PL} (nm)	τ_1 (ns)	τ_2 (ns)	τ_3 (ns)	α_1	α_2	α_3	τ_{av} (ns)	χ^2
320	380	0.36 ± 0.09	3.29 ± 0.38	9.37 ± 0.07	0.69	0.21	0.10	5.94	1.34
	420	0.51 ± 0.01	4.08 ± 0.12	10.12 ± 0.04	0.63	0.23	0.14	6.85	1.28
	460	0.61 ± 0.08	4.57 ± 0.11	11.01 ± 0.05	0.65	0.25	0.11	6.84	1.36

3.4. Hydrogen Peroxide Sensing

3.4.1. Effect of H2O2 on the absorption and PL of WS2 QDs

All the measurements were carried out with freshly synthesised WS_2 QDs in DI water [116]. Upon adding a small amount of H_2O_2, e.g., 0.33 nM in a colloidal WS_2 QDs dispersed in water, the absorption intensity of the excitonic band with a peak at 334 nm as well as the intensity of the band-edge absorption at ~274 nm decreased (Fig. 3.5a). With increasing the concentration of H_2O_2, the intensity of these absorption

bands decreased gradually. With a 594 µM concentration of H_2O_2, for example, the band at 274 nm became almost flat, while the 334 nm band diminished substantially. The plots of (A_0−A), where A_0 and A represent absorbance in the absence and presence of H_2O_2, respectively, as a function of the concentration of H_2O_2 in a range of 0 to 594 µM give a straight line with a fitting parameter of R^2 =0.98, as shown in the inset of Fig. 3.5(a), suggesting that the absorption intensity can be employed as a probe to detect H_2O_2 in a given environment. Figure 3.5(b) shows PL spectra of WS_2 QDs observed in the absence and presence of H_2O_2, having different concentrations ranging from 0.33 nM to 594 µM. The PL intensity, which decreased significantly even with a small amount of H_2O_2 (0.33 nM), further decreased gradually with increasing H_2O_2 concentration. Thus, the PL quenching occurred in the presence of H_2O_2, but the shape of the absorption band didn't change. Upon addition of H_2O_2 (594 µM), the PL intensity diminished by ~ 98 % (Fig. 3.5b), and the color change was clearly observed. Pictures of WS_2 QDs solution were taken at different concentrations of H_2O_2 under white light and UV light irradiations, respectively. As shown in Fig. 3.5(c), color change was observed with H_2O_2. As shown in Fig. 3.5(c), the yellowish color of the sample observed under white light irradiation changed to no color, and the blue color observed under UV irradiation disappeared with increasing H_2O_2 concentration.

Usually, PL is quenched either due to a complex formation in the ground state, i.e., the static quenching, or due to diffusion and collision of photoexcited species, resulting in dynamic quenching [110,117]. To explore the quenching mechanism, PL intensity was measured as a function of H_2O_2 concentration, that is, Stern-Volmer (S–V) plots given by Eq. 3.3 were obtained [65,118].

$$I_0/I = 1 + K_{SV}[H_2O_2] \quad (3.3)$$

where I and I_0 are the PL intensities observed with and without H_2O_2, respectively. The S-V plots showed a linear relation between PL intensity and H_2O_2 concentration with R^2= 0.98 (inset of Fig. 3.5b). Then, the plots can be used as a calibration curve to detect the quencher concentration. K_{SV}, called as S-V constant or quenching constant, was estimated from the linear plots, to be 5.1×10^3 M^{-1} with Eq. (3.3). The corresponding LoD for H_2O_2 was estimated with 3σ/K [119,120], where 'σ' represents

the standard deviation (counted from ten measurements of blank QDs samples, without the quencher) and 'K' is the slope in the plots, to be 1.7×10^{-6} M (S/N=3).

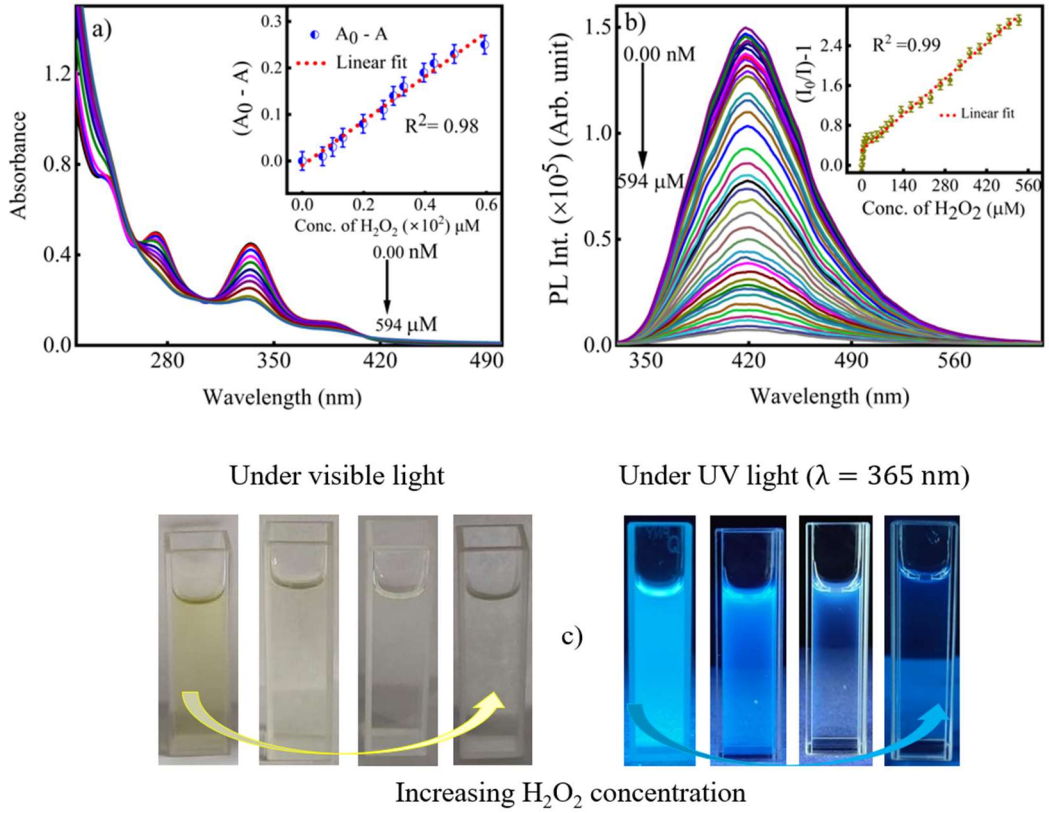

Fig. 3.5 *Absorption spectra of WS_2 QDs in the absence and presence of various (0.33 nM to 594 µM) H_2O_2 concentrations (a) PL spectra of WS_2 QDs in the absence and presence of various (0.33 nM to 594 µM) concentrations of H_2O_2 with 320 nm excitation (b) and inset of (a) shows the plot of (A_0–A) as a function of the concentration of H_2O_2 over a range of 0 to 594 µM and (b) inset of represents the corresponding linear S-V plot and photographs under UV and visible illumination for H_2O_2 concentration of 0, 231, 495 and 594 µM (c).*

In order to confirm that H_2O_2 selectively quenches PL of WS_2 QDs, similar experiments have been done with other chemicals. As common chemicals [121], toluene (TOL), benzoic acid (BZA), benzene (BZ), aniline (ANI) and benzaldehyde (BAL) were used instead of H_2O_2 with equivalent concentration (594 µM) of all analytes. The results are shown in Fig. 3.6. Then, it was confirmed that the PL of WS_2 QDs was selectively quenched by H_2O_2, whereas such a quenching was not confirmed with other chemicals.

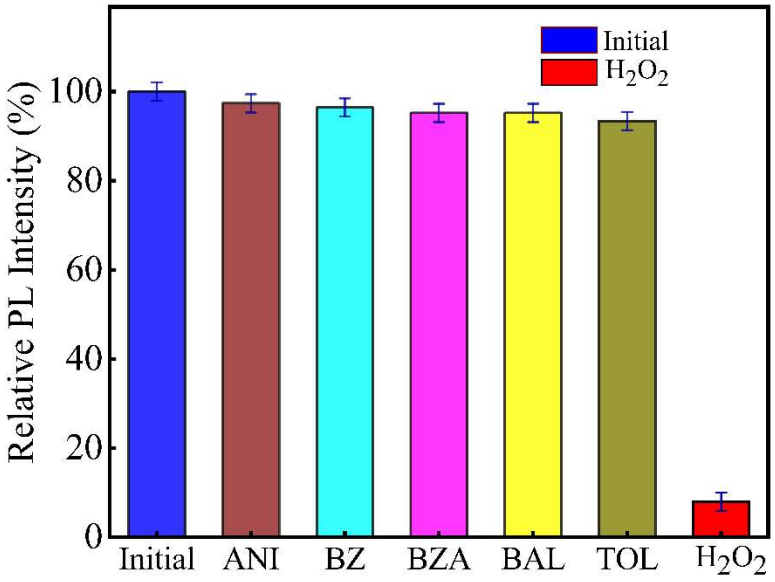

Fig. 3.6 *Selectivity of PL quenching in WS_2 QDs was examined by using various chemicals. Plots of the PL intensity (%) of WS_2 QDs in the presence of each of chemicals (ANI, BZ, BZA, BAL, TOL and H2O2) relative to the intensity in the absence of chemicals (Initial). The concentration of the chemical was 594 μM in every case.*

3.4.2. Effect of H_2O_2 on PL lifetime of WS_2 QDs

PL decays are usually measured to understand excitation dynamics. For example, static quenching and dynamic quenching can be distinguished. Accordingly, PL decays of WS_2 QDs were measured with 320 nm excitation by monitoring the PL at the peak position. Decay profiles were measured at various concentrations of H_2O_2 under the same experimental conditions as used for the steady-state PL measurements. The observed decay profiles could be fitted with a tri-exponential function. The parameters used for the fitting are summarized in Table 3.2, and fitted decay profiles are shown in Fig. 3.7. It is noted that small baseline signals (about 10-20 counts) in different decay profiles are different from each other because of the experimental uncertainty. As mentioned in the previous section, the multiple lifetimes may be assigned to different emitting states and polydispersity of QDs.

The lifetime τ_1 decreased from 0.51 ns to 0.26 ns with increasing H_2O_2 concentration up to 495 μM (Table 3.2). The lifetimes of the second decaying component, τ_2, also decreased slightly with increasing H_2O_2, but the lifetime of the slowest decaying component, τ_3, was nearly independent of H_2O_2. Not only the

lifetime but also the pre-exponential factors are influenced by H_2O_2; α_1 increases from 0.63 to 0.79, whereas α_2 and α_3 decreased with increasing H_2O_2 (Table 3.2). As a result, the average lifetime (τ_{av}) in the absence of H_2O_2, i.e., 6.85 ns is nearly the same as the one in the presence of 396 μM H_2O_2 (6.81 ns). The inverse of τ_i is plotted for each component as a function of H_2O_2 concentration. As shown in Fig. 3.7, τ_0/τ_1 as a function of H_2O_2 shows a straight line, indicating the presence of dynamic quenching for this component. Note that τ_0 represents the lifetime of each component in the absence of H_2O_2, and the S-V plots given by the following equation could be obtained: $\tau_0/\tau = 1 + K_{SV}[H_2O_2]$. The K_{SV} and LoD estimated from the linear plot for τ_1 are 1.0 $\times 10^3$ M^{-1} and 0.6 $\times 10^{-6}$ M, respectively. These values are different from the ones determined from the steady-state measurements of the PL quenching because the quenching mechanism is different from each other; steady-state PL quenching mainly comes from the complex formation, which results in the decrease of absorption intensity of the emissive WS_2 QDs and PL quenching (static quenching), while the linear S-V plots derived from the PL lifetime of τ_1 results from dynamic quenching by a collision of emitting excited species with H_2O_2. Thus, the steady-state and time-resolved PL measurements indicate the involvement of both static quenching caused by the complex formation in the ground state and dynamic quenching caused by a collision of emitting species of WS_2 QDs with H_2O_2, respectively. Here, it should be stressed that the present static quenching doesn't mean the decrease of QY of PL, though PL intensity decreases.

Table 3.2 *PL lifetime and pre-exponential factors of WS_2 QDs at the excitation wavelength of 320 nm and PL wavelength of 420 nm at different concentrations of H_2O_2.*

Conc. of H_2O_2 (µM)	τ_1 (ns)	τ_2 (ns)	τ_3 (ns)	α_1	α_2	α_3	τ_{av} (ns)	χ^2
00	0.51 ± 0.01	4.08 ± 0.12	10.12 ± 0.04	0.63	0.23	0.14	6.85	1.28
33	0.36 ± 0.01	3.97 ± 0.12	10.74 ± 0.05	0.74	0.17	0.09	6.89	1.32
99	0.33 ± 0.01	3.89 ± 0.11	10.93 ± 0.05	0.77	0.16	0.08	6.88	1.33
198	0.30 ± 0.01	3.70 ± 0.10	10.83 ± 0.05	0.78	0.15	0.08	6.95	1.41
297	0.31 ± 0.01	3.90 ± 0.11	11.04± 0.05	0.78	0.16	0.07	6.73	1.40
396	0.29 ± 0.01	3.86 ± 0.11	11.09 ± 0.05	0.79	0.16	0.07	6.81	1.29
495	0.26 ± 0.04	3.36 ± 0.01	10.49 ± 0.09	0.79	0.13	0.07	6.70	1.39

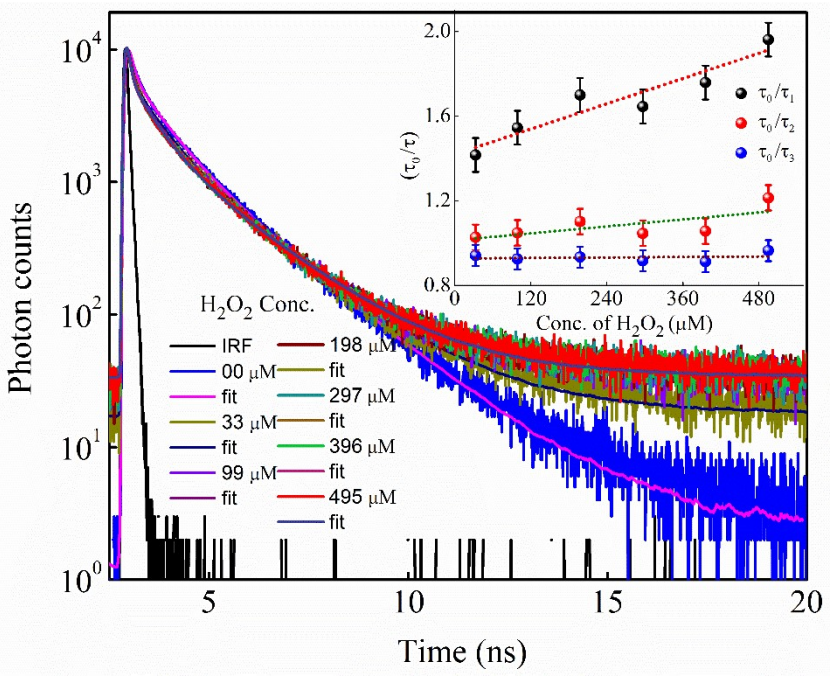

Fig. 3.7 *Fitted decay profiles of WS_2 QDs in the presence of various concentrations of H_2O_2 with 320 nm excitation and monitored at 420 nm. The inset shows the S-V plots of individual lifetimes.*

3.4.3. Restoring the PL of the sensing probe

The reversible nature of sensors is very important for their use in real practical applications. To examine the reversibility of the sensor probe, 0.1 N HCl was added to WS_2 QDs water solution, which contained H_2O_2 (with 594 µM). Upon adding HCl we see PL intensity starts increasing sequentially and at an adequate amount of HCl (297 µM), the quenched PL of WS_2 QDs recovered by nearly 100 %, as shown in Fig. 3.8(a),

where the bar diagram of PL quenching and recovery following the addition of H_2O_2 and HCl, respectively, are presented. The photographs observed under UV irradiation (365 nm) are also presented. Similar to the PL, absorption intensity of WS_2 QDs has also been recovered (~100%) with addition of HCl, as shown in Fig. 3.8(b).

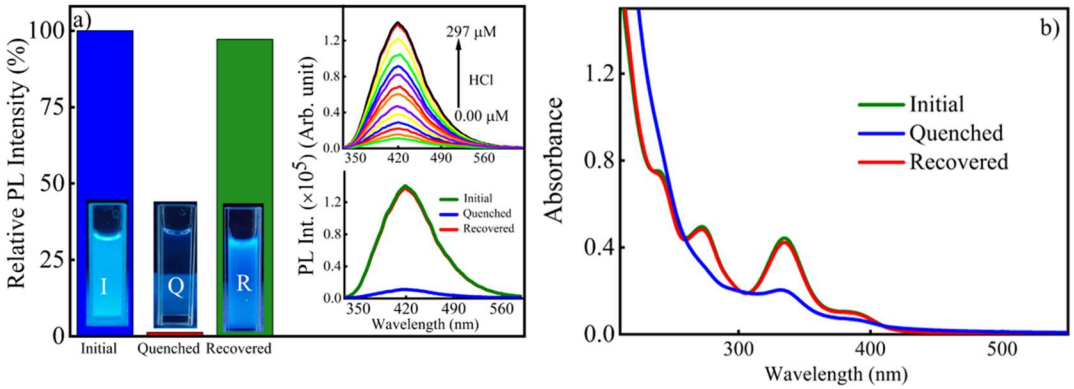

Fig. 3.8 *Bar diagram of relative PL intensity (%) of WS_2 QDs in the absence (initial) and presence of 594 μM H_2O_2 (quenched) along with the insets of recovered PL intensity (%) by adding sequentially and at 297 μM of 0.1 N HCl (recovered). Insets show the sequentially restored PL by adding HCl and at initial, quenched and recovered PL spectra of WS_2 QDs along with their photographs under UV irradiation (a), absorption spectra of WS_2 QDs observed in the absence (Initial, green line) and presence of 594 μM of H_2O_2 (Quenched, blue line). Absorption spectrum observed upon addition of 297 □M of 0.1 N HCl to the sample having H_2O_2 (594 □M) is also shown (Recovered, red line) (b).*

In order to examine the cyclic stability of WS_2 QDs-based fluorescent sensor, PL quenching and recovery cycles were monitored by sequentially adding H_2O_2 and HCl. The results are shown in Fig. 3.9. The PL intensity of the developed chemosensor slightly decreased after nine cycles of adding H_2O_2 (594 μM in each cycle) and HCl (297 μM in each cycle), but it is clearly shown that WS_2 QDs can be used to detect H_2O_2 for more than nine cycles. Thus, the synthesized fluorescent probe of WS_2 QDs, i.e., chemosensor, is known to be applicable as a selective and sensitive sensor of H_2O_2 for many cycles.

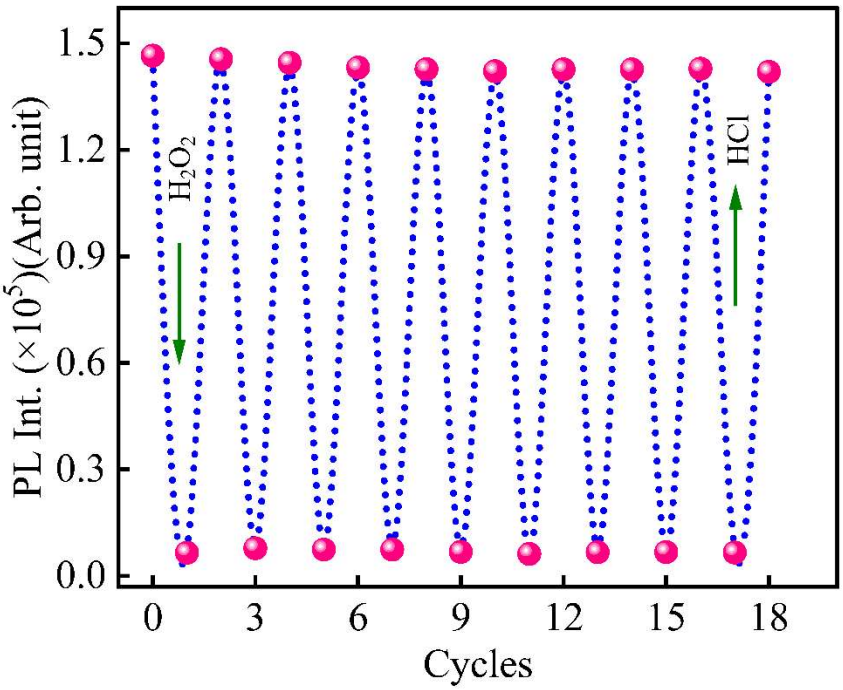

Fig. 3.9 *PL intensity of the developed fluorescent probe (QDs) upon successive addition of H_2O_2 (594 µM) and HCl (297 µM) up to nine cycles. The plot shows excellent cyclic stability for more than nine cycles.*

3.4.4. Promising recovery mechanism

Colloidal WS_2 QDs, which showed PL with 8% QY were synthesized in DI water at a certain pH. As already mentioned, PL decay profiles could be fitted with a multiexponential function, probably due to the presence of different emitting states arising from different surface states. The PL of WS_2 QDs diminished by 98% upon adding a certain amount of H_2O_2, but the diminished PL intensity was restored entirely upon adding a certain amount of 0.1N HCl. The absorption and PL intensities of colloidal WS_2 QDs decreased gradually upon successive addition of H_2O_2. The absorbance of WS_2 QDs decreased drastically with H_2O_2 without any change in the peak position, and PL of WS_2 QDs also decreased drastically with H_2O_2. As a mechanism, WS_2 QDs are considered to get oxidized in an alkaline aqueous environment in the presence of H_2O_2; the conversion to W(VI) from W(IV) is considered to occur by making a complex of WS_2 QD with H_2O_2, resulting in quenching of both absorption intensity and PL intensity [96,122]. Upon adding a certain amount of 0.1 N HCl, the absorption and PL intensity recovered to the original value due to the conversion from W(VI) to W(IV) [120,123,124], as demonstrated in Fig. 3.10. Various probes which respond to H_2O_2, as well as used methods reported so

far are summarized in Table 3.3, where the sensing effect of WS_2 on H_2O_2 is compared with other probes for H_2O_2. It is known that the present probe, WS_2 QD, is very sensitive to H_2O_2 and very useful in a wide range of concentrations.

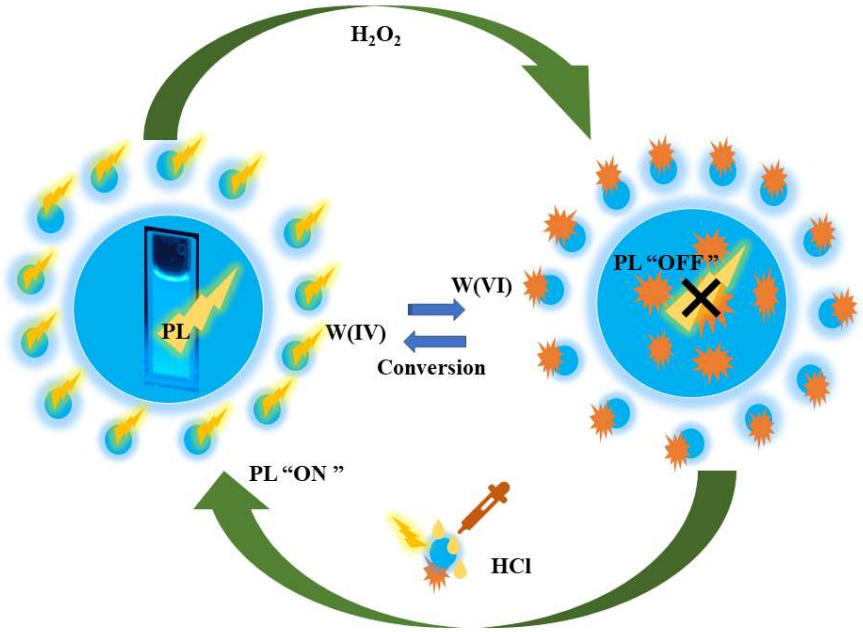

Fig. 3.10 *The pictorial representation of the conversion of W(IV) to W(VI).*

Table 3.3 *A comparison of different probes claimed for H2O2 detection.*

Probe used	Detection method	Linear range	LoD (μM)	Reference
Colloidal WS_2 QDs	Absorption, PL, Lifetime (oxidation and reduction)	0.33 nM-594 μM	1.7	This work
Graphene quantum dots (GQDs)	Surface plasmon resonance (SPR)	0.0 μM-100 μM	1.0	[125]
Biosynthesized AgNPs	SPR	0.0 μM-140 μM	21.0	[126]
Pd-decorated PEDOT nanospheres	Biosensor	2.5 μM-1.0 mM	2.84	[127]
Fe_3O_4 nanocomposites	Coprecipitation	0.1 μM-6.0 mM	3.20	[128]
CNF electrode	Electrochemical	1.0 μM-800 μM	0.60	[129]
Ultrathin Pt@Au NPs	Redox	1.0 μM-450 μM	0.18	[130]
AgNPs/TiO_2 NTs	Electrophoresis	0.75 μM-11.2 mM	0.09	[131]

Pt/TeO_2-NWs	Amperometric	2.0 µM-16 mM	0.60	[132]
Black phosphorus	Electrochem.	0.1 µM-50 µM	10.0	[133]
MnOOH/CC	Electrocatalyst	20 µm-9.67 mM	3.20	[134]
PDA–Ag hybrid hollow microspheres	Self-polymerization	92 µM-20.0 mM	1.97	[135]
Ag-NPs/MB biocomposite	Biocomposite	1.0 µM-3.0 mM	0.09	[136]

3.5. Conclusion

A bottom-up one-step hydrothermal method was used without any subsequent treatments to prepare stable functionalized WS_2 QDs with an average size of 4.5 nm in an aqueous medium. TEM, HR-TEM and FT-IR were used to examine size, shape, bonding as well as presence of functional groups. WS_2 QDs emit a bright blue PL, which depends on the excitation wavelength, with a QY of nearly 8 %. Non-exponential decay profile of PL, along with a large redshift of the PL spectra with increasing excitation wavelength, suggests that PL emissions were caused from multiple emitting states arising from different surface states. Addition of H_2O_2 to water solution diminished absorption intensity of WS_2 QDs. Increasing the H_2O_2 concentration decreased PL intensity by about 98 %. The decrease in PL intensity gives linear Stern-Volmer plots as a function of H_2O_2 concentration in the range from 0 to 594 µM. The average lifetime of PL was roughly the same, irrespective of the presence of H_2O_2. The limit of detection (LoD) was estimated to be 0.6×10^{-6} M and 1.7×10^{-6} M with S/N=3, based on the time-resolved and steady-state PL measurements, respectively. The quenching of both absorption and PL by H_2O_2 was recovered nearly 100% by adding HCl. The PL quenching/recovery demonstrated excellent cyclic stability. Thus, the study of in situ fabrication of functionalized QDs with loss and recovery of PL intensity opened a new pathway as efficient probes for optical, biosensing, bioimaging, and other applications.

Chapter 4: Waterborne Explosives: A Rapid Detection Method using $MoSe_2$ Quantum Dots

4.1 Introduction

Due to national security concerns, selective and careful identification of **explosive nitroaromatic compounds** (NACs) has gained much attention recently. This depends on environmental impact calculation, homeland security, community safety, and real-world uses. Rapid and affordable methods for recognizing explosive components must be developed in light of the expanding frequency of violent crimes involving NACs. Moreover, NACs are considered perilous pollutants that pose a significant ecological risk [137]. Among numerous explosive components, commonly found compounds are **2,4,6-TNP**, 2,4-dinitrotoluene (DNT), 2,4,6-trinitrotoluene (TNT), 2,4,6-trinitrobenzene (TNB), and 1,3-dinitrobenzene (DNB) [138]. **Among,** TNT, DNT and **2,4,6-TNP** are the main components of detonated landmines [121]. Prolonged exposure to TNT may result in skin irritation, anemia, and headaches. However, **2,4,6-TNP** has a far more explosive tendency than TNT [139]. The explosive characteristics of 2,4,6-TNP separate it from other eminent NACs due to its fast detonation velocity and slow safety coefficient [110]. In addition, 2,4,6-TNP's **remarkable** water solubility and high acidity make it an environmental pollutant that poses a significant risk to marine ecosystems and agricultural land [110,139]. The extensive use of **2,4,6-TNP** in industries **such as** waste management, **construction**, mirror manufacturing, and rocket **production** exacerbates the harm caused by this hazardous material [140,141]. The release of **2,4,6-TNP** into the atmosphere during the fabrication and use of these products contributes to water and soil pollution. The haematotoxin and hepatotoxic effects of 2,4,6-TNP are well-documented, with known associations with carcinogenesis and mutagenesis in living cells [142]. For this reason, trailing buried explosives and monitoring ecological pollution depend severely on detecting 2,4,6-

TNP in soil and water. Numerous approaches and techniques, including Raman scattering, mass spectroscopy, gas chromatography, and chromatographic technologies, have been used to perceive explosives [142–144]. However, the genuine uses of these techniques are hindered by their constraints, which include sophisticated arrangement, lengthier processing times, intricate synthesis procedures, restricted selectivity, and lesser sensitivity. So, creating innovative techniques that provide faster and more precise explosive identification is crucial. Fluorescence-based practices have gathered considerable interest among sensing technologies because of their virtuous selectivity, high sensitivity, low cost, and ease of use [110,145–147]. Explosive recognition has special appeal in the fluorescence approach because of its practical benefits and adaptability, which utilize light emission upon excitation [141,148,149]. PL is a phenomenon where light excites fluorescent molecules or materials, causing them to emit light at longer wavelengths. By identifying and studying the emitted light, it is possible to gain valuable insights into the target chemicals. This research aims to develop a highly selective sensing method for 2,4,6-TNP, along with an exploration of the underlying energy transfer mechanisms [110]. The energy transfer (ET) system consists of an excited fluorescein (donor) that transfers its energy to an acceptor via dipole-dipole interactions, resulting in a reduction in the total lifespan of donor species [150].

Molybdenum diselenide ($MoSe_2$), an earth-abundant and incipient star in the transition metal dichalcogenides (TMDs) family that seems to be encouraging material for a variety of **applications,** including photovoltaic cells [151], heterogeneous catalysis [152,153], photoresistors [154], surfactants [152], and rechargeable batteries [155]. Layered semiconducting material $MoSe_2$ comprises weakly interacting Se–Mo–Se layers stacked vertically and bound together by van der Waals interactions [156]. It shows both an indirect and a direct bandgap of 1.1 eV and 1.5 eV in bulk and monolayer form, respectively [157]. $MoSe_2$ displays remarkable suitability for optoelectronic devices due to its highly tuneable bandgap and substantial light interaction throughout a broad range spanning from infrared to ultraviolet regions [158]. Additionally, $MoSe_2$ displays a supplementary metallic character compared to MoS_2 [159], resulting in enlarged electrical conductivity, which is advantageous for hydrogen evolution reaction (HER) and sensing processes. By adding diverse

functional groups and identifying different receptors, $MoSe_2$ QDs vary their properties uniquely, permitting the selective detection of definite targets and other probes [83,158]. Combined with the advantageous characteristics of $MoSe_2$, this aspect adjustment capability makes synthesized QDs a perfect option for sensing applications [153,154,160].

In this study, $MoSe_2$ QDs were developed and their optical transitions were thoroughly examined. These QDs were then employed to monitor 2,4,6-TNP by observing changes in PL intensity. The variation in PL intensity with respect to 2,4,6-TNP concentrations offers valuable insights into the sensing mechanism. This work establishes a foundation for designing and optimizing future sensing systems based on $MoSe_2$ and similar materials.

4.2. Experimental Sections

4.2.1. Materials

The synthesis utilized high-purity precursors and solvents directly [28]. Sodium molybdate ($Na_2MoO_4 \cdot 2H_2O$), selenium powder, nitro-aromatic chemicals, i.e., 2,4,6-trinitrophenol, 1,2-dinitrobenzene, 2,6-dinitrotoluene, 2-nitrotoluene (2-NT) and 4-nitrotoluene (4-NT) were procured from Sigma-Aldrich. Hydrazine hydrate, benzoic acid (BzCOOH), toluene (tol), benzene (bz), benzaldehyde (BzCHO), aniline (ANI), and acetonitrile (ACN) were obtained from Thermo Fisher Scientific India, and SRL Chem Pvt. Ltd., respectively. To attain the best possible outcomes, all experiments were carried out using ultrapure (UP) water, which is necessary for applications that demand a low ionic content and have a resistivity of 18.2 MΩ cm. It is important to note that proper cautionary measures were followed when handling and using explosive nitroaromatic chemicals such as 2,4,6-TNP. These hazardous materials were used in small quantities following safety protocols and guidelines.

4.2.2. Synthesis method

$MoSe_2$ QDs were synthesised via a hydrothermal method. Briefly, solution A was prepared by dissolving 0.01 mol of sodium molybdate dihydrate in 30 mL of DI water at room temperature (RT) under magnetic stirring [29]. Simultaneously, solution (B) was prepared by dissolving 0.02 mol of Se powder in 20 mL of hydrazine hydrate with magnetic stirring for 25 minutes, resulting in a coal-black suspension [29]. After

stirring solution, A for 25 minutes, solution B was slowly added dropwise while maintaining continuous magnetic stirring. This combination yielded a peach-brown solution with a pH of 7.4. Following preparation, the mixture was put into a pressure vessel with a Teflon lined and kept for 24 hours at 200 °C to heat in a oven. The vessel was then allowed to cool to RT over a period of 12 hours. The resulting solution containing $MoSe_2$ QDs underwent purification with centrifugation at 6000 rpm for ~15 minutes to remove impurities and residual bulk particles. This washing process was repeated several times using ethanol to remove residual reaction products. Finally, the purified $MoSe_2$ QDs were rinsed with DI water and subsequent redispersion for further analysis and characterization. Scheme 1 visually depicts the sequential steps involved in the synthesis process. This approach successfully yielded high-quality $MoSe_2$ QDs for potential applications in explosive NACs detection and analysis [30,31].

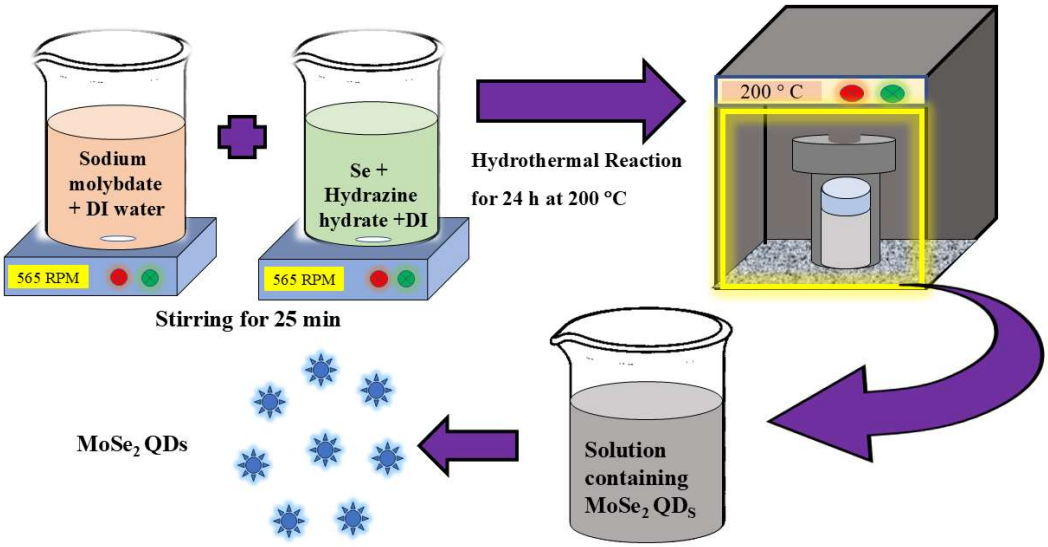

Scheme 4.1 *Schematic representation of the synthesis process of $MoSe_2$ QDs.*

4.2.3 Characterization Techniques:

X-ray diffraction (XRD) analysis was performed using a D8 Bruker Advance diffractometer with a copper radiation source (CuKα) [32]. The instrument operated at 40kV and 20 mA of accelerating voltage and current, respectively, to collect the XRD patterns. The FT-IR (Fourier transform infrared) spectrum was monitored using two-spectrum FTIR spectrometers, Perkin Elmer, with a 400 to 4000 cm^{-1} range. HRTEM (High-resolution transmission electron microscopy) images were obtained using a

Thermo Fisher scientific microscope (TALOS) [33], operating at 200 kV of accelerating voltage. Steady-state UV/vis spectra were measured using a double-beam UV/VIS/NIR spectrophotometer, Perkin Elmer Lambda 750. A fluorolog-3 spectrometer, Horiba Jobin Yvon, equipped with double gratings on excitation and emission monochromators [163], was used to monitor the PL and PL excitation spectra. A transparent quartz cuvette of dimensions 1 cm × 1 cm was used for all these measurements.

4.3 Results and discussion

4.3.1. XRD analysis

The crystalline characteristics of the produced $MoSe_2$ QDs were obtained using X-ray diffractometry, which was carried out at RT. The obtained XRD pattern for $MoSe_2$ QDs is demonstrated in Fig. 4.1(a). The characteristic diffraction peaks were noticed at 2θ angles 13.6, 31.8, 37 and 56.1, corresponding to the diffraction planes (002), (100), (103) and (110) respectively, that exactly matched with the standard hexagonal 2H–$MoSe_2$ (JCPDS No. 29-0914) [158]. The broad diffraction peaks indicate the nano-crystalline character of the produced QDs [35,36]. The average crystallite size was estimated to be 4.93 nm by employing the Debye–Scherrer equation [35,36].

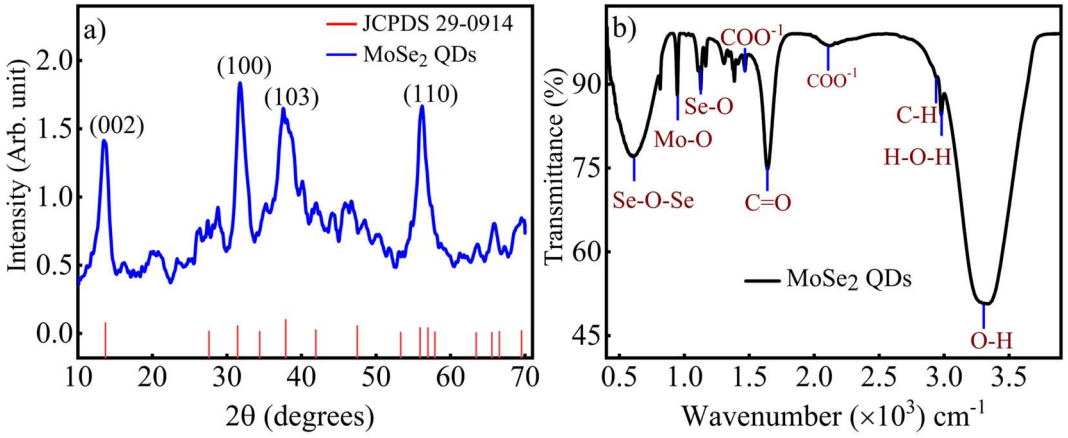

Fig. 4.1 *XRD pattern of obtained $MoSe_2$ QDs thin film and JCPDS cards details (a), FT-IR spectrum of synthesised $MoSe_2$ QDs dispersed in water along with the band's identification.*

4.3.2 FT-IR Spectrum analysis

Due to the infrared activity of the produced $MoSe_2$ QDs, FT-IR was utilized to discuss the validation of the structure of synthesized QDs [83]. FT-IR is a widely used

technique for identifying organic, polymeric, and inorganic compounds, as well as detecting functional groups [37]. FT-IR spectrum of $MoSe_2$ QDs recorded in the 400-4000 cm^{-1} range is represented by Fig. 4.1(b). Several characteristic peaks were observed in the spectrum. The Se-O-Se stretching vibration appears at 561 cm^{-1}, while the O-Mo-O stretch is observed at 828 cm^{-1} [38]. Peaks corresponding to Se-O and COO^{-1} peaks are appeared at 1110 cm^{-1} and 1393 cm^{-1}, respectively [38]. The bands at 3311 cm^{-1} is attributed to the O-H stretching and bending vibrations of water molecules [37]. The C=O [157] and C–H stretching vibrations are responsible for the peaks at 1675 cm^{-1} and 2926 cm^{-1}, respectively. Additional peaks at 2972 cm^{-1} and 2157 cm^{-1} are attributed to C-H and (H-O-H) & COO^{-} functional groups present in the $MoSe_2$ QDs [21,38,39]. These FT-IR findings further confirm the structure and functional groups in the synthesized MoSe2 QDs.

4.3.3 Transmission electron microscopy (TEM) analysis

HR-TEM was employed to examine the structural and morphological features of the synthesized $MoSe_2$ QDs. The HR-TEM images of MoSe2 QDs captured at various magnifications are shown in Fig. 4.2, reveal important insights into their structure. Fig. 4.2(b) and 4.2(c) display the $MoSe_2$ QDs, which are spherical in shape and exhibit a uniform distri bution, with small particles sized between 3 and 6 nm. The crystalline nature of the $MoSe_2$ QDs is confirmed by the clear, well-ordered, and parallel lattice fringes seen in Fig. 4.2(a). The inset of Fig. 4.2(a) shows the (103) crystal plane of $MoSe_2$, with the calculated crystal lattice D- spacing of 0.23 nm, further supporting the crystalline structure. The average particle size of the $MoSe_2$ QDs was determined to be 4.78 nm, as calculated from the Gaussian distribution curve in Fig. 4.2(d). This narrow distribution range of particle sizes indicates a consistent synthesis method, which is advantageous for potential applications in various fields.

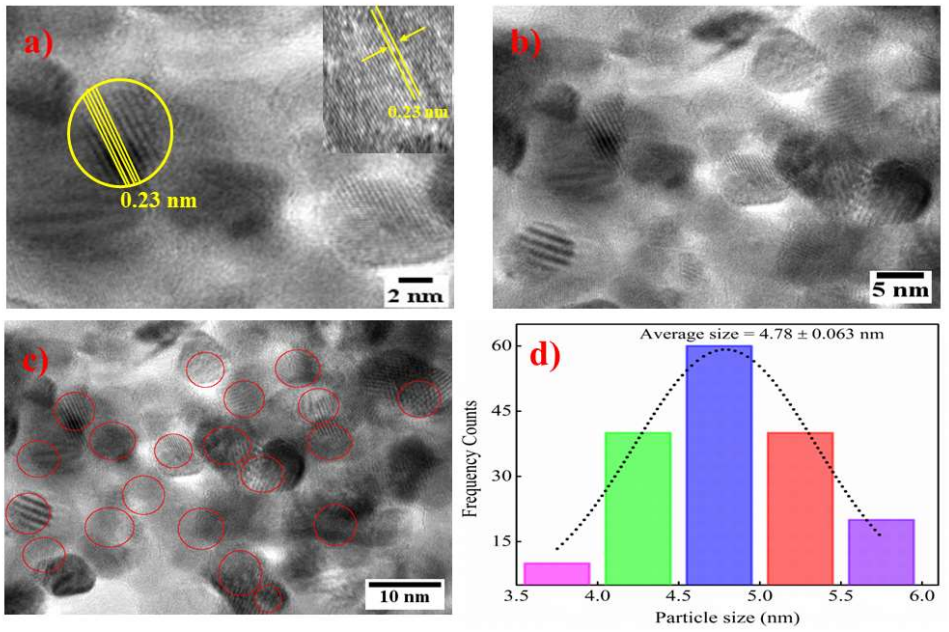

Fig. 4.2 *HR-TEM images of obtained $MoSe_2$ QDs at different magnifications (a-c) with particle size distribution (d). The inset of (a) shows the extended view of the calculated d-spacing.*

4.3.4. Optical properties of obtained MoSe2 QDs

Fig. 4.3(a) shows the absorption spectrum of produced colloidal $MoSe_2$ QDs along with the Gaussian bands used to reproduce the absorption and the second derivative of the absorption spectrum. The second derivative and Gaussian bands reveal the presence of two primary absorption peaks: a strong peak at 260 nm and a weaker one around 305 nm. These bands are attributed to the transition from excitonic bands [40,41]. The inset of Fig. 4.3(a) shows the appearance of the colloidal solution under ordinary white light (LED) and UV light, highlighting the distinct color of the sample under different lighting conditions. Fig. 4.3(b) displays the PL spectra of the $MoSe_2$ QDs as a function of excitation wavelength, ranging from 270 to 450 nm at ambient temperature. The PL intensity increases as the excitation wavelength shifts from 270 nm (4.59 eV) to 340 nm (3.64 eV). Beyond this, as the excitation wavelength increases from 350 nm (3.54 eV) to 450 nm (2.75 eV), the PL intensity decreases. The maximum PL intensity is observed at 410 nm when excited with 340 nm light. A gradual shift in the PL peak to longer wavelengths is seen when moving from 270 nm to 450 nm, as shown in the normalized PL spectra (Fig. 4.3(c)), with a total shift of about 105 nm.

This excitation-dependent PL behaviour indicates that the $MoSe_2$ have a polydisperse or inhomogeneous size distribution[28].

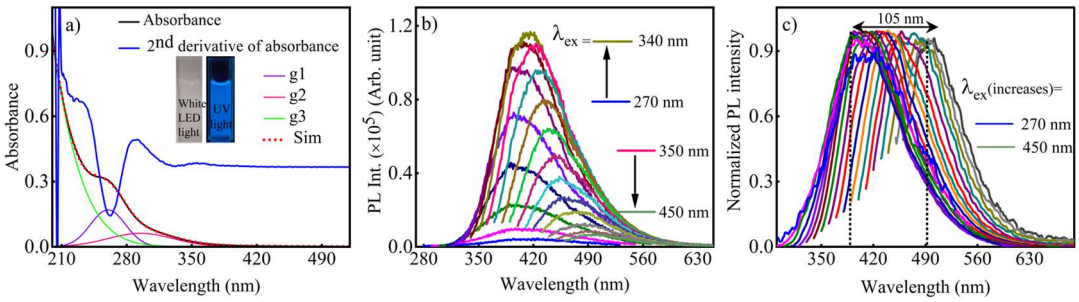

Fig. 4.3 *Absorption spectrum of synthesised $MoSe_2$ QDs with its 2nd order derivative (blue solid line) and Gaussian bands g1, g2 and g3 used to reproduce the measured absorption. The inset represents the colour of the solution under white LED and UV irradiation (~365 nm) (a). PL spectra of synthesised $MoSe_2$ QDs with different excitations ranging from 270 to 450 nm (b) and normalized PL spectra at different excitations (c).*

Fig. 4.4(a) presents the PL spectra of the colloidal $MoSe_2$ QDs along with Gaussian bands used to reproduce the observed PL spectra. The PL spectra observed with 300 and 340 nm excitations were reproduced with three Gaussian bands at 387, 432 and 456 nm. However, with 380 nm excitation, an additional band at approximately 498 nm appears, and its intensity increases with excitation at 420 nm. At 450 nm excitation, only a single band at 498 nm is observed, which can be reproduced by a single Gaussian fit, suggesting that this emission is from a single emitting state. This indicates that the emitting state can be populated by different excitation wavelengths. Additionally, the photoluminescence excitation (PLE) spectra (Fig. 4.4b), were recorded at PL wavelengths ranging from 400 to 500 nm. The inset shows the normalized PLE spectra, which broaden with increasing monitoring wavelengths, indicating the presence of multiple excitation bands. The observed PL spectra can be well reproduced by four Gaussian bands, which correspond to four different emitting states. These states are populated by direct excitation along with defect and trap states [42].

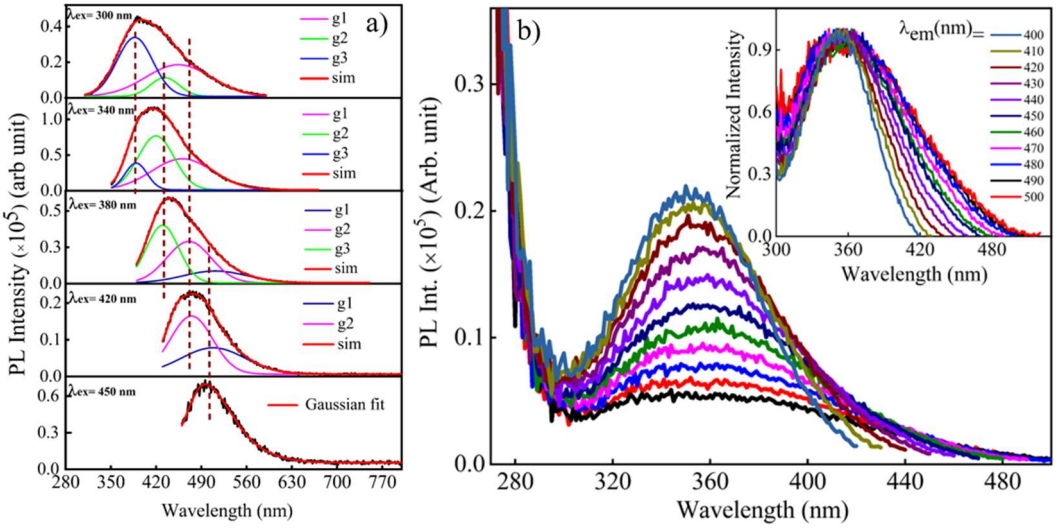

Fig. 4.4 *Photoluminescence spectra of colloidal $MoSe_2$ QDs at different excitation wavelengths along with the Gaussian band used to reproduce the observed spectra (a), PL excitation (PLE) spectra of $MoSe_2$ QDs with variable emission wavelengths (varying from 400 to 500 nm). The inset represents the normalized PLE spectra (b).*

Further, utilizing absorption and PL spectra of synthesized $MoSe_2$ QDs and quinine sulfate (as a standard reference), the quantum yield /efficiency (QY), a remarkable parameter of fluorescent materials, was computed. Using the formula [5,32], the calculated QY value is 12 %. The PL properties of $MoSe_2$ QDs were also studied with respect to pH. The corresponding data shows that the PL intensity remains nearly constant over a wide pH range from 2.0 to 13.0 (Figs. 4.5a,b), indicating that $MoSe_2$ QDs are highly stable and exhibit exceptional tolerance to pH changes in solution [43,44]. This pH stability is desirable for practical applications, as it suggests that $MoSe_2$ QDs can maintain their optical properties in diverse environments without significant degradation.

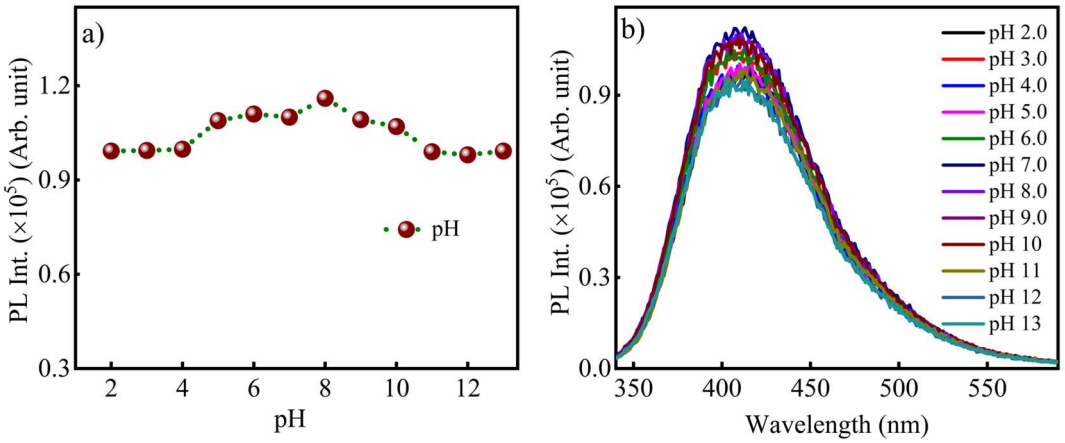

Fig. 4.5 Plot of PL intensity at 410 nm of $MoSe_2$ QDs as a function of pH (2-13) (a), and corresponding PL plot (b).

4.3.5. 2,4,6-TNP explosive sensing

Using $MoSe_2$ QDs as a fluorescent probe, a decrease in PL was used to monitor 2,4,6-TNP. The relation/interaction between $MoSe_2$ QDs and 2,4,6-TNP was investigated by titrating a freshly prepared 2,4,6-TNP solution with a concentrations range of 3.3 to 99 nM into a quartz cuvette containing a 3.0 mL $MoSe_2$ QDs solution. To evaluate the selectivity of $MoSe_2$ QDs as a sensing probe for 2,4,6-TNP, various potential interfering analytes (each at a concentration of 99 nM) were introduced into a solution containing both $MoSe_2$ QDs and 2,4,6-TNP (both at 99 nM). After ensuring thorough homogenization, changes in the PL intensity were monitored by measuring the PL at an excitation wavelength of 340 nm. These results demonstrate the selectivity of $MoSe_2$ QDs to 2,4,6-TNP compared to other analytes, showcasing the potential of $MoSe_2$ QDs in specific detection applications.

4.3.5.1 Impact of 2,4,6-TNP on absorption and PL properties of MoSe2 QDs

Fig. 4.6(a) illustrates the effect of varying concentrations of 2,4,6-TNP on the absorption spectra of $MoSe_2$ QDs dispersed in UP water. Upon the addition of 2,4,6-TNP, there was a noticeable increase in the overall optical density (OD), indicated by a rise in absorbance and a flattening of the absorption peak around 260 nm, especially at the highest concentration of 99 nM. This increase is attributed to the independent ab sorption of the 2,4,6-TNP molecules themselves, as demonstrated by the absorption spectra of 2,4,6-TNP at 99 nM concentration, which also shows an increase in OD [5].

Notably, the observed spectral changes can be used to differentiate between static and dynamic quenching mechanisms. Static quenching involving complex formation in the ground state [36], leads to spectral shifts in the absorption band. On the other hand, dynamic quenching, characterized by collisions between fluorophore and quencher molecules, primarily affects higher excited states and does not alter the ground state or absorption spectrum. This indicates that the observed increase in OD is due to the 2,4,6-TNP absorption, which overlaps with the absorption of $MoSe_2$ QDs, rather than a classical quenching process [5,45,46].

The PL intensity of $MoSe_2$ QDs, rather than a classical QDs was remarkably reduced in the presence of a modest amount of 2,4,6-TNP in the QDs solution. Upon adding a 3.3 nM of 2,4,6-TNP to the $MoSe_2$ QDs, a considerable reduction in PL intensity was observed (Fig. 4.6b). As the concentration of 2,4,6- TNP increased up to 65 nM, the PL intensity of the $MoSe_2$ QDs was quenched to 70 % of its original value. However, when the concentration of 2,4,6-TNP reached 99 nM, the PL intensity of $MoSe_2$ QDs gradually decreased to around 94 % of its initial intensity. To elucidate the quenching mechanism, a Stern-Volmer (S-V) plot was constructed by plotting the PL intensity (F_0/F) against the quencher (2,4,6-TNP) concentration according to Eq. (4.1) [47].

$$I_0/I = 1 + K_{SV}[2,4,6\text{-TNP}] \quad (4.1)$$

where the PL intensities with (I) and without (I_0) of 2,4,6-TNP, and [2,4,6-TNP] denotes the molar concentration of 2,4,6-TNP, the resulting S-V plot exhibited excellent linearity with a high correlation coefficient (R^2) of 0.99 (inset of Fig. 4.6b). The linear fit of the plot yielded a Stern-Volmer quenching constant (K_{SV}) of 9.28 × 10^6 L mol^{-1}. The Slope is further used to calculate the detection limit (LoD) for 2,4,6-TNP with formula 3σ/K, where 'σ' signifies the standard deviation of the blank measurement obtained from ten replicate measurements of the PL spectrum of pure $MoSe_2$ QDs and 'K' represents the slope of the plot [48]. The determined LoD was 1.43 nM.

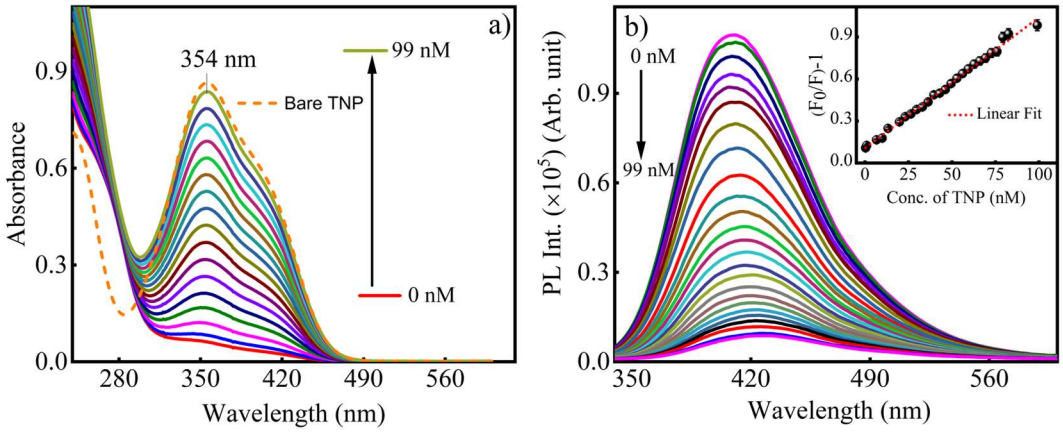

Fig. 4.6 *Absorption spectra of $MoSe_2$ QDs in the absence and presence of varying concentrations of 2,4,6-2,4,6-TNP (3.3 to 99 nM) along with the absorption of bare 2,4,6-2,4,6-TNP at a fixed concentration of 99 nM (a), Photoluminescence spectra of $MoSe_2$ QDs in the absence and presence of various concentrations (3.3 to 99 nM) of 2,4,6-TNP with 340 nm excitation. The inset represents the corresponding S-V plot (b).*

To assess the selectivity, the change in PL of $MoSe_2$ QDs was conducted with various potential analytes, including BzCOOH, 4-NT, tol, BzCHO, 2,6-DNT, bz, ANI, 2-NT, and 1,2-DNB. The PL titrations were performed in aqueous environments for analytes with moderate water solubility, while for analytes (NACs) with lower solubility, water-acetonitrile (ACN) mixtures were used. Fig. 4.7(a) presents a bar graph illustrating the percentage quenching of PL intensity by each analyte. Furthermore, a separate study was conducted to evaluate the anti-interference capability of the $MoSe_2$ QDs as a sensing probe with the presence of other analytes. A fixed concentration of 2,4,6-TNP (99 nM) was introduced into samples containing the same concentration (99 nM) of each potential interfering analyte used. The results are depicted as a bar graph in Fig. 4.7(b), confirming negligible interference from these co-existing compounds.

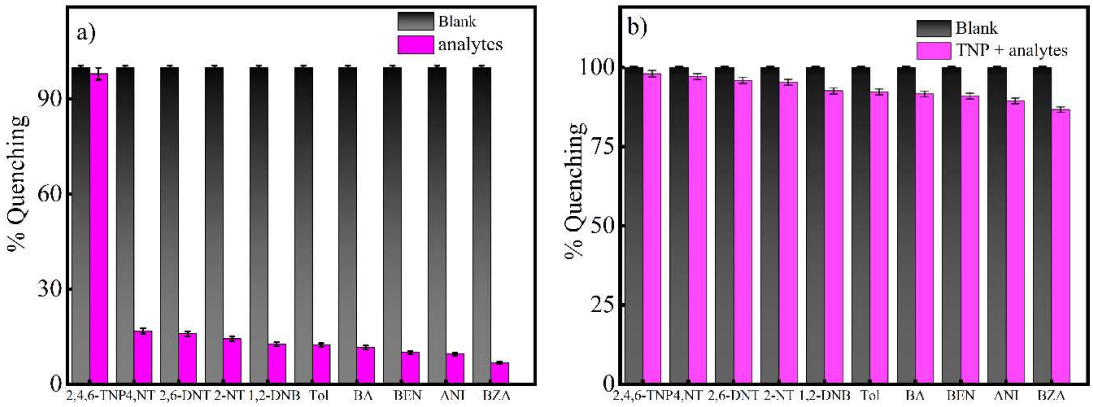

Fig. 4.7 *The bar graphs of PL intensity quenching (%) of $MoSe_2$ QDs with fixed concentration (99 nM) of different analytes (a) and with a fixed concentration of 2,4,6-2,4,6-TNP (99 nM) and different analyst (99 nM) representing the anti-interference effect (b). The pink bar shows the change in PL intensity (%) in the presence of various analytes, whereas the black bars of (a) and (b) represent the PL intensity in the absence of analytes.*

Thus, KSV of 2,4,6-TNP ≫ compared to other analytes (1,2-DNB >bz >ANI >tol >2-NT ≈BzCHO ≈2,6-DNT ≈ BzCOOH ≈4-NT) (Fig. 4.8a). This suggests that $MoSe_2$ QDs have a good selectivity for 2,4,6-TNP, with a selectivity factor (SF) of 1, calculated by dividing the K_{SV} of 2,4,6-TNP by the K_{SV} of each interfering analyte [43] (Table 4.1). The selectivity was further examined using a different excitation wavelength, specifically the absorption maximum of one of the NACs, 4-NT. The PL results showed slightly higher quenching (~23 %) with 290 nm excitation (corresponding to the absorption band maximum) compared to 330 nm excitation (~17 %), which was used for all the NACs, as discussed earlier. The results are shown in Figs. 4.8(b) and 4.8(c). This confirms that $MoSe_2$ QDs are highly selective for 2,4,6-TNP, as highlighted by their SF compared to other NACs and interferents [2]. Further, changes in PL intensity of QDs as a function of time with the addition of 99 nM of 2,4,6-TNP were measured. Notably, the decrease in PL intensity was observed within < 1 min of 2,4,6-TNP addition, which may be consider a response time of the probe (Fig. 4.8 d)

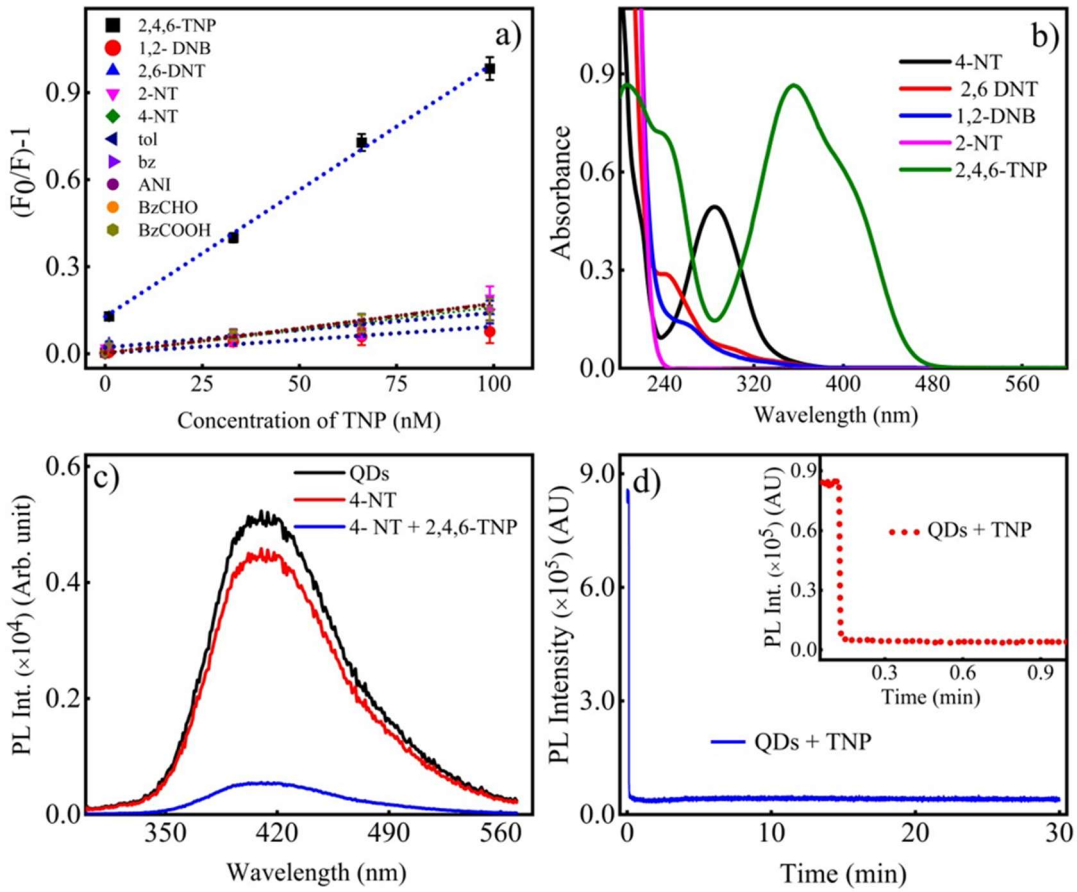

Fig. 4.8 *Stern Volmer (S-V) plot of all analytes with the varying concentrations ranging from 3.3 to 99 nM (a), Absorption spectra of different NACs at a fixed concentration of 99 nM alongwith 2,4,6-TNP (b), Photoluminescence spectra of $MoSe_2$ QDs: in the absence (black solid line), in the presence of 4-NT at a fixed concentration of 99 nM (red solid line), and with 2,4,6-TNP (blue solid line) under 290 nm excitation (c), sensing response time of the probe in the presence of 2,4,6-TNP (99 nM) in an aqueous medium is < 0.3 min. Plots of PL intensity at 410 nm as a function of time upon adding 2,4,6-TNP. The inset of represents the time response of the probe in about seconds (d).*

Table 4.1 *Parameters estimated from Stern−Volmer plots of PL intensity of $MoSe_2$ QDs at 410 nm with various NACs at fixed concentrations of 99 nM.*

Analytes	K_{sv} ($\times 10^{-6}$ M^{-1})	Correlation (R^2)	Intercept (nm)	SF
2,4,6-TNP	0.928	0.99	0.091	1.0000
1,2-DNB	0.748	0.97	0.007	0.8060
2,6-DNT	0.001	0.97	0.019	0.0011
2-NT	0.002	0.92	0.008	0.0021
4-NT	0.001	0.98	0.017	0.0011
tol	0.006	0.98	0.002	0.0064
BzCOOH	0.001	0.98	0.007	0.0011
bz	0.009	0.97	0.009	0.0097
ANI	0.008	0.97	0.012	0.0086
BzCHO	0.002	0.93	0.056	0.0021

4.3.5.2 Impact of 2,4,6-2,4,6-TNP on PL lifetime of MoSe2 QDs

Furthermore, the excitation dynamics and specific quenching behaviour can be ascertained by measuring time-resolved photoluminescence (TRPL). TRPL of $MoSe_2$ QDs were measured in the presence of the quencher to elucidate the PL quenching mechanism. As a reference, TRPL measurements were also conducted without 2,4,6-TNP. The decay profiles obtained in the absence of 2,4,6-TNP were best described by a tri-exponential fitting function (Eq. 4.2), revealing distinct lifetime components τ_1, τ_2 and τ_3 as 0.42, 3.54 and 11.5 ns. Notably, the 11.5 ns component (τ_3) possess the highest amplitude (51 %). However, the lowest contribution (13 %) is seen for the shortest lifetime component (τ_1), which is 0.42 ns. Fig. 4.9 illustrates the PL decay curves of $MoSe_2$ QDs monitored at a fixed excitation and emission of 340 nm and 410 nm, respectively. Single or bi-exponential functions could not adequately describe the observed decay profiles [5]. Instead, they were well-fitted with tri-exponential functions, as shown in Eq. (4.2):

$$I(t) = \alpha_1 e^{-\frac{t}{\tau_1}} + \alpha_2 e^{-\frac{t}{\tau_2}} + \alpha_3 e^{-\frac{t}{\tau_3}} \quad \text{(Eq. 4.2)}$$

where τ_1, τ_2 and τ_3 symbolize the lifetime components with α_1, α_2 and α_3 pre-exponential factors, respectively. The deconvolution of PL spectra of $MoSe_2$ QDs (Fig. 4.4a) revealed that the PL spectrum could be resolved in three distinct Gaussian bands, supporting the existence of three different types of luminescent sites within the QDs depending on the excitation wavelengths [49]. It has been noted that the lifetimes (τ_1, τ_2 and τ_3) show a slight decrease when the quencher (2,4,6-TNP) concentration increases from 3.3 to 99 nM. In addition, the variance in the relative change in PL lifetime is depicted in the inset of Fig. 4.9. The average PL lifetimes (τ_{avg}) were calculated using Eq. 4.3:

$$\tau_{avg} = \frac{\Sigma(\alpha_i \tau_i^2)}{\Sigma(\alpha_i \tau_I)} \quad (4.3)$$

As shown in Table 4.2, the average lifetime decreased from 10.01 ns to 9.68 ns, indicating a slight influence of 2,4,6-TNP on the excited state dynamics of $MoSe_2$ QDs [110].

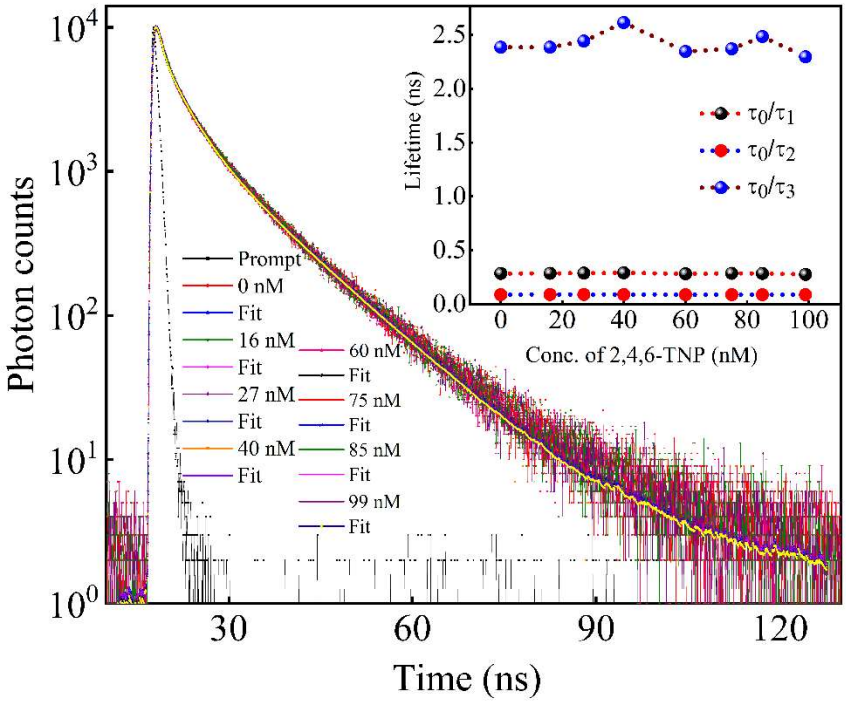

Fig. 4.9 *Fitted decay curves of $MoSe_2$ QDs with different concentrations of 2,4,6-TNP (3.3 to 99 nM) with 340 nm excitation and monitored at 410 nm.*

Table 4.2 *PL lifetime and pre-exponential factors of $MoSe_2$ QDs at the excitation wavelength of 340 nm and PL wavelength of 410 nm at different concentrations of 2,4,6-TNP.*

Conc. (nM)	τ_1 (ns)	τ_2 (ns)	τ_3 (ns)	α_1	α_2	α_3	τ_{av} (ns)	χ^2
00	0.42 ± 0.01	3.54 ± 0.05	11.5 ± 0.03	13.1	35.7	51.2	10.01	1.28
16	0.42 ± 0.01	3.51 ± 0.05	11.5 ± 0.03	13.1	35.7	51.2	10.01	1.25
27	0.41 ± 0.01	3.49 ± 0.05	11.5 ± 0.03	13.1	35.8	51.1	10.01	1.32
40	0.38 ± 0.03	3.44 ± 0.05	11.4 ± 0.01	13.1	35.6	51.2	9.93	1.27
60	0.42 ± 0.01	3.52 ± 0.06	11.3 ± 0.03	13.2	35.9	50.9	9.85	1.42
75	0.41 ± 0.01	3.41 ± 0.05	11.2 ± 0.03	12.9	35.9	51.1	9.79	1.38
85	0.39 ± 0.01	3.42 ± 0.05	11.1 ± 0.03	12.8	35.9	51.2	9.68	1.23
99	0.42 ± 0.03	3.52 ± 0.06	11.1 ± 0.01	13.3	36.3	50.4	9.64	1.35

4.3.5.3 Fluorescence Quenching Mechanism of MoSe2 QDs with 2,4,6-TNP

NACs can diminish the PL of QDs through three mechanisms that are known to deactivate excited states in various systems: photoinduced electron transfer (PET), Förster resonance energy transfer (FRET), and inner filter effect (IFE) [5]. One primary reported mechanism involves photo-induced electron transfer (PET) due to the electron-deficient nature of NACs [5,50–52]. However, unlike PL, the lifetime of $MoSe_2$ QDs in the presence and absence of 2,4,6-TNP is nearly the same (Table 4.2); hence, FRET can be ruled out [2,53,54]. The observed nearly constant lifetime of $MoSe_2$ QDs as a function of 2,4,6-TNP concentration may be due to static quenching; however, there is no complex formation or very weak formation. Furthermore, a

significant overlap between the absorption spectrum of 2,4,6-TNP and the excitation spectrum of $MoSe_2$ QDs (Fig. 4.10a) along with constant lifetime supports the IFE mechanism [55–59]. The absorption of 2,4,6-TNP reduces the number of excited MoSe2 QDs, leading to a decrease in overall PL intensity. The S-V plots, generated by recording PL spectra at the right angle (RA) and front face (FF) detection modes, as shown in Fig. 4.10(b), reveal a significant difference in slope, confirming the role of IFE. In addition to IFE, a small possibility of a PET process cannot be entirely ruled out. Further, analysis of radiative and non-radiative decay rates could provide further evidence [57] (Table 4.3). In PET, the excited state electron of the donor ($MoSe_2$ QDs) can transfer to the electron-deficient acceptor (2,4,6-TNP). This electron transfer process from $MoSe_2$ QDs (donor) with a potentially high radiative decay rate (fast emission) to 2,4,6-TNP (acceptor) with a potentially low non-radiative decay rate (slow relaxation back to ground state), could contribute to the observed quenching alongside IFE [57,60–62].

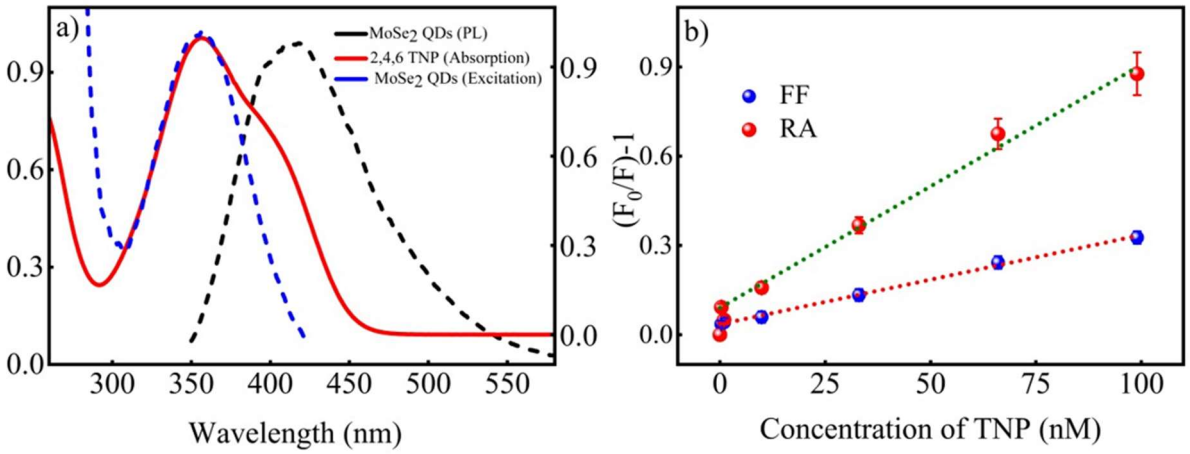

Fig. 4.10 *Spectral overlap of absorption spectrum of 2,4,6-TNP, PL and PL- excitation spectra of $MoSe_2$ QDs (a), S-V plots of $MoSe_2$ QDs with 2,4,6-TNP obtained in RA and FF detection modes (b).*

Table 4.4 summarizes various reported probes responsive to 2,4,6-TNP and their associated methodologies. It also compares the sensing performance of $MoSe_2$ QDs for 2,4,6-TNP detection with that of other established 2,4,6-TNP probes. Notably, the present $MoSe_2$ QDs probe demonstrates good sensitivity for 2,4,6-TNP detection across a wide concentration range.

Table 4.3 *Comparison of $MoSe_2$ QDs-based probe with the reported probes for 2,4,6-2,4,6-TNP sensing.*

Fluorescence probes	**Linearity range (nM)**	**Correlation coefficient (R^2)**	**LoD (nM)**	**Refs**
$MoSe_2$ QDs	3.3- 99	0.99	1.43	This
N, S-CNPs	1.0×10^2 - 4×10^4	0.99	43.0	Work
NCPs & CPEs	1.0×10^2 - 5.0×10^3	0.99	5.0	[64]
CDs	1.0×10^3 - 1.0×10^5	0.99	840	[65]
BSA-$CuInS_2$ QDs	3.0×10^3 - 5.0×10^4	0.99	28.0	[66]
BZQZPy	0.0 - 2.2×10^9	0.99	20.0	[67]
DE-CDs	2.0×10^2 - 5.0×10^4	0.99	50.0	[150]
S@GQDs	1.0×10^2 -1.0×10^5	0.99	93.0	[68]
CQDs	0.0-1.0×10^5	0.99	355	[53]
CDs	1.0×10^2 - 2.6×10^5	0.99	51.0	[69]
Tb@CDs	5.0×10^2 -1.0×10^5	0.99	200	[70]
Cy-Cu NCs	2.5×10^3 - 2.5×10^4	0.99	190	[71]
MoS_2 QDs	99.0 - 3.6×10^4	0.99	95.0	[72]
MoS_2QDs@1,2 DAB	3.0×10^3 - 4.0×10^5	0.98	50×10^2	[43]
f-ZnSe QDs	2.0×10^3 - 2.5×10^5	0.98	$12.4 \times$	[54]
Zn-MOF	1.0×10^6	-	10^3	[110]
O-fNPs	0.0 – 6.0×10^3	-	560	[73]
g-$C3N_4$	5.0×10^2 – 1.0×10^4	0.99	7.46	[140]
N-GQDs	0.0 – 4.0×10^3	0.99	8.50	[44]
BN-CNPs	0.0 – 2.0×10^5	-	420	[74]
			10.0	[75]

Additionally, the stability of the $MoSe_2$ QDs was evaluated by monitoring the PL intensity at 410 nm over a period of 8 months. This exceptional stability makes them promising candidates for long-term sensing applications (Fig. 4.11a). Moreover, $MoSe_2$ QDs were continuously irradiated under a UV lamp with a power output of 8 W at a wavelength of 365 nm for 180 min, as shown in the bar graph in Fig. 4.11(b)

The results demonstrated minimal variation in PL intensity, indicating excellent photostability of the $MoSe_2$ QDs.

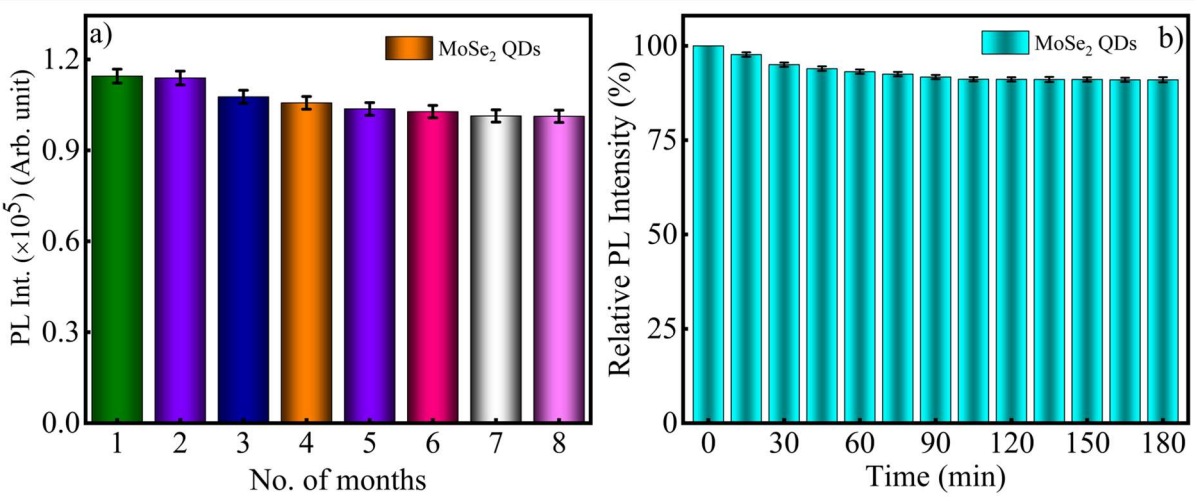

Fig. 4.11 *Photoluminescence intensity of $MoSe_2$ QDs at 410 nm monitored in the repeated interval up to 8 months, representing stability of QDs longer than 8 months (a), Photoluminescence intensity (%) of $MoSe_2$ QDs monitored at 410 nm under continuous UV lamp irradiation (365 nm) for 180 min, representing the photostability of QDs (b).*

4.3.5.4 Validation and Analysis of Real Samples

Real water samples were examined to assess the realistic sensing ability of $MoSe_2$ QDs for 2,4,6-TNP detection. Three water samples were gathered: Yamuna River, DTU Lake and tap water. The Yamuna River, one of the largest tributaries of the Ganga River, was chosen due to its high pollution levels, particularly in Delhi, caused by household sewage, industrial effluents, and agricultural runoff [36]. TNP was initially added to the collected water samples at different concentrations, ranging from 3.3 to 99 nM, to mimic actual contamination levels. A $MoSe_2$ QDs solution made in UP water was then added to the spiked water samples to dilute them and maintain the ideal concentration of QDs for PL measurements. Each type of water sample was diluted by 0.5 mL of $MoSe_2$ QDs solution to a final volume of 10 mL for the tests. For PL measurements, 3ml of the diluted solution was then placed in a quartz cuvette (1cm×1 cm). In the presence of TNP at fixed doses ranging from 3.3 to 99 nM, the PL quenching behavior was methodically examined in all water samples. Fig. 4.12(a-c), show the corresponding PL spectra for Yamuna river, DTU lake and tap water, respectively, along with the S–V plots (inset), which shows the linearity and quenching

efficiency for TNP detection.Table 4.5 summarizes LOD values determined for every water sample, highlighting the excellent sensitivity of the proposed system.

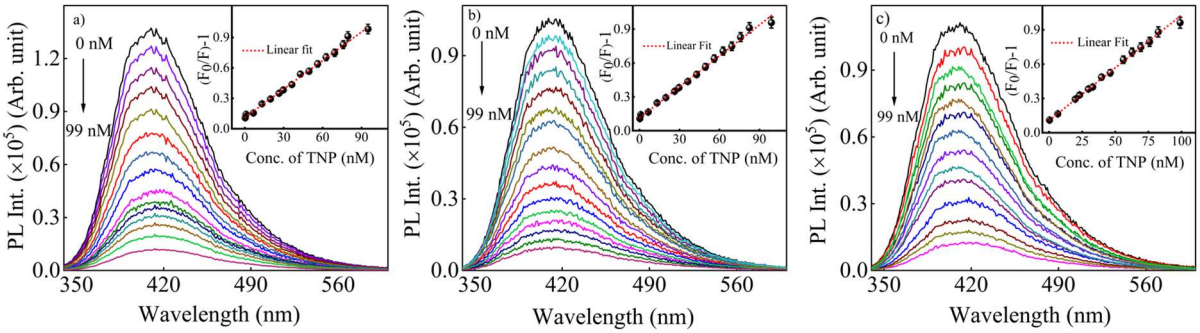

Fig. 4.12 *Photoluminescence spectra of $MoSe_2$ QDs in Yamuna River (a), DTU lake (b), tap water (c) in the absence and presence of various concentrations (3.3 to 99 nM) of 2,4,6-TNP with 340 nm excitation. The insets represent the corresponding S-V plots.*

Table 4.4 *Calculated LoD values with quenching percentage for $MoSe_2$ QDs in different water samples.*

Water Sample	Quenching (%)	Limit of detection (LoD) (nM)
Ultrapure water	94	1.43
DTU lake water	92	6.69
Tap water	90	3.49
Yamuna river water	92	7.38

Additionally, the sensing performance across the three distinct water matrices, including an original sample in UP water, is visually represented by comparative bar chart [63], as shown in Fig. 4.13. These findings demonstrate the efficacy of $MoSe_2$ QDs in real-sample analysis for TNP detection in various water sources and environmental monitoring.

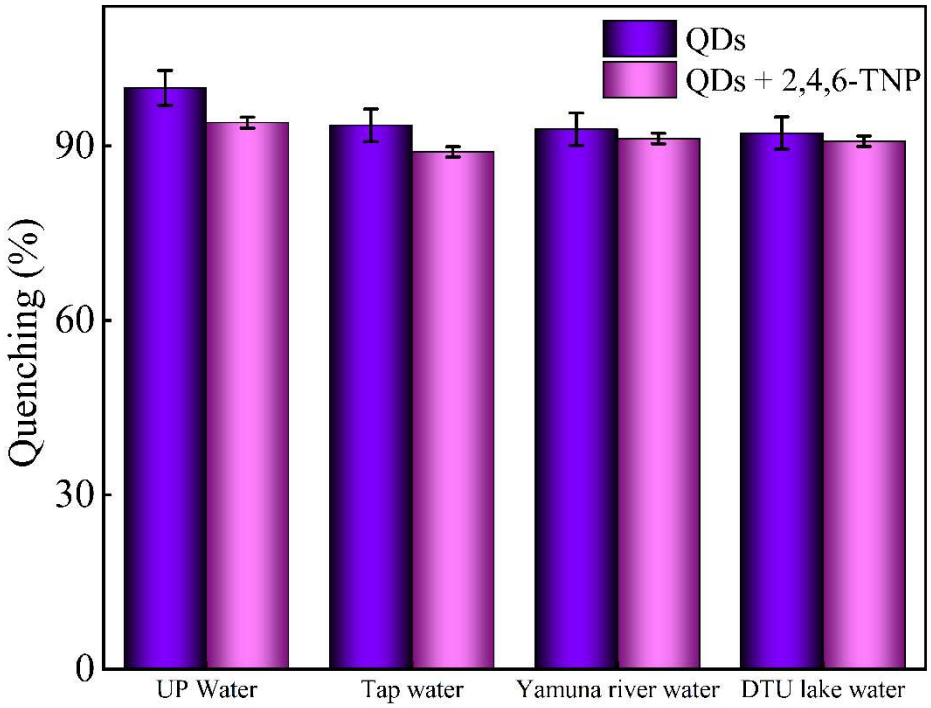

Fig. 4.13 *Percentage quenching of PL intensity (at 410 nm) of $MoSe_2$ QDs in different water samples. A comparative bar graph representing 2,4,6-TNP sensing in real samples, highlighting the efficiency of QDs as a sensor for explosive detection in real-world samples monitoring.*

4.4. Conclusion

In summary, the work demonstrates that $MoSe_2$ QDs can be successfully synthesized using a hydrothermal method and can be employed to detect waterborne explosives. The $MoSe_2$ QDs exhibited strong light absorption and PL properties. The PL intensity at 410 nm displayed a significant change with increasing 2,4,6-TNP concentration, showcasing the high sensitivity towards this specific nitroaromatic compound. The probe/sensor demonstrated a linear response over an extensive 2,4,6-TNP concentration range (3.3 - 99 nM) with high sensitivity and selectivity and an impressive detection limit (1.43 nM). IFE likely dominate as a quenching mechanism. Overall, these finding pave the way for developing highly sensitive and selective

$MoSe_2$ QD-based sensors for detecting various environmental pollutants and explosives.

Chapter 5: Reusable fluorescent WS_2 QDs Sensor for Ultralow-Level Detection of Cr^{6+} in Real Water Samples

5.1 Introduction

Transition metal dichalcogenides (TMDs) are attracting considerable attention due to their remarkable properties and numerous applications in various sectors, including sensing, electronics, and photonics [1–3]. Due to its exceptional chemical stability, tungsten disulfide (WS_2) has become a top contender among TMDs with a broad absorption spectrum and unique PL properties [3,4]. WS_2 quantum dots (QDs) can be synthesised in several ways, but the hydrothermal method is the most widely used and effective. The production process is simplified by the hydrothermal approach, which eliminates the need for post-functionalization or capping agents [5–7]. This process produces WS_2 QDs with superior optical properties and good stability, making them ideal for sensing applications [1,8]. Given the needs of modern technology, there is a growing demand for portable, affordable, and rapid-response sensors that can detect hazardous gases and heavy metals. The development of sensors that meet these criteria is crucial for effective environmental monitoring and public health management [9,10].

Chromium (Cr) is a d-block transition metal that can exist in multiple oxidation states, namely elemental (0), divalent (+2), trivalent (+3) and hexavalent (+6) forms [11]. Among these, the hexavalent form of Cr^{6+} is of particular concern due to its highly toxic and carcinogenic nature. Cr^{6+} is dangerous primarily because of the mechanism by which it interacts with biological systems. Upon reduction within cells, Cr^{6+} releases reactive hydroxyl radicals, which cause extensive cellular damage and can

bind to DNA, leading to mutations and the development of cancer [12–14]. Whether from ingestion, inhalation, or contact with tainted food or water, exposure to Cr^{6+} increases the risk of cancer and other serious health problems [11,15]. The lack of cost-effective treatments for diseases like cancer further underscores the importance of early detection and prevention [16–18]. Identifying and managing carcinogens at a premature stage is crucial for reducing the risk of cancer. Various analytical techniques, such as differential pulse voltammetry, atomic absorption spectrometry, and ICP-MS, are used for Cr^{6+} detection. However, many require costly instruments, complex procedures, or lack suitability for rapid, on-site monitoring [14,17,19–23]. Given these challenges, there is an urgent need to develop efficient, rapid, and straightforward methods for detecting Cr^{6+}, particularly in liquid matrices like food and water. As a result, there is now more interest in optical and chemical sensors that use nanomaterials. Among them, nanoparticle-based sensors, especially those that utilise noble metals and other cutting-edge materials, are the subject of considerable investigation due to their potential for detecting a wide range of hazardous compounds.

Fluorescent QDs, including carbon dots, CdSe-based QDs and other TMD QDs, have garnered significant attention as highly sensitive probes for detecting various heavy metal ions such as Pb^{2+}, Hg^{2+}, and Cr^{6+} [24,25]. These nanomaterials exhibit excellent PL properties and tunable surface chemistry, enabling specific and selective recognition of toxic ions in environmental samples. For instance, carbon QDs synthesised from renewable sources have demonstrated effective PL quenching upon interaction with Cr^{6+} and other metal ions, enabling detection at trace levels [9,26,27]. CdTe and ternary I–III–VI QDs have also been successfully employed for multiplexed detection of heavy metals with low limits of detection (LoD) [28,29]. Although these advancements highlight the potential of QD sensors, studies specifically leveraging WS_2 QDs for Cr^{6+} detection remain limited, which motivates the present investigation into a WS_2 QD-based turn-off/on PL sensor.

Here, we explore the use of hydrothermally synthesised WS_2 QDs as a turn-off/on PL sensor for Cr^{6+} detection. The sensing mechanism involves a significant quenching of PL when Cr^{6+} is introduced via static conditions, with the recovery of PL upon the addition of ascorbic acid (AA), which reduces Cr^{6+} to its less toxic trivalent form, Cr^{3+}. This dual-action detection and reduction strategy offers an efficient and

eco-friendly approach for monitoring and mitigating chromium contamination. The practical feasibility of the developed sensing platform was established through testing with real environmental matrices, including river water from the Triveni Sangam (Prayagraj), a holy place, and tap water, confirming its reliability and potential for real-world deployment.

5.2 Experimental section

5.2.1. Chemicals and reagents

The synthesis was carried out using commercially available precursors and analytically pure solvents without the need for further purification steps. Sodium tungstate dihydrate ($Na_2WO_4 \cdot 2H_2O$, 96%), L-cysteine ($HSCH_2CHNH_2COOH$, 98%) and various metal ions (99.8%), including potassium dichromate (Cr^{6+}), iron (III) perchlorate hexahydrate (Fe^{3+}), erbium (III) chloride hexahydrate (Er^{3+}), calcium (II) perchloride tetrahydrate (Ca^{2+}), europium (III) chloride hexahydrate (Eu^{3+}), terbium (III) chloride hexahydrate (Tb^{3+}), lead (II) perchlorate trihydrate (Pb^{2+}), cadmium (II) chloride hydrate (Cd^{2+}), iron (II) perchlorate hydrate (Fe^{2+}), zinc (II) perchlorate hexahydrate (Zn^{2+}), aluminum (III) perchlorate nonahydrate (Al^{3+}), nickel (II) perchlorate hexahydrate (Ni^{2+}), magnesium (II) perchloride hexahydrate (Mg^{2+}), barium (II) perchlorate anhydrous (Ba^{2+}), and mercury (II) perchlorate hydrate (Hg^{2+}), copper (II) chloride dehydrated (Cu^{2+}), chromium (III) chloride (Cr^{3+}) was sourced from Sigma Aldrich. DI water (18.2 MΩ·cm) of ultrapure grade was used throughout the experiments. Furthermore, actual water samples were gathered in order to assess the WS_2 QDs-based probe's practical sensing capabilities.

5.2.2. Synthesis

WS_2 QDs were synthesised using a previously described, simple one-step hydrothermal method with slight modifications [1]. In summary, an aqueous solution was used to simultaneously dissolve sodium tungstate (A) and L-cysteine (B) at a molar ratio of 0.5:1. To adjust the mixture (A+B) to a slightly acidic pH (~4), 0.1 M H_2SO_4 was added, while continuously stirring and maintaining a temperature of 30°C. Post 30 minutes of stirring, the solution was subsequently sonicated. The prepared

mixture was poured into a 100 mL stainless steel autoclave lined with polytetrafluoroethylene (PTFE) and subjected to hydrothermal treatment at 200 °C for 36 hours. After allowing the vessel to cool naturally for 10 hours, the autoclave was opened, and the yellow dispersion containing WS_2 QDs was collected and purified by centrifugation. No additional capping or stabilising agents or post-synthesis treatments were done. L-cysteine offers intrinsic stability due to its photo-resistant properties, simplifying the synthesis process and enhancing its applicability. Scheme 5.1 illustrates the synthesis of WS_2 QDs, and the reaction details are presented in the subsequent section.

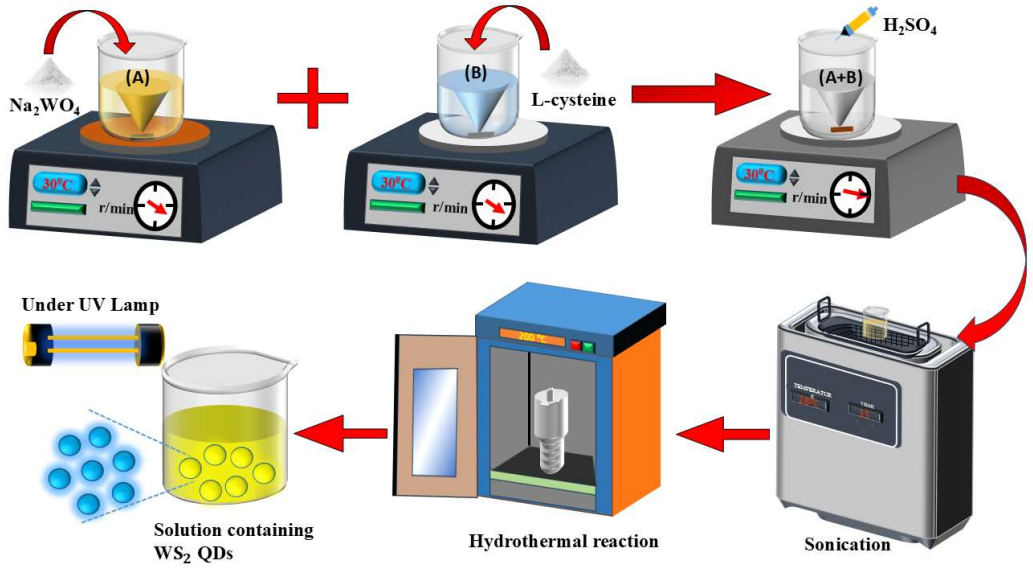

Scheme 5.1 *Schematic representation of the one-step hydrothermal synthesis route for colloidal WS_2 QDs.*

5.2.3. Reaction Pathway

L-cysteine undergoes oxidative decomposition in the presence of DI, yielding pyruvic acid (an α-keto acid bearing carboxylic and ketone functional groups) while releasing hydrogen sulfide (H_2S) and ammonia gas (NH_3). The H_2S, identifiable by its characteristic pungent odour, subsequently participates in a redox reaction with tungstate ions (WO_4^{2-}), forming a colloidal solution of WS_2 QDs [30].

$$HSCH_2CHNH_2COOH + H_2O \rightarrow CH_3COCOOH + NH_3\uparrow + H_2S\uparrow$$

$$4WO_4^{2-} + 9H_2S + 6CH_3COCOOH \rightarrow 4WS_2 + SO_4^{2-} + 6CH_3COCOO^- + 12H_2O$$

These reactions outline the chemical pathway involved in the synthesis of WS_2 QDs.

5.2.4. *Analytical Instruments used*

UV–vis absorption and PL spectroscopy were employed as primary techniques for evaluating the optical characteristics of the samples, owing to their high sensitivity and minimal sample requirement. UV-vis absorption spectra were recorded using a double-beam spectrophotometer (Lambda 750, PerkinElmer, USA). PL and excitation spectra were obtained with a Fluorolog-3 spectrofluorometer (Horiba Jobin Yvon, France). Time-resolved fluorescence measurements were conducted using the time-correlated single-photon counting (TCSPC) method on a DeltaFlex-01-DD system (Horiba Jobin Yvon IBH Ltd, UK), featuring a PPD 850 detector and a 320 nm Delta diode source operating at 4 MHz. The instrument response function (IRF) was acquired using Ludox colloidal silica as a scattering reference. All spectroscopic analyses were carried out in standard 1 cm path length quartz cuvettes. HR-TEM was performed using a TALOS microscope (Thermo Scientific) operated at 200 kV to determine morphology and particle size. Fourier transform infrared (FTIR) spectra were collected in the 400–4000 cm^{-1} range using a PerkinElmer FTIR spectrometer to identify surface functional groups. Crystallinity and phase identification were achieved through X-ray diffraction (XRD) analysis using a Bruker D8 Advance diffractometer with CuK_{α} radiation (λ=1.54 Å), operated at 40 kV and 20 mA. XPS was utilised to investigate the surface chemical composition and oxidation states using a Specs system with a monochromatic Al source (hν =1486.6 eV) and a Phoibos 150 hemispherical analyser. The base pressure during X-ray photoelectron spectroscopy (XPS) analysis was maintained near 1×10^{-9} mbar. Spectra were calibrated to the C 1s peak of adventitious carbon at 284.8 eV. Data analysis and peak deconvolution were performed using OriginLab, employing a Gaussian–Lorentzian fitting profile and linear background subtraction.

5.3 Results and discussion

5.3.1. XRD and FTIR study

Fig. 5.1(a) illustrates the XRD pattern of the synthesised WS_2 QDs dispersed on a glass substrate, with weakly discernible peaks at (002), (004) and (006), corresponding to 2θ values of 13.2°, 32.1°, and 44.2°, respectively. Previous studies, such as those by Ren et al. [31] and Wu et al. [32], have demonstrated that when the particle size is

extremely small, the XRD pattern typically lacks distinct peaks [1,33]. This is attributed to the nanoscale nature of the material, which often results in the broadening or absence of sharp diffraction features [31,32]. The weak diffraction humps observed here support the formation of nanoscale WS_2 QDs with a very small and thin structure, consistent with their QD size. Figure 5.1(b) illustrates the FT-IR spectrum of the WS_2 QDs. The IR absorption band around 1025 cm^{-1} is attributed to the C-O stretching vibration of hydroxyl groups [34]. The 1632 cm^{-1} and 3285 cm^{-1} peaks correspond to the N-H out-of-plane bending and/or N-H_2 bending vibrations from the amide group and the dimer formed due to the hydroxyl group, respectively [30,35]. The bands at 545 cm^{-1} and 2115 cm^{-1} are associated with the C-H bending vibration and N=C stretching vibration, respectively [1,19]. The presence of hydrophilic groups, such as -OH and -COOH, on the surface of the synthesised QDs is crucial for their excellent water dispersibility [36]. These surface groups enhance the QDs stability and expand their potential applications in aqueous environments, similar to the behaviour observed in various carbon dots [37,38].

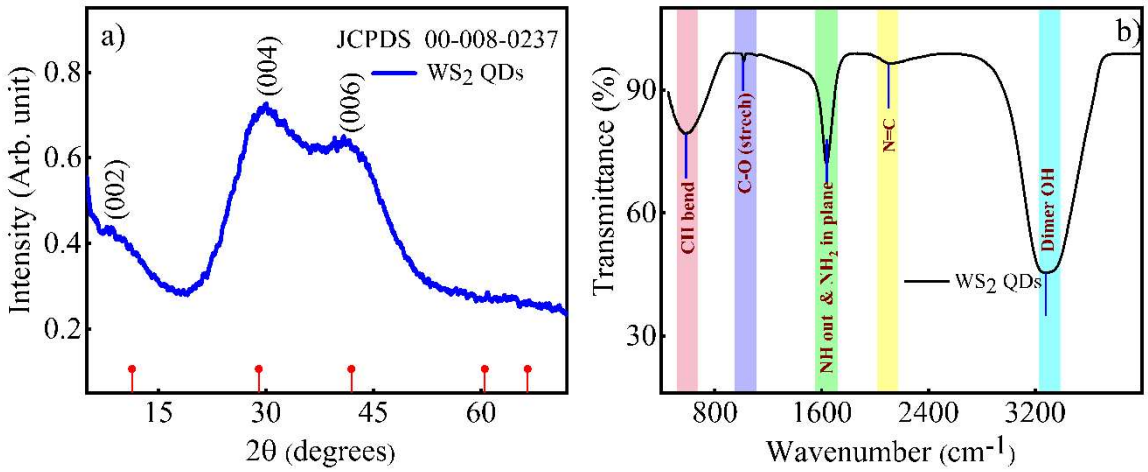

Fig. 5.1 *XRD pattern of synthesised WS2 QDs deposited on thin film (a) and FT-IR spectrum of WS2 QDs dispersed in aqueous medium (b).*

5.3.2 HR-TEM analysis

The HR-TEM images of the prepared WS_2 QDs, captured at various magnifications (Fig. 5.2 a,b) confirm their spherical morphology with homogeneous distribution, whose size ranges from 1.5 to 3.5 nm. The high-resolution image shown in the inset of Fig. 5.2(b)displays well–ordered and parallel lattice fringes, demonstrating the

crystallinity of the WS_2 QDs. The calculated interplanar spacing (d-spacing) of 0.2 nm matched with the (100) lattice plane of WS_2, consistent with prior reports [1,39,40]. Particle size distribution analysis, performed through Gaussian fitting, showed an average particle size of about 2.5 nm. The narrow distribution suggests that the synthesised QDs are monodisperse (Fig. 5.2c). Such uniformity in particle size enhances their stability and suitability for further applications.

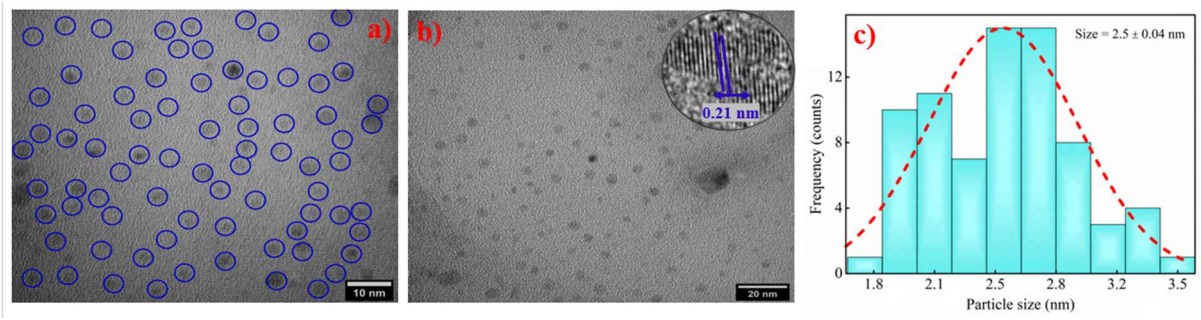

Fig. 5.2 *HR-TEM visuals of obtained WS_2 QDs at various magnifications (a,b) and particle size distribution (c). The enlarged view of the image with computed d-spacing is displayed in the inset of (b).*

5.3.3. Photophysical Performance and Properties of WS2 QDs

Figure 5.3 shows the UV-Vis absorption spectrum of the synthesised WS_2 QDs, which exhibits distinct peaks at 242 nm (5.12 eV), 276 nm (4.49 eV), 336 nm (3.69 eV) and a shoulder band at 392 nm (3.16 eV), indicating characteristic electronic transitions. The strong absorption band at 336 nm (3.69 eV) corresponds to the excitonic absorption from direct bandgap transitions at the K point in the Brillouin zone, a hallmark feature of WS_2 QDs [1,30]. The peak at 276 nm (4.49 eV) is attributed to the optical transition from the valence band to the conduction band [1,41], while the absorption at 242 nm (5.12 eV) is linked to electronic transitions influenced by quantum confinement effects. The additional broad feature at 392 nm (3.16 eV) is associated with surface states and defect-related absorption, likely influenced by functional groups such as -OH and $-SO_4^{2-}$ adsorbed on the QD surface [30,42], or due to the agglomeration of the QDs. A second-order derivative spectrum analysis was performed to further validate these absorption features, which distinctly resolved these peak positions and confirmed their accuracy. The derivative spectrum enhances clarity

by minimising background interference and ensuring precise peak identification. Additionally, the visual appearance of WS_2 QDs is depicted in the inset of Fig. 5.3, where the colloidal solution appears light yellow under white LED illumination but exhibits blue PL when exposed to ~365 nm under a UV lamp.

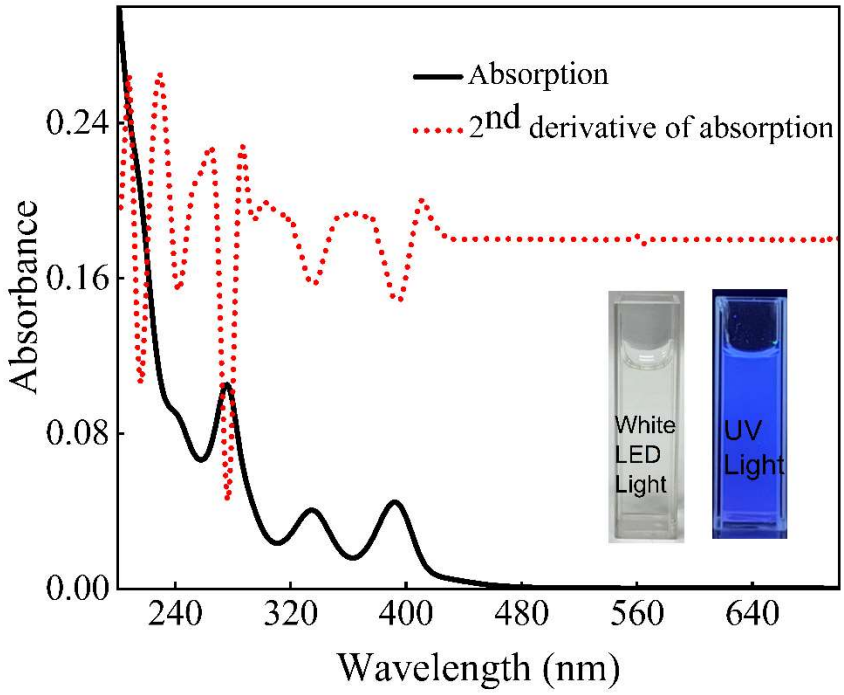

Fig. 5.3 *Absorption spectrum of synthesised WS_2 QDs overlaid with its 2nd order derivative (red dotted line). The inset displays the visible colour representation under white LED illumination and UV irradiation (365 nm).*

Fig. 5.4(a) shows the overlapped absorption spectrum, PL spectrum with an excitation of 320 nm (3.87 eV), and PL-excitation spectrum (PLE) at 420 nm (2.95 eV). Fig. 5.4(b) shows the PL spectra recorded at room temperature (RT) for different excitation wavelengths (280-420 nm), exhibiting an increase in PL intensity from 280 to 320 nm, with an emission peak at 420 nm (2.95 eV) at an optimal excitation at 320 nm. Beyond 320 nm, the PL intensity gradually declined. A red shift of 82 nm was observed in the PL spectrum as the excitation wavelength varied from 280 to 420 nm shown by the normalized PL spectra in Fig. 5.4(c), indicating an inhomogeneous size distribution and multiple localized defect states. This excitation-wavelength-dependent behaviour is attributed to polydispersity and defect states in the WS_2 QDs [43,44], as represented by the CIE plot (Fig. 5.4d).

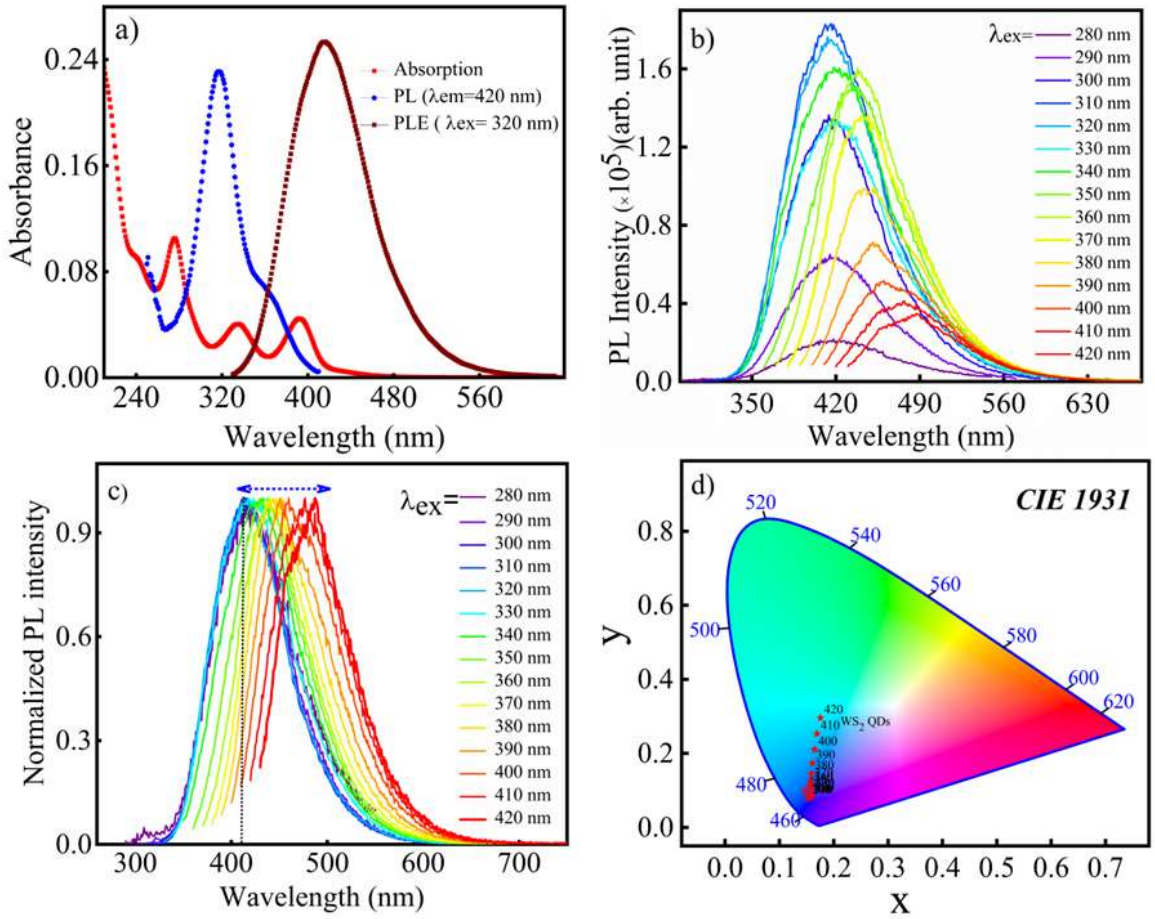

Fig. 5.4 Overlapped absorption, PL, and PLE spectra of colloidal WS_2 QDs (a). PL spectra of WS_2 QDs recorded at various excitation wavelengths (b) and normalized PL spectra to highlight PL shift and profile consistency (c). CIE 1931 chromaticity diagram representing the colour coordinates of WS_2 QDs emissions (d).

PLE were recorded by monitoring the emission at various wavelengths. The excitation spectra exhibited dependence on the emission monitoring wavelength, with a prominent excitation band observed near ~320 nm. Additionally, a secondary excitation feature around 362 nm displayed a slight blue shift as the monitored emission wavelength decreased. Further, PLE spectra of synthesized WS_2 QDs recorded at different emission wavelengths ranging from 420 to 500 nm were deconvoluted using three Gaussian bands g1, g2 and g3 centered at 320 nm, 362 nm, and 388 nm, indicating the involvement of three distinct excitation states in the luminescence process as illustrated in Fig. 5.5(a). These excitation bands show a strong

correlation with the observed absorption bands at 276 nm, 336 nm, and 392 nm, respectively. For the calculation of the quantum efficiency/quantum yield (QY) of WS_2 QDs, a standard comparative method was employed, using quinine sulfate with known QY 0.54 as a reference [1].

$$QY_{sam} = QY_{ref} \times \frac{Area_{sam}}{Area_{ref}} \times \frac{Abs_{ref}}{Abs_{sam}} \times \left(\frac{\eta_{sam}}{\eta_{ref}}\right)^2 \quad (5.1)$$

Where QY_{ref} and QY_{sam} are the QY of quinine sulfate and WS_2 QDs, Abs is the absorbance, Area is the integrated PL emission, and η is the solvent refractive index for each sample, which yielded an estimated value of 8.4%, higher than previously reported [1,30]. The significant QY of WS_2 QDs indicates efficient radiative recombination. Additionally, PL decay profiles of WS_2 QDs were collected using a 320 nm excitation source while monitoring the emission at 370 nm, 410 nm and 490 nm, as shown in Fig. 5.5(b) along with the instrument response function (IRF) and residual plots (Fig. 5.5c) corresponding to decay fitting, along with chi-square (χ^2) values indicating goodness of fit.

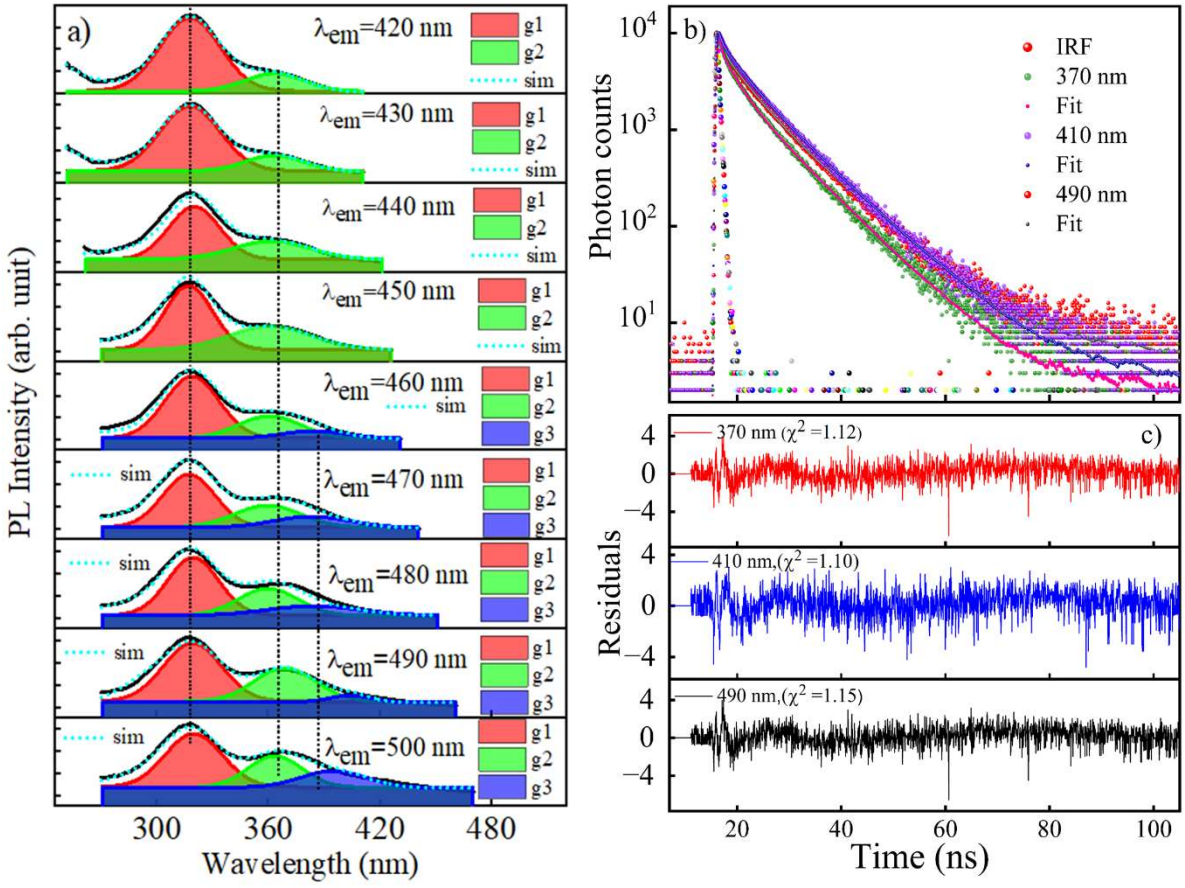

Fig. 5.5 *PLE spectra of synthesised WS_2 QDs at different emission wavelengths along with deconvoluted Gaussian bands g1, g2, and g3 (a). TRPL decay curves of WS_2 QDs excited at 320 nm, recorded at different emission wavelengths, along with IRF (b) and residual plots corresponding to the fitted decay profiles along with the associated χ^2 values (c).*

The TRPL decay curves were well-fitted using a tri-exponential decay function as described by Eq. 5.2:

$$I(t) = \sum_{i=1}^{3} \alpha_i \exp(-t/\tau_i) \quad (5.2)$$

where α_i represents the pre-exponential factor and τ_i denotes the lifetime corresponding to the i-th decay component.

At a PL wavelength of 370 nm, the decay was dominated by the fasted component (τ_1 = 0.20 ns, α_1 = 0.79), while the slowest component (τ_3= 8.18 ns) had a minor contributed (α_3 = 0.09). The intermediate component displayed a lifetime ranging from 2.92 to 4.33 ns, depending on the PL wavelength, which varied from 370 to 490 nm. These three decay lifetimes are attributed to distinct emissive states or recombination centres, likely arising from a combination of quantum confinement and surface defects state generated following photoexcitation. All the three lifetime components show a gradual increase when monitoring at longer wavelengths. This trend is likely due to the contribution of defect states or the polydispersity of the QDs, leading to the broader distribution of emissive sites. The average PL lifetime (τ_{av}), calculated using Eq. 5.3,

$$\tau_{av} = \frac{\sum_{i=1}^{3} \alpha_i \tau_i^2}{\sum_{i=1}^{3} \alpha_i \tau_i} \quad (5.3)$$

also increased with increasing PL wavelength. This behaviour suggests the presence of multiple surface-related emissive states, further supported by polydispersity in the QDs population, as summarized in Table 5.1.

Table 5.1 *Tri-exponential fitted PL lifetimes and pre-exponential factors of colloidal WS_2 QDs.*

λ_{ex} (nm)	λ_{PL} (nm)	τ_1 (ns)	τ_2 (ns)	τ_3 (ns)	α_1	α_2	α_3	τ_{av} (ns)	χ^2

320	**370**	0.20 ± 0.01	2.92 ± 0.07	8.18 ± 0.03	0.79	0.12	0.09	5.69	1.12
	410	0.34 ± 0.02	4.15 ± 0.03	8.87 ± 0.01	0.61	0.19	0.20	6.88	1.10
	490	0.49 ± 0.01	4.33 ± 0.15	9.37 ± 0.04	0.61	0.22	0.17	6.74	1.15

5.3.4. Photostability and Environmental stability of synthesized WS2 QDs under different conditions

The stability of synthesised WS_2 QDs was evaluated under varying pH, temperature, UV exposure, and long-term storage conditions. The PL intensity of WS_2 QDs remained nearly unchanged across a broad pH range from 2 to 12, indicating their exceptional chemical stability in highly acidic and alkaline environments represented by the bar graph shown in Fig. 5.6(a). This stability is consistent with previous studies on TMDs such as MoS_2 and WS_2 etc. [25,45], which attribute their robustness to strong covalent bonding and minimal surface oxidation [43]. Further, under prolonged UV exposure at 365 nm for 2 hours, the PL intensity exhibited negligible variation, demonstrating the excellent photostability of WS_2 QDs. Such resistance to photodegradation makes them suitable for PL-based sensing applications. Fig. 5.6(b) represents the corresponding relative change in PL intensity under different time exposures. The temperature-dependent PL studies also revealed an increase in PL intensity at lower temperature ranges (-5 to 15°C), likely due to suppressed non-radiative recombination processes at reduced thermal energy [46,47]. However, as the temperature increased from RT, ~30 to 105°C, a very slight decrease in PL intensity was observed. Figure 5.6(c) shows the bar graph corresponding to the relative change in PL intensity at various temperature ranges from -5 to 105 °C. This minor reduction is attributed to enhanced thermal vibrations, which cause increased non-radiative recombination–a common phenomenon observed in WS_2 and MoS_2 QDs [48,49]. Furthermore, a long-term stability analysis was conducted over a two-month period, with PL intensity measurements taken at 15-day intervals at RT. The results showed an almost negligible change, confirming the outstanding structural and optical stability of WS_2 QDs over extended periods. The bar graph showed the corresponding relative

change in intensity at different intervals of days (Fig. 5.6d). This long-term stability is crucial for their future applications.

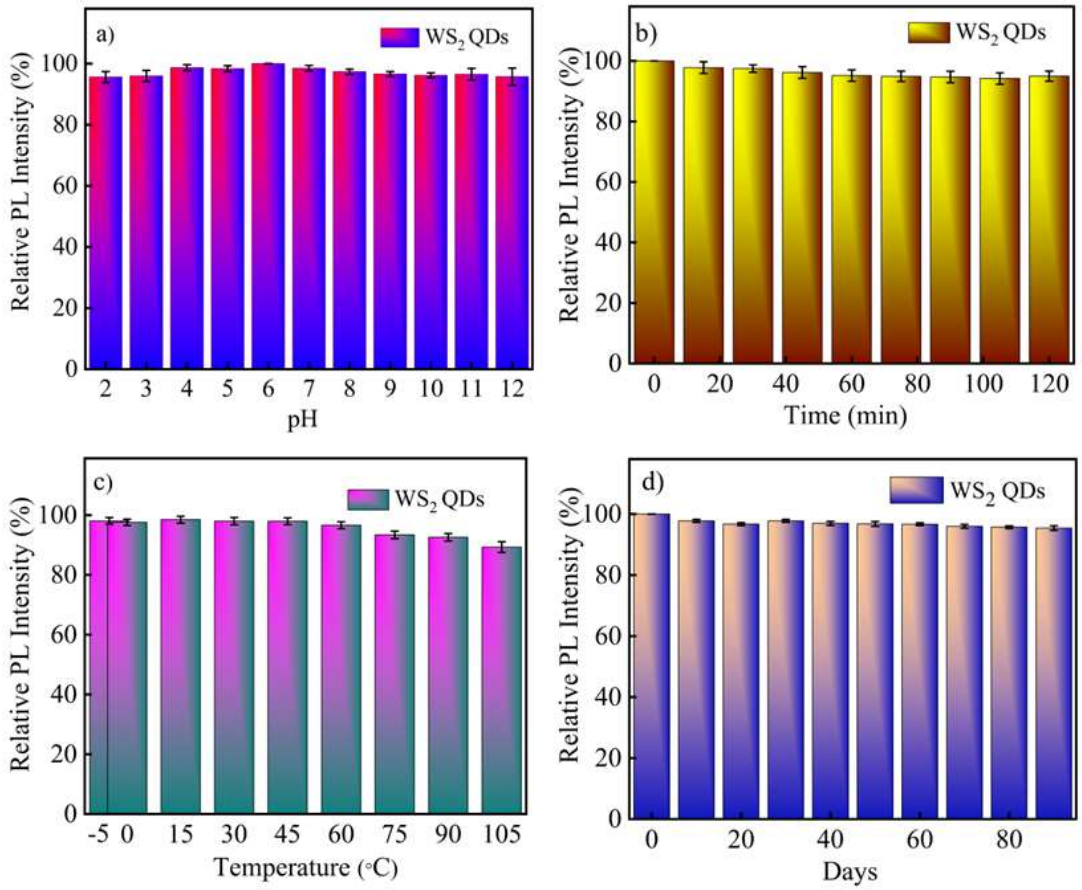

Fig. 5.6 *Bar graphs showing the relative PL intensity (%) of WS_2 QDs under different conditions: pH-dependent PL stability (a), UV irradiation (λ=365 nm) indicating photobleaching resistance (b), temperature-dependent PL response representing thermal stability (c) and long-term shelf-life stability at RT (d).*

5.4. Cr6+ sensing

5.4.1 Effect of Cr6+ on UV-vis Absorption and PL spectra of WS2 QDs

Fig. 5.7(a) illustrates the UV-vis absorption spectra of synthesised WS_2 QDs in the presence of varying concentrations of Cr^{6+} ions. Upon the addition of a small amount of Cr^{6+} (0.66 nM), a slight increase in optical density (OD) is observed for the absorption peak at 336 nm (3.69 eV), along with the characteristic peaks at 242 nm (5.2 eV) and 392 nm (3.16 eV). As the Cr^{6+} concentration increases to 660 nM, this trend continues, leading to significant spectral changes. The peak at 242 nm (5.12 eV) progressively flattens at higher concentrations, while the absorbance at 336 nm (3.69

eV) and 392 nm (3.16 eV) continues to increase substantially. In contrast, the 276 nm (4.49 eV) band remains largely unaffected, exhibiting only a slight decrease at elevated concentrations. Interestingly, an isosbestic point appears nearer to 220 nm. These spectral modifications suggest strong electronic interactions between WS_2 QDs and Cr^{6+} ions, potentially forming a WS_2 QDs/Cr^{6+} complex in the ground state. A similar trend has been observed in MoS_2 QDs, where Pb^{2+} ion binding increased absorbance and spectral sharpening, indicating complex formation [25]. The plots of (A_0-A), where A_0 and A represent the absorbance in the absence and presence of Cr^{6+}, respectively, as a function of increasing concentrations of Cr^{6+} varying from 0.66 to 660 nM, exhibits a linear relationship with the fitting parameter of R^2 =0.98, as shown in the inset of Fig. 7a, which supports the hypothetical 1:1 complex formation. To further validate the presence of an isosbestic point, a Benesi-Hildebrand (B-H) plot was constructed by plotting 1/(A-A_0) vs 1/[Cr^{6+}] by using a well-known B-H Eq. 5.4 [50].

$$\frac{1}{(A-A_0)} = \frac{1}{(A_{max}-A_0)}\left[\frac{1}{K\,[Cr^{6+}]} + 1\right] \quad (5.4)$$

The linearity of the plot, as represented by Fig. 5.7(b), between $\frac{1}{\Delta A}$ vs $\frac{1}{Cr^{6+}}$, confirm the formation of 1:1 complex between WS_2 QDs and Cr^{6+} with calculated binding constant (intercept/slope) as 3.31×10^6 M^{-1}. This suggests that the absorption intensity of WS_2 QDs can be effectively utilised as a probe for Cr^{6+} detection in aqueous environments.

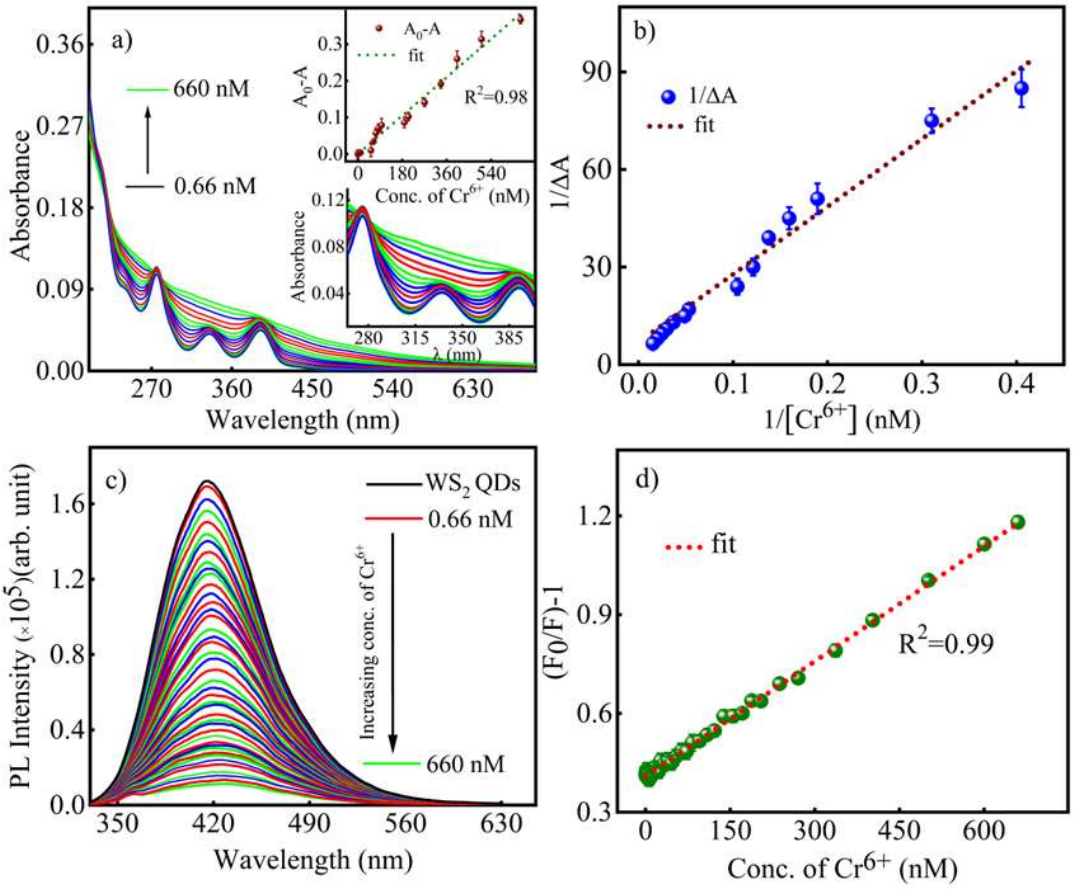

Fig. 5.7 *UV–vis absorption spectra of WS_2 QDs recorded in the absence and presence of Cr^{6+} ions over a concentration range of 0.66 to 660 nM. The insets displays the corresponding (A_0- A) plot as a function of Cr^{6+} concentration at 336 nm and enlarged characteristic peak (a) and the corresponding B-H plot between 1/ΔA vs 1/[Cr^{6+}] (b) PL spectra at λ_{ex} = 320 nm and corresponding S-V plot of WS_2 QDs recorded upon incremental addition of Cr^{6+} ions over the entire concentration range of 0.66 to 660 nM (c,d). The concentration gradient was obtained by serial dilution of 10^{-6}, 10^{-5}, and 10^{-4} M Cr^{6+} stock solutions, added in different volumes (μL) to a fixed WS_2 QDs dispersion.*

To further elucidate the underlying quenching mechanism, PL titration studies were conducted to investigate the nature of electronic transitions and their role in Cr^{6+} sensing. Fig. 5.7(c) illustrates the PL spectra of WS_2 QDs monitored in the absence and presence of Cr^{6+} at the same concentration range used in absorption spectra (0.66 to 660 nM). A significant decrease in PL intensity was observed even at the lowest Cr^{6+} concentration (0.66 nM), and the quenching effect progressively intensified with increasing Cr^{6+} levels. After adding 660 nM Cr^{6+}, the PL intensity diminished by

~94%. However, the shape and position of the PL band, centred at 420 nm under 320 nm excitation, remained unaltered, suggesting a dominant quenching mechanism without additional transitions. As PL quenching can typically arise from either static quenching involving ground-state complex formation or dynamic quenching due to diffusion and collision of photoexcited species [1,51]. To investigate the PL quenching mechanism of WS_2 QDs upon exposure to Cr^{6+} ions, a Stern–Volmer (S-V) plot was constructed by plotting the ratio of PL intensities (F_0/F) against the molar concentration of Cr^{6+} ions. The data were fitted to the classical S-V Eq. 5.5:

$$F_0/F = 1+K_{SV}[Cr^{6+}] \quad (5.5)$$

where F_0 and F represent the PL intensities of WS_2 QDs in the absence and presence of Cr^{6+}, respectively, and K_{SV} denotes the Stern–Volmer quenching constant. The resulting plot, as shown in Fig. 5.7(d), exhibited excellent linearity with a correlation coefficient (R^2) of 0.99, confirming a well-defined quenching interaction. The linear regression yielded a quenching constant (K_{SV}) of 1.16×10^6 M^{-1}. Using this slope, the LoD and limit of quantification (LoQ) were calculated based on the formulas LoD = 3σ/K and LoQ = 10σ/K, where σ represents the standard deviation of the PL intensity of pristine WS_2 QDs computed by repeated ten PL spectra. The corresponding values were found to be 39.5 and 129 pM, respectively, demonstrating the high sensitivity of the probe toward Cr^{6+} ions. This value aligns well with the World Health Organization (WHO) guideline for Cr^{6+} in drinking water, which is <50 mg/L (<0.96 mM) [52]. The calculated LoD was found to be the lowest, to the best of our knowledge, for reported Cr^{6+} detection using various sensors. Notably, the detection range achieved in this work spans from 0.66 to 660 nM, making it highly suitable for practical sensing applications. To date, such picomolar-level sensitivity has not been previously reported for this concentration range. A comparative overview of relevant studies is presented in Table 5.2 to support this finding.

Table 5.2 *Summary of reported Cr^{6+} detection probes and their analytical performance parameters.*

Sensing Probe	**Linear range (nM)**	**LoD (nM)**	**Refs.**
WS_2 QDs	0.66 -660	39.5 pM	This work

Ag-NPs	0.3-166.6	95 pM	[11]
N, S-doped CDs	10 -66×10^2	0.33	[53]
N, Zn-doped CDs	5-135	0.47	[54]
N-doped CDs	1×10^1 -25×10^4	05	[55]
Au NCs-CDs	5×10^4 - 1×10^4	5.34	[56]
CDs	1×10^3 - 1×10^5	250	[57]
N-GQDs	0 - 14×10^4	40	[58]
Si QDs	1.25 - 4×10^4	650	[59]
C QDs	25×10^1 - 25×10^3	140	[60]
S QDs	1×10^4 to 12×10^4	360	[61]
B, N@CDs	3×10^2 to 5×10^5	240	[62]
N@CQDs	0 - 15×10^3	300	[63]
Se QDs	5×10^3-105×10^3	145	[64]
Si-N CQDs	0-2×10^5	995	[65]
Fe_3O_4 QDs	1-190	181	[66]
N-GQDs	0-2×10^5	800	[67]
N,B CQDs	0-1×10^5	49	[68]

5.4.2 Effect of Cr6+ on PL Lifetime of WS2 QDs

The PL decay measurements provide insights into the excitonic dynamics and PL quenching mechanisms of WS_2 QDs in the presence of Cr^{6+}. TRPL decays, modeled using a tri-exponential fitting approach (Fig. 5.8a), reveal three distinct lifetime components, as previously discussed. With increasing Cr^{6+} concentration (up to 660 nM), alterations in decay behavior are observed. Specifically, the fastest lifetime component (τ_1) decreases notably from 0.34 ns to 0.18 ns, while the intermediate lifetime (τ_2) declines from 4.15 to 3.30 ns. Conversely, the slowest lifetime (τ_3) exhibits a slight increase from 8.87 to 9.44 ns, suggesting enhanced surface defect related trapping with higher Cr^{6+} levels [69,70]. Also, the contribution of short-lived states (τ_1 and τ_2) increases, while the long-lived state (τ_3) becomes less dominant. This means non-radiative (non-light-emitting) processes become more common, while radiative (light-emitting) processes are reduced when Cr^{6+} is added (see Fig. 5.8, Table 5.3). The

average lifetime decreases only slightly from 6.88 to 6.40 ns, which points mainly to static quenching. In this case Cr^{6+} bind to the QDs surface and form non-emissive complexes [70]. However, the small drop in average lifetime (τ_{av}) also suggest some dynamic quenching, where Cr^{6+} briefly interacts with QDs in solution, possibly limited by surface coatings or functional groups [71,72]. Further, the S–V plots based on individual and average lifetimes remain linear (see Fig. 5.8b), which supports a **mixed quenching mechanism,** both static and dynamic [75,76]. This behavior is consistent with other studies on similar TMD quantum dots, where both stable complexes and temporary interactions play a role in reducing PL.

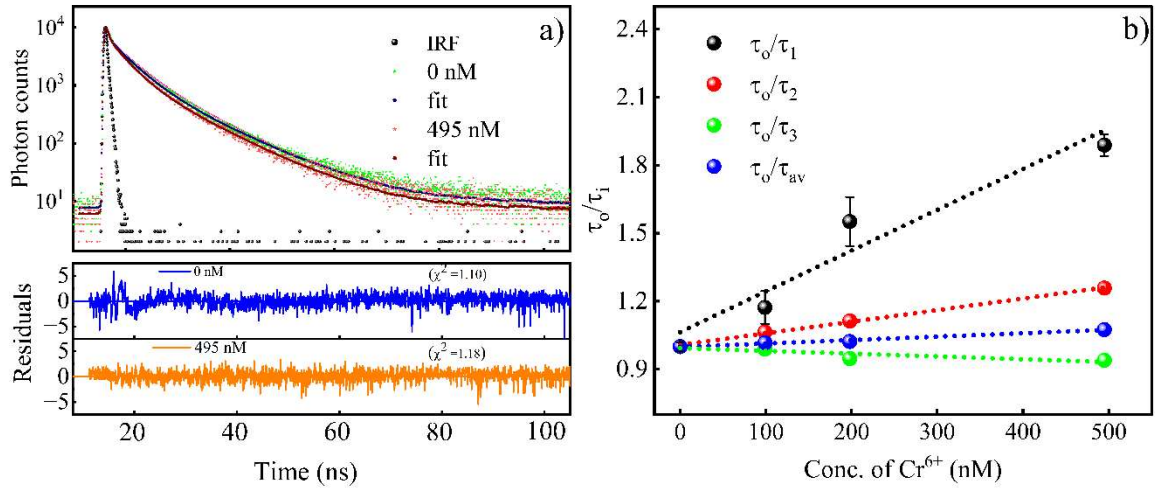

Fig. 5.8 *Fitted TRPL decay profiles of WS_2 QDs at 320 nm excitation and monitored at 410 nm emission, recorded in the absence and presence of Cr^{6+} (660 nM) concentration (a), S-V plots based on individual PL lifetimes of varying concentrations of Cr^{6+} ions (b).*

Table 5. 3 *PL lifetimes and pre-exponential parameters of WS_2 QDs dispersed in water excited with 320 nm and monitored at 410 nm for different concentrations of Cr^{6+}.*

Conc. (nM)	**τ_1 (ns)**	**τ_2 (ns)**	**τ_3 (ns)**	**α_1**	**α_2**	**α_3**	**τ_{av} (ns)**	**χ^2**
0	0.34 ± 0.02	4.15 ± 0.03	8.87 ± 0.01	0.61	0.19	0.20	6.88	1.10
99	0.29 ± 0.04	3.90 ± 0.04	8.92 ± 0.07	0.62	0.21	0.17	6.77	1.19

198	0.21 ± 0.03	3.73 ± 0.06	9.37 ± 0.01	0.63	0.23	0.14	6.73	1.15
495	0.18 ± 0.05	3.30 ± 0.05	9.44 ± 0.03	0.67	0.22	0.11	6.40	1.18

Further, to evaluate the selectivity of the WS_2 QD-based probe, PL quenching experiments were conducted in the presence of various potentially interfering analytes. As illustrated in Fig. 5.9(a), none of the tested analytes exhibited significant fluorescence quenching, Fe^{3+} and Pb^{2+} showing a minor reduction in emission intensity (<20%). Furthermore, to assess the interference effect in a competitive environment, a fixed and maximum concentration (660 nM) of each analyte was introduced along with Cr^{6+} ions. The PL intensity remained nearly the same as that observed for Cr^{6+} alone, as depicted in the bar graphs in Fig. 5.9(b). Furthermore, to visually confirm the interaction, images of WS_2 QDs solutions were captured at a fixed concentration of 660 nM of all analytes, including Cr^{6+}, under normal LED light and UV illumination at 365 nm, which is represented in Fig. 5.9(c). These observations indicate that the presence of coexisting analytes in aqueous media does not significantly affect the detection efficiency for Cr^{6+}, confirming the high selectivity and minimal interference of the WS_2 QDs-based probe.

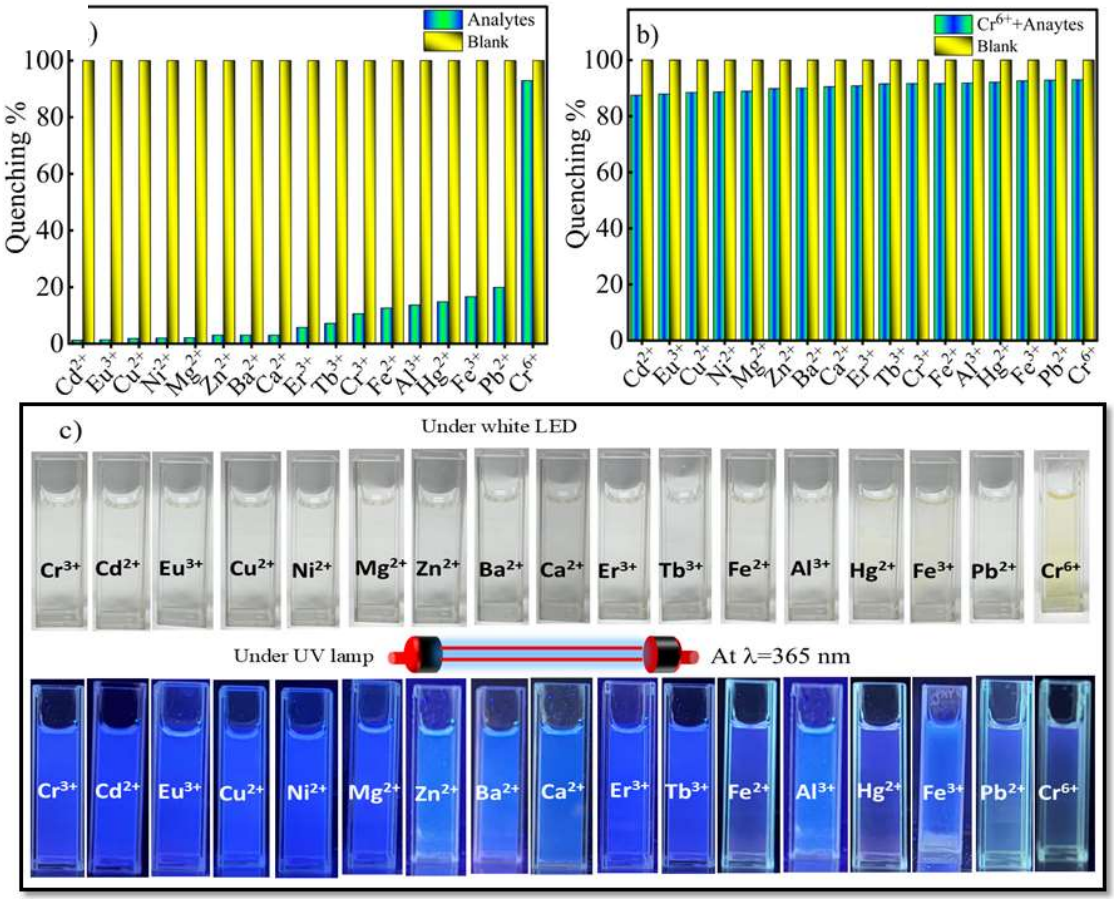

Fig. 5.9 *Bar diagrams showing the quenching (%) response of WS_2 QDs in the presence of different analytes at fixed concentrations of 660 nM (a). Quenching (%) of colloidal WS_2 QDs exposed at 660 nM concentration of Cr^{6+} along with other interfering analytes at the same concentrations (b), showing negligible interference effects. The yellow bars in both (a) and (b) represent control samples without any analytes, and the blue-green bars represent the presence of analytes. Corresponding visual images of the QDs under white LED and 365 nm UV illumination, depicting PL changes with different analytes at 660 nM concentration (c).*

5.4.3 XPS analysis after Cr6+ addition

The surface compositions, oxidation states, and bonding properties of the as-synthesised WS_2 QDs were examined using XPS. The survey spectrum confirms the presence of W, S, C, N, O, and Cr, revealing the composition of the QDs and potential Cr interactions. High-resolution core-level spectra of W 4f, S 2p, C 1s, N 1s, O 1s, and Cr 2p provide insights into their oxidation states and chemical environments. The XPS spectrum in the binding energy (BE) range of 29 - 43 eV, W 4f after Cr addition, exhibits three distinct deconvoluted peaks at 35.04 eV, 37.18 eV, and 40.65 eV as

shown in Fig. 5.10(a). These peaks can be attributed to the W $4f_{7/2}$ and W $4f_{5/2}$ components of W^{4+} along with an additional peak corresponding to W^{6+} ($4f_{5/2}$) [73,74]. Compared to previously reported values for pristine WS_2 QDs, where W^{4+} appears at approximately 32.8 eV and 34.9 eV, and W^{6+} at 39.3 eV [30], the observed shift toward higher BE indicates a slight modification in the tungsten oxidation environment, implying an interaction with Cr^{6+} ions that can induce surface oxidation or local electronic structure changes [71]. Further, standard WS_2 QDs, the doublet peaks of S 2p appear at 162.5 eV and 163.7 eV, corresponding to the S $2p_{3/2}$ and S $2p_{1/2}$ states of S^{2-}, along with an additional peak at 167.9 eV attributed to residual sodium sulfate [30,52,75]. After Cr addition, the S 2p peaks shift slightly to higher values at 163.05 eV and 164.25 eV (Fig. 5.10b), indicating partial oxidation or altered S–W bonding due to Cr^{6+} adsorption. The oxidation and binding energy shifts further corroborate the formation of new chemical interactions at the WS_2 QD surface upon Cr^{6+} binding, supporting quenching mechanisms via charge transfer or surface trapping sites. The high-resolution C 1s XPS spectrum in the 280–290 eV BE range was deconvoluted into three distinct peaks centered at 284.3, 285.6, and 288.9 eV (Fig. 5.10c). These peaks are respectively attributed to the C–C/C=C (sp^2 hybridized carbon), C–N (carbon bonded to nitrogen), and O–C=O (carboxyl or ester groups), indicating the presence of graphitic carbon, nitrogen functionalities, and oxygenated species on the surface [76,77]. The high-resolution N 1s XPS spectrum in the BE range of 397–405 eV was deconvoluted into two prominent peaks located at 399.34 and 401.1 eV (Fig. 5.10d). These peaks can be ascribed to nitrogen functionalities corresponding to C–N and O=C–N bonding environments, respectively, suggesting the incorporation of nitrogen-containing groups such as amides or imides on the surface of the as-synthesized WS_2 QDs [78,79]. These surface functionalities can modulate colloidal stability and participate in Cr^{6+} adsorption, as indicated in the literature [80–82]. Additionally, the O 1s core-level spectrum in the range of 527–536 eV was deconvoluted into two peaks centered at 530.2 and 531.37 eV (Fig. 5.10e). The peak at 530.2 eV is assigned to lattice oxygen (O^{2-}) involved in W=O bonds, while the peak at 531.37 eV corresponds to surface hydroxyl groups (O–H) [30,82,83]. The presence of W=O and O–H groups further confirms partial surface oxidation at the edges of WS_2 QDs, contributing to their enhanced colloidal stability in aqueous media. Fig.

5.10(f) represents the XPS spectrum of chromium in the BE range of 571–597 eV. The detection of Cr in its hexavalent form (Cr $2p_{3/2}$ at 578.48 eV and Cr $2p_{1/2}$ at 588.50 eV) strongly supports the selective interaction of Cr^{6+} species on the QD surface [16,71].

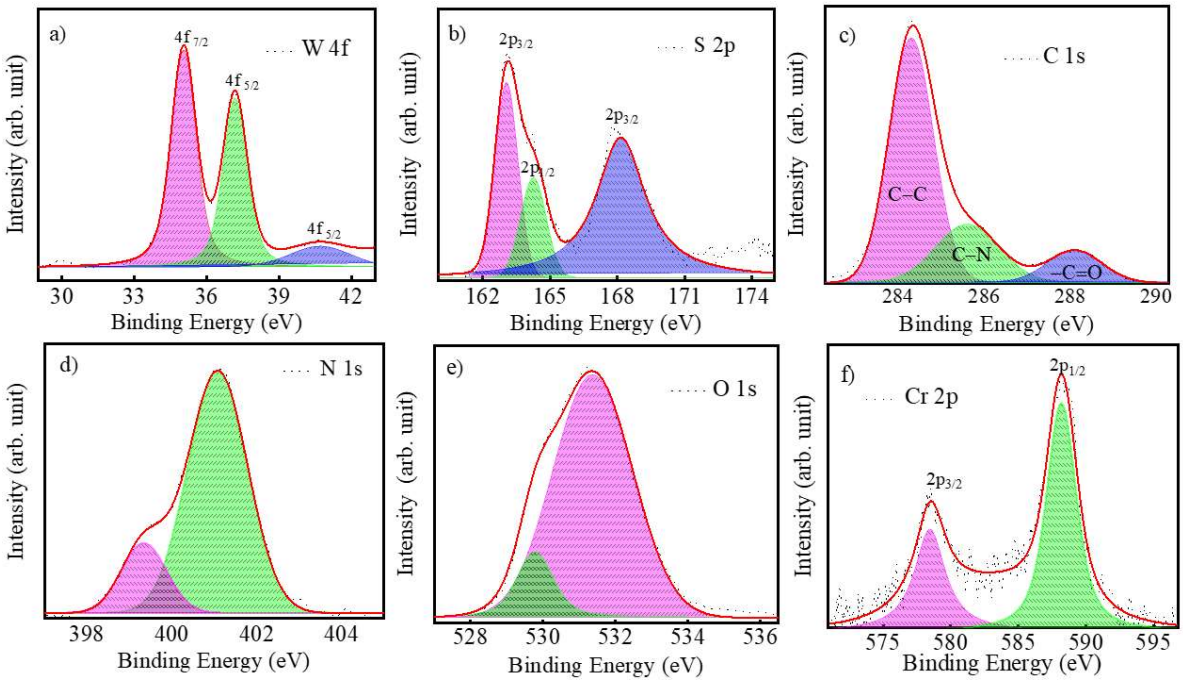

Fig. 5.10 *High-resolution XPS spectra of WS_2 QDs/Cr^{6+} system: W 4f, (a) S 2p, (b) C 1s, (c) N 1s, (d) O 1s, (e) and Cr 2p (f).*

5.4.4 Performance Analysis of EDTA as a General Chelator in Cr6+ Detection

To investigate the potential masking effect of EDTA (ethylenediaminetetraacetic acid) on Cr^{6+} ion detection using WS_2 QDs as a PL probe, systematic experiments were conducted with varying EDTA concentrations (99, 198, 297, 396, 495, 594, and 660 nM). Initially, a fixed amount of Cr^{6+} solution (660 nM) was introduced in a cuvette containing WS_2 QDs solution to establish a consistent quenching interaction. Subsequently, different concentrations of EDTA were added individually to the Cr^{6+}/WS_2 QDs system. After the addition of EDTA to the WS_2 QDs/Cr^{6+} system, the mixture was allowed to stabilise for 5 seconds, and the PL spectra were immediately recorded. PL measurements were performed with an excitation wavelength of 320 nm, and the obtained spectra for different concentrations of EDTA are given in Fig. 5.11(a). The analysis revealed that the incremental addition of EDTA did not significantly

influence the PL quenching of WS_2 QDs by Cr^{6+} ions. These results demonstrate that the WS_2 QDs-based sensing platform retains its selectivity and sensitivity toward Cr^{6+} detection even in the presence of EDTA, highlighting its robustness against common chelating agents.

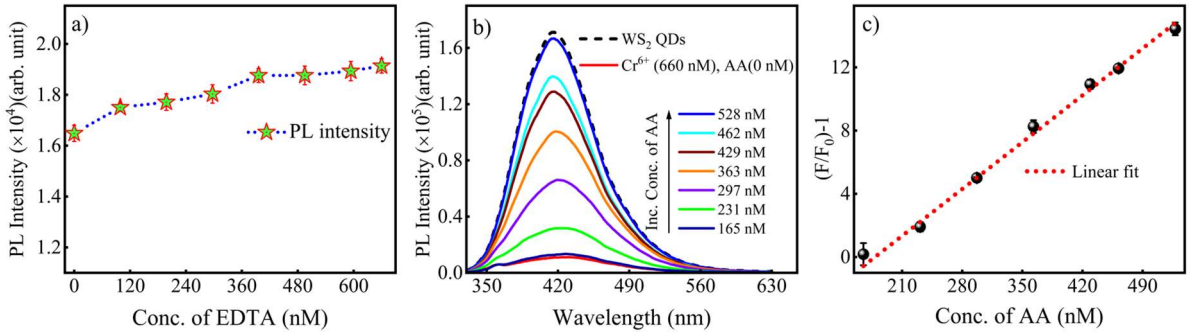

Fig. 5.11 *Effect of different EDTA concentrations (99, 198, 297, 396, 495, 594, and 660 nM) for Cr^{6+} detection (a), Effect of different ascorbic acid concentrations (165, 231, 297, 393, 429, 462, and 528 nM) for Cr^{6+} detection (b), S-V plot of WS_2 QDs constructed by plotting $\left(\frac{F}{F_0}\right) - 1$ vs conc. of AA recorded upon incremental addition of AA concentrations (165, 231, 297, 393, 429, 462, and 528 nM)(c).*

5.4.5 Restoring the PL of sensing probe WS2 QDs using AA (ascorbic acid)

To demonstrate the reversible nature of our WS_2 QDs/Cr^{6+} sensing probe, an essential feature for practical and reusable sensors, we investigated its ability to recover PL upon the addition of a reducing agent. After PL quenching by 660 nM Cr^{6+}, we introduced different concentrations of AA as represented in Fig. 5.11(b) and found that at 528 nM of AA, the original PL intensity was successfully restored. Also, the S-V plot for AA is given in Fig. 5.11(c) and the calculated LoD is 94.9 pM. This effective recovery highlights the redox conversion of Cr^{6+} to Cr^{3+}, confirmed by the XPS spectrum of chromium (Fig. 5.12a), where newly appearing Cr^{3+} peaks were observed alongside the reduction of Cr^{6+} signals. The molar ratio of Cr^{6+}: AA = 1.25:1 indicates that a sub-stoichiometric amount of AA is sufficient for complete PL restoration, enhancing the probe's sensitivity. Additionally, the probe maintained a consistent PL response across 18 consecutive quenching and recovery cycles, demonstrating excellent cyclic stability and reversibility. These results confirm that developed WS_2 QD-based probe functions effectively through a reliable and efficient molar ratio-driven mechanism. This complete and reversible redox transformation is confirmed over 18 cycles of

quenching and recovery, demonstrating the robustness and recyclability of the system illustrated in Fig. 5.12(b).

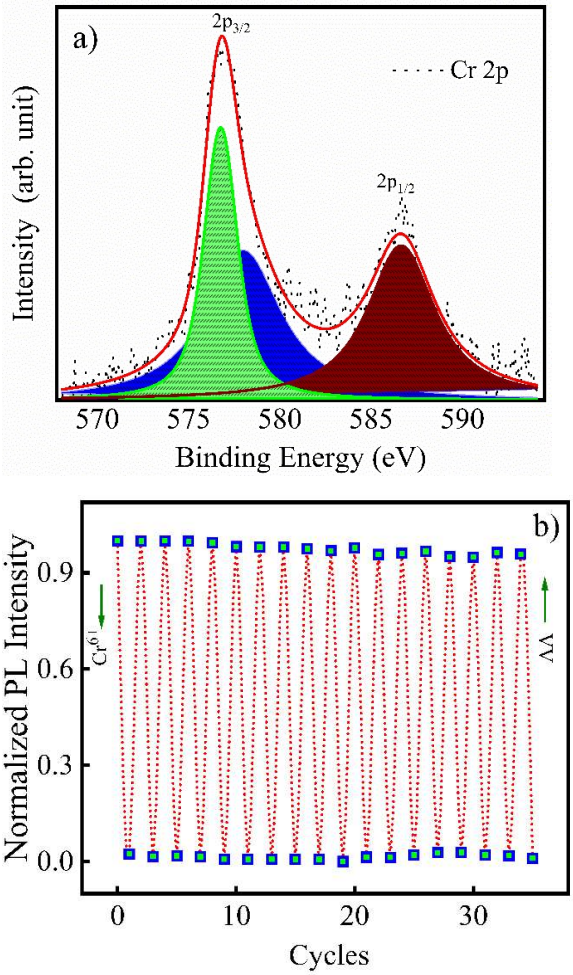

Fig. 5.12 *High-resolution XPS spectra of Cr 2p in WS_2 Qds/Cr^{6+}/AA system (a) and cyclic PL response of the developed WS_2 QDs-based probe upon successive alternate additions of Cr^{6+} (660 nM) and AA (528 nM) over 18 cycles. The plot demonstrates excellent reversibility and stability of the PL signal.*

For the visible test strip experiments, Whatman Grade 1 filter paper was employed as a solid support for immobilising WS_2 QDs. The paper substrate was first modified with WS_2 QDs, yielding a uniform blue PL under 365 nm UV light. Six representative images, presented in Fig. 5.13, illustrate the sequential sensing process: unmodified paper under UV irradiation, WS_2 QD-modified paper exhibiting bright PL, exposure

to Cr^{6+} at 99 nM resulting in slight quenching, exposure to Cr^{6+} at 660 nM showing near-complete PL inhibition, partial PL restoration upon addition of AA at 99 nM, and full PL recovery at 528 nM AA. The distinct PL changes confirm the practical applicability of WS_2 QD-based paper strips for rapid, portable, and visual detection of non-colored analytes.

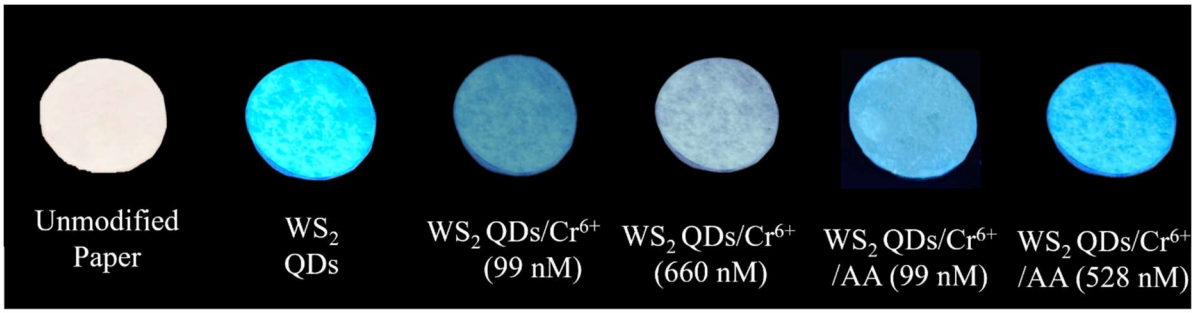

Fig. 5.13 *WS_2 QD-based paper strip assay showing PL quenching by Cr^{6+} and recovery with AA under 365 nm UV light.*

5.4.6 Promising Mechanism of PL Quenching and Recovery of WS2 QDs upon Cr6+ Interaction

Upon introducing Cr^{6+} ions into the WS_2 QDs system, a significant quenching of PL intensity is observed. Mechanistically, this quenching arises from a combination of processes. This quenching is primarily governed by static interactions, particularly the formation of ground-state complexes between Cr^{6+} ions and the surface of WS_2 QDs. The formation of a non-emissive ground-state complex is supported by the notable spectral changes in the UV-Vis absorption spectra, including the appearance of an isobestic point at approximately 220 nm (Fig. 5.7a). However, time-resolved PL lifetime measurements reveal a minimal change in the excited-state lifetime from 6.88 to 6.40 ns of the QDs in the presence of maximum concentration (660 nM) of Cr^{6+}. The obtained lifetime suggests a predominantly static quenching, likely through complex formation and PCT from the excited WS_2 QDs to Cr^{6+} ions adsorbed on their surface with a small contribution of dynamic behaviour. XPS provides compelling evidence supporting this redox-based interaction. After Cr^{6+} treatment, the W 4f peaks of WS_2 shift notably from 34.9 eV to 35.04 eV (W^{4+}) and further to 37.18 eV, indicating that W^{4+} undergoes partial oxidation. An additional high-energy component at 40.65 eV corresponds to W^{6+}, confirming surface oxidation of tungsten. Deconvolution of

peak areas shows that W^{6+} increases from 0% to ~10.22%, while W^{4+} decreases proportionally, reflecting a partial redox process between Cr^{6+} and WS_2. Simultaneously, the S 2p doublets, initially at 162.5 eV and 163.7 eV for pristine S^{2-}, shift to 163.05 eV and 164.25 eV after Cr^{6+} exposure, suggesting a modification in the local electronic environment around sulfur. A higher BE peak at 168.14 eV is attributed to oxidised sulfur species, potentially from residual sulfate or S–O bond formation due to surface oxidation. Area analysis indicates that ~60% of sulfur remains as S^{2-}, while ~40% converts to oxidised forms. The chromium XPS spectrum monitored in the range 571-597 eV after the addition of Cr^{6+} shows two distinct peaks at 578.48 eV (Cr^{6+} $2p_{3/2}$) and 588.5 eV (Cr^{6+} $2p_{1/2}$), confirming the presence of high-valent Cr^{6+} species with no signature of other oxidation states of chromium. These species act as strong electron acceptors, efficiently withdrawing photogenerated electrons from WS_2, thereby quenching the PL without affecting the lifetime. Upon subsequent introduction of 528 nM of AA, a known reductant, the PL intensity of WS_2 QDs is fully restored. XPS analysis after AA treatment shows complete disappearance of Cr^{6+} peaks and emergence of new Cr^{3+} peaks at 576.72 eV, 577.09 eV ($2p_{3/2}$), and 586.65 eV ($2p_{1/2}$), signifying full reduction of Cr^{6+} to Cr^{3+}. The proposed redox reaction is given in Eq. 5.6 [84], where the total number of electrons involved in the reduction of Cr^{6+} is three:

$$HCrO_4^- + 7H^+ + 3e^- \rightarrow Cr^{3+} + 4H_2O \quad (5.6)$$

Cr^{3+}, being less electron-deficient, does not facilitate effective electron extraction, hence allowing radiative recombination and PL restoration. Additionally, to compare the different chemical states of W, S, N, O, C and Cr, the total atomic concentrations were corrected based on the peak area ratios derived from the deconvolution of their respective high-resolution XPS spectra (refer to Table 5.4) [76].

Table 5.4 *Peak area, FWHM, and total organic contribution from different elements present in XPS analysis of WS_2 QDs/Cr^{6+} system.*

Sample	Peak 1 (eV)	Area (%)	FWHM (eV)	Peak 2 (eV)	Area (%)	FWHM (eV)	Peak 3 (eV)	Area (%)	FWHM (eV)	Organics (%)

W 4f	34.9	50.96	1.02	37.18	37.56	1.21	40.65	11.47	1.30	21.7
S 2p	163.7	24.59	0.75	164.25	14.86	0.80	168.14	60.55	1.10	48.4
N 1s	401.05	82.0	0.80	399.35	18.0	0.90	—	—	—	10–15
O 1s	531.37	86.8	1.05	529.78	13.2	0.89	—	—	—	10–15
C 1s	284.30	61.5	1.10	285.61	19.2	1.20	288.1	9.9	1.13	5-10
Cr^{3+}	576.76	42.35	0.95	577.09	32.12	1.05	586.65	25.53	1.30	6-10
Cr^{6+}	578.48	41.75	0.90	583.5	25.97	1.10	588.5	32.28	1.20	8-11

To further clarify the mechanism, absorption spectra of all metals were monitored at fixed concentrations of 660 nM, as shown in Fig. 5.14. Notably, the UV–vis absorption of Cr^{6+} falls within the optical response range of WS_2 QDs, enhancing its selective recognition.

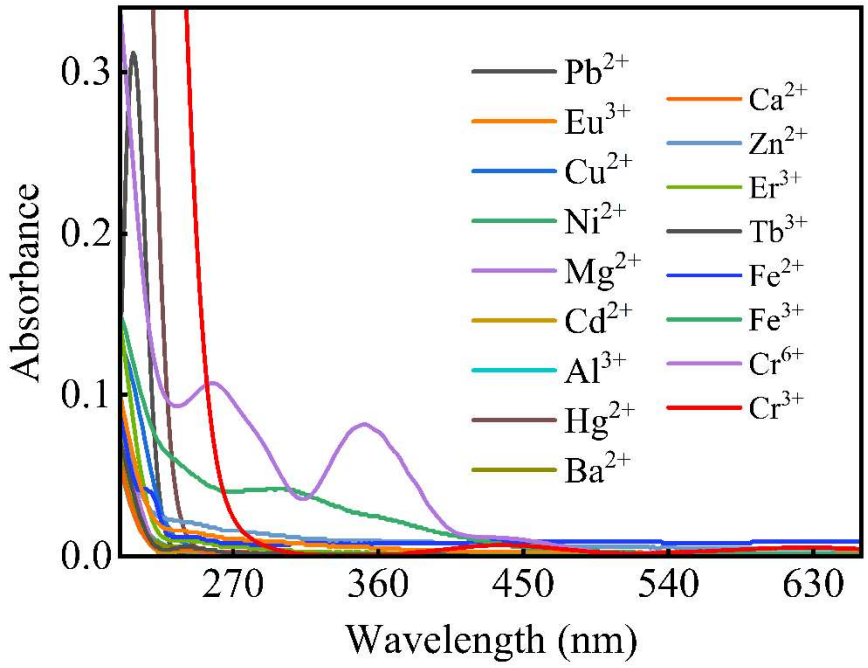

Fig. 5.14 *UV-vis spectra of different analytes at fixed concentration of 660 nM.*

5.4.7 Application of WS2 QDs nanoprobe to quantify $Cr6^{+}$ in real samples

The practical applicability of the WS_2 QDs-based sensor was evaluated through the detection of Cr^{6+} in real water samples. These included municipal tap water and river water collected from the Triveni Sangam region in Prayagraj, India—a sacred confluence of the Ganga, Yamuna, and the mythical Saraswati rivers—during March 2025. The collected samples were first filtered through a 0.22 µm membrane to remove suspended particles and then used it for further experiments. Upon addition of Cr^{6+} ions with a similar concentration range (0.66 to 660 nM), the PL intensity exhibited significant quenching of approximately 93% in tap water and 91% in Triveni Sargam water, while maintaining the original PL spectral shape with no noticeable shifts, confirming the preservation of WS_2 QDs' optical properties (see Fig. 5.15a and 5.15b). Inset of Figs. 5.15(a) and 5.15(b) demonstrate excellent linearity in both cases. The calculated LoDs were 88 and 154 pM for tap water and Triveni Sangam water, underscoring the sensor's high sensitivity in complex real-world matrices. A comparative overview of LoD values in different water systems is presented in Table 5.5, highlighting the superior performance of the developed WS_2 QD-based sensor for reliable environmental chromium monitoring.

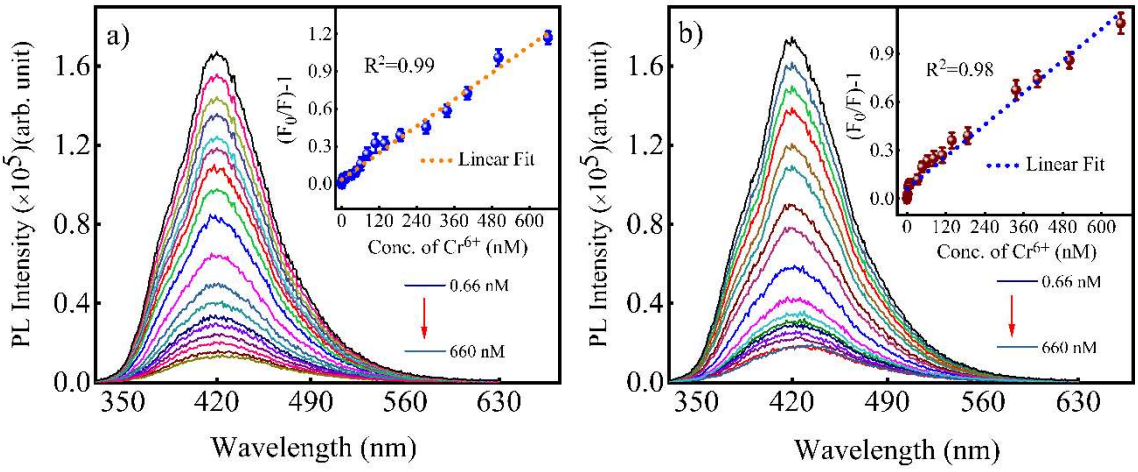

Fig. 5.15 *PL spectra of WS_2 QDs in tap water (a) and Triveni Sangam water (b) recorded upon incremental addition of Cr^{6+} ions over a concentration range of 0.66 to 660 nM. The insets present the corresponding S-V plots.*

Table 5.5 *Calculated values of LoD with quenching percentage for WS_2 QDs in different water samples.*

Water Sample	Quenching (%)	LoD (pM)	LoQ (pM)
Ultrapure water	94	39.5	129
Tap water	93	88	292
Triveni Sangam	91	154	512

Additionally, recovery studies were performed with known amounts of Cr^{6+} ions that were spiked into these matrices at concentrations ranging from 0.66 nM to 660 nM (9.9, 33, 99, 330, and 594 nM), as presented in Table 5.6. The prepared spiked solutions were mixed thoroughly to ensure homogeneous dispersion of the analyte before proceeding with PL quenching measurements under the optimised experimental conditions. These results confirm that the as-synthesised WS_2 QDs-based fluoroprobe is highly sensitive and meets the technical criteria required for trace-level monitoring of Cr^{6+} in drinking water. Compared to previously reported probes, the present system offers a significantly lower LoD and a comparable or wider linear range, highlighting its potential as a low-cost and effective tool for routine environmental monitoring of Cr^{6+} in real samples.

Table 5.6 *Cr^{6+} detection in real water samples at different spiked concentrations (9.9, 33, 99, 330 and 594 nM)*

Sample Type	Spiked Cr^{6+} Conc. (nM)	Detected Cr^{6+} Conc. (nM)	Recovery (%)	SD	RSD (%)
Tap Water	9.9	9.81	99.13	0.02	0.22
	33	33.58	101.75	0.61	1.89
	99	98.42	99.42	0.55	0.56
	330	328.23	98.43	1.19	0.36
	495	491.34	99.46	0.58	0.10
	9.9	9.78	98.86	0.27	2.81
	33	31.80	96.35	1.25	3.98

Triveni Sangam	99	99.16	100.16	1.52	1.59
	330	333.39	101.02	1.15	0.36
	495	495.70	100.34	0.57	0.10

5.5. Conclusion

This study demonstrates the successful development of a highly sensitive and reusable WS_2 QDs PL-based sensor for detecting toxic Cr^{6+} ions in various water samples. The PL-based sensor operates via a predominantly static quenching mechanism driven by complexation and PCT, with a minor contribution from dynamic behaviour. Its ability to fully recover PL upon AA treatment enables multiple cycles of detection and regeneration, highlighting excellent durability and cost-effectiveness. The wide linear detection range and ultralow LoD achieved in UP (0.0116 ppb), tap and real Triveni Sangam water validate its practical applicability for environmental monitoring. Overall, this work presents a promising approach for on-site, real-time chromium sensing, contributing to safer water quality management and pollution control.

Chapter 6: Toward Real-World Vitamin B12 Diagnostics: WS_2 QDs as a Next-Generation PL Sensing Platform

6.1 Introduction

Vitamin B12 (cobalamin, Cbl) is a crucial water-soluble vitamin that plays a vital role in DNA synthesis, red blood cell (RBC) formation, and neurological function [1]. Its complex molecular structure, characterized by a corrin ring with a central cobalt ion, is shown in Scheme 1, which influences its unique chemical properties and biological activity [2].

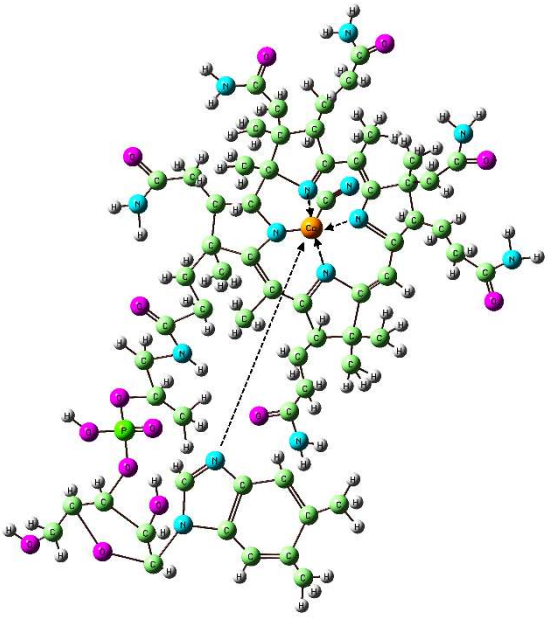

Scheme 6. 1 The molecular structure of vitamin B12 (Cbl) featuring a corrin ring with a centrally bound cobalt ion, surrounded by four nitrogen atoms from pyrrole groups.

Deficiency of Cbl is an important public health problem, which has been reported to cause around 3.6 to 15 % of the adult population worldwide [3,4], that is much more common in seniors and some vulnerable groups such as expectant mothers, people suffering from digestive diseases and those who follow a very strict plant-based diet [5,6]. The clinical manifestations of Cbl deficiency represent a wide spectrum, which may consist of symptoms that are not severe, for instance, weakness and paleness of the skin and to extensive and very alarming that affect the nervous system and can be permanent like peripheral neuropathy [7], ataxia [8], cognitive disturbances [7] subacute combined degeneration of the spinal cord [4,9]. Deficiency is frequently associated with megaloblastic anaemia, which is characterised by the presence of large and structurally nucleated RBCs. Histologically, changes may include leukopenia, thrombocytopenia, and pancytopenia [5,10]. In pregnant and breastfeeding women, insufficient Cbl can result in neural tube defects, developmental delays [11,12] and anaemia in offspring [1]. The causes of Cbl deficiency are multifactorial, encompassing inadequate dietary intake, malabsorption syndromes (such as pernicious anaemia or atrophic gastritis), gastrointestinal surgeries [13,14], chronic use of certain medications (e.g., proton pump inhibitors, metformin) and rare congenital disorders affecting absorption or transport [13–15]. One of the main reasons that a Cbl deficiency can be hard to detect is that the body stores a large amount of the vitamin in the liver. These hepatic reserves can mask the development of deficiency for a long time, thereby postponing the identification of the disorder and increasing the risk of permanent bodily injury [4,11,16]. Early and accurate detection of Cbl deficiency is therefore crucial for preventing long-term complications and improving patient outcomes. However, current diagnostic methods, including serum B12 measurement and functional biomarkers, can be confounded by subclinical deficiency, comorbidities and limitations in assay specificity and sensitivity [17,18]. This underscores the urgent need for the development of rapid, sensitive, and selective sensing platforms capable of detecting Cbl at low concentrations in complex biological matrices.

Recent advances in nanomaterial-based optical sensors have opened new avenues for highly sensitive and selective detection of biomolecules in complex environments. Among these, QDs and noble metal nanomaterials have emerged as leading

candidates due to their unique optical and electronic properties [19,20]. QDs have attracted significant attention in biosensing due to their unique optical properties, such as size-tunable photoluminescence (PL),

High quantum yield (QY) and remarkable photostability [21,22]. These features allow QDs to serve as highly sensitive fluorescent probes for detecting a wide range of biological molecules, including vitamins [6], proteins [23] and nucleic acids [24], often outperforming traditional organic dyes in terms of brightness and stability [26]. Their

surfaces can be easily modified to enhance selectivity for specific targets, making the m versatile tools in the development of next-generation biosensors. Despite the promise of QDs, most conventional sensor technologies for biomolecule detection still rely on electrochemical (EC) and electroluminescent (EL) methods. EC sensors, which measure electrical signals generated by redox reactions, are valued for their sensitivity and potential for miniaturisation [28]. However, their performance is often hindered by matrix interference from complex biological samples, surface fouling and the need for extensive sample preparation to reduce background noise and improve selectivity [30,31]. These factors can complicate the analysis and limit the reliability of results, especially in real-world applications. EL sensors, which detect light emitted from chemical reactions or electrical excitation, offer high sensitivity and low background noise. Nevertheless, they typically require sophisticated and expensive instrumentation, as well as precise control of experimental conditions to maintain signal stability. Additionally, the luminescent materials used in these sensors may degrade over time or be affected by components in biological samples, leading to issues with reproducibility and long-term reliability [32]. Both EC and EL approaches often struggle with multiplexed detection and are less suited for rapid, real-time analysis compared to optical methods based on QDs. Noble metal nanomaterials, such as gold and silver nanoparticles, also contribute to enhanced sensing through plasmonic effects and surface-enhanced Raman scattering, but QDs stand out for their versatility in emission wavelength and ease of surface modification [35,36]. Within the family of QDs, tungsten disulfide (WS_2) QDs have attracted significant attention for sensing applications. WS_2 QDs possess a highly tunable bandgap, strong light-matter interaction, and both direct and indirect band gap transitions, which enable

efficient absorption and emission across a broad spectral range [37]. Their layered structure, combined with the ability to introduce diverse functional groups, allows for the selective detection of specific targets by modulating their PL response. Studies have shown that surface-functionalized WS_2 QDs can achieve exceptional selectivity and sensitivity for various analytes, with detection limits (LoD) reaching the nanomolar range in real samples [22,38]. The spectroscopic PL sensing approach using WS_2 QDs offers several advantages over traditional methods. It provides rapid, non-invasive, and highly sensitive detection, often requiring minimal sample preparation and enabling compatibility with real-world samples [39,40]. The strong and stable PL emission of WS_2 QDs ensures a reliable signal output, while their chemical tunability supports the development of selective sensors for a wide range of biomolecules [38,41]. Despite these advances, a research gap remains in fully exploiting the potential of WS_2 QDs for the detection of clinically relevant targets, such as Cbl. Addressing this gap, the present work aims to develop and optimise a WS_2 QD-based spectroscopic sensor, leveraging their unique physical and chemical properties to achieve sensitive, rapid, and selective detection of Cbl in complex matrices.

6.2 Experimental Section

6.2.1 Materials used

All chemicals utilised in this work were of analytical grade and employed without any additional purification. Sodium tungstate dihydrate ($Na_2WO_4 \cdot 2H_2O$) was supplied by Thermo Fisher Scientific India Pvt. Ltd., and L-cysteine ($HSCH_2CHNH_2COOH$) was obtained from Sigma-Aldrich. The target analyte, Cbl ($C_{63}H_{88}CoN_{14}O_{14}P$), was procured from Central Drug House (CDH), India. Various potentially interfering and biologically relevant species, including urea, cholesterol (chol), 7-azaindole (7AI), 6-hydroxyquinoline (6HQ), glucose (Gluc), vitamin K (Vit K), bovine serum albumin (BSA), and dopamine (DA) were procured from CDH, India. All aqueous solutions were prepared using ultrapure deionised water (DI) with resistivity 18.2 MΩ·cm, provided by an Adrona ultra-water purification system.

6.2.2 Synthesis

WS_2 QDs were synthesised via a previously reported single-step and facile hydrothermal method with minor modifications [42]. Briefly, sodium tungstate and L-cysteine were simultaneously dissolved in an aqueous medium with a molar ratio of 0.5:1. The pH value of the solution was adjusted with a pH meter to be ~6 by using 0.1 N H_2SO_4 solution with continuous stirring at 500 rpm at ambient laboratory temperature (~32 ºC). After swirling for 20 minutes, the solution was further sonicated for 15 minutes, and the prepared solution was transferred to a Teflon-lined stainless-steel autoclave and heated at 202 °C for 36 hours in an oven. Upon natural cooling, a yellow colloidal solution was collected and centrifuged to obtain the WS_2 QDs. No additional capping or post-synthesis treatments were required. L-cysteine acts as a stabiliser due to its photo-resistant properties, simplifying the synthesis. The process is summarised in Scheme 2, with reaction details discussed in the following section.

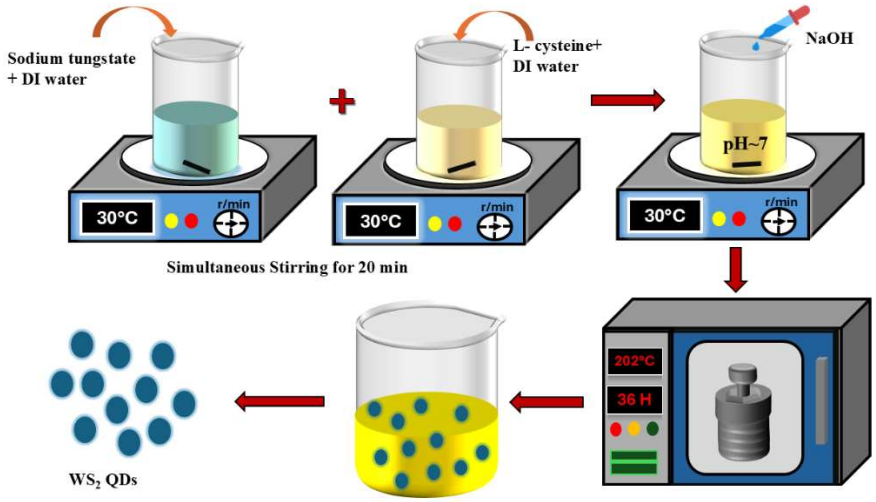

Scheme 6. 2 *Facile single-step hydrothermal preparation of water-soluble WS_2 QDs.*

6.2.3 Reaction dynamics in WS_2 QDs formation

L-cysteine undergoes hydrolytic degradation in DI water, yielding pyruvic acid– characterised by both carboxylic acid and ketone functional groups– along with the evolution of ammonia (NH_3) and hydrogen sulfide (H_2S) gas. The release of H_2S is evidenced by its typical foul odour, resembling that of rotten eggs [43].

$$HSCH_2CHNH_2COOH + H_2O \rightarrow CH_3COCOOH + NH_3 + H_2S \uparrow$$

Subsequently, tungstate ions react with the generated chalcogen hydride (H_2S) and pyruvic acid, resulting the in situ formation of colloidal WS_2 QDs

$$4\ WO_4^{2-} + 9\ H_2S + 6\ CH_3COCOOH \rightarrow 4WS_2 + SO_4^{2-} + 6CH_3COCOO^- + 12\ H_2O$$

This synthetic reaction outline highlights the dual role of L-cysteine as both a reductant and sulfur donor, facilitating the bottom-up nucleation of WS_2 nanocrystals under mild conditions. The gaseous byproducts and organic acids generated can also influence the colloidal stability, nucleation rate, and emission properties of QDs.

6.2.4 Analytical Techniques

38

The crystal structure of the synthesised WS_2 QDs was confirmed by X-ray diffraction (XRD) analysis using a Bruker D8 Advance diffractometer equipped with Cu Kα radiation (λ = 1.54 Å), operated at 40 kV and 20 mA. Functional groups present on the WS_2 QDs were identified through Fourier transform infrared (FT-IR) spectroscopy, with spectra recorded across a range of 400 to 4000 cm^{-1} using a Thermo Scientific Nicolet Summit X FTIR spectrometer. The morphology and particle size distribution were examined by high-resolution transmission electron microscopy (HR-TEM) utilising a TECNAI TEM (Fei Electron Optics) system, operated at an accelerating voltage of 200 kV. These characterization techniques collectively provide comprehensive insights into the structural, chemical, and morphological properties of the WS_2 QDs, facilitating a deeper understanding of their material quality and potential applications. Further, UV-visible absorption and PL spectroscopies are widely employed techniques for detecting and identifying chemically active species due to their high sensitivity, even with small sample volumes. Steady-state absorption spectra were recorded using a double-beam UV/VIS/NIR spectrophotometer (Lambda 750, Perkin Elmer, USA), while PL and PL-excitation spectra were measured using a customised JASCO spectrofluorometer (FP-8500). PL decay curves were measured using a time-correlated single-photon counting (TCSPC) setup (DeltaFlex-01-DD, Horiba Jobin Yvon IBH Ltd), equipped with a detector (PPD 850) and a Delta Diode of 320 nm with a repetition rate of 10 MHz. The instrument response function (IRF) was captured by the Ludox scatterer. A transparent quartz cuvette cell with dimensions of 1 cm × 1 cm was used for the measurements. Moreover, the experiments were carried out with WS_2 QDs upon adding various concentrations of vitamin B12 (Cbl),

ranging from 0.33 to 565 nM. For photostability experiments, a Cole-Parmer UV lamp with an excitation wavelength of 365 nm and an output power of 8 watts was used, and for pH experiments, Fisher brand accumet XL600 dual channel pH/mV/ion/conductivity/DO were used.

6.3 Results and discussion

6.3.1 XRD and FT-IR analysis

As represented by Fig. 6.1, the XRD pattern of the WS_2 QDs exhibited a broad peak at 2θ = 30°, corresponding to the (004) crystallographic plane, which aligns well with the patterns documented for WS_2 QDs in the literature [42]. When TMDs transition from bulk materials to QDs, distinct signatures in XRD patterns often become obscure or vanish altogether. Specifically, many studies have noted the absence of characteristic peaks or signals in the XRD patterns of WS_2 and MoS_2 QDs, attributed primarily to their ultrasmall particle size and quantum confinement effects [44] The average crystallite size was further calculated by using the Debye-Scherrer equation, using Eq. (7.1) [45]

$$D = \frac{K\lambda}{\beta cos\theta} \tag{6.1}$$

where K (= 0.94), λ, β, and θ represent the geometric factor, wavelength of X-ray associated with copper (CuK_α) source, full width at half maxima (FWHM) of the observed peak, and the angle of diffraction peak, respectively. The value of D, as calculated using Eq. 1, was found to be 3.14 nm.

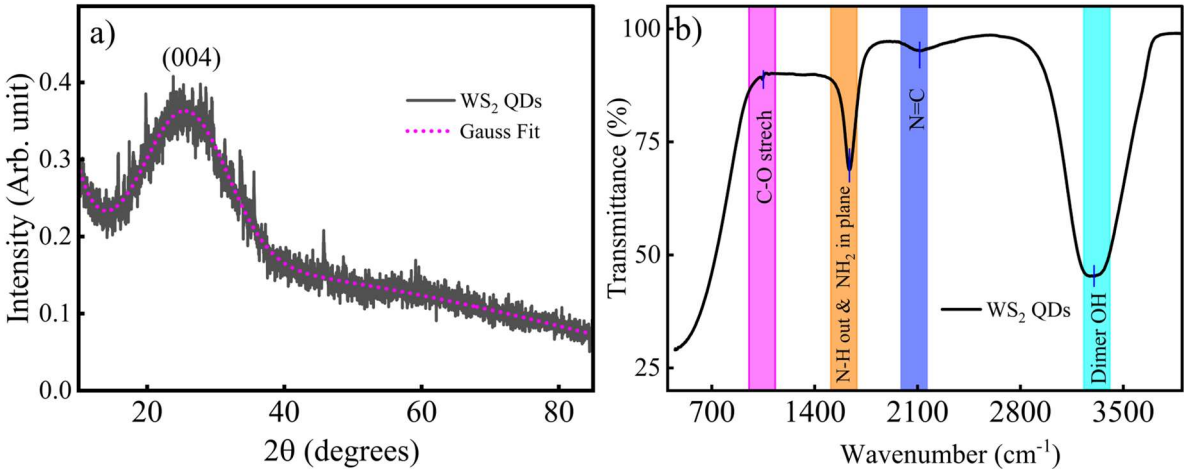

Fig 6. 1 *XRD pattern of WS_2 QDs thin film exhibiting characteristic diffraction peaks indicative of*

crystalline phase (a), FT-IR spectrum of colloidal WS_2 QDs dispersed in water showing vibrational modes corresponding to surface functional groups (b).

Fig. 6.1(b) represents the FT-IR spectrum of the obtained WS_2 QDs. The band at around 1042 cm^{-1} can be attributed to the C-O stretching vibration of hydroxyl groups [46]. The band observed at 1637 cm^{-1} represents the N-H out-of-plane bending and N-H_2 bending vibrations associated with the amide functional group. Additionally, the band observed at 2111 cm^{-1} is assigned to N=C stretching vibration [43,47]. The surface of the synthesised QDs is predominantly decorated with hydrophilic groups such as –OH dimer and –COOH, which confer excellent water dispersibility to the QDs, thereby significantly enhancing their applicability in aqueous sensing environments [48].

6.3.2 HR-TEM analysis

The HR-TEM images of the synthesised WS_2 QDs at various magnifications are represented in Fig. 6.2, revealing that QDs are predominantly spherical and homogeneously dispersed with minor particle aggregation (Fig. 6.2a-c). The particle size is observed to range from 2 to 5 nm. Clear and parallel lattice fringes visible in the inset of Fig. 6.2(a) demonstrate the crystalline nature of the QDs, with a lattice spacing of approximately 0.2 nm corresponding to the (100) plane of the WS_2 crystal. The particle size distribution, fitted with a Gaussian function, indicates an average diameter of about 3.3 nm (Fig. 6.2d), which closely relates to the average crystallite size obtained from the XRD pattern. Such a narrow size distribution is advantageous for consistency and performance in further applications.

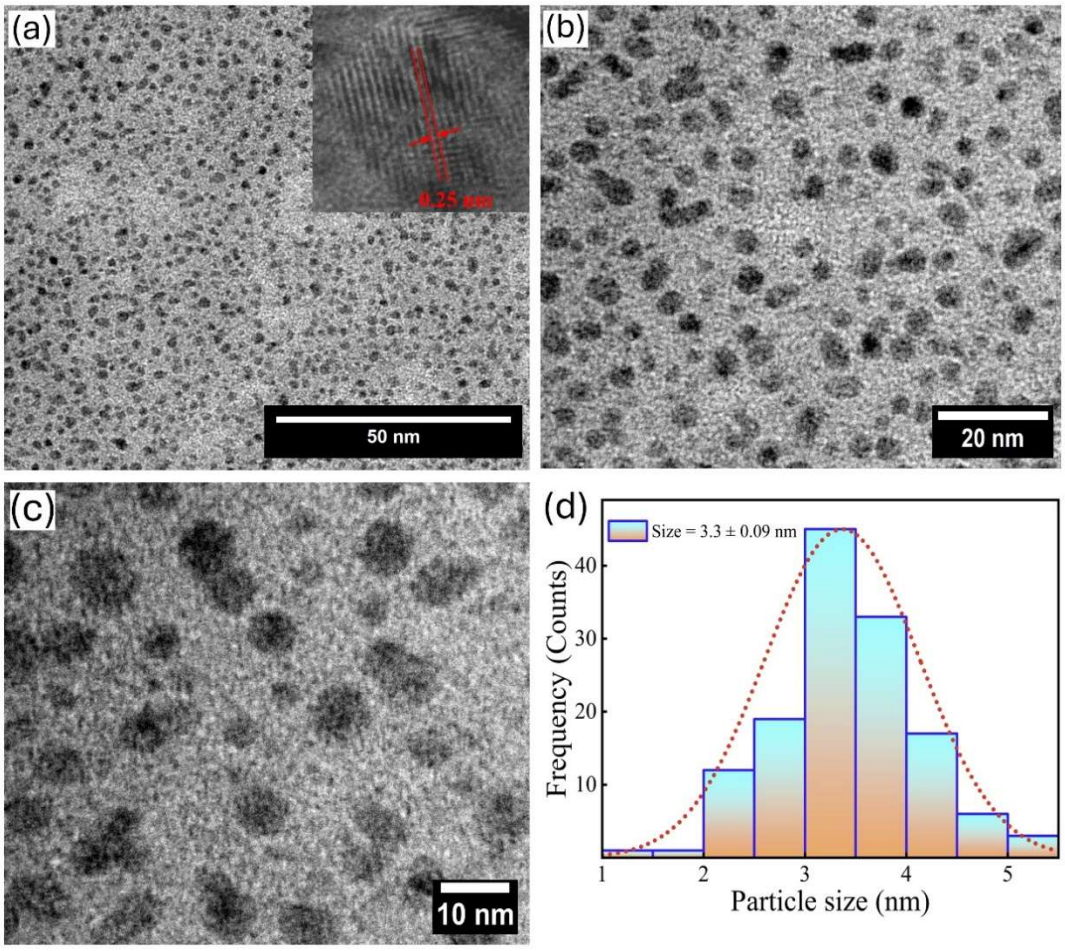

Fig 6. 2 *HR-TEM images of WS_2 QDs at various magnifications (a-c) with particle size distribution (d). Inset of (a) shows an enlarged image with measured d-spacing.*

6.3.3. UV-Vis absorption and PL spectra of obtained WS2 QDs

The absorption spectrum of colloidal WS_2 QDs dispersed in DI, as shown in Fig. 6.3(a), exhibits predominant intense bands at 336, 275 and 241 nm, along with a strong hump at 391 nm**.** The band at 336 nm is attributed to excitonic absorption stemming from direct bandgap transitions at the K point in the Brillouin zone [49]. The absorption feature at 275 nm corresponds to electronic transitions from the valence band to the conduction band. Meanwhile, the bands observed at 241 nm and 391 nm are associated with the absorption of surface-adsorbed functional groups, such as sulfate and hydroxyl ions [43,44]. The inset displays the colour images of WS_2 QDs observed under white light irradiation and UV light irradiation, respectively.

Furthermore, the Tauc plot method was utilised to estimate the direct bandgap of WS_2 QDs, by plotting $(\alpha h\nu)^2$ versus photon energy $(h\nu)$, where α is the absorption coefficient, h is Planck's constant and ν is the frequency of incident light (inset of Fig. 6.3a). Considering the direct bandgap nature of WS_2, the value of n was taken to be 2 [45]. The linear portion of the plot was extrapolated to the energy axis, revealing the bandgap of the WS_2 QDs to be approximately 4.21 eV. Fig. 3(b) represents the PL spectra of WS_2 QDs observed at ambient temperature with different excitation wavelengths in the range of 270-420 nm. As the excitation wavelength increased from 270 to 320 nm, the PL intensity increased; however, it decreased when the excitation wavelength increased from 330 to 420 nm. A gradual redshift of the PL peak was noted as the excitation wavelength shifted from 270 to 420 nm, with the maximum peak shift reaching approximately 76 nm as represented by Fig. 6.3(c). The highest PL intensity was observed at 320 nm excitation, with an emission peak centred at 410 nm and a full width at half maximum (FWHM) of 70 nm. The excitation-dependent PL behaviour and the FWHM suggest multiple possible transition pathways, likely due to the abundance of surface defects, as observed in carbon nanodots [50]. The excitation-dependent PL further indicates polydispersity and/or an inhomogeneous distribution of WS_2 QDs, attributed to photogenerated carriers becoming trapped in localised states, then either radiatively recombining or scattering into lower-energy states [51]. Photons of higher energy emission may arise if carrier relaxation within highly localised states is slow, explaining the excitation-wavelength dependency in the PL spectr. The color coordinates of the PL of WS_2 QDs were analyzed using the CIE chromaticity diagram (Fig. 3d). The PL maxima, spanning 398–475 nm at different excitation wavelengths, are tightly grouped within the blue-cyan region of the visible spectrum, illustrating the highly tunable and pure emission attainable with these QDs. The narrow clustering of PL coordinates visually demonstrates both the strong color purity and high color stability of WS_2 QDs. This behaviour is retained for excitation-dependent PL spectra, which arise from multiple radiative recombination channels within the QDs. The specific position of WS_2 QDs in the CIE plot underlines their promise for device applications demanding pure and tunable color emissions across the blue-cyan range. Additionally, PL excitation (PLE) spectra monitored at different wavelengths (Fig. S1 of the Supplementary Information, SI) showed near

independence of the excitation band on emission wavelength, with a dominant peak around 315 nm and a slight blue shift in the PL peak near 360 nm as the monitoring wavelength decreased.

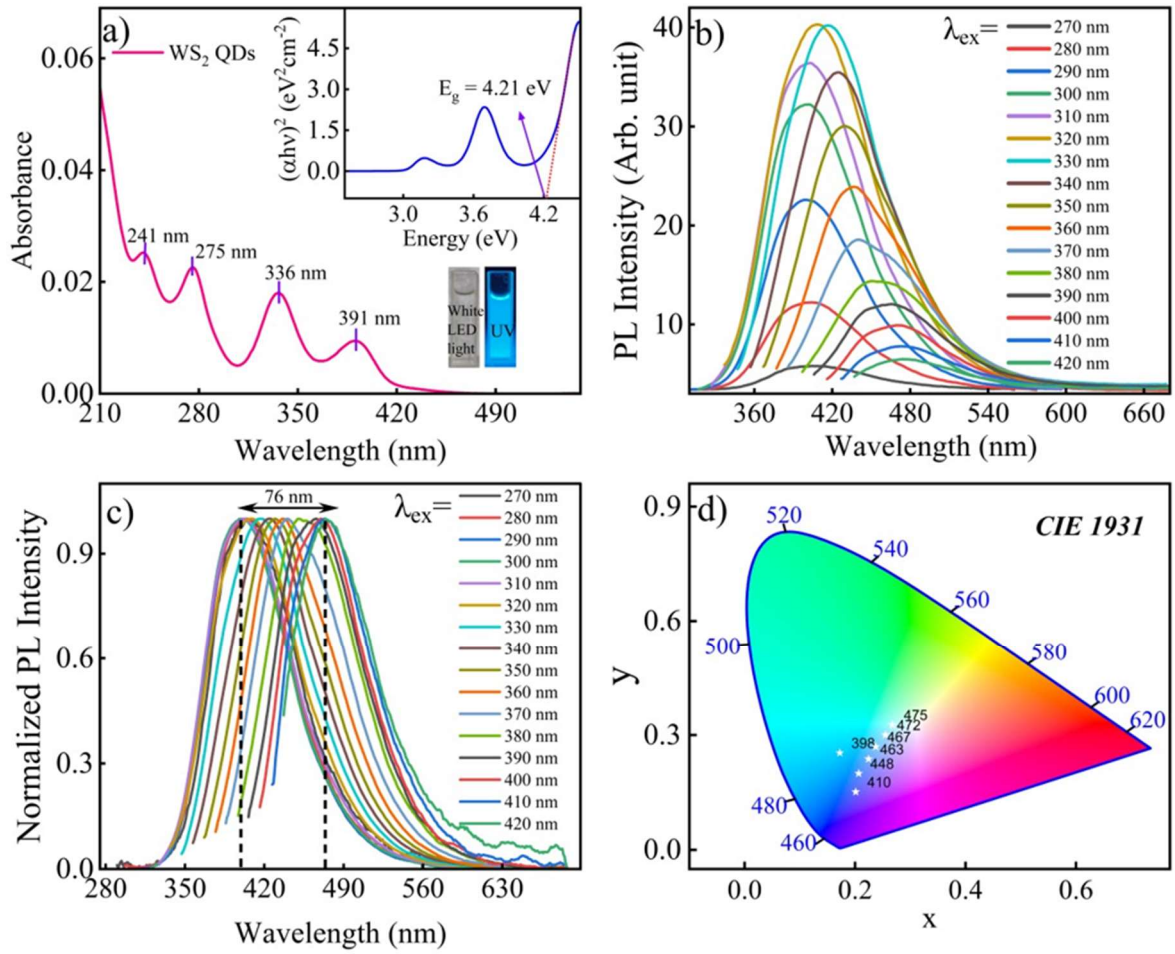

Fig 6. 3 *Absorption spectrum of colloidal WS_2 QDs. Inset represents the color photographs under visible illumination and UV irradiation (~365 nm) (a), PL spectra (b), normalized PL spectra (c) at different excitations ranging from 270 nm to 420 nm and CIE 1931 plot with blue emission (d) of the synthesised WS_2 QDs.*

Further, using quinine sulfate (with a quantum yield of 54%) as a reference, the quantum yield of WS_2 QDs was calculated via the standard comparative method, and the resulting quantum yield was about 8.67 %, exceeding previously reported values for WS_2 QDs [52].

6.3.4 PL decay analysis

PL decay curves of WS_2 QDs were monitored at an excitation wavelength of 320 nm by measuring the PL at 380, 410, and 480 nm. These decay curves were best described by a tri-exponential function, indicating the presence of multiple emissive components, with the intensity expressed by Eq. (7.2).

$$I(t) = \alpha_1 \exp(-t/\tau_1) + \alpha_2 \exp(-t/\tau_2) + \alpha_3 \exp(-t/\tau_3) \quad (6.2)$$

where α_i and τ_i represent the pre-exponential factor and lifetime of the respective components. The results are summarised in Table 7.1, and typical fitted decay curves are illustrated in Fig. 6.4 along with corresponding residuals.

PL at 380 nm shows that α_i of the fastest decaying component, which gives a lifetime of 0.29 ± 0.06 ns, was 0.65, while for the slowest decaying component, which gives a lifetime of 2.91 ± 0.08 ns, it was only 0.16. As the monitoring wavelength increased from 380 to 480 nm, the lifetime of all the decaying components also increased. Consequently, the average PL lifetime, calculated accordingly using $\tau_{av} = \sum(\alpha_i \tau_i^2)/\sum(\alpha_i \tau_i)$ relation, systematically increases with longer monitoring wavelengths (refer to Table 7.1). This dependence of PL lifetime on monitoring wavelength is likely attributed to the presence of multiple emissive states originating from different surface defect states within the WS_2 QDs.

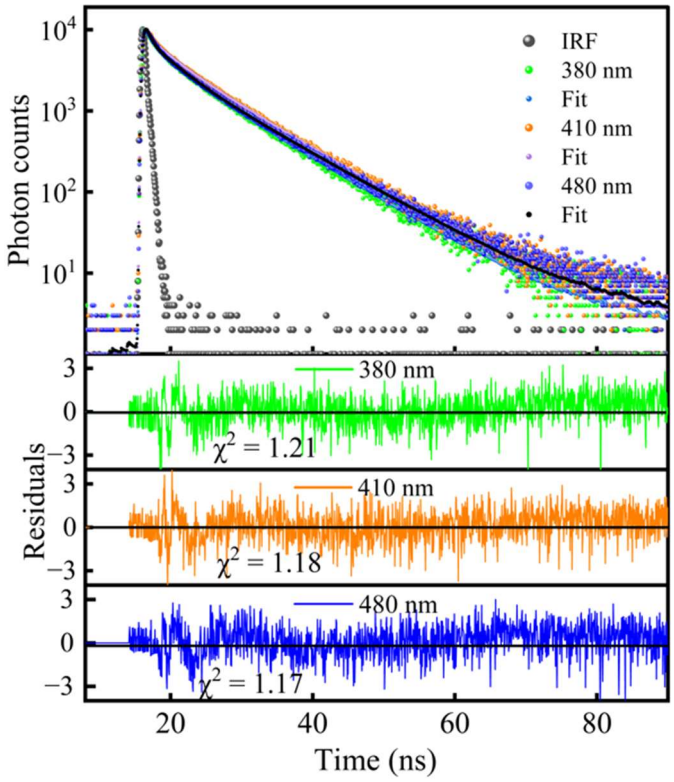

Fig 6. 4 *Fitted PL decay curves for WS_2 QDs at different emission wavelengths at λ_{ex} = 320 nm, along with IRF and their corresponding residuals and χ^2 values.*

Table 6. 1 PL lifetime and pre-exponential factors of WS_2 QDs dispersed in water at 320 nm excitation.

λ_{ex} (nm)	λ_{PL} (nm)	τ_1 (ns)	τ_2 (ns)	τ_3 (ns)	α_1	α_2	α_3	τ_{av} (ns)	χ^2
320	380	0.29 ± 0.06	2.91 ± 0.08	8.22 ± 0.38	0.65	0.16	0.19	6.43	1.21
	410	0.37 ± 0.01	3.15 ± 0.04	8.55 ± 0.12	0.57	0.17	0.26	6.98	1.18
	480	0.46 ± 0.08	3.45 ± 0.05	8.84 ± 0.11	0.58	0.20	0.22	6.78	1.17

6.3.5 Stability Analysis of WS2 QDs Under Environmental Stressors

To assess the optical durability and environmental robustness of the synthesised WS_2 QDs, systematic stability tests were conducted under varying conditions. The

photostability was evaluated by exposing WS_2 QDs to continuous UV irradiation for 3 hours, as represented by the relative change in PL intensity (Fig. 7.5(a) and Fig. S2 of SI), demonstrating negligible variation in PL intensity and indicating excellent resistance to photo-induced degradation. The pH stability was examined over a broad range from 3 to 12, with relative change in Fig. 7.5(b) and Fig. S3 (SI) revealing that the PL intensity remains constant across both acidic and alkaline environments, confirming outstanding chemical stability. Shelf-life stability monitoring over approximately 6 months at 4 °C indicated that the WS_2 QDs retained almost their original PL intensity, as depicted in Fig. 7.5(c) and Fig. S4 (SI), reflecting minimal environmental degradation and strong surface passivation. This exceptional stability is attributed to the robust W–S lattice structure and effective surface chemistry, which mitigate oxidation and hydrolysis, underscoring the practical suitability of WS_2 QDs for long-term use in sensing and optoelectronic applications.

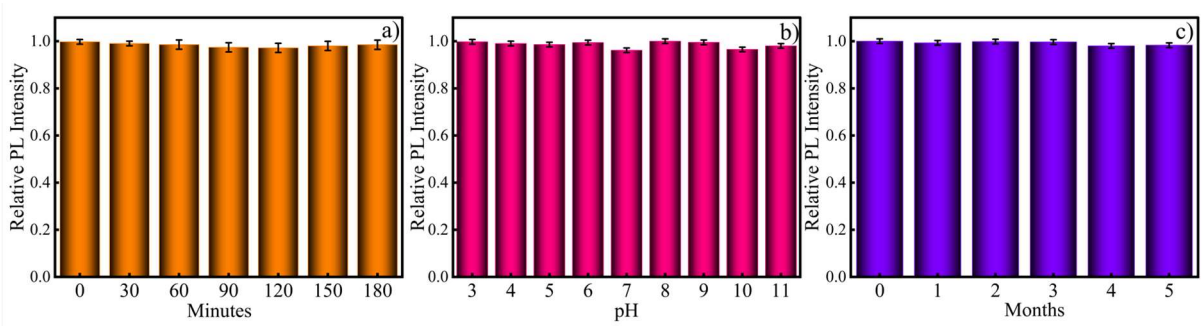

Fig 6. 5 *Bar graphs showing relative PL intensity of WS_2 QDs with 3h of continuous UV irradiation (λ=365 nm) (a), across a range of pH from 3 to 11 (b) and over a period of 6 months (c), indicating excellent stability.*

6.4. Vitamin B12 (Cbl) Sensing

Figure 7.6(a) illustrates the effect of varying concentrations of Cbl on the absorption spectra of colloidal WS_2 QDs dispersed in DI water. Upon the addition of 0.33 nM Cbl, no spectral shift or new absorption features corresponding to WS_2 QDs are observed. Instead, a progressive increase in the overall absorbance intensity is evident as Cbl concentration increases. However, with further incremental increases in Cbl concentration up to 565 nM, the intensity of these absorption bands independently rises. This enhancement originates from the intrinsic absorption peaks of Cbl, which display well-defined bands at 278 nm and 361 nm, along with a characteristic broad

shoulder in the 510–550 nm region due to corrin-ring electronic transitions. These newly introduced Cbl features rise independently with increasing concentration, simply overlaying the WS_2 QD spectrum without perturbing its excitonic transitions. The absence of peak shifts, band broadening, or emergence of new spectral features in the WS_2 QDs region confirms that no significant ground-state complexation occurs between WS_2 QDs and Cbl. Instead, the observed absorbance increase is solely attributed to the independent optical contribution of Cbl, rather than any modification of the electronic structure of the WS_2 QDs [53].

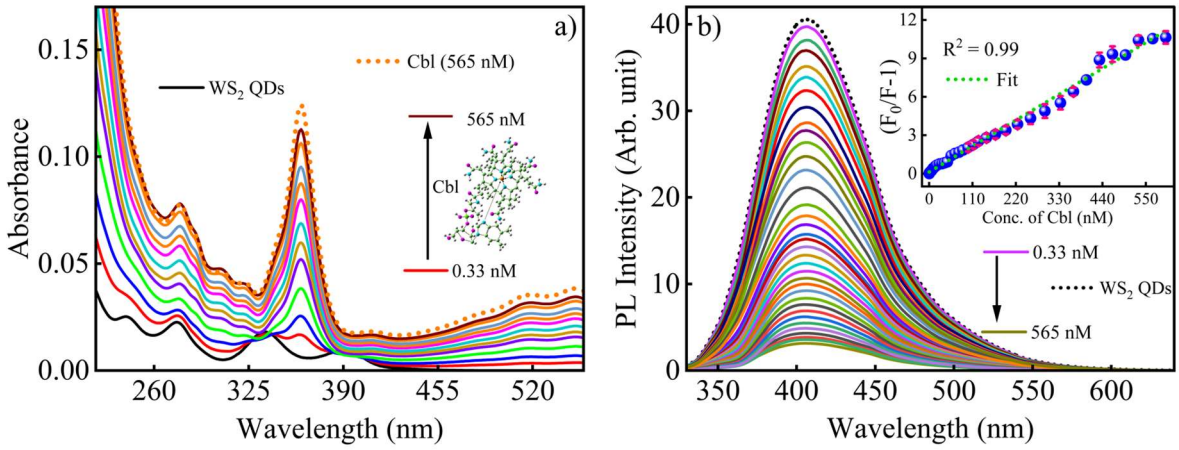

Fig 6. 6 *Absorption spectra and PL spectra (λ_{ex} = 320 nm) of WS_2 QDs in the presence of different concentrations of Cbl ranging from 0.33 to 565 nM (a,b). Inset of (b) represents the corresponding S-V plot.*

Figure 7.6(b) illustrates the PL response of WS_2 QDs in the presence of increasing concentrations of Cbl (0.33–565 nM). A significant decrease in PL intensity is observed even at the lowest concentration (0.33 nM), and the quenching progressively intensifies with increasing Cbl concentration, ultimately reaching ~94% suppression at 565 nM. Importantly, the emission peak position and spectral shape of WS_2 QDs remain unchanged throughout the titration, indicating that the emissive state of the QDs is not structurally or electronically perturbed. PL quenching may arise from dynamic (collisional) or static (ground-state complexation) processes; therefore, Stern–Volmer (SV) analysis was carried out to identify the dominant mechanism.

$$F_0/F = K_{SV}[Cbl] + 1 \quad (6.3)$$

where F_0 and F represent the PL intensities without and with Cbl, respectively, revealed an excellent linear correlation between PL intensity ratio and Cbl concentration ($R^2 = 0.99$), as shown in the inset of Fig. 6.6(b). The linearity of the S-V plot across the full concentration range indicates a single, uniform quenching pathway, and the quenching constant (K_{SV}) was determined to be 1.83×10^7 M^{-1}. The limit of detection (LOD), calculated using 3σ/K, where σ is the standard deviation from ten blank WS_2 QD measurements and K is the slope of the calibration plot, was found to be 555 pM (0.753 ng/mL). The corresponding limit of quantification (LOQ), determined using 3σ/K, was 1850 pM (2.51ng/mL), demonstrating the sensitivity of WS_2 QDs toward trace-level Cbl detection. The obtained LoD values for Cbl detection are significantly lower than those reported in previous literature (Table 6.2), highlighting the superior sensitivity of the WS_2 QDs-based sensing platform.

Table 6. 2 *Comparative data of WS_2 QDs-based probe with prior investigated probes for the detection of Cbl.*

Probe Used	Linearity Range	Limit of Detection (LoD)	Ref.
t-CDs	1-12 µg/mL	74nM (19)	[54]
CDs	03-15µM	93 nM(22)	[55]
NA-CQDs	0.1-60 µM	31.7 nM	[55]
CdTe QDs	0.5-300 µM	81nM	[56]
PN-CQDs	2.0-31 µM	3.0 nM	[57]
Boron CDs	0.2-24 µM	6.1 nM	[58]
CdTe QD	0.02-70 µM	20 nM(24)	[59]
WS_2 QDs	*0.33 – 565 nM*	*555 pM*	*This Work*

6.4.1. Effect of Cbl on PL lifetime of WS2 QDs

PL decays are usually measured to understand excitation dynamics. For example, static quenching and dynamic quenching can be distinguished. Accordingly, PL decays of WS_2 QDs were measured with 320 nm excitation by monitoring the PL at the peak position. Decay profiles were measured at various concentrations of Cbl under the same experimental conditions as used for the steady-state PL measurements. The

observed decay profiles could be fitted with a tri-exponential function. The parameters used for the fitting are summarised in Table 3, and fitted decay curves are shown in Fig. 6.7. It is noted that small baseline signals (about 10-20 counts) in different decay curves are different from each other because of the experimental uncertainty. As mentioned in the previous section, multiple lifetimes may be assigned to different emitting states and the polydispersity of QDs.

The lifetime (τ_1) decreased from 0.37 ns to 0.32 ns with increasing Cbl concentration up to 565 nM (Table 3). The lifetimes of the second decaying component (τ_2) decreased slightly from 3.51 to 3.42 ns, and the third component (τ_3) remained almost constant with increasing Cbl. However, the corresponding pre-exponential factors are not significantly influenced by Cbl; α_1 α_2 and α_3 with increasing Cbl (see Table 3). As a result, the average lifetime (τ_{av}) in the absence of Cbl, i.e., 6.98 ns is nearly constant as the one in the presence of maximum concentration of Cbl (6.95 ns).

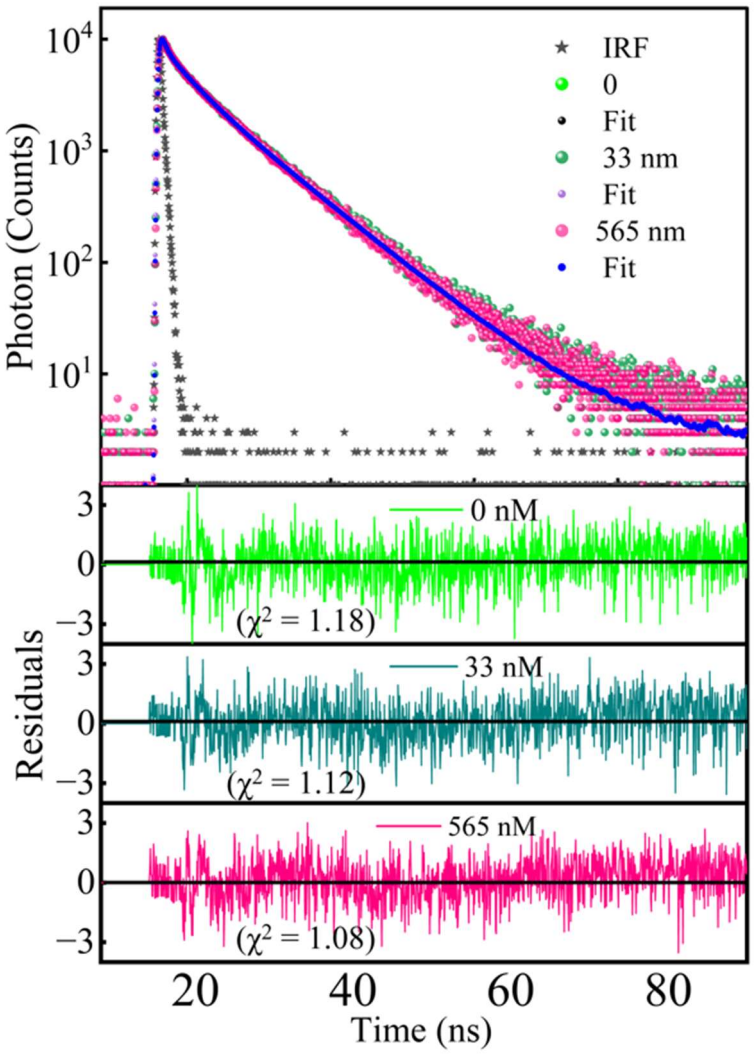

Fig 6. 7 *Fitted PL Decay curves at λ_{ex}=320 nm of WS_2 QDs in the absence and presence of the lowest concentration 0.33 nM and the highest concentration of 565 nM of Cbl, along with their respective residual profiles and χ^2 values.*

Table 6. 3 PL lifetimes and pre-exponential parameters of WS_2 QDs dispersed in DI, excited with 320 nm and monitored at 410 nm for different concentrations of Cbl.

Conc. (nM)	**τ_1 (ns)**	**τ_2 (ns)**	**τ_3 (ns)**	**α_1**	**α_2**	**α_3**	**τ_{av} (ns)**	**χ^2**
0	0.37 ± 0.03	3.51 ± 0.02	8.55 ± 0.03	0.57	0.17	0.26	6.98	1.18

33	0.36± 0.02	3.49 ± 0.06	8.55 ± 0.03	0.57	0.18	0.25	6.92	1.12
165	0.36 ± 0.01	3.47 ± 0.08	8.54 ± 0.02	0.58	0.17	0.25	6.94	1.16
363	0.33 ± 0.05	3.45 ± 0.03	8.44 ± 0.05	0.57	0.17	0.26	6.94	1.09
565	0.32 ± 0.04	3.42 ± 0.01	8.44 ± 0.03	0.57	0.17	0.26	6.95	1.08

6.4.2 Selective Detection of Cbl Using WS2 QDs: Interference and Anti-Interference Analysis with Other Analytes

To evaluate the selectivity of the WS_2 QD-based probe, PL quenching experiments were conducted using various potentially interfering analytes, including urea, chol, 7AI, 6 HQ, Gluc, Vit K, DA, and BSA. As shown in Fig. 6.8(a) and Fig. S5 (SI), none of these analytes caused significant PL quenching, with only minimal reductions in emission intensity (<20%) observed for certain species. Additionally, to assess interference in a competitive setting, each analyte was added at a fixed high concentration (565 nM) in the presence of Cbl ions. The resultant PL intensity closely resembled that of Cbl alone, as illustrated in Fig. 7.8(b) and Fig. S6 (SI). These results collectively confirm that WS_2 QDs exhibit high selectivity and negligible interference from coexisting compounds in aqueous matrices, substantiating their suitability as reliable probes for selective detection applications.

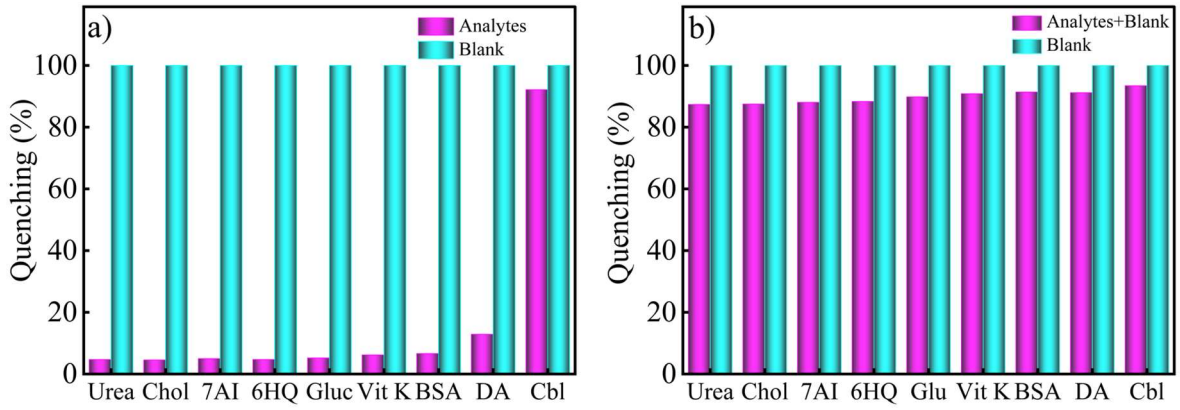

Fig 6. 8 *Bar diagrams showing the quenching (%) response of WS_2 QDs in the absence of different analytes at fixed concentrations of 565 nM (a). Quenching (%) of colloidal WS_2 QDs exposed at 565*

nM concentration of Cbl, along with other interfering analytes at the same concentrations 565 nM (b), showing negligible interference effects. The cyan bars in both (a) and (b) represent control samples without any analytes, and the magenta bars represent the presence of analytes.

6.3. Mechanism of Fluorescence Quenching Between WS2 QDs and Cbl

The interaction mechanism between WS_2 QDs and Cbl was systematically investigated through UV vis absorption, steady-state PL, and time-resolved PL measurements. Cbl exhibits its characteristic absorption peaks at 278 and 361 nm along with a broad shoulder around 510–550 nm, typical of its corrin-ring electronic transitions. Upon incremental addition of Cbl (0.33–565 nM) to the WS_2 QDs, only the intrinsic absorption features of Cbl increased in intensity without any observable peak shift, band broadening, or new absorption features attributable to WS_2 QDs. The WS_2 QD spectrum remained unchanged, indicating the absence of significant ground-state complex formation or electronic coupling between the two species. This conclusion is further supported by time-resolved PL results, where the average lifetime of WS_2 QDs remained essentially constant upon Cbl addition up to 565 nM, confirming that the excited-state radiative and nonradiative decay pathways of the QDs were not altered.

Despite the unchanged lifetime, the steady-state PL of WS_2 QDs exhibited strong quenching, reaching up to ~94% with increasing Cbl concentration. The corresponding S-V plot showed excellent linearity across the entire concentration range, indicating a single dominant quenching pathway. The combination of unchanged absorption of WS_2 QDs, absence of spectral shifts, preserved PL lifetime, and linear SV behaviour collectively rules out dynamic (collisional) quenching, Förster resonance energy transfer (FRET), and photoinduced electron transfer (PET) as the primary quenching mechanisms. Instead, the experimental evidence strongly supports an optical inner-filter effect (IFE) as the dominant cause of PL attenuation [12,60]. The strong absorption bands of Cbl overlap with both the excitation and emission wavelengths of WS_2 QDs, enabling primary IFE (attenuation of excitation light reaching QDs) and secondary IFE (reabsorption of emitted photons by Cbl) [2,61]. These processes reduce the detected PL intensity without modifying the intrinsic lifetime of the fluorophore, fully consistent with the observed behaviour.

6.5. Conclusions

In summary, WS_2 QDs were successfully developed as an efficient fluorescent probe for the sensitive and label-free detection of Cbl. The absence of spectral shifts in the absorption profiles confirmed that no ground-state complex forms between WS_2 QDs and Cbl. Nevertheless, a strong concentration-dependent PL quenching was observed, reaching ~94% at 565 nM. The unchanged PL lifetime, together with excellent S-V plot linearity, established that the quenching mechanism is primarily governed by the inner filter effect (IFE). The probe exhibited a wide linear detection range of 0.33–565 nM and achieved a LOD 555 pM (0.753 ng/mL), demonstrating high analytical sensitivity. Overall, the findings highlight WS_2 QDs as a promising, cost-effective, and rapid sensing platform for Cbl detection, with potential applicability in biomedical, nutritional, and environmental monitoring.

Chapter 7: A Spectroscopic Approach for Amoxicillin Sensing: Insights from UV-Vis and photoluminescence studies

7.1 INTRODUCTION

Amoxicillin (AMX) is a widely used broad–spectrum antibiotic (Abx) that belongs to the β-lactam class, specifically the penicillin family, with its structure as shown in Scheme 1 ($C_{16}H_{19}N_3O_5S$) [1].

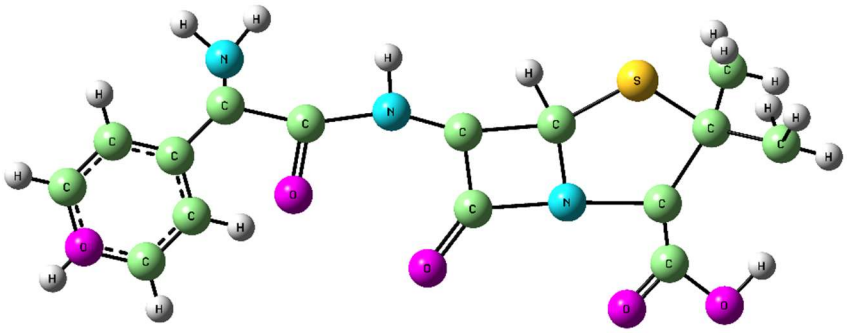

Scheme 7. 1 *Chemical structure of amoxicillin (AMX)*

It is frequently prescribed to treat a range of bacterial infections, including those of the respiratory tract, urinary system, gastrointestinal tract, skin and soft tissues [2,3]. Its effectiveness, affordability, and broad availability have made it one of the most consumed Abx globally. However, with its growing and often unregulated usage, concerns have emerged regarding the presence of AMX residues in food products such as milk and meat, as well as in water sources [4,5]. The presence of such residues, even

in trace amounts, poses a significant threat to human health and the environment. Long-term exposure to residual Abx can lead to allergic reactions, disruption of the beneficial gut microbiota, and most alarmingly, the development of Abx-resistant bacteria- a major health challenge in the 21st century [6].

Beyond human health, the environmental implications of uncontrolled AMX contamination are equally serious. Residual antibiotics enter the ecosystem through pharmaceutical waste, agricultural runoff, and improper disposal. These substances can persist in natural waters and soils, disrupting microbial communities and contributing to the spread of resistance genes [7,8]. As a result, the ability to detect and monitor AMX at low concentrations in various media has become a critical need. Regulatory bodies in several countries have established maximum residual limits (MRLs) for Abx in food and water, which further emphasizes the need for reliable and sensitive detection methods. In this context, the development of rapid, sensitive, cost-effective, and user-friendly sensors for AMX detection is not just scientifically relevant, but also socially and environmentally imperative [8]. Conventional methods for detecting AMX include high-performance liquid chromatography [9], enzyme-linked immunosorbent assays [10], and electrochemical sensors [11]. While these techniques are accurate and sensitive, they are often expensive, time-consuming, and require complex instrumentation and trained personnel. Moreover, sample pre-treatment and preparation are usually necessary, further complicating the analytical process. As a result, there has been increasing interest in the development of alternative methods that are simple, faster, and more adaptable to field applications without compromising on sensitivity and specificity [12].

In recent years, nanomaterials have attracted considerable attention for sensor development due to their unique physicochemical properties [13,14]. Among them, quantum dots (QDs)- semiconductor nanoparticles with size-dependent optical and electronic properties- have emerged as promising candidates for chemical sensing applications. Transition metal dichalcogenides (TMDs), such as tungsten disulfide (WS_2), have demonstrated significant potential due to their tunable bandgap, high surface area, and excellent photoluminescence (PL) properties [15,16]. WS_2 QDs are a relatively new class of TMD-based nanostructures that offer strong and stable PL, good aqueous dispersibility, and the ability to interact selectively with various analytes through surface adsorption or charge transfer mechanisms [17,18]. Despite their promising properties, the use of WS_2 QDs for antibiotic detection, particularly for AMX, remains underexplored. Only a few studies have investigated the interaction between WS_2 QDs and Abx molecules in optical sensing platforms. This presents a clear research gap and an opportunity to explore the optical behaviour of WS_2 QDs in the presence of AMX. By exploiting the changes in PL intensity upon interaction with target analytes, a sensitive and label-free optical sensing mechanism can be developed. Such a method would not only be rapid and cost-effective but also suitable for real-time detection without the need for complex procedures.

In this study, we address the pressing need for a simple, sensitive, and cost-effective detection method for AMX by exploring the potential of WS_2 QDs as an optical sensor. AMX, chemically known as [D(-)-α.amino-p-hydroxybenzylpenicillin], contains both β-lactum and phenolic groups, which can interact with the nanomaterial's surface through hydrogen bonding, π-π stacking, or electron transfer [19,20]. These

interactions have the potential to influence the PL behaviour of WS_2 QDs. This study aims to develop a label-free, PL-based detection platform by addressing a clear gap in the current body of knowledge and leveraging the unique properties of WS_2 QDs. This work provides a significant step toward the development of new-generation, TMD-based sensors for Abx detection. The findings of this study could not only enhance the understanding of QD-analyte interactions but also pave the way for designing similar sensors for other pharmaceutical compounds of concern.

7.2. EXPERIMENTAL SECTION

7.2.1 Materials used

All reagents used in this study were of analytical grade and used without further purification. Sodium tungstate dihydrate ($Na_2WO_4.2H_2O$) and hydrochloric acid (HCl) were procured from Thermo Fisher Scientific India Pvt. Ltd. L-cysteine ($HSCH_2CHNH_2COOH$) was purchased from Sigma-Aldrich. The target analyte, amoxicillin trihydrate ($C_{16}H_{19}N_3O_5S$), along with structurally related antibiotics tetracycline (TC), doxycycline (DOX), norfloxacin (NOR), ampicillin (AMP) and other biologically relevant compounds, including uric acid (UA), fructose (Fru), glucose (Glu), Dopamine (DA), sucrose (Suc), and cholesterol (Chol), were purchased from Central Drug House (CDH), India. All aqueous solutions were prepared using ultrahigh-purity deionised water (DI) with a resistivity of 18.2 MΩ.cm, obtained from an Adrona ultra water purification system.

7.2.2 Synthesis

Water-soluble WS_2 QDs were synthesised via a modified hydrothermal route, optimised for lower energy consumption, and enhanced reproducibility [21]. In a typical synthesis, 0.082 g (0.25 mmol) of sodium tungstate dihydrate, used as tungstate

(W) precursor, was dissolved in 12.5 mL of DI water using a stirrer and ultrasonicated for 15 minutes to ensure uniform dissolution. Subsequently, 0.0605 g (0.5 mmol) of L-cysteine, used as sulfur (S) precursor, was added to the solution along with an additional 50 mL of DI water, and the pH of the solution was then adjusted to ~5 using 0.1 M HCl under magnetic stirring and was further ultrasonicated for 25 minutes to obtain a clear and homogenous reaction mixture. This sets the molar ratio of W:S precursor at 1:2, which was found to be optimal for achieving a small particle size and strong PL, as cysteine acts as both an S precursor and a stabilising ligand. The prepared solutions were then transferred into a 100 mL Teflon-lined stainless-steel autoclave and heated in an oven at 180 °C for 24 hours. The reduction in temperature and reaction time, compared to previous synthesis, was made possible by optimising the precursor concentration and pH, which facilitated more efficient nucleation and growth kinetics without compromising the crystalline quality of the QDs. After natural cooling to room temperature (RT), the resulting yellowish dispersion was centrifuged at 8000 rpm for 15 minutes to remove large aggregates and unreacted species. Further, filtered the supernatant containing well-dispersed WS_2 QDs using Whatman filter paper of Grade 1 and stored at 4°C for further use. The product required no additional purification or capping steps, as the presence of L-cysteine ensured excellent water solubility, colloidal stability, and surface passivation of the synthesised WS_2 QDs.

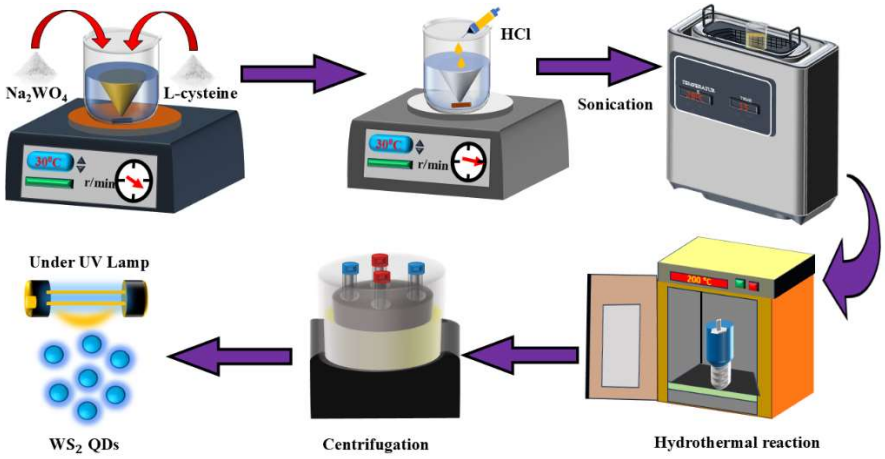

Scheme 7.2 *Schematic illustration of modified hydrothermal synthesis of water-soluble WS_2 QDs.*

7.2.3 Optimised reaction pathway

During hydrothermal treatment, L-cysteine undergoes thermal decomposition in an aqueous medium, yielding pyruvic acid ($CH_3COCOOH$), ammonia (NH_3) as a major product and chalcogen hydride gas (H_2S), as confirmed by its unpleasant rotten egg smell.

$$HSCH_2CHNH_2COOH + H_2O \rightarrow CH_3COCOOH + NH_3 + H_2S\uparrow$$

Simultaneously, the release of H_2S reduces the tungstate ions (WO_4^{2-}). Pyruvic acid may also contribute as a mild reducing agent. The reduction reaction forms colloidal WS_2 nanocrystals along with by-products such as sulfate and acetate ions.

$$4WO_4^{2-} + 9H_2S + 6CH_3COCOOH \rightarrow 4WS_2 + SO_4^{2-} + 6CH_3COCOO^- + 12H_2O$$

The reaction occurs effectively at milder conditions as reported earlier [22], yet sufficient to facilitate complete reduction and crystallisation. The formation of WS_2

QDs is visually confirmed by the appearance of a light-yellow fluorescent colloidal solution, indicating successful nucleation and quantum confinement.

7.2.4 Characterization techniques

To evaluate the optical and structural properties of the synthesised WS_2 QDs, a series of characterisation techniques was employed. The crystal structure of the synthesised material was confirmed by X-ray diffraction (XRD), performed on a Bruker D8 Advance diffractometer equipped with a Cu K_α radiation source (λ=1.54 Å), operated at 40 kV and 20 mA. For the identification of functional groups, Fourier transform infrared (FT-IR) spectra were recorded in the spectral range of 400-4000 cm^{-1} using a Thermo Scientific, Nicolet Summit X FTIR spectrometer. High-resolution transmission electron microscopy (HR-TEM) was carried out using a TECNAI TEM (Fei Electron Optics) system, operated at an accelerating voltage of 200 kV to analyse the morphology and particle size distribution of the WS_2 QDs. UV-visible absorption and PL spectroscopy were primarily used to probe the optical behaviour of the QDs due to their sensitivity to even low concentrations of analytes. Steady state absorption spectra were acquired using a Lambda 750 UV/VIS/NIR double-beam spectrophotometer (Perkin Elmer, USA), while PL and excitation spectra were recorded with a customized JASCO spectrofluorometer (FP-8500). Time-resolved PL measurements were carried out using the time-correlated single-photon counting (TCSPC) technique, implemented through the DeltaFlex-01-DD system (Horiba Jobin Yvon IBH Ltd.) equipped with a PPD-850 photon detector and a 320 nm pulsed DeltaDiode laser operating at a repetition rate of 10 MHz. The instrument response function (IRF) was determined using a standard Ludox colloidal silica scatterer. All

optical measurements were performed in a 1cm path length quartz cuvette to ensure transparency across the UV-vis range.

7.3. RESULTS AND DISCUSSION

7.3.1 XRD analysis

Fig. 7.1 illustrates that the XRD of the as-prepared WS_2 QDs displays only very weak and broadened features rather than the sharp reflections observed for bulk WS_2. This loss of well-defined diffraction peaks is expected for materials that have been reduced to the QDs regime, where strong size broadening and a high fraction of edge/defect sites reduce long-range crystallographic order and lower peak intensities. The most pronounced feature is a broad hump centred near $2\theta \sim 30°$, which can be attributed to the diminished (004) - type stacking reflection of WS_2 in the quasi-0D structure. The position and diffuse nature of this hump are consistent with earlier reports [23,24] and matched with the JCPDS card (00-008-0237) of WS_2 on hydrothermally synthesised and liquid-exfoliated WS_2 QDs and reflecting the transition from layered, long-range order (in the bulk) to small, often turbostratic or defect-rich QDs. Further, the average crystallite size was calculated using the Debye-Scherrer equation [25].

$$D = \frac{K\lambda}{\beta cos\theta} \tag{6.1}$$

where K (= 0.94), λ, β, and θ represent the geometric factor, wavelength of X-ray associated with copper (CuK_α) source, full width at half maxima (FWHM) of the observed peak, and the angle of diffraction peak, respectively. The value of D, as calculated using Eq. 1, was found to be 3.03 nm.

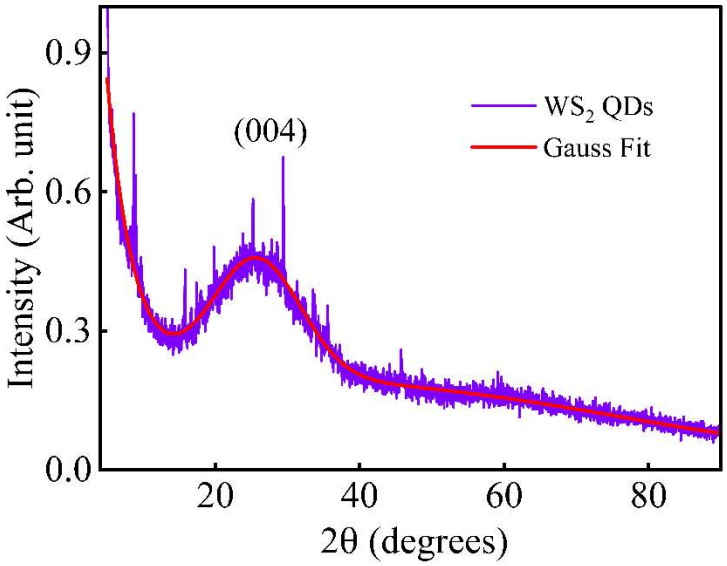

Fig 7. 1 XRD structure of synthesised WS_2 QDs deposited on a thin film.

7.3.2 High-resolution transmission electron microscopy (HRTEM) analysis

The HR-TEM images of the synthesised WS_2 QDs at different magnifications are displayed in Fig. 7.2. The HR-TEM micrograph in Fig. 7.2(a) (recorded at 50 nm scale) reveals that the WS_2 QDs possess a nearly spherical morphology with uniform dispersion and minor aggregation among the particles. At higher magnification (Fig. 7.2(b), 20 nm scale), the individual QDs are clearly visible and appear to be homogeneously distributed with nanoscale dimensions. The inset of Fig. 7.2(b) exhibits distinct lattice fringes, confirming the crystalline nature of the WS_2 QDs. The measured interplanar spacing (d) of approximately 0.2 nm corresponds to the (100) plane of hexagonal WS_2, in good agreement with previously reported values [26,27]. The particle-size distribution histogram (Fig. 7.2(c)) follows a Gaussian profile with an average particle size of 3.12 nm, indicating a narrow size distribution. This narrow and uniform size distribution is beneficial for their application in various nanodevices.

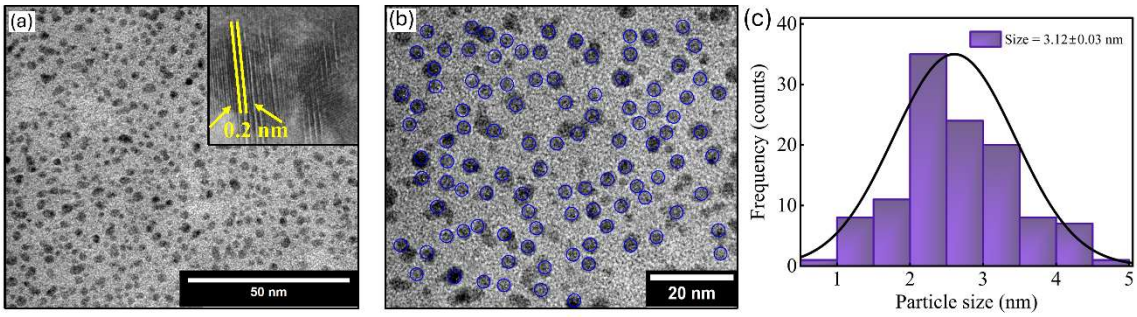

Fig 7.2 *HR-TEM image of the obtained WS_2 QDs at different magnifications (a,b), with particle size distribution (c).*

7.3.3 Optical Properties of WS_2 QDs

The optical behaviour of the synthesised WS_2 QDs was investigated through absorption and PL spectroscopy, as presented in Fig. 7.3. The absorption spectrum (Fig. 7.3(a)) exhibits a distinct excitonic absorption feature with a peak at 260 nm, characteristic of the quantum-confined WS_2 structure. The insets of Fig. 7.3(a) show the optical appearance of the colloidal WS_2 QDs solution under white LED and UV light illumination, where a clear difference in colour emission can be observed, confirming strong luminescent behaviour under UV excitation. Further, the band-gap energy (E_g) of WS_2 QDs was determined using a widely accepted method based on the Tauc relation $(\alpha h\nu)^n = A(h\nu - E_g)$, where α is the absorption coefficient, hν is the photon energy, A is a proportionality constant, and n depends on the nature of the electronic transition (with n = 2 for a direct bandgap semiconductor). By plotting $(\alpha h\nu)^2$ against hν and extrapolating the linear portion near the band edge to the energy axis, the value of E_g was obtained to be 5.67eV (inset of Fig.7.3 (a)). Fig. 7.3(b) displays the excitation-dependent PL spectra of the WS_2 QDs recorded at RT for excitation wavelengths ranging from 280 to 400 nm. The PL intensity increases as

the excitation wavelength shifts from 280 nm (4.42 eV) to 320 nm (3.87 eV), reaching a maximum emission at 380 nm when excited with 320 nm light. Beyond this, a gradual decrease in intensity is observed with further increase in excitation wavelength up to 400 nm (3.09 eV). The normalized PL spectra (Fig. 7.3 c) demonstrate a redshift of approximately 85 nm in the emission peak with increasing excitation wavelength, indicating the presence of excitation-dependent (wavelength-tunable) emission, typically attributed to surface states and size-dependent quantum confinement effects [28]. The CIE chromaticity diagram (Fig. 7.3d) further illustrates the emission behaviour of WS_2 QDs under different excitation wavelengths. The emission coordinates are mainly confined within the blue-cyan region of the visible spectrum, validating the tunable blue luminescence nature of the synthesised QDs. The close clustering of PL coordinates in the CIE diagram indicates a narrow emission distribution, suggesting high color purity and photostability of the WS_2 QDs. Such excitation-dependent, tunable PL behaviour suggests multiple radiative recombination pathways, including band-edge and surface-defect emissions, which contribute to the observed optical response [29,30].

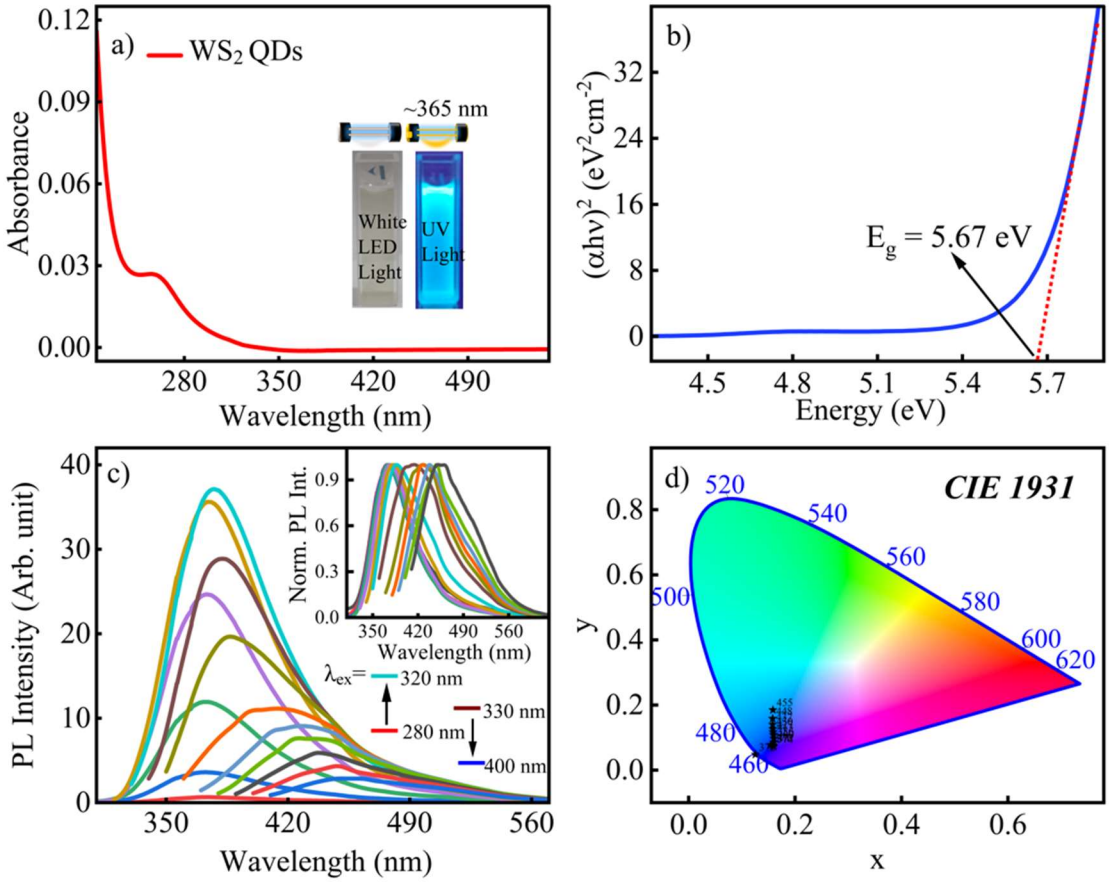

Fig 7. 3 *Absorption spectrum of WS_2 QDs with inset representing the visible color under normal LED light and UV light (a), PL spectra (b), normalized PL spectra (c) at different excitations ranging from 280 nm to 400 nm and CIE 1931 plot with blue cyan emission (d) of the synthesised WS_2 QDs.*

Figure 7.4 presents the deconvoluted PL (Fig. 7.4a) and photoluminescence excitation (PLE) (Fig. 7.4(b)) spectra of the synthesised WS_2 QDs, revealing distinct emission and excitation features corresponding to multiple radiative centres. The PL spectra, recorded at excitation wavelengths (λ_{ex}) of 280, 300, and 320 nm, can be deconvoluted into three Gaussian components centred at approximately 370, 390, and 440 nm, indicating the coexistence of three efficient emissive states. When excited above 350 and 380 nm, the PL profiles can be well-fitted with two Gaussian bands,

suggesting the dominance of fewer emissive transitions at higher excitation wavelengths. To further elucidate the excitation-dependent PL behaviour, PLE spectra were recorded at emission wavelengths (λ_{em}) of 370, 390, 410, 440, and 480 nm, corresponding to the PL deconvoluted components. The PLE spectra monitored at λ_{em} = 370, 390, and 410 nm can be resolved into two Gaussian bands centred at 300 and 323 nm, attributed to high-energy excitonic transitions. In contrast, the PLE spectrum at λ_{em} = 440 nm requires two excitation bands at 300 and 380 nm, while the spectrum recorded at λ_{em}= 480 nm, an additional excitation band around 410 nm, reflecting the presence of multiple excited-state manifolds and relaxation channels. The high-energy excitations (300 and 323 nm) correspond to intrinsic excitonic transitions within the confined WS_2 QDs core, which relax radiatively to produce short-wavelength emissions around 370 nm. Conversely, the lower-energy transitions (380 and 410 nm) originate from defect/surface states that dominate the longer-wavelength emissions at 430 and 470 nm [27,31]. The coexistence and persistence of both excitonic and defect-associated features across varying excitation and emission wavelengths confirm the presence of two major recombination pathways-direct excitonic recombination and defect/surface-state-mediated emission [32]. Fig. 7.4(c) represents the fitted decay curves along with their residuals of the synthesised WS_2 QDs was investigated under 320 nm excitation by monitoring the emission at 350, 380, and 410 nm.

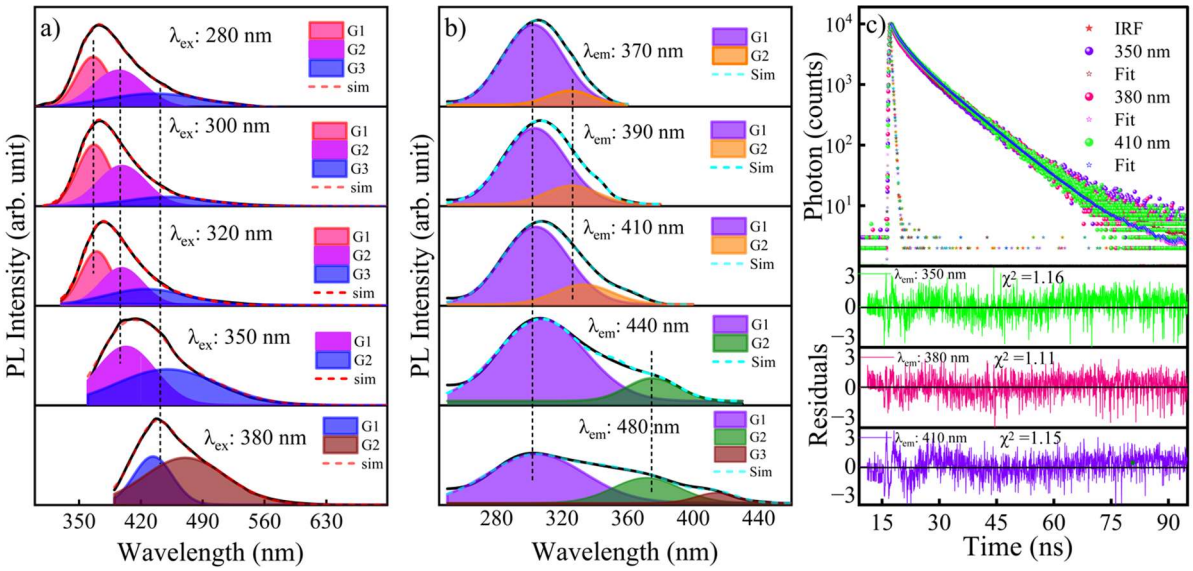

Fig 7. 4 *PL (a) and PLE (b) spectra of WS_2 QDs, along with Gaussian bands used and simulated (Sim) spectra. Fitted PL decay transients for WS_2 QDs at various emission wavelengths at an excitation wavelength of 320 nm, along with IRF and their corresponding residuals (c).*

Furthermore, the decay transients were well-fitted using a tri-exponential function (Eq. 7.2), indicating the presence of multiple recombination processes contributing to the overall emission:

$$I(t) = \alpha_1 e^{\left(\frac{-t}{\tau_1}\right)} + \alpha_2 e^{\left(\frac{-t}{\tau_2}\right)} + \alpha_3 e^{\left(\frac{-t}{\tau_3}\right)} \quad (7.2)$$

where α_i and τ_i represent the pre-exponential factor and lifetime of the i-th component, respectively [33]. At the emission wavelength of 350 nm, the fastest decay component (τ_1= 0.23) exhibited the highest amplitude contribution (α_1=0.72), indicating a dominant radiative recombination from shallow excitonic states. In contrast, the slowest component (τ_3= =8.54) contributed only marginally (α_3=0.12) corresponding

to long-lived trap-assisted emission. As the monitored emission wavelength increased from 380 to 410 nm, all decay components exhibited progressively longer lifetimes, and the calculated average lifetime was obtained by using the relation $\tau_{av} = \sum(\alpha_i \tau_i^2) / \sum(\alpha_i \tau_i)$ also increased accordingly and the obtained fitting parameters are summarized in Table 7.1. This wavelength-dependent increase in lifetime reflects the involvement of multiple emissive centres within the WS_2 QDs, including both intrinsic excitonic and surface/defect-related states [29]. The slower decay components are attributed to radiative transitions originating from surface defect states, whereas the faster components correspond to direct excitonic recombination. Such multi-exponential decay behaviour is characteristic of quantum-confined WS_2 nanostructures and confirms the coexistence of radiative pathways that contribute to the observed excitation-dependent PL, consistent with recent findings for TMDs QDs [34].

Table 7. 1 *PL lifetime and pre-exponential factors of colloidal WS_2 QDs at λ_{ex} = 320 nm.*

λ_{em} (nm)	τ_1 (ns)	τ_2 (ns)	τ_3 (ns)	α_1	α_2	α_3	τ_{av} (ns)	χ^2
350	0.23 ± 0.03	2.38 ± 0.07	8.54 ± 0.03	0.72	0.16	0.12	6.17	1.16
380	0.31 ± 0.01	2.97 ± 0.09	8.49 ± 0.06	0.57	0.21	0.22	6.65	1.11
410	0.39 ± 0.02	3.28 ± 0.11	9.42 ± 0.08	0.58	0.26	0.16	6.61	1.05

Additionally, the PL quantum yield/efficiency (QY) of the synthesised WS_2 QDs, which quantifies the efficiency of photon emission relative to photon absorption, was determined using quinine sulfate (QY = 0.54 in 0.1 M H_2SO_4) as a standard reference. The QY was calculated according to [21]Eq. (7.3)

$$QY_S = QY_R \times \frac{A_S}{A_R} \times \frac{Abs_R}{Abs_S} \times \left(\frac{\eta_S}{\eta_R}\right)^2 \quad (7.3)$$

where QY_R and QY_S; A_R and A_S; Abs_R and Abs_S; η_R and η_S represents the quantum yields of the reference and sample, as well as the integrated areas under the PL spectra, absorbance values at the excitation wavelength, and the refractive indices of the solvents used for the reference and sample, respectively. The calculated QY of the WS_2 QDs was found to be 9.7% which is higher than the previously used method [21].

7.3.4 Systematic Assessment of the Optical and Environmental Stability of WS_2 QDs:

Influence of pH, Temperature, UV Exposure, and Shelf Life

To evaluate the optical durability and environmental robustness of the synthesised WS_2 QDs, stability tests were conducted under varying environmental conditions, as represented in Fig. 7.5.

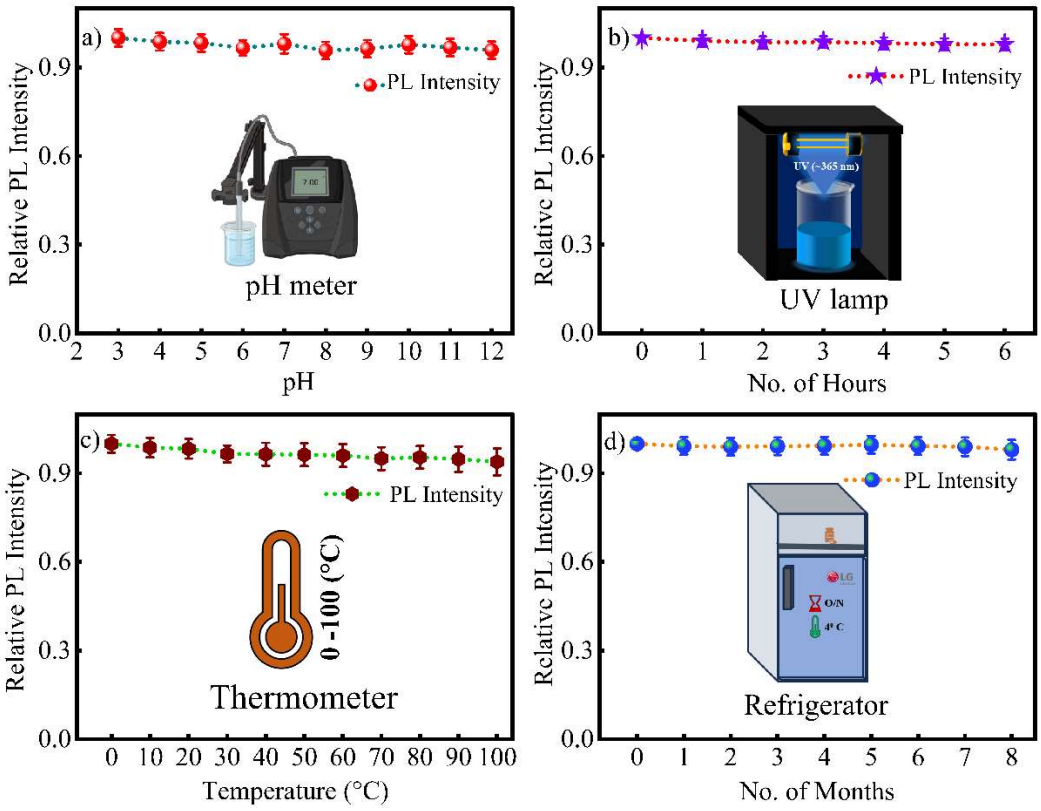

Fig 7. 5 *Relative PL intensity of WS_2 QDs across a range of pH from 3 to 12 (a), with 6 h of UV irradiation (λ=365 nm) (b) change in temperature from 0 to 100 ℃ (c), and over a period of 8 months (d), indicating excellent stability.*

The pH stability of WS_2 QDs was assessed over a broad pH range from 3 to 12, as shown in Fig. 7.5(a) and Fig. S1 of Supplementary Information (SI). The PL intensity remained nearly constant across both acidic and alkaline environments, signifying excellent chemical stability. This strong pH tolerance can be attributed to the robust covalent W-S bonding framework and limited susceptibility to surface oxidation, consistent with previously reported behaviour of TMDs [35,36]. Photostability was examined by exposing the WS_2 QDs to continuous UV irradiation of a Cole-Parmer UV lamp, with an excitation wavelength of 365 nm and an output power of 8 watts for

6 h, as shown by Fig. 7.5(b) and Fig. S2 of SI. The PL intensity exhibited negligible variation throughout the exposure period, indicating remarkable resistance to photo-induced degradation. This superior photostability is likely due to the intrinsic structural integrity of WS_2 layers that effectively prevents photooxidation and surface reconstruction under prolonged illumination. Temperature-dependent PL measurements are shown in Fig. 7.5(c) and Fig. S3 of SI, revealing a slight enhancement in PL intensity within the 0–30 °C range, which can be ascribed to the suppression of non-radiative relaxation processes at lower temperatures [25,37]. A gradual and minor decline in PL intensity was observed as the temperature increased from RT (~30 °C) to 100 °C, reflecting the expected thermal quenching due to enhanced phonon interactions at elevated temperatures. Overall, the temperature response confirmed the thermally resilient nature of WS_2 QDs. Furthermore, the shelf-life stability of WS_2 QDs was monitored over an 8-month storage period at 4 °C in a refrigerator, as shown in Fig. 7.5(d) and Fig. S4 of SI. The QDs retained more than 98% of their initial PL intensity, confirming minimal environmental degradation and strong chemical passivation. The exceptional stability can be attributed to the inherent rigidity of the W–S lattice and the surface chemistry that suppresses oxidation and hydrolysis during long-term storage. These findings underscore the practical durability and optical reliability of WS_2 QDs for diverse sensing and optoelectronic applications.

7.4. AMOXICILLIN (AMX) SENSING

7.4.1 Influence of Incubation Time on PL Response

To determine the optimal incubation time required for the interaction between WS_2 QDs and AMX, the PL response was monitored at different time intervals after adding the maximum quenching concentration of AMX (607 nM) to the WS_2 QDs dispersion.

As shown in Fig. 7.6 and corresponding PL spectra in Fig. S5 of SI, the PL intensity of WS_2 QDs decreased rapidly with increasing incubation time and reached a stable value within 7 min, indicating that the quenching process occurred almost instantaneously. No significant change in PL intensity was observed beyond 7 min, suggesting that the interaction between WS_2 QDs and AMX molecules reached equilibrium rapidly. Therefore, an incubation time of 7 min was selected as the optimum time for all subsequent PL quenching experiments [38].

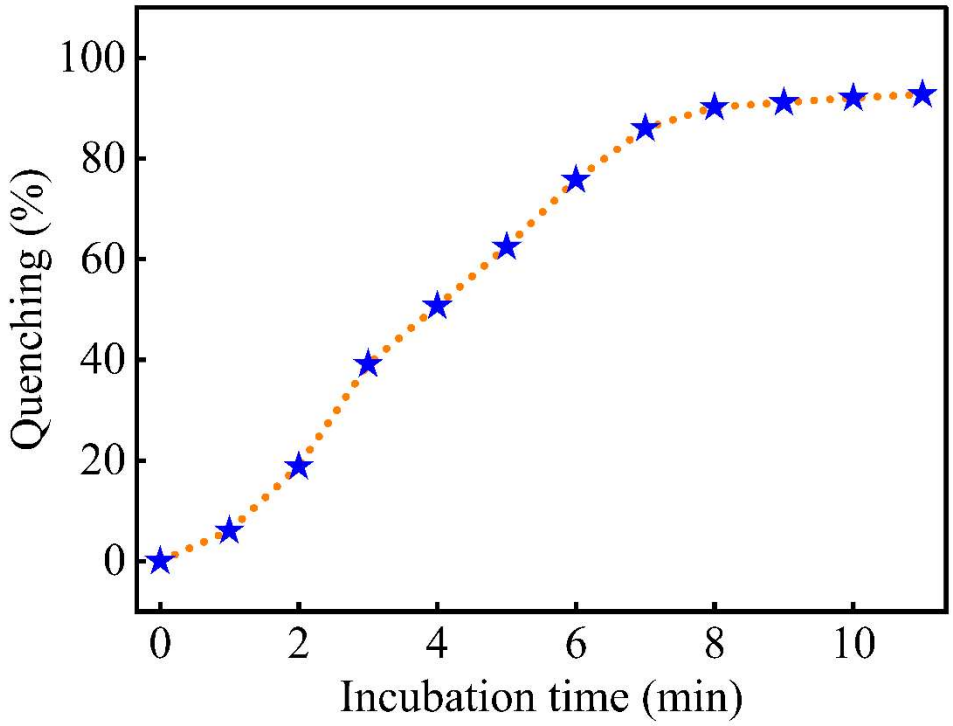

Fig 7. 6 *Quenching (%) of WS_2 QDs as a function of incubation time, in the presence of a fixed amount of AMX (607 nM).*

7.4.2 FT-IR Characterization of WS2 QDs and Their Interaction with AMX

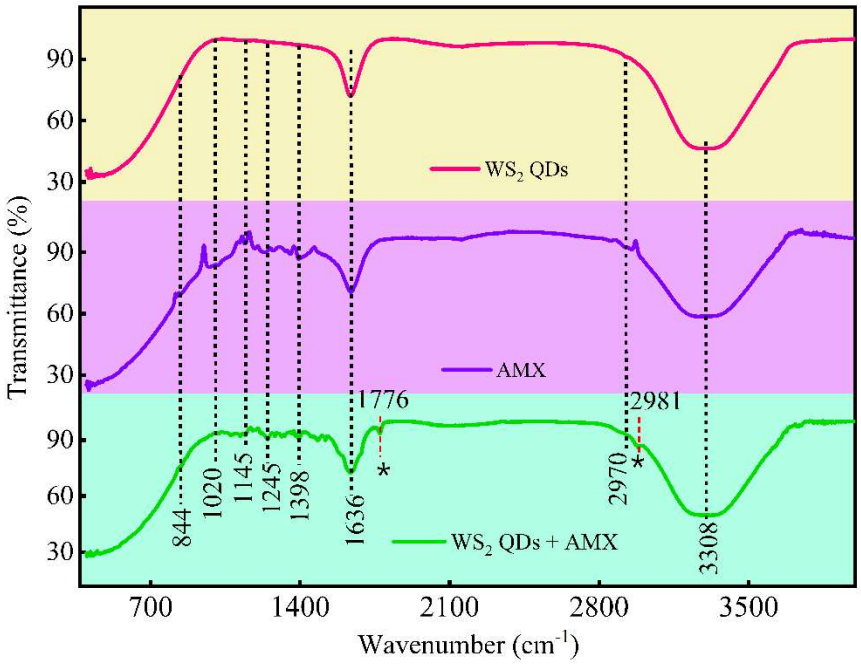

Fig 7. 7 *FT-IR spectra of WS_2 QDs, AMX and WS_2 QDs/AMX dispersed in DI.*

Fig. 7.7 represents the FTIR spectra, which illustrate the chemical interactions among WS_2 QDs, AMX, and their composite (WS_2 QDs/AMX). The absorption band at 1025 cm^{-1} corresponds to C–O stretching of hydroxyl groups, while peaks at 1630 cm^{-1} and 3289 cm^{-1} [39] are attributed to N–H bending vibrations of amide and hydroxyl dimers, respectively. The bands at 545 cm^{-1} and 2115 cm^{-1} correspond to C–H bending and N=C stretching vibrations, respectively. The presence of hydrophilic surface groups (-OH, -COOH) enhances the aqueous dispersibility and stability of WS_2 QDs [33,40].

In the spectrum of pure amoxicillin, distinct peaks appear at 844, 1020, 1145, 1245, 1398, 1636, 2970, and 3308 cm^{-1}, corresponding to characteristic functional groups of the antibiotic [41,42]. After interaction with WS_2 QDs, new peaks emerge at 1776 and 2981 cm^{-1}, indicating possible chemical interactions or hydrogen bonding between

functional groups of amoxicillin and the QD surface, confirming successful conjugation [41,43].

7.4.3 Impact of AMX on optical properties of WS2 QDs

Figure 7.8(a) illustrates the effect of varying concentrations of AMX on the UV vis absorption spectra of WS_2 QDs dispersed in DI. With the gradual addition of AMX, from 0.33 nM to 607 nM, a progressive increase in overall absorbance was observed, accompanied by a slight flattening of the characteristic absorption band of WS_2 QDs, centred around 260 nm. This increase in absorbance is primarily attributed to the intrinsic absorption of AMX, which shows characteristic bands around 242 nm and 343 nm. These bands partially overlap with the absorption region of WS_2 QDs, leading to an additive enhancement of the measured spectrum. To verify this contribution, the absorption profile of pure AMX at 607 nM was recorded, which exhibited a slightly higher absorbance than the WS_2 QDs/AMX mixture at the same concentration. This confirms that the major contribution to the rising absorbance originates from AMX itself. However, a slight flattening and marginal broadening of the WS_2 QDs absorption band upon AMX addition suggest weak ground-state interactions between AMX molecules and the surface of WS_2 QDs. Although no new absorption peak or prominent spectral shift appears- indicating the absence of a strong ground-state complex [19,44,45]. Figure 6.8(b) shows the effect of increasing AMX concentration (0.33–607 nM) on the PL behaviour of WS_2 QDs. The WS_2 QDs exhibit a strong emission band centred at approximately 380 nm when excited at 320 nm. Upon the gradual addition of AMX, the PL intensity of WS_2 QDs decreased progressively without any significant shift in the main emission peak, indicating PL quenching. The extent of quenching increased with increasing AMX concentration, reaching a

maximum of 95.5% at 607 nM. Furthermore, at intermediate concentrations above 231 nM, a slight overlapping and broadening of the PL spectra were observed near 450 nm, which can be attributed to the intrinsic PL of AMX molecules. At the highest concentration (607 nM), the PL signal from AMX became more pronounced, confirming spectral overlap between the emission of WS_2 QDs and the inherent PL band of AMX.

The quenching behavior exhibited a clear concentration-dependent response, enabling the construction of Stern-Volmer (S-V) plots to analyze the quenching efficiency. The S-V plot was generated by plotting the ratio of PL intensities of WS_2 QDs ($^{F_0}/_{F}$) against AMX concentration following Eq. 7.4 [46],

$$^{F_0}/_{F} = 1 + K_{SV}[AMX] ,$$

(7.4)

where the PL intensities without and with different concentrations of AMX are represented by F_o and F, respectively, and [AMX] indicates the concentration of AMX. The SV plots of AMX (inset of Fig. 7.8(b)) were observed to be linear, with a good correlation coefficient of $R^2 = 0.98$. These linear plots were further used to evaluate the quenching constant, which was calculated from the slope of the SV plots. The quenching constant (K_{sv}) was observed to be $7.76\times10^7\ M^{-1}$ .Furthermore, the limit of detection (LoD) was calculated using 3σ/Ksv, where σ represents the standard deviation calculated from the ten blank PL measurements of QDs, and was estimated to be 1.24 nM. A comparative data of various probes reported for the detection of AMX is summarised in Table 7.2. The obtained LoD values for AMX are significantly lower

than those reported in previous literature, highlighting the superior sensitivity of the WS_2 QDs-based sensing platform.

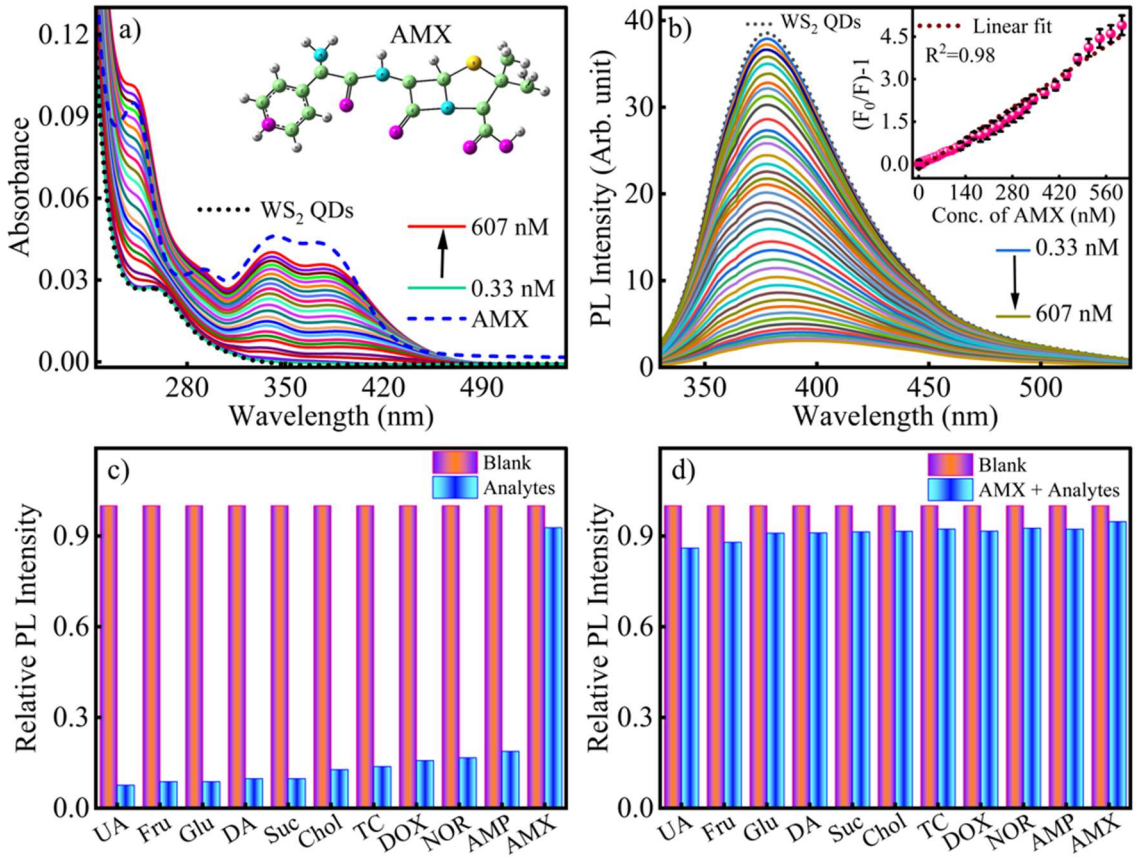

Fig 7. 8 *Absorption spectra and PL spectra (λ_{ex} = 320 nm) of WS_2 QDs in the presence of different concentrations of AMX ranging from 0.33 nM to 607 nM (a, b), and an Inset of (b) corresponding S-V plot. Bar diagrams showing the relative quenching response of WS_2 QDs in the presence of different analytes at fixed concentrations of 607 nM (c), and the same concentration of AMX (607 nM) along with other interfering analytes (d), showing negligible interference effects. The blue-cyan bars in both (a) and (b) represent control samples without any analytes, and the magenta bars represent the presence of analytes.*

Table 7. 2 Comparative data of WS_2 QDs-based probe with prior investigated probes for the detection of AMX.

Probe Used	Linearity Range	Limit of Detection (LoD)	Ref.
B-CQDs	1.43-429.12μM	0.825 μM	[47]
MIP-QDs	0.20-50.0 gL^{-1}	0.14 gL^{-1}	[48]
MPA-CdS QDs	5-30 μgL^{-1}	5.19 μgL^{-1}	[49]
Cu,N@CQDs	0.2-120.0 μM	0.06 μM	[50]
Si-capped ZnO QDs	0.2-24 μM	77.86 nM	[51]
Cds@CdTe@MIP	0-100 μgL^{-1}	0.15 μgL^{-1}	[52]
WS_2 QDs	*0.33 –607 nM*	*1.24 nM*	*This Work*

7.4.4 Selectivity and sensitivity of AMX towards WS_2 probe

To evaluate the selectivity of the WS_2 QDs–based PL probe toward AMX, potential interfering species, including UA, Fru, Glu, DA, Suc, Chol, TC, DOX, NOR, and AMP, were tested under identical conditions. As illustrated in Fig. 7.8(a) and Fig. S6 of SI, none of the tested analytes exhibited significant PL quenching, AMP and NOR showing a minor reduction in PL intensity (<20%). Furthermore, to assess the interference effect in a competitive environment, a fixed and maximum concentration (607 nM) of each analyte was introduced along with AMX. The PL intensity remained nearly the same as that observed for AMX alone, as depicted in the bar graphs in Fig. 7.8(b) and Fig. S7 of SI. These observations indicate that the presence of coexisting analytes in aqueous media does not significantly affect the detection efficiency for AMX, confirming the high selectivity and minimal interference of the WS_2 QDs-based probe.

7.4.5 Impact of AMX on PL decay of WS_2 QDs

PL decay measurements were performed to understand the excitation dynamics of WS_2 QDs and to distinguish between static and dynamic quenching processes. Time-resolved PL decay profiles were recorded at an excitation wavelength of 320 nm by monitoring the emission at the PL peak position. The decay profiles were obtained at different AMX concentrations under the same experimental conditions as those used for steady-state PL studies. All decay profiles were well fitted with a tri-exponential function, and the corresponding fitting parameters are summarised in Table 6.3. The slight variations in the baseline signals (~10–20 counts) among individual decay curves are due to normal experimental uncertainty. As discussed earlier, the presence of multiple lifetime components is attributed to different emissive states and the polydispersity of the QDs.

The shortest lifetime component (τ_1) remained nearly constant (0.31 ns) up to 231 nM AMX and then gradually increased to 0.41 ns at 607 nM of AMX. In contrast, the second and third lifetime components (τ_2 and τ_3) showed a slight increase with increasing AMX concentration, from 2.97 to 2.58 ns and from 8.49 to 8.64 ns, respectively. The pre-exponential factors were also influenced by AMX; α_1 increased from 0.57 to 0.64 and α_2 from 0.21 to 0.27, while α_3 decreased from 0.22 to 0.09 (see Table 6.3). Consequently, the average lifetime (τ_{av}) showed a modest decrease from 6.65 ns (without AMX) to 4.97 ns at 607 nM AMX, indicating the presence of dynamic quenching.

These results, combined with steady-state PL quenching, confirm that both static and dynamic quenching mechanisms are involved. The steady-state PL quenching mainly

arises from ground-state complex formation between WS_2 QDs and AMX, which reduces the effective absorbance of emissive species (static quenching). Meanwhile, the PL decay profiles support dynamic quenching due to collisional interactions between AMX and the excited states of WS_2 QDs. It is noteworthy that static quenching in this system refers to the reduction in emission intensity due to complex formation and does not imply a reduction in the intrinsic QY yield of the fluorophore.

AMX molecules.

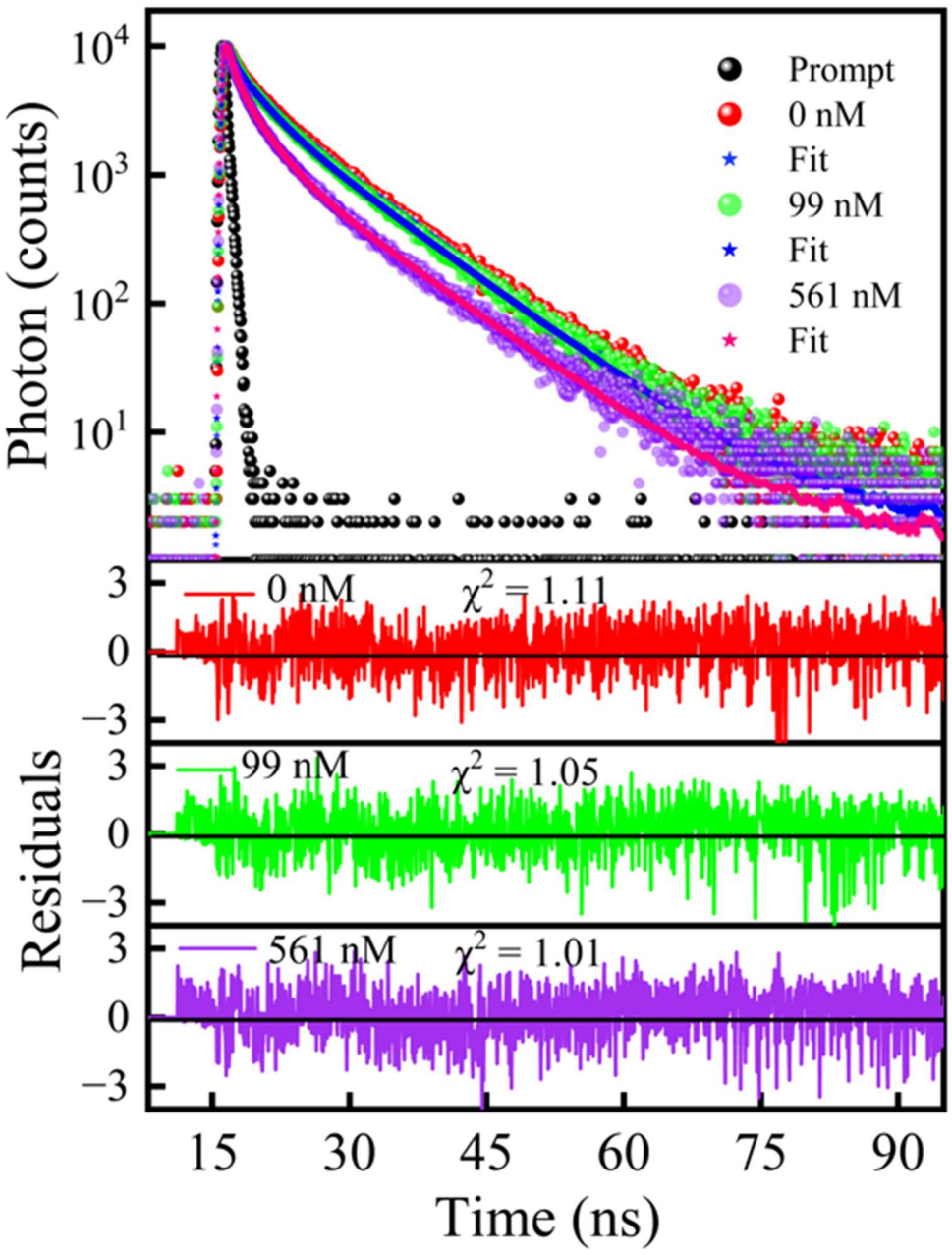

Fig 7. 9 *Fitted PL Decay profiles of WS_2 QDs in the absence and presence of AMX, along with their respective residual profiles and χ^2 values at λ_{ex} = 320 nm and λ_{em} = 380 nm.*

Table 7. 3 *PL lifetime and pre-exponential factors of WS_2 QDs upon addition of different concentrations of AMX at λ_{ex} = 320 nm and λ_{em} = 380 nm.*

Conc. (AMX) (nM)	τ_1 (ns)	τ_2 (ns)	τ_3 (ns)	α_1	α_2	α_3	τ_{av} (ns)	χ^2
0	0.31 ± 0.01	2.97 ± 0.09	8.49 ± 0.06	0.57	0.21	0.22	6.65	1.15
33	0.32 ± 0.03	2.75 ± 0.08	8.41 ± 0.06	0.55	0.22	0.23	6.62	1.10
99	0.31 ± 0.01	2.85 ± 0.10	8.39 ± 0.05	0.55	0.22	0.23	6.61	1.05
231	0.32 ± 0.02	2.86 ± 0.09	8.45 ± 0.09	0.58	0.23	0.20	6.40	1.01
607	0.41 ± 0.05	2.58 ± 0.08	8.64 ± 0.07	0.64	0.27	0.09	4.97	1.13

7.4.6 Proposed Photoluminescence Quenching Mechanism

The interaction between WS_2 QDs and AMX was elucidated using FTIR, UV–Vis, steady-state PL, and time-resolved PL decay analyses. FTIR spectra of the WS_2 QDs/AMX system exhibited new bands at 1776 and 2981 cm^{-1}, indicating the formation of surface-level interactions such as hydrogen bonding or weak chemical coordination between AMX functional groups and the WS_2 QD surface. These new

vibrational features confirm the formation of a ground-state WS_2/AMX surface complex, pointing to a predominant static quenching contribution. UV–vis absorption spectra further supported this by showing an overall increase in absorbance with AMX addition, attributable to the intrinsic absorption of AMX (bands at 242 and 343 nm), without any new absorption peaks. Although no major spectral shifts were observed, the slight absorbance difference between AMX alone and the WS_2/AMX mixture at higher concentrations suggests weak complex formation at the ground state.

Steady-state PL measurements showed a substantial decrease in emission intensity, reaching ~95.5% quenching at 607 nM AMX, consistent with strong static quenching, where ground-state complexation reduces the population of emissive WS_2 QDs available for excitation. A minor shoulder at ~450 nm appeared at high AMX concentrations due to AMX's intrinsic fluorescence. The SV plot, although largely linear ($R^2 = 0.98$), indicates the presence of an additional quenching route beyond pure static quenching. Time-resolved PL decay profiles revealed only a slight decrease in average lifetime τ_{av} from 6.66 ns to 4.97 ns, demonstrating that dynamic quenching is present but significantly weaker compared to the dominant static effect. This modest lifetime reduction is attributed to weak collisional interactions and partial photoinduced electron transfer (PET) between AMX and excited WS_2 QDs [33,39,53]. Thus, the proposed PL quenching mechanism of WS_2 QDs by AMX involves both strong static quenching and weak dynamic quenching.

7.5. Conclusion

In summary, WS_2 QDs were successfully employed as a highly sensitive fluorescent probe for detecting AMX. Comprehensive spectroscopic analyses– including FTIR,

UV–vis absorption, steady-state PL, and time-resolved PL measurements– revealed a pronounced and concentration-dependent quenching of WS_2 QD PL in the presence of AMX. The system exhibited a high quenching percentage (~95.5%) and an excellent SV linearity, demonstrating reliable and quantitative sensing behaviour. Mechanistic investigations confirmed that the quenching arises primarily from strong static interactions between AMX and the WS_2 QD surface, as supported by the appearance of new FTIR bands and a reduced effective absorption of emissive species. A secondary but weaker dynamic contribution was also identified, as reflected by the slight decrease in PL lifetime from 6.65 ns to 4.97 ns. The synergistic involvement of dominant static quenching, assisted by minor dynamic quenching through excited-state collisions and partial PET effects, establishes the overall sensing mechanism. These findings highlight the potential of WS_2 QDs as an efficient, selective, and reliable fluorescent nanosensor for AMX detection, providing a foundational understanding for designing next-generation QD-based antibiotic sensing platforms.

Chapter 8: Conclusion, Future Scope of Work and Social Impact

8.1 Conclusion

This thesis presents a comprehensive investigation into the synthesis, optical behaviour, and sensing applications of WS_2 and $MoSe_2$ QDs, establishing them as versatile, eco-friendly, and highly responsive fluorescent NMs. By employing controlled hydrothermal routes, stable and finely dispersed QDs were obtained, exhibiting strong excitation-dependent PL and tunable surface functionality–features that enabled their adaptation for diverse analytical applications.

The studies collectively demonstrate that the optical responses of these QDs can be precisely modulated through surface interactions, electron-transfer processes, and inner-filter effects, allowing selective and sensitive detection of a wide spectrum of environmentally and biologically relevant targets. WS_2 QDs showed robust, reversible, and redox-driven detection of H_2O_2 and Cr^{6+}, with excellent stability over multiple sensing cycles. $MoSe_2$ QDs facilitated highly selective detection of trace-level nitroaromatic pollutants, supported by strong spectral overlap and efficient quenching pathways.

Biomedical relevance was highlighted through the sensitive quantification of Cbl, achieved predominantly through the static quenching, while pharmaceutical monitoring was advanced through a modified hydrothermal synthesis of WS_2 QDs that produced smaller, brighter nanostructures suitable for efficient AMX detection. This improved formulation also offers promising prospects for future nanosensor development.

Overall, the findings of this thesis establish WS_2 and $MoSe_2$ QDs as powerful, adaptable, and cost-effective fluorescent probes, with significant potential for real-world environmental monitoring, water quality assessment, biomedical diagnostics,

and pharmaceutical analysis. The systematic understanding developed here provides a solid foundation for advancing next-generation TMD-based nanosensing technologies.

8.2 Future Scope of Work

The findings of this thesis open several promising directions for advancing WS_2 and $MoSe_2$ QD–based sensing systems. While the present work establishes their high sensitivity, selectivity, and recyclability, further research is needed to expand their applicability, improve performance, and move toward real-world deployment. The key future avenues are outlined below.

8.2.1 Surface Engineering and Doping

Future studies can explore controlled surface modification of WS_2 and $MoSe_2$ QDs to further enhance selectivity and optical tunability.
This includes heteroatom doping (Eu^{3+}, Sm^{3+}, Tb^{3+}, N, B, P) to introduce new emissive states or shift the PL to desired wavelengths, biomolecular functionalization using aptamers or peptides to achieve higher specificity toward biological analytes, and ligand passivation strategies to improve chemical stability and performance under complex environmental and biological conditions.

8.2.2 Development of Multi-Analyte and Ratiometric Sensors

To move beyond single-analyte detection, future work may focus on developing dual-emission or ratiometric QD systems that enable simultaneous monitoring of multiple pollutants with improved accuracy. Additionally, creating hybrid nanocomposites by integrating WS_2 or $MoSe_2$ QDs with carbon dots, MXenes, or noble metal NPs can enhance signal strength and selectivity, offering versatile sensing platforms suitable for complex and mixed environmental samples.

8.2.3 Integration into Portable and On-Site Devices

A major future direction involves translating QD-based probes into practical, field-deployable devices. This can be achieved by developing paper-based microfluidic strips, smartphone-assisted fluorometric detection platforms, and solid-state QD films or coatings designed for continuous environmental monitoring. Such device-level integration will enable rapid, affordable, and on-site sensing, making it suitable for real-world environmental and biomedical applications.

8.2.4 Biological Applications and Toxicity Studies

To extend these NMs into biomedical diagnostics, comprehensive in vitro and in vivo toxicity assessments are required to evaluate their biocompatibility. Future work may also explore their potential in cellular and tissue imaging, leveraging excitation-dependent PL, and further test their performance in clinical samples such as serum or urine for detecting biomarkers like vitamin B12 or oxidative stress indicators.

8.2.5 Mechanistic and Theoretical Investigations

Deeper mechanistic understanding can be achieved through DFT simulations to model analyte–QD interactions and charge-transfer behaviour, along with ultrafast spectroscopic techniques such as transient absorption or time-resolved PL to analyse excited-state dynamics. These studies will provide fundamental insights necessary for the rational design and optimisation of next-generation QD sensors.

8.2.6 Environmental and Industrial Applications

Future research should explore the deployment of QD-based sensors in real and complex environmental systems, including industrial wastewater, agricultural runoff, and natural river sources. Coupling detection with photocatalytic degradation could allow simultaneous monitoring and remediation of pollutants. Additionally, developing flow-through sensing platforms will enable continuous, real-time monitoring in treatment plants and industrial settings.

8.2.7 Electrochemical and Photocatalytic Sensing

Beyond PL, WS_2 and $MoSe_2$ QDs possess promising electrochemical and photocatalytic properties that can be leveraged for broader sensing applications. Future studies can investigate their use in electrochemical detection of redox-active species and in photocatalytic degradation of antibiotics or organic dyes, thereby expanding the applicability of TMD-based QDs well beyond optical sensing.

8.3 Society Impact

The outcomes of this research offer several meaningful contributions to society, reflected across environmental, health, and technological domains:

8.3.1 Environmental Benefits

- ✓ Early detection of water contaminants such as Cr^{6+}, 2,4,6-TNP, H_2O_2, and pharmaceutical residues helps prevent long-term ecological damage.
- ✓ Ultrasensitive and selective nanosensors enable real-time monitoring of polluted water bodies, protecting aquatic life and ecosystems.
- ✓ Regenerable sensing systems reduce chemical waste and support sustainable environmental practices.

8.3.2 Public Health and Safety

- ✓ Trace-level detection of toxic metals and explosive residues contributes to safer drinking water and reduced health risks.
- ✓ Monitoring antibiotics like amoxicillin helps control AMR by identifying pharmaceutical contamination in water.
- ✓ Sensitive detection of Cbl supports affordable nutritional assessment and early diagnosis of deficiency-related disorders.

8.3.3 Economic and Technological Advancement

- ✓ Low-cost hydrothermal synthesis promotes scalable, eco-friendly nanomaterial production suitable for widespread use.
- ✓ QD-based sensing platforms can be integrated into portable and smartphone-based devices, enabling accessible on-site testing for communities and industries.
- ✓ Reusable sensors reduce operational costs compared to conventional single-use detection systems.

8.3.4 Sustainability and Green Chemistry

- ✓ The synthesis approach uses minimal hazardous chemicals, aligning with green chemistry principles.
- ✓ Long-term reusable probes decrease environmental burden and foster sustainable technological development.

8.3.5 Real-World Applicability

- ✓ The sensors are validated in real water samples (tap water, river water, lake water), demonstrating direct relevance for municipal water testing.
- ✓ They can be adapted for community-level water monitoring, industrial effluent testing, and healthcare diagnostics.
- ✓ Potential to support policy-making by providing accurate data on water pollution and public health indicators.

References

[1] L. Kool, F. Dekker, A. Bunschoten, G.J. Smales, B.R. Pauw, A.H. Velders, V. Saggiomo, Gold and silver dichroic nanocomposite in the quest for 3D printing the Lycurgus cup, Beilstein J. Nanotechnol. 11 (2020) 16–23. https://doi.org/10.3762/bjnano.11.2.

[2] I. Freestone, N. Meeks, M. Sax, C. Higgitt, A Roman Nanotechnology, Gold Bull. 40 (2007) 270–277.

[3] P.P. Edwards, J.M. Thomas, Gold in a metallic divided state - From Faraday to present-day nanoscience, Angew. Chemie - Int. Ed. 46 (2007) 5480–5486. https://doi.org/10.1002/anie.200700428.

[4] M. Faraday, X. The Bakerian Lecture. —Experimental relations of gold (and other metals) to light, Philos. Trans. R. Soc. London. 147 (1857) 145–181. https://doi.org/10.1098/rstl.1857.0011.

[5] R. Society, His 1857 Lecture to the Royal Society in London, Gold Bull. (2007) 267–269.

[6] I. Ijaz, E. Gilani, A. Nazir, A. Bukhari, Detail review on chemical, physical and green synthesis, classification, characterizations and applications of nanoparticles, Green Chem. Lett. Rev. 13 (2020) 59–81. https://doi.org/10.1080/17518253.2020.1802517.

[7] F. Pacheco-Torgal, S. Jalali, Nanotechnology: Advantages and drawbacks in the field of construction and building materials, Constr. Build. Mater. 25 (2011) 582–590. https://doi.org/10.1016/j.conbuildmat.2010.07.009.

[8] C. Buzea, I.I. Pacheco, K. Robbie, Nanomaterials and nanoparticles: Sources and toxicity, Biointerphases. 2 (2007) MR17–MR71. https://doi.org/10.1116/1.2815690.

[9] R. Komanduri, D.A. Lucca, Y. Tani, Technological advances in fine abrasive processes, CIRP Ann. - Manuf. Technol. 46 (1997) 545–596. https://doi.org/10.1016/S0007-8506(07)60880-4.

[10] B. Cirera, A. Sáez-Coronado, D. Arribas, J. Méndez, A. Sagwal, R. de C. Ferreira, M. Švec, P. Merino, Upgrade of a variable temperature scanning tunneling microscope for nanometer-scale spectromicroscopy, MethodsX. 14

(2025). https://doi.org/10.1016/j.mex.2025.103156.

[11] K. Sakai, Atomic Force Microscope (AFM), Meas. Tech. Pract. Colloid Interface Phenom. 56 (2019) 51–57. https://doi.org/10.1007/978-981-13-5931-6_8.

[12] S. Bayda, M. Adeel, T. Tuccinardi, M. Cordani, F. Rizzolio, The history of nanoscience and nanotechnology: From chemical-physical applications to nanomedicine, Molecules. 25 (2020) 1–15. https://doi.org/10.3390/molecules25010112.

[13] K. Kang, -Hyeok Yang, Synthesis of transition metal dichalcogenides, in: Synth. Model. Charact. 2D Mater. Their Heterostruct., Elsevier, 2020: pp. 247–264.

[14] B. Mekuye, B. Abera, Nanomaterials: An overview of synthesis, classification, characterization, and applications, Nano Sel. 4 (2023) 486–501. https://doi.org/10.1002/nano.202300038.

[15] and M.Y. Xin Wang, Li-Hong Liu, Olof Ramström, 基因的改变NIH Public Access, Exp Biol Med. 234 (2009) 1128–1139. https://doi.org/10.3181/0904-MR-134.Engineering.

[16] D.R. Hang, D.Y. Sun, C.H. Chen, H.F. Wu, M.M.C. Chou, S.E. Islam, K.H. Sharma, Facile Bottom-up Preparation of WS2-Based Water-Soluble Quantum Dots as Luminescent Probes for Hydrogen Peroxide and Glucose, Nanoscale Res. Lett. 14 (2019). https://doi.org/10.1186/s11671-019-3109-5.

[17] Á. Coogan, Y.K. Gun'Ko, Solution-based "bottom-up" synthesis of group VI transition metal dichalcogenides and their applications, Mater. Adv. 2 (2021) 146–164. https://doi.org/10.1039/d0ma00697a.

[18] G. Speranza, Carbon nanomaterials: Synthesis, functionalization and sen[1] Speranza, G., Carbon nanomaterials: Synthesis, functionalization and sensing applications, Nanomaterials 11 (2021).sing applications, Nanomaterials. 11 (2021) 1–99.

[19] F. Mirzadeh-rafie, F. Rahbarizadeh, N. Shoaei, F. Nasiri, M.R. Akbarizadeh, M. Khatami, Carbon nanoparticle-based COVID-19 biosensors, Sensors Int. 4 (2023) 100246. https://doi.org/10.1016/j.sintl.2023.100246.

[20] P. Serna-Gallén, K. Mužina, Metallic nanoparticles at the forefront of research: Novel trends in catalysis and plasmonics, Nano Mater. Sci. (2024). https://doi.org/10.1016/j.nanoms.2024.10.009.

[21] T.P. Araujo, J. Quiroz, E.C.M. Barbosa, P.H.C. Camargo, Understanding plasmonic catalysis with controlled nanomaterials based on catalytic and plasmonic metals, Curr. Opin. Colloid Interface Sci. 39 (2019) 110–122. https://doi.org/10.1016/j.cocis.2019.01.014.

[22] S. Kim, J.M. Kim, J.E. Park, J.M. Nam, Nonnoble-Metal-Based Plasmonic Nanomaterials: Recent Advances and Future Perspectives, Adv. Mater. 30 (2018) 1–24. https://doi.org/10.1002/adma.201704528.

[23] N. Bhatt, M.S. Mehata, A Sustainable Approach to Develop Gold Nanoparticles with Kalanchoe fedtschenkoi and Their Interaction with Protein and Dye: Sensing and Catalytic Probe, Plasmonics. 18 (2023) 845–858. https://doi.org/10.1007/s11468-023-01814-z.

[24] X. Zhou, H. Sun, X. Bai, Two-Dimensional Transition Metal Dichalcogenides: Synthesis, Biomedical Applications and Biosafety Evaluation, Front. Bioeng. Biotechnol. 8 (2020) 1–13. https://doi.org/10.3389/fbioe.2020.00236.

[25] R. Lv, J.A. Robinson, R.E. Schaak, D. Sun, Y. Sun, T.E. Mallouk, M. Terrones, Transition metal dichalcogenides and beyond: Synthesis, properties, and applications of single- and few-layer nanosheets, Acc. Chem. Res. 48 (2015) 56–64. https://doi.org/10.1021/ar5002846.

[26] B. Begines, T. Ortiz, M. Pérez-Aranda, G. Martínez, M. Merinero, F. Argüelles-Arias, A. Alcudia, Polymeric nanoparticles for drug delivery: Recent developments and future prospects, Nanomaterials. 10 (2020) 1–41. https://doi.org/10.3390/nano10071403.

[27] H.K. Kordasht, M. Hasanzadeh, F. Seidi, P.M. Alizadeh, Poly (amino acids) towards sensing: Recent progress and challenges, TrAC - Trends Anal. Chem. 140 (2021) 116279. https://doi.org/10.1016/j.trac.2021.116279.

[28] M.A. Beach, U. Nayanathara, Y. Gao, C. Zhang, Y. Xiong, Y. Wang, G.K. Such, Polymeric Nanoparticles for Drug Delivery, Chem. Rev. 124 (2024) 5505–5616. https://doi.org/10.1021/acs.chemrev.3c00705.

[29] Onteru Sujeevan, Lipid-based nanoparticles and their recent advances, GSC Adv. Res. Rev. 18 (2024) 182–188. https://doi.org/10.30574/gscarr.2024.18.3.0096.

[30] M. Mehta, T.A. Bui, X. Yang, Y. Aksoy, E.M. Goldys, W. Deng, Lipid-Based Nanoparticles for Drug/Gene Delivery: An Overview of the Production Techniques and Difficulties Encountered in Their Industrial Development, ACS Mater. Au. 3 (2023) 600–619. https://doi.org/10.1021/acsmaterialsau.3c00032.

[31] Y. Zheng, J. Orbulescu, X. Ji, F.M. Andreopoulos, S.M. Pham, R.M. Leblanc, Development of fluorescent film sensors for the detection of divalent copper, J. Am. Chem. Soc. 125 (2003) 2680–2686. https://doi.org/10.1021/ja0293610.

[32] A. Puri, K. Loomis, B. Smith, J.H. Lee, A. Yavlovich, E. Heldman, R. Blumenthal, Lipid-based nanoparticles as pharmaceutical drug carriers: From concepts to clinic, Crit. Rev. Ther. Drug Carrier Syst. 26 (2009) 523–580. https://doi.org/10.1615/CritRevTherDrugCarrierSyst.v26.i6.10.

[33] J.N. Tiwari, R.N. Tiwari, K.S. Kim, Zero-dimensional, one-dimensional, two-dimensional and three-dimensional nanostructured materials for advanced electrochemical energy devices, Prog. Mater. Sci. 57 (2012) 724–803. https://doi.org/10.1016/j.pmatsci.2011.08.003.

[34] T. Edvinsson, Optical quantum confinement and photocatalytic properties in two-, one- and zerodimensional nanostructures, R. Soc. Open Sci. 5 (2018). https://doi.org/10.1098/rsos.180387.

[35] A. Kafel, S.N. Turki Al-Rashid, Examining the impact of quantum confinement energy on the optical characteristics of zinc sulfide and gallium nitrate in the ultraviolet spectral range, Chalcogenide Lett. 20 (2023) 423–429. https://doi.org/10.15251/CL.2023.206.423.

[36] C.Y. Hsu, A.M. Rheima, Z. sabri Abbas, M.U. Faryad, M.M. Kadhim, U.S. Altimari, A.H. Dawood, A. dhari jawad al-bayati, Z.T. Abed, R.S. Radhi, A.S. Jaber, S.K. Hachim, F.K. Ali, Z.H. Mahmoud, G. Behzadi pour, E. Kianfar, Nanowires Properties and Applications: A Review Study, South African J. Chem. Eng. 46 (2023) 286–311. https://doi.org/10.1016/j.sajce.2023.08.006.

[37] M. Nasrollahzadeh, S.M. Sajadi, M. Sajjadi, Z. Issaabadi, An Introduction to

Nanotechnology, 1st ed., Elsevier Ltd., 2019. https://doi.org/10.1016/B978-0-12-813586-0.00001-8.

[38] E. Garnett, L. Mai, P. Yang, Introduction: 1D Nanomaterials/Nanowires, Chem. Rev. 119 (2019) 8955–8957. https://doi.org/10.1021/acs.chemrev.9b00423.

[39] Z. Tang, J. Zhang, Y. Zhang, Renaissance of One-Dimensional Nanomaterials, Adv. Funct. Mater. 32 (2022) 1–3. https://doi.org/10.1002/adfm.202113192.

[40] X. Duan, H. Zhang, Introduction: Two-Dimensional Layered Transition Metal Dichalcogenides, Chem. Rev. 124 (2024) 10619–10622. https://doi.org/10.1021/acs.chemrev.4c00586.

[41] A.K. Mia, M. Meyyappan, P.K. Giri, Two-Dimensional Transition Metal Dichalcogenide Based Biosensors: From Fundamentals to Healthcare Applications, Biosensors. 13 (2023) 1–28. https://doi.org/10.3390/bios13020169.

[42] L. Yang, C. Xie, J. Jin, R.N. Ali, C. Feng, P. Liu, B. Xiang, Properties, preparation and applications of low dimensional transition metal dichalcogenides, Nanomaterials. 8 (2018) 1–40. https://doi.org/10.3390/nano8070463.

[43] N. Baig, Two-dimensional nanomaterials: A critical review of recent progress, properties, applications, and future directions, Compos. Part A Appl. Sci. Manuf. 165 (2023) 107362. https://doi.org/10.1016/j.compositesa.2022.107362.

[44] G. Paramasivam, V.V. Palem, T. Sundaram, V. Sundaram, S.C. Kishore, S. Bellucci, Nanomaterials: Synthesis and applications in theranostics, Nanomaterials. 11 (2021). https://doi.org/10.3390/nano11123228.

[45] A.A. Adul-Rasool, D.M. Athair, H.K. Zaidan, A.M. Rheima, Z.T. Al-Sharify, S.H. Mohammed, E. kianfar, 0,1,2,3D nanostructures, types of bulk nanostructured materials, and drug nanocrystals: An overview, Cancer Treat. Res. Commun. 40 (2024) 100834. https://doi.org/10.1016/j.ctarc.2024.100834.

[46] N.H. Al-mutairi, A.H. Mehdi, B.J. Kadhim, Available Online at : https://www.scholarzest.com NANOCOMPOSITES MATERIALS

DEFINITIONS , TYPES AND SOME OF THEIR APPLICATIONS : A REVIEW, 3 (2022) 102–108.

[47] P. Blood, Quantum confinement, Quantum Confin. Laser Devices. (2015) 110–132. https://doi.org/10.1093/acprof:oso/9780199644513.003.0008.

[48] Paras, K. Yadav, P. Kumar, D.R. Teja, S. Chakraborty, M. Chakraborty, S.S. Mohapatra, A. Sahoo, M.M.C. Chou, C. Te Liang, D.R. Hang, A Review on Low-Dimensional Nanomaterials: Nanofabrication, Characterization and Applications, Nanomaterials. 13 (2023) 1–44. https://doi.org/10.3390/nano13010160.

[49] R. Mohan, Quantum Effects and Spectroscopy in Nanoscale Material Analysis, Int. Ref. J. Eng. Sci. 4 (2015) 88–93. https://doi.org/10.9790/5736-0801017075.

[50] A.H.C. Neto, The electronic properties of graphene, 81 (2009). https://doi.org/10.1103/RevModPhys.81.109.

[51] F. Creazzo, Engineering of MoSe2 and WSe2 Monolayers and Heterostructures by DFT-Molecular Dynamics Simulations, ACS Appl. Mater. Interfaces. 17 (2025) 39676–39693. https://doi.org/10.1021/acsami.5c07971.

[52] R.P. Sedhain, G.C. Kaphle, STRUCTURAL AND ELECTRONIC PROPERTIES OF TRANSITION METAL DI-CHALCOGENIDES (MX2) M=(Mo, W) AND X=(S, Se) IN BULK STATE: A FIRST-PRINCIPLES STUDY, J. Inst. Sci. Technol. 22 (2017) 41–50. https://doi.org/10.3126/jist.v22i1.17738.

[53] X. Hu, L. Kou, L. Sun, Stacking orders induced direct band gap in bilayer MoSe2 -WSe2 lateral heterostructures, Sci. Rep. 6 (2016) 1–9. https://doi.org/10.1038/srep31122.

[54] E.D. Hanson, L.M. Lilley, J.D. Cain, S. Hao, E. Palacios, K. Aydin, C. Wolverton, T. Meade, V.P. Dravid, Phase engineering and optical properties of 2D MoSe 2 : Promise and pitfalls, Mater. Chem. Phys. 225 (2019) 219–226. https://doi.org/10.1016/j.matchemphys.2018.11.069.

[55] H. Terrones, F. López-Urías, M. Terrones, Novel hetero-layered materials with tunable direct band gaps by sandwiching different metal disulfides and

diselenides, Sci. Rep. 3 (2013) 1–7. https://doi.org/10.1038/srep01549.

[56] L. Hristova, R. Martínez-Moro, E. Fernández-García, L. Vázquez, M.D. Petit-Domínguez, E. Casero, C. Quintana, M. del Pozo, Optical sensor based on WS2 quantum dots for lamotrigine determination, Enviado. (2025). https://doi.org/10.1021/acsomega.4c09476.

[57] C. Zhu, Y. Huang, F. Xu, P. Gao, B. Ge, J. Chen, H. Zeng, E. Sutter, P. Sutter, L. Sun, Defect-Laden MoSe2 Quantum Dots Made by Turbulent Shear Mixing as Enhanced Electrocatalysts, Small. 13 (2017) 1–7. https://doi.org/10.1002/smll.201700565.

[58] A.M. Ealias, M.P. Saravanakumar, A review on the classification, characterisation, synthesis of nanoparticles and their application, IOP Conf. Ser. Mater. Sci. Eng. 263 (2017). https://doi.org/10.1088/1757-899X/263/3/032019.

[59] A. Biswas, I.S. Bayer, A.S. Biris, T. Wang, E. Dervishi, F. Faupel, Advances in top-down and bottom-up surface nanofabrication: Techniques, applications & future prospects, Adv. Colloid Interface Sci. 170 (2012) 2–27. https://doi.org/10.1016/j.cis.2011.11.001.

[60] A. Lippitz, T. Hübert, XPS investigations of chromium nitride thin films, Surf. Coatings Technol. 200 (2005) 250–253. https://doi.org/10.1016/j.surfcoat.2005.02.091.

[61] N. Baig, I. Kammakakam, W. Falath, I. Kammakakam, Nanomaterials: A review of synthesis methods, properties, recent progress, and challenges, Mater. Adv. 2 (2021) 1821–1871. https://doi.org/10.1039/d0ma00807a.

[62] K.A. Altammar, A review on nanoparticles: characteristics, synthesis, applications, and challenges, Front. Microbiol. 14 (2023) 1–20. https://doi.org/10.3389/fmicb.2023.1155622.

[63] V. Sharma, M.S. Mehata, Synthesis of photoactivated highly fluorescent Mn2+-doped ZnSe quantum dots as effective lead sensor in drinking water, Mater. Res. Bull. 134 (2021) 111121. https://doi.org/10.1016/j.materresbull.2020.111121.

[64] V.K. Singh, H. Mishra, R. Ali, S. Umrao, R. Srivastava, S. Abraham, A. Misra, V.N. Singh, H. Mishra, R.S. Tiwari, A. Srivastava, In Situ

Functionalized Fluorescent WS2-QDs as Sensitive and Selective Probe for Fe3+ and a Detailed Study of Its Fluorescence Quenching, ACS Appl. Nano Mater. 2 (2019) 566–576. https://doi.org/10.1021/acsanm.8b02162.

[65] P. Sharma, M.S. Mehata, Colloidal MoS2 quantum dots based optical sensor for detection of 2,4,6-TNP explosive in an aqueous medium, Opt. Mater. (Amst). 100 (2020) 109646. https://doi.org/10.1016/j.optmat.2019.109646.

[66] H.S. Neira, Ines S., Kolen'ko, Yury V., Lebedev, Oleg I., Tendeloo, Gustaaf Van, Gupta, F.& Y.M. Guitian, An Effective Morphology Control of Hydroxyapatite Crystals via & DESIGN 2009 ND, An Eff. Morphol. Control Hydroxyapatite Cryst. via Hydrothermal Synth. (2009).

[67] Y.X. Gan, A.H. Jayatissa, Z. Yu, X. Chen, M. Li, Hydrothermal Synthesis of Nanomaterials, J. Nanomater. 2020 (2020). https://doi.org/10.1155/2020/8917013.

[68] L. Zhu, D. Shen, K. Hong Luo, Triple-emission nitrogen and boron co-doped carbon quantum dots from lignin: Highly fluorescent sensing platform for detection of hexavalent chromium ions, J. Colloid Interface Sci. 617 (2022) 557–567. https://doi.org/10.1016/j.jcis.2022.03.039.

[69] Y. Wang, Y. Ni, Molybdenum disulfide quantum dots as a photoluminescence sensing platform for 2,4,6-trinitrophenol detection, Anal. Chem. 86 (2014) 7463–7470. https://doi.org/10.1021/ac5012014.

[70] J. Zhang, C. Jing, B. Wang, A Label-Free Fluorescent Sensor Based on Si,N-Codoped Carbon Quantum Dots with Enhanced Sensitivity for the Determination of Cr(VI), Materials (Basel). 15 (2022). https://doi.org/10.3390/ma15051733.

[71] B.D. Cullity, Elements of X-Ray Diffraction, 1956. https://doi.org/10.1088/0031-9112/8/7/008.

[72] L.H. Schwartz, J.B. Cohen, The Nature of Diffraction, in: Diffr. from Mater., Springer Berlin Heidelberg, 1987: pp. 46–76.

[73] C.N. Banwell, Fundamentals of molecular spectroscopy, 2nd Editio, McGraw-Hill, 1972.

[74] H.H. Willard, J.L.L. Merritt, J.A. Dean, J.F.A. Settle, Instrumental methods of analysis, 7th Editio, 1988.

[75] S.M. Bhagyaraj, O.S. Oluwafemi, N. Kalarikkal, S. Thomas, Characterization of nanomaterials: Advances and key technologies, Elsevier, 2018.

[76] G. Wypych, ed., Handbook of UV Degradation and Stabilization, ChemTec Publishing, 2015.

[77] J.R. Lakowicz, Principles of fluorescence spectroscopy, 2006. https://doi.org/10.1007/978-0-387-46312-4.

[78] C.R. Ronda, Luminescence: from theory to applications, Wiley-VCH Verlag GmbH & Co. KGaA, 2008.

[79] K. Wakabayashi, Y. Yamaguchi, T. Sekiya, S. Kurita, Time-resolved luminescence spectra in colorless anatase TiO2 single crystal, J. Lumin. 112 (2005) 50–53.

[80] R. Gatensby, N. McEvoy, K. Lee, T. Hallam, N.C. Berner, E. Rezvani, S. Winters, M. O'Brien, G.S. Duesberg, Controlled synthesis of transition metal dichalcogenide thin films for electronic applications, Appl. Surf. Sci. 297 (2014) 139–146. https://doi.org/10.1016/j.apsusc.2014.01.103.

[81] M.C.F. Costa, S.G. Echeverrigaray, D. V Andreeva, K.S. Novoselov, A.H.C. Neto, Two-Dimensional Quantum Dots : From Photoluminescence to Biomedical Applications, (2022) 578–602.

[82] J. Yao, M. Yang, Y. Duan, Chemistry , Biology , and Medicine of Fluorescent Nanomaterials and Related Systems : New Insights into Biosensing , Bioimaging , Genomics , Diagnostics , and Therapy, (2014).

[83] E. Chikukwa, E. Meyer, J. Mbese, N. Zingwe, Colloidal synthesis and characterization of molybdenum chalcogenide quantum dots using a two-source precursor pathway for photovoltaic applications, Molecules. 26 (2021). https://doi.org/10.3390/molecules26144191.

[84] X. Zhao, D. He, Y. Wang, C. Fu, Facile fabrication of tungsten disulfide quantum dots (WS2 QDs) as effective probes for fluorescence detection of dopamine (DA), Mater. Chem. Phys. 207 (2018) 130–134. https://doi.org/10.1016/j.matchemphys.2017.12.045.

[85] W. Dai, H. Dong, B. Fugetsu, Y. Cao, H. Lu, X. Ma, X. Zhang, Tunable Fabrication of Molybdenum Disulfide Quantum Dots for Intracellular MicroRNA Detection and Multiphoton Bioimaging, Small. 11 (2015) 4158–

4164. https://doi.org/10.1002/smll.201500208.

[86] R. Liu, H. Li, W. Kong, J. Liu, Y. Liu, C. Tong, X. Zhang, Z. Kang, Ultra-sensitive and selective Hg2+ detection based on fluorescent carbon dots, Mater. Res. Bull. 48 (2013) 2529–2534. https://doi.org/10.1016/j.materresbull.2013.03.015.

[87] V. Sharma, M.S. Mehata, Synthesis of photoactivated highly fluorescent Mn2+-doped ZnSe quantum dots as effective lead sensor in drinking water, Mater. Res. Bull. 134 (2021) 111121. https://doi.org/10.1016/j.materresbull.2020.111121.

[88] P. Sharma, M.S. Mehata, Rapid sensing of lead metal ions in an aqueous medium by MoS2quantum dots fluorescence turn-off, Mater. Res. Bull. 131 (2020) 110978. https://doi.org/10.1016/j.materresbull.2020.110978.

[89] S.O. Souza, Methods for Intracellular Delivery of Quantum Dots, 2021. https://doi.org/10.1007/s41061-020-00313-7.

[90] L. Haghighi, N. Haghnazari, C. Karami, Tungsten disulfide quantum dots (WS2 QDs) as a fluorescence probe for detection of dopamine (DA), J. Mater. Sci. Mater. Electron. 32 (2021) 28042–28050. https://doi.org/10.1007/s10854-021-07098-5.

[91] Y. Yan, C. Zhang, W. Gu, C. Ding, X. Li, Y. Xian, Facile Synthesis of Water-Soluble WS 2 Quantum Dots for Turn-On Fluorescent Measurement of Lipoic Acid, (2016). https://doi.org/10.1021/acs.jpcc.6b01868.

[92] L. Wirtz, Phonons in single-layer and few-layer MoS 2 and WS 2, Phys. Rev. B. 155413 (2011) 1–8. https://doi.org/10.1103/PhysRevB.84.155413.

[93] T. Sun, Y. Su, M. Sun, Y. Lv, Homologous chemiluminescence resonance energy transfer on the interface of WS 2 quantum dots for monitoring photocatalytic H 2 O 2 evaluation, 168 (2021). https://doi.org/10.1016/j.microc.2021.106344.

[94] M.H. Irani-nezhad, A. Khataee, J. Hassanzadeh, Y. Orooji, A Chemiluminescent Method for the Detection of H 2 O 2 and Glucose Based on Intrinsic Peroxidase-Like, (2019) 1–14. https://doi.org/10.3390/molecules24040689.

[95] I. Martin-Litas, P. Vinatier, A. Levasseur, J.C. Dupin, D. Gonbeau, F. Weill,

Characterisation of r.f. sputtered tungsten disulfide and oxysulfide thin films, Thin Solid Films. 416 (2002) 1–9. https://doi.org/10.1016/S0040-6090(02)00717-4.

[96] M.J. Kim, S.J. Jeon, T.W. Kang, J.M. Ju, D. Bin Yim, H.I. Kim, J.H. Park, J.H. Kim, 2H-WS2 Quantum Dots Produced by Modulating the Dimension and Phase of 1T-Nanosheets for Antibody-Free Optical Sensing of Neurotransmitters, ACS Appl. Mater. Interfaces. 9 (2017) 12316–12323. https://doi.org/10.1021/acsami.7b01644.

[97] C.Y. Luan, S. Xie, C. Ma, S. Wang, Y. Kong, M. Xu, Elucidation of luminescent mechanisms of size-controllable MoSe2 quantum dots, Appl. Phys. Lett. 111 (2017). https://doi.org/10.1063/1.4999444.

[98] G.K. Mani, J.B.B. Rayappan, ZnO nanoarchitectures: Ultrahigh sensitive room temperature acetaldehyde sensor, Sensors Actuators, B Chem. 223 (2016) 343–351. https://doi.org/10.1016/j.snb.2015.09.103.

[99] MINIREVIEW Iron and Oxidative Stress in Bacteria 1, Arch. Biochem. Biophys. 373 (2000) 1–6.

[100] W. Chen, S. Cai, Q.Q. Ren, W. Wen, Y. Di Zhao, Recent advances in electrochemical sensing for hydrogen peroxide: A review, Analyst. 137 (2012) 49–58. https://doi.org/10.1039/c1an15738h.

[101] C. Lv, W. Di, Z. Liu, K. Zheng, W. Qin, Luminescent CePO4:Tb colloids for H2O2 and glucose sensing, Analyst. 139 (2014) 4547–4555. https://doi.org/10.1039/c4an00952e.

[102] S.N.A. Shah, Y. Zheng, H. Li, J.M. Lin, Chemiluminescence character of ZnS quantum dots with bisulphite-hydrogen peroxide system in acidic medium, J. Phys. Chem. C. 120 (2016) 9308–9316. https://doi.org/10.1021/acs.jpcc.6b01925.

[103] D.S. Moore, Instrumentation for trace detection of high explosives, Rev. Sci. Instrum. 75 (2004) 2499–2512. https://doi.org/10.1063/1.1771493.

[104] Z. Li, Y. Jiang, C. Liu, Z. Wang, Z. Cao, Y. Yuan, M. Li, Y. Wang, D. Fang, Z. Guo, D. Wang, G. Zhang, J. Jiang, Emerging investigator series: dispersed transition metals on a nitrogen-doped carbon nanoframework for environmental hydrogen peroxide detection, Environ. Sci. Nano. 5 (2018)

1834–1843. https://doi.org/10.1039/c8en00498f.

[105] V. Nguyen, Q. Dong, L. Yan, N. Zhao, P.H. Le, Facile synthesis of photoluminescent MoS2 and WS2 quantum dots with strong surface-state emission, J. Lumin. 214 (2019) 116554. https://doi.org/10.1016/j.jlumin.2019.116554.

[106] A. Bayat, E. Saievar-Iranizad, Synthesis of blue photoluminescent WS2 quantum dots via ultrasonic cavitation, J. Lumin. 185 (2017) 236–240. https://doi.org/10.1016/j.jlumin.2017.01.024.

[107] X. Ren, L. Pang, Y. Zhang, X. Ren, H. Fan, S. Liu, One-step hydrothermal synthesis of monolayer MoS2 quantum dots for highly efficient electrocatalytic hydrogen evolution, J. Mater. Chem. A. 3 (2015) 10693–10697. https://doi.org/10.1039/c5ta02198g.

[108] S. Xu, D. Li, P. Wu, One-pot, facile, and versatile synthesis of monolayer MoS2 /WS2 quantum dots as bioimaging probes and efficient electrocatalysts for hydrogen evolution reaction, Adv. Funct. Mater. 25 (2015) 1127–1136. https://doi.org/10.1002/adfm.201403863.

[109] J. Kim, S. Kwon, D.H. Cho, B. Kang, H. Kwon, Y. Kim, S.O. Park, G.Y. Jung, E. Shin, W.G. Kim, H. Lee, G.H. Ryu, M. Choi, T.H. Kim, J. Oh, S. Park, S.K. Kwak, S.W. Yoon, D. Byun, Z. Lee, C. Lee, Direct exfoliation and dispersion of two-dimensional materials in pure water via temperature control, Nat. Commun. 6 (2015) 1–9. https://doi.org/10.1038/ncomms9294.

[110] V. Sharma, M.S. Mehata, Rapid optical sensor for recognition of explosive 2,4,6-TNP traces in water through fluorescent ZnSe quantum dots, Spectrochim. Acta - Part A Mol. Biomol. Spectrosc. 260 (2021) 119937. https://doi.org/10.1016/j.saa.2021.119937.

[111] M. Hamada, K. Okoshi, S. Rana, K. Awasthi, T. Iimori, E.W.G. Diau, N. Ohta, Inhomogeneous Photoluminescence Characteristic in Carbon Nanodots and Electrophotoluminescence Measurements, J. Phys. Chem. C. 122 (2018) 6463–6474. https://doi.org/10.1021/acs.jpcc.8b00841.

[112] H. Dong, S. Tang, Y. Hao, H. Yu, W. Dai, G. Zhao, Y. Cao, H. Lu, X. Zhang, H. Ju, Fluorescent MoS2 Quantum Dots: Ultrasonic Preparation, Up-Conversion and Down-Conversion Bioimaging, and Photodynamic Therapy,

ACS Appl. Mater. Interfaces. 8 (2016) 3107–3114. https://doi.org/10.1021/acsami.5b10459.

[113] S.P. Caigas, S. Reina, M. Santiago, T. Lin, C.J. Lin, C. Yuan, J. Shen, T. Lin, Origins of excitation-wavelength-dependent photoluminescence in WS2 quantum dots Origins of excitation-wavelength-dependent photoluminescence in WS 2 quantum dots, 092106 (2018) 1–5. https://doi.org/10.1063/1.5009638.

[114] R.A. Velapoldi, H.H. Tønnesen, Corrected emission spectra and quantum yields for a series of fluorescent compounds in the visible spectral region, J. Fluoresc. 14 (2004) 465–472. https://doi.org/10.1023/B:JOFL.0000031828.96368.c1.

[115] M.S. Mehata, Y. Yang, K. Han, Probing charge-transfer and short-lived triplet states of a biosensitive molecule, 2,6-ANS: Transient absorption and time-resolved spectroscopy, ACS Omega. 2 (2017) 6782–6785. https://doi.org/10.1021/acsomega.7b00921.

[116] Z. Pan, B. Zeng, H. Lin, J. Teng, H. Zhang, H. Hong, M. Zhang, Fundamental thermodynamic mechanisms of membrane fouling caused by transparent exopolymer particles (TEP) in water treatment, Sci. Total Environ. 820 (2022) 153252. https://doi.org/10.1016/j.scitotenv.2022.153252.

[117] K. Pillai, S. Alwarappan, M.O. Valappil, A. Anil, M. Shaijumon, V.K. Pillai, quantum dots COMMUNICATION A Single step electrochemical synthesis of luminescent WS 2 quantum dots, (n.d.). https://doi.org/10.1002/chem.201701277.

[118] K. Wang, Q. Liu, X.Y. Wu, Q.M. Guan, H.N. Li, Graphene enhanced electrochemiluminescence of CdS nanocrystal for H 2O2 sensing, Talanta. 82 (2010) 372–376. https://doi.org/10.1016/j.talanta.2010.04.054.

[119] K.M. Kubachka, J.A. Caruso, Limit of Detection Validation of Chromatographic Meth- ods of Analysis : Application for Drugs That Derived From Herbs A practical guide to validation and ver- ification of analytical methods in the clinical laboratory, (2016) 3–9.

[120] T. Sun, Y. Su, M. Sun, Y. Lv, Homologous chemiluminescence resonance energy transfer on the interface of WS2 quantum dots for monitoring photocatalytic H2O2 evaluation, Microchem. J. 168 (2021).

https://doi.org/10.1016/j.microc.2021.106344.

[121] N. Pallikkarathodi Mani, J. Cyriac, Hydrothermal synthesis of WS2quantum dots and their application as a fluorescence sensor for the selective detection of 2,4,6-trinitrophenol, New J. Chem. 44 (2020) 10840–10848. https://doi.org/10.1039/c9nj06159b.

[122] Y. Jiao, J. Li, J. Xiang, Z. Chen, Tungsten disulfide nanosheets-based colorimetric assay for glucose sensing, Spectrochim. Acta - Part A Mol. Biomol. Spectrosc. 242 (2020) 118706. https://doi.org/10.1016/j.saa.2020.118706.

[123] F. Zou, W. Zhou, W. Guan, C. Lu, B.Z. Tang, Screening of Photosensitizers by Chemiluminescence Monitoring of Formation Dynamics of Singlet Oxygen during Photodynamic Therapy, Anal. Chem. 88 (2016) 9707–9713. https://doi.org/10.1021/acs.analchem.6b02611.

[124] K. Sato, Green oxidation with aqueous hydrogen peroxide, AIST Today (International Ed. (2004) 32. https://doi.org/10.5363/tits.14.3_60.

[125] M.S. Mehata, S. Biswas, Synthesis of fluorescent graphene quantum dots from graphene oxide and their application in fabrication of GQDs@AgNPs nanohybrids and sensing of H2O2, Ceram. Int. 47 (2021) 19063–19072. https://doi.org/10.1016/j.ceramint.2021.03.252.

[126] Ruby, Aryan, M.S. Mehata, Surface plasmon resonance allied applications of silver nanoflowers synthesized from: Breynia vitis-idaea leaf extract, Dalt. Trans. 51 (2022) 2726–2736. https://doi.org/10.1039/d1dt03592d.

[127] F. Jiang, R. Yue, Y. Du, J. Xu, P. Yang, A one-pot “green” synthesis of Pd-decorated PEDOT nanospheres for nonenzymatic hydrogen peroxide sensing, Biosens. Bioelectron. 44 (2013) 127–131. https://doi.org/10.1016/j.bios.2013.01.003.

[128] Y. Ye, T. Kong, X. Yu, Y. Wu, K. Zhang, X. Wang, Enhanced nonenzymatic hydrogen peroxide sensing with reduced graphene oxide/ferroferric oxide nanocomposites, Talanta. 89 (2012) 417–421. https://doi.org/10.1016/j.talanta.2011.12.054.

[129] Y. Liu, D. Wang, L. Xu, H. Hou, T. You, A novel and simple route to prepare a Pt nanoparticle-loaded carbon nanofiber electrode for hydrogen peroxide

sensing, Biosens. Bioelectron. 26 (2011) 4585–4590. https://doi.org/10.1016/j.bios.2011.05.034.

[130] Y. Li, Q. Lu, S. Wu, L. Wang, X. Shi, Hydrogen peroxide sensing using ultrathin platinum-coated gold nanoparticles with core@shell structure, Biosens. Bioelectron. 41 (2013) 576–581. https://doi.org/10.1016/j.bios.2012.09.027.

[131] Y. Jiang, B. Zheng, J. Du, G. Liu, Y. Guo, D. Xiao, Electrophoresis deposition of Ag nanoparticles on TiO2 nanotube arrays electrode for hydrogen peroxide sensing, Talanta. 112 (2013) 129–135. https://doi.org/10.1016/j.talanta.2013.03.015.

[132] M.R. Guascito, D. Chirizzi, C. Malitesta, T. Siciliano, A. Tepore, Te oxide nanowires as advanced materials for amperometric nonenzymatic hydrogen peroxide sensing, Talanta. 115 (2013) 863–869. https://doi.org/10.1016/j.talanta.2013.06.032.

[133] S. Yan, B. Wang, Z. Wang, D. Hu, X. Xu, J. Wang, Y. Shi, Supercritical carbon dioxide-assisted rapid synthesis of few-layer black phosphorus for hydrogen peroxide sensing, Biosens. Bioelectron. 80 (2016) 34–38. https://doi.org/10.1016/j.bios.2016.01.043.

[134] W. Xu, J. Liu, M. Wang, L. Chen, X. Wang, C. Hu, Direct growth of MnOOH nanorod arrays on a carbon cloth for high-performance non-enzymatic hydrogen peroxide sensing, Anal. Chim. Acta. 913 (2016) 128–136. https://doi.org/10.1016/j.aca.2016.01.055.

[135] A.J. Wang, Q.C. Liao, J.J. Feng, Z.Z. Yan, J.R. Chen, In situ synthesis of polydopamine-Ag hollow microspheres for hydrogen peroxide sensing, Electrochim. Acta. 61 (2012) 31–35. https://doi.org/10.1016/j.electacta.2011.11.063.

[136] S. Palanisamy, C. Karuppiah, S.M. Chen, R. Emmanuel, P. Muthukrishnan, P. Prakash, Direct electrochemistry of myoglobin at silver nanoparticles/myoglobin biocomposite: Application for hydrogen peroxide sensing, Sensors Actuators, B Chem. 202 (2014) 177–184. https://doi.org/10.1016/j.snb.2014.05.069.

[137] S. Kumar, N. Venkatramaiah, S. Patil, Fluoranthene based derivatives for

detection of trace explosive nitroaromatics, J. Phys. Chem. C. 117 (2013) 7236–7245. https://doi.org/10.1021/jp3121148.

[138] P. Sharma, M.S. Mehata, Colloidal MoS2 quantum dots based optical sensor for detection of 2,4,6-TNP explosive in an aqueous medium, Opt. Mater. (Amst). 100 (2020) 109646. https://doi.org/10.1016/j.optmat.2019.109646.

[139] D.K. Singha, S. Bhattacharya, P. Majee, S.K. Mondal, M. Kumar, P. Mahata, Optical detection of submicromolar levels of nitro explosives by a submicron sized metal-organic phosphor material, J. Mater. Chem. A. 2 (2014) 20908–20915. https://doi.org/10.1039/c4ta05014b.

[140] M. Ahmed, S. Hameed, A. Ihsan, M.M. Naseer, Fluorescent thiazol-substituted pyrazoline nanoparticles for sensitive and highly selective sensing of explosive 2,4,6-trinitrophenol in aqueous medium, Sensors Actuators, B Chem. 248 (2017) 57–62. https://doi.org/10.1016/j.snb.2017.03.125.

[141] X. Zhang, L. Liu, W. Zhang, L. Na, R. Hua, Detection of 2,4,6-trinitrophenol based on f–f transition of Eu2+, J. Rare Earths. 39 (2021) 952–958. https://doi.org/10.1016/j.jre.2020.06.016.

[142] Ö.K. Koç, A. Üzer, R. Apak, High Quantum Yield Nitrogen-Doped Carbon Quantum Dot-Based Fluorescent Probes for Selective Sensing of 2,4,6-Trinitrotoluene, ACS Appl. Nano Mater. 5 (2022) 5868–5881. https://doi.org/10.1021/acsanm.2c00717.

[143] V. Kumar, S.K. Saini, N. Choudhury, A. Kumar, B. Maiti, P. De, M. Kumar, S. Satapathi, Highly Sensitive Detection of Nitro Compounds Using a Fluorescent Copolymer-Based FRET System, ACS Appl. Polym. Mater. 3 (2021) 4017–4026. https://doi.org/10.1021/acsapm.1c00540.

[144] S. Wang, X. Wang, K. Ning, G. Xiang, Fluorescent Molybdenum Disulfide Quantum Dots for Sensitive Detecting Curcumin in Food Samples through FRET Mechanism, J. Fluoresc. (2024). https://doi.org/10.1007/s10895-024-03720-x.

[145] K. Murugan, V.K. Jothi, A. Rajaram, A. Natarajan, Novel Metal-Free Fluorescent Sensor Based on Molecularly Imprinted Polymer N-CDs@MIP for Highly Selective Detection of TNP, ACS Omega. 7 (2022) 1368–1379. https://doi.org/10.1021/acsomega.1c05985.

[146] L. Zhang, K. Shao, Y. Zhong, L. Guo, J. Ge, Z. Lu, D. Wang, Molybdenum disulfide quantum dots for rapid fluorescence detection of glutathione and ascorbic acid, Spectrochim. Acta - Part A Mol. Biomol. Spectrosc. 326 (2025) 125189. https://doi.org/10.1016/j.saa.2024.125189.

[147] Y. Zhong, L. Guo, Y. Zou, Y. Chen, Z. Lu, D. Wang, Rapid and ratiometric fluorescent detection of hypochlorite by glutathione functionalized molybdenum disulfide quantum dots, Spectrochim. Acta - Part A Mol. Biomol. Spectrosc. 295 (2023) 122649. https://doi.org/10.1016/j.saa.2023.122649.

[148] N. Jiang, G. Li, W. Che, D. Zhu, Z. Su, M.R. Bryce, Polyurethane derivatives for highly sensitive and selective fluorescence detection of 2,4,6-trinitrophenol (TNP), J. Mater. Chem. C. 6 (2018) 11287–11291. https://doi.org/10.1039/c8tc04250k.

[149] K. Shao, L. Guo, Y. Zhong, L. Zhang, Z. Lu, D. Wang, Carbon Quantum Dots for Rapid and Ratiometric Fluorescence Determination of Hypochlorite, ACS Appl. Nano Mater. 7 (2024) 8645–8654. https://doi.org/10.1021/acsanm.3c06131.

[150] V. Saini, A. Gupta, K. Rangan, B. Khungar, A selective turn-off fluorescence detection of nitroexplosive 2,4,6-trinitrophenol by pyridinium-based chemosensor in pure aqueous medium, Dye. Pigment. 180 (2020) 108447. https://doi.org/10.1016/j.dyepig.2020.108447.

[151] S.K. Balasingam, J.S. Lee, Y. Jun, Few-layered MoSe2 nanosheets as an advanced electrode material for supercapacitors, Dalt. Trans. 44 (2015) 15491–15498. https://doi.org/10.1039/c5dt01985k.

[152] C.L. Manzanares Palenzuela, J. Luxa, Z. Sofer, M. Pumera, MoSe2 Dispersed in Stabilizing Surfactant Media: Effect of the Surfactant Type and Concentration on Electron Transfer and Catalytic Properties, ACS Appl. Mater. Interfaces. 10 (2018) 17820–17826. https://doi.org/10.1021/acsami.7b19744.

[153] A. Eftekhari, Molybdenum diselenide (MoSe2) for energy storage, catalysis, and optoelectronics, Appl. Mater. Today. 8 (2017) 1–17. https://doi.org/10.1016/j.apmt.2017.01.006.

[154] H. Lee, J. Ahn, S. Im, J. Kim, W. Choi, High-Responsivity Multilayer MoSe2 Phototransistors with Fast Response Time, Sci. Rep. 8 (2018) 1–7. https://doi.org/10.1038/s41598-018-29942-1.

[155] W. Guo, Y. Chen, L. Wang, J. Xu, D. Zeng, D.L. Peng, Colloidal synthesis of MoSe2 nanonetworks and nanoflowers with efficient electrocatalytic hydrogen-evolution activity, Electrochim. Acta. 231 (2017) 69–76. https://doi.org/10.1016/j.electacta.2017.02.048.

[156] X. Zhou, J. Jiang, T. Ding, J. Zhang, B. Pan, J. Zuo, Q. Yang, Fast colloidal synthesis of scalable Mo-rich hierarchical ultrathin MoSe2-xnanosheets for high-performance hydrogen evolution, Nanoscale. 6 (2014) 11046–11051. https://doi.org/10.1039/c4nr02716g.

[157] N. Dhenadhayalan, T.W. Lin, H.L. Lee, K.C. Lin, Multisensing Capability of MoSe2 Quantum Dots by Tuning Surface Functional Groups, ACS Appl. Nano Mater. 1 (2018) 3453–3463. https://doi.org/10.1021/acsanm.8b00634.

[158] H. Tang, K. Dou, C.C. Kaun, Q. Kuang, S. Yang, MoSe2 nanosheets and their graphene hybrids: Synthesis, characterization and hydrogen evolution reaction studies, J. Mater. Chem. A. 2 (2014) 360–364. https://doi.org/10.1039/c3ta13584e.

[159] M. Bougouma, A. Batan, B. Guel, T. Segato, J.B. Legma, F. Reniers, M.P. Delplancke-Ogletree, C. Buess-Herman, T. Doneux, Growth and characterization of large, high quality MoSe2 single crystals, J. Cryst. Growth. 363 (2013) 122–127. https://doi.org/10.1016/j.jcrysgro.2012.10.026.

[160] Y. Zhong, L. Guo, Y. Zou, J. Ge, Y. Chen, Z. Lu, D. Wang, Cys-Functionalized MoS2 Quantum Dots and Calcium Ion for Ratiometric Fluorescence Probes for Doxycycline, ACS Appl. Nano Mater. 6 (2023) 22355–22362. https://doi.org/10.1021/acsanm.3c04589.

[161] M.D. Sharma, C. Mahala, M. Basu, Nanosheets of MoSe2@M (M = Pd and Rh) function as widespread pH tolerable hydrogen evolution catalyst, J. Colloid Interface Sci. 534 (2019) 131–141. https://doi.org/10.1016/j.jcis.2018.09.018.

[162] M.S. Mehata, M.K. Singh, K. Awasthi, P. Sharma, S. Rana, N. Ohta, Temperature-Dependent Electric Field-Induced Optical Transitions of 2D

Molybdenum Disulfide (MoS2) Thin Films: Temperature-Dependent Electroabsorption and Absorption, J. Phys. Chem. C. 125 (2021) 26566–26574. https://doi.org/10.1021/acs.jpcc.1c06706.

[163] M.K. Singh, M.S. Mehata, Phase-dependent optical and photocatalytic performance of synthesized titanium dioxide (TiO2) nanoparticles, Optik (Stuttg). 193 (2019) 163011. https://doi.org/10.1016/j.ijleo.2019.163011.

[164] R. Khalfi, D. Talantikite-Touati, A. Tounsi, A. Souici, F.A. Merzeg, A. Azizi, Effect of manganese doping on the structural, morphological and optical properties of zinc selenide thin films prepared by chemical bath deposition method, Appl. Phys. A Mater. Sci. Process. 129 (2023) 1–15. https://doi.org/10.1007/s00339-023-06515-2.

[165] F. Ansari, A. Sobhani, M. Salavati-Niasari, Simple sol-gel synthesis and characterization of new CoTiO3/CoFe2O4 nanocomposite by using liquid glucose, maltose and starch as fuel, capping and reducing agents, J. Colloid Interface Sci. 514 (2018) 723–732. https://doi.org/10.1016/j.jcis.2017.12.083.

[166] W. Lai, J. Guo, N. Zheng, Y. Nie, S. Ye, D. Tang, Selective determination of 2,4,6-trinitrophenol by using a novel carbon nanoparticles as a fluorescent probe in real sample, Anal. Bioanal. Chem. 412 (2020) 3083–3090. https://doi.org/10.1007/s00216-020-02558-z.

[167] J. Yao, Z. Zhuang, H. Yao, R. Shi, C. Chang, J. Zhou, Z. Zhao, Tetraphenylethene-based polymeric fluorescent probes for 2,4,6-trinitrophenol detection and specific lysosome labelling, Dye. Pigment. 182 (2020) 108588. https://doi.org/10.1016/j.dyepig.2020.108588.

[168] B. Chen, S. Chai, J. Liu, C. Liu, Y. Li, J. He, Z. Yu, T. Yang, C. Feng, C. Huang, 2,4,6-Trinitrophenol detection by a new portable sensing gadget using carbon dots as a fluorescent probe, Anal. Bioanal. Chem. 411 (2019) 2291–2300. https://doi.org/10.1007/s00216-019-01670-z.

[169] S. Liu, F. Shi, L. Chen, X. Su, Bovine serum albumin coated CuInS2 quantum dots as a near-infrared fluorescence probe for 2,4,6-trinitrophenol detection, Talanta. 116 (2013) 870–875. https://doi.org/10.1016/j.talanta.2013.07.073.

[170] K. Wang, X. Wang, X. Liu, E. Li, R. Zhao, S. Yang, Facile synthesis of dual emission carbon dots for the ratiometric fluorescent detection of 2,4,6-

trinitrophenol and cell imaging, J. Mol. Struct. 1263 (2022) 133167. https://doi.org/10.1016/j.molstruc.2022.133167.

[171] S. Kadian, G. Manik, A highly sensitive and selective detection of picric acid using fluorescent sulfur-doped graphene quantum dots, Luminescence. 35 (2020) 763–772. https://doi.org/10.1002/bio.3782.

[172] M.P. Sk, A. Chattopadhyay, Induction coil heater prepared highly fluorescent carbon dots as invisible ink and explosive sensor, RSC Adv. 4 (2014) 31994–31999. https://doi.org/10.1039/c4ra04264f.

[173] Y.Z. Fan, Y. Zhang, N. Li, S.G. Liu, T. Liu, N.B. Li, H.Q. Luo, A facile synthesis of water-soluble carbon dots as a label-free fluorescent probe for rapid, selective and sensitive detection of picric acid, Sensors Actuators, B Chem. 240 (2017) 949–955. https://doi.org/10.1016/j.snb.2016.09.063.

[174] B. Bin Chen, Z.X. Liu, H.Y. Zou, C.Z. Huang, Highly selective detection of 2,4,6-trinitrophenol by using newly developed terbium-doped blue carbon dots, Analyst. 141 (2016) 2676–2681. https://doi.org/10.1039/c5an02569a.

[175] K. Shanmugaraj, S.A. John, Inner filter effect based selective detection of picric acid in aqueous solution using green luminescent copper nanoclusters, New J. Chem. 42 (2018) 7223–7229. https://doi.org/10.1039/c8nj00789f.

[176] S. Xing, Q. Bing, H. Qi, J. Liu, T. Bai, G. Li, Z. Shi, S. Feng, R. Xu, Rational Design and Functionalization of a Zinc Metal-Organic Framework for Highly Selective Detection of 2,4,6-Trinitrophenol, ACS Appl. Mater. Interfaces. 9 (2017) 23828–23835. https://doi.org/10.1021/acsami.7b06482.

[177] M. Rong, L. Lin, X. Song, T. Zhao, Y. Zhong, J. Yan, Y. Wang, X. Chen, A label-free fluorescence sensing approach for selective and sensitive detection of 2,4,6-trinitrophenol (TNP) in aqueous solution using graphitic carbon nitride nanosheets, Anal. Chem. 87 (2015) 1288–1296. https://doi.org/10.1021/ac5039913.

[178] M. Kaur, S.K. Mehta, S.K. Kansal, Nitrogen doped graphene quantum dots: Efficient fluorescent chemosensor for the selective and sensitive detection of 2,4,6-trinitrophenol, Sensors Actuators, B Chem. 245 (2017) 938–945. https://doi.org/10.1016/j.snb.2017.02.026.

[179] H.K. Sadhanala, K.K. Nanda, Boron and nitrogen Co-doped carbon

nanoparticles as photoluminescent probes for selective and sensitive detection of picric acid, J. Phys. Chem. C. 119 (2015) 13138–13143. https://doi.org/10.1021/acs.jpcc.5b04140.

[180] Aneesha, N. Ohta, M.S. Mehata, In situ synthesis of WS2 QDs for sensing of H2O2: Quenching and recovery of absorption and photoluminescence, Mater. Today Commun. 34 (2023) 105013. https://doi.org/10.1016/j.mtcomm.2022.105013.

[181] M.Q. Xue, Controllable synthesis and properties of MoSe2 nanostructures, Chalcogenide Lett. 13 (2016) 73–78.

[182] V.K. Singh, H. Mishra, R. Ali, S. Umrao, R. Srivastava, Supporting Information In Situ Functionalized Fluorescent WS 2 -QDs as Sensitive and Selective Probe for Fe 3 + and a Detailed Study of Its Fluorescence Quenching, (n.d.) 1–7.

[183] M. Shellaiah, T. Simon, N. Thirumalaivasan, K.W. Sun, F.H. Ko, S.P. Wu, Cysteamine-capped gold-copper nanoclusters for fluorometric determination and imaging of chromium(VI) and dopamine, Microchim. Acta. 186 (2019). https://doi.org/10.1007/s00604-019-3974-8.

[184] J. Shen, H. Gu, Z. He, W. Lin, Wattle-Bark-Tannin-Derived Carbon Quantum Dots as Multi-Functional Nanomaterials for Intelligent Detection of Cr6+Ions, Bio-Imaging, and Fluorescent Ink Applications, Ind. Eng. Chem. Res. 62 (2023) 3622–3634. https://doi.org/10.1021/acs.iecr.2c04348.

[185] S. Shukla, M.S. Mehata, Selective picomolar detection of carcinogenic chromium ions using silver nanoparticles capped via biomolecules from flowers of Plumeria obtusa, J. Mol. Liq. 380 (2023) 121705. https://doi.org/10.1016/j.molliq.2023.121705.

[186] M. Shellaiah, K.W. Sun, K. Anandan, M. Bhushan, A. Murugan, W.T. Li, Biocompatible rhodamine functionalized nanodiamond for heavy metal ions detection: Demonstration by paper strips, cellular imaging, and real water investigations, Diam. Relat. Mater. 158 (2025) 1–10. https://doi.org/10.1016/j.diamond.2025.112698.

[187] P. Zandi, A. Phani, S. Kim, Detecting Cr6+ at ≈100 pM Concentration with Fluorescence Enhancement Signatures in a Novel Eco-Fluorophore: Matching

WHO's 96 pM Recommended Standard for Drinking Water, Adv. Mater. 37 (2025). https://doi.org/10.1002/adma.202504142.

[188] V.A. Yolshina, L.A. Yolshina, V.I. Pryakhina, SEM and XPS Study of Cr6+ Removal from Wastewater via Reduction and Adsorption by Hierarchically Structured Carbon Composite in Neutral Media, J. Inorg. Organomet. Polym. Mater. 31 (2021) 3624–3635. https://doi.org/10.1007/s10904-021-02003-3.

[189] A. Shawky, R.M. Mohamed, N. Alahmadi, Z.I. Zaki, Enhanced photocatalytic reduction of hexavalent chromium ions over S-Scheme based 2D MoS2-supported TiO2 heterojunctions under visible light, Colloids Surfaces A Physicochem. Eng. Asp. 641 (2022) 128564. https://doi.org/10.1016/j.colsurfa.2022.128564.

[190] A. Ghosh, B. Boro, S.S. Chowdhury, R. Ranjan, N. Dasgupta, S. Ranjan, Ultrasensitive and Selective Detection of Chromium(VI) Using Biowaste Derived Fluorescent Nanoprobes of Hydrothermally Synthesized Carbon-Dots, ChemistrySelect. 9 (2024) 1–9. https://doi.org/10.1002/slct.202404198.

[191] M. Grabarczyk, L. Kaczmarek, M. Korolczuk, Determination of Cr(VI) by catalytic adsorptive stripping voltammetry with application of nitrilotriacetic acid as a masking agent, Electroanalysis. 16 (2004) 1503–1507. https://doi.org/10.1002/elan.200402977.

[192] S.M. Saleh, R. Ali, A. Algreiby, B. Alfeneekh, I.A.I. Ali, A novel organic chromo-fluorogenic optical sensor for detecting chromium ions, Heliyon. 10 (2024) e37480. https://doi.org/10.1016/j.heliyon.2024.e37480.

[193] O. Domínguez-Renedo, L. Ruiz-Espelt, N. García-Astorgano, M.J. Arcos-Martínez, Electrochemical determination of chromium(VI) using metallic nanoparticle-modified carbon screen-printed electrodes, Talanta. 76 (2008) 854–858. https://doi.org/10.1016/j.talanta.2008.04.036.

[194] DPV 65.pdf, (n.d.).

[195] M.E. Sánchez-Fernández, L.M. Cubillana-Aguilera, J.M. Palacios-Santander, I. Naranjo-Rodríguez, J.L. Hidalgo-Hidalgo De Cisneros, An oxidative procedure for the electrochemical determination of chromium(VI) using modified carbon paste electrodes, Bull. Electrochem. 21 (2005) 529–535.

[196] J. Golimowski, B. Krasnodębska, E. Najdeker, Voltammetric determination of

Cr(III) in plating baths containing Cr(III) salts as the main component, Fresenius. J. Anal. Chem. 352 (1995) 544–546. https://doi.org/10.1007/BF00323070.

[197] N. Dawra, N. Dabas, Advances in spectrophotometric determination of Chromium(III) and Chromium(VI) in water: a review, Int. J. Environ. Anal. Chem. 104 (2022) 2994–3015. https://doi.org/10.1080/03067319.2022.2076224.

[198] P.T. Chou, G.R. Wu, C.Y. Wei, C.C. Cheng, C.P. Chang, F.T. Hung, Excited-state amine - imine double proton transfer in 7-azaindoline, J. Phys. Chem. B. 104 (2000) 7818–7829. https://doi.org/10.1021/jp001001g.

[199] S. Maity, S. Kumar, G. Singh, S. Patra, D. Pareek, P. Paik, Selective sensing of heavy metal ions using carbon dots synthesized from Azadirachta indica seeds, Sensors and Diagnostics. 4 (2025) 407–415. https://doi.org/10.1039/d4sd00350k.

[200] P. Gupta, G. Tamrakar, S. Biswas, R.S. Dhundhel, V.K. Soni, H.S. Das, P. Sahu, A.K. Chaturwedi, N.K. Kashyap, T. Akitsu, M. Hait, Quantum Dots as a Fluorescent Sensor for Detecting Heavy Metal Ions in Aqueous Environment: An Overview, ES Chem. Sustain. (2024) 1–12. https://doi.org/10.30919/escs1359.

[201] B.M. May, M.F. Bambo, S.S. Hosseini, U. Sidwaba, E.N. Nxumalo, A.K. Mishra, A review on I-III-VI ternary quantum dots for fluorescence detection of heavy metals ions in water: optical properties, synthesis and application, RSC Adv. 12 (2022) 11216–11232. https://doi.org/10.1039/d1ra08660j.

[202] M.K. Chini, V. Kumar, A. Javed, S. Satapathi, Graphene quantum dots and carbon nano dots for the FRET based detection of heavy metal ions, Nano-Structures and Nano-Objects. 19 (2019) 100347. https://doi.org/10.1016/j.nanoso.2019.100347.

[203] A. Ghorai, S. Bayan, N. Gogurla, A. Midya, S.K. Ray, Highly luminescent WS2 quantum dots/ZnO heterojunctions for light emitting devices, ACS Appl. Mater. Interfaces. 9 (2017) 558–565. https://doi.org/10.1021/acsami.6b12859.

[204] L. Lin, Y. Xu, S. Zhang, I.M. Ross, A.C.M. Ong, D.A. Allwood, Fabrication of luminescent monolayered tungsten dichalcogenides quantum dots with

giant spin-valley coupling, ACS Nano. 7 (2013) 8214–8223. https://doi.org/10.1021/nn403682r.

[205] N. Pallikkarathodi Mani, J. Cyriac, Hydrothermal synthesis of WS2quantum dots and their application as a fluorescence sensor for the selective detection of 2,4,6-trinitrophenol, New J. Chem. 44 (2020) 10840–10848. https://doi.org/10.1039/c9nj06159b.

[206] B. Mahato, P.K. Das, A. Bhardwaj, InP/ZnS Quantum Dots for High-Sensitivity Temperature Sensors, ACS Omega. (2024). https://doi.org/10.1021/acsomega.4c05644.

[207] O. Korepanov, D. Kozodaev, O. Aleksandrova, A. Bugrov, D. Firsov, D. Kirilenko, D. Mazing, V. Moshnikov, Z. Shomakhov, Temperature- and Size-Dependent Photoluminescence of CuInS2 Quantum Dots, Nanomaterials. 13 (2023). https://doi.org/10.3390/nano13212892.

[208] N. Bel Haj Mohamed, M. Haouari, Z. Zaaboub, M. Nafoutti, F. Hassen, H. Maaref, H. Ben Ouada, Time resolved and temperature dependence of the radiative properties of thiol-capped CdS nanoparticles films, J. Nanoparticle Res. 16 (2014). https://doi.org/10.1007/s11051-013-2242-9.

[209] L. Tang, Y. Zhang, C. Liao, Y. Guo, Y. Lu, Y. Xia, Y. Liu, Temperature-Dependent Photoluminescence of CdS/ZnS Core/Shell Quantum Dots for Temperature Sensors, Sensors. 22 (2022). https://doi.org/10.3390/s22228993.

[210] M.S. Mehata, An efficient excited-state proton transfer fluorescence quenching based probe (7-hydroxyquinoline) for sensing trivalent cations in aqueous environment, J. Mol. Liq. 326 (2021) 115379. https://doi.org/10.1016/j.molliq.2021.115379.

[211] M. Xia, H. Mei, Q. Qian, R.A. Dahlgren, M. Gao, X. Wang, Sulfur quantum dot-based “ON-OFF-ON” fluorescence platform for detection and bioimaging of Cr(vi) and ascorbic acid in complex environmental matrices and biological tissues, RSC Adv. 11 (2021) 10572–10581. https://doi.org/10.1039/d1ra00401h.

[212] J. Wang, Z. Wu, S. Chen, R. Yuan, L. Dong, A novel multifunctional fluorescent sensor based on N/S co-doped carbon dots for detecting Cr (VI) and toluene, Microchem. J. 151 (2019) 104246.

https://doi.org/10.1016/j.microc.2019.104246.

[213] E.K. Adotey, M. Amouei Torkmahalleh, P.K. Hopke, M.P. Balanay, N,Zn-Doped Fluorescent Sensor Based on Carbon Dots for the Subnanomolar Detection of Soluble Cr(VI) Ions, Sensors. 23 (2023). https://doi.org/10.3390/s23031632.

[214] Y. Zhang, X. Fang, H. Zhao, Z. Li, A highly sensitive and selective detection of Cr(VI) and ascorbic acid based on nitrogen-doped carbon dots, Talanta. 181 (2018) 318–325. https://doi.org/10.1016/j.talanta.2018.01.027.

[215] S.A. Miscoria, C. Jacq, T. Maeder, R. Martín Negri, Screen-printed electrodes for electroanalytical sensing, of chromium VI in strong acid media, Sensors Actuators, B Chem. 195 (2014) 294–302. https://doi.org/10.1016/j.snb.2014.01.013.

[216] Q. Huang, Q. Bao, C. Wu, M. Hu, Y. Chen, L. Wang, W. Chen, Carbon dots derived from Poria cocos polysaccharide as an effective “on-off” fluorescence sensor for chromium (VI) detection, J. Pharm. Anal. 12 (2022) 104–112. https://doi.org/10.1016/j.jpha.2021.04.004.

[217] F. Cai, X. Liu, S. Liu, H. Liu, Y. Huang, A simple one-pot synthesis of highly fluorescent nitrogen-doped graphene quantum dots for the detection of Cr(vi) in aqueous media, RSC Adv. 4 (2014) 52016–52022. https://doi.org/10.1039/c4ra09320h.

[218] L.M.T. Phan, S.H. Baek, T.P. Nguyen, K.Y. Park, S. Ha, R. Rafique, S.K. Kailasa, T.J. Park, Synthesis of fluorescent silicon quantum dots for ultra-rapid and selective sensing of Cr(VI) ion and biomonitoring of cancer cells, Mater. Sci. Eng. C. 93 (2018) 429–436. https://doi.org/10.1016/j.msec.2018.08.024.

[219] H.Y. Li, D. Li, Y. Guo, Y. Yang, W. Wei, B. Xie, On-site chemosensing and quantification of Cr(VI) in industrial wastewater using one-step synthesized fluorescent carbon quantum dots, Sensors Actuators, B Chem. 277 (2018) 30–38. https://doi.org/10.1016/j.snb.2018.08.157.

[220] Q. Tan, X. An, S. Pan, H. Liu, X. Hu, Hydrogen peroxide assisted synthesis of sulfur quantum dots for the detection of chromium (VI) and ascorbic acid, Spectrochim. Acta - Part A Mol. Biomol. Spectrosc. 247 (2021) 119122.

https://doi.org/10.1016/j.saa.2020.119122.

[221] Y. Wang, X. Hu, W. Li, X. Huang, Z. Li, W. Zhang, X. Zhang, X. Zou, J. Shi, Preparation of boron nitrogen co-doped carbon quantum dots for rapid detection of Cr(VI), Spectrochim. Acta - Part A Mol. Biomol. Spectrosc. 243 (2020) 118807. https://doi.org/10.1016/j.saa.2020.118807.

[222] B.K. John, N. John, S. Mathew, B.K. Korah, M.S. Punnoose, B. Mathew, Fluorescent carbon quantum dots as a novel solution and paper strip-based dual sensor for the selective detection of Cr(VI) ions, Diam. Relat. Mater. 126 (2022). https://doi.org/10.1016/j.diamond.2022.109138.

[223] Z. Gao, J. Liao, X. Li, L. Zhou, Metal-Free Elemental Selenium Quantum Dots: A Novel and Robust Fluorescent Nanoprobe for Cell Imaging and the Sensitive Detection of Cr(VI), Materials (Basel). 18 (2025) 1–12. https://doi.org/10.3390/ma18092119.

[224] B. Le Ouay, Pr ep rin t n pe er r Pr ep t n, (n.d.).

[225] C. Sen Ni, W.J. Zhang, W.Z. Bi, M.X. Wu, S.X. Feng, X.L. Chen, L.B. Qu, Facile synthesis of N-doped graphene quantum dots as a fluorescent sensor for Cr(vi) and folic acid detection, RSC Adv. 14 (2024) 26667–26673. https://doi.org/10.1039/d4ra05016a.

[226] A. Bora, L.P.L. Mawlong, R. Das, P.K. Giri, Understanding the excitation wavelength dependent spectral shift and large exciton binding energy of tungsten disulfide quantum dots and its interaction with single-walled carbon nanotubes, J. Colloid Interface Sci. 561 (2020) 519–532. https://doi.org/10.1016/j.jcis.2019.11.027.

[227] P. Mishra, A.S. Patel, S.K. Chauhan, A. Chakraborti, Photoinduced Charge Transfer in Transition Metal Dichalcogenide Quantum Dots, (2024). http://arxiv.org/abs/2405.21035.

[228] M. Shellaiah, K. Awasthi, S. Chandran, B. Aazaad, K.W. Sun, N. Ohta, S.P. Wu, M.C. Lin, Methylammonium Tin Tribromide Quantum Dots for Heavy Metal Ion Detection and Cellular Imaging, ACS Appl. Nano Mater. 5 (2022) 2859–2874. https://doi.org/10.1021/acsanm.2c00028.

[229] H.D. Cai, B. Nie, P. Guan, Y.S. Cheng, X.D. Xu, F.H. Wu, G. Yuan, X.W. Wei, Tuning the Interactions in CuO Nanosheet-Decorated CeO2Nanorods for

Controlling the Electrochemical Reduction of CO2to Methane or Ethylene, ACS Appl. Nano Mater. 5 (2022) 7259–7267. https://doi.org/10.1021/acsanm.2c01164.

[230] H. Martinez, A. Benayad, D. Gonbeau, P. Vinatier, B. Pecquenard, A. Levasseur, Influence of the cation nature of high sulfur content oxysulfide thin films MO y S z (M = W, Ti) studied by XPS, Appl. Surf. Sci. 236 (2004) 377–386. https://doi.org/10.1016/j.apsusc.2004.05.010.

[231] G. Murtaza, S.P. Venkateswaran, A.G. Thomas, P. O'Brien, D.J. Lewis, Chemical vapour deposition of chromium-doped tungsten disulphide thin films on glass and steel substrates from molecular precursors, J. Mater. Chem. C. 6 (2018) 9537–9544. https://doi.org/10.1039/c8tc01991f.

[232] W. Xu, L. Yu, H. Xu, S. Zhang, W. Xu, Y. Lin, X. Zhu, Water-dispersed silicon quantum dots for on-off-on fluorometric determination of chromium(VI) and ascorbic acid, Microchim. Acta. 186 (2019). https://doi.org/10.1007/s00604-019-3751-8.

[233] B.P. Payne, M.C. Biesinger, N.S. McIntyre, X-ray photoelectron spectroscopy studies of reactions on chromium metal and chromium oxide surfaces, J. Electron Spectros. Relat. Phenomena. 184 (2011) 29–37. https://doi.org/10.1016/j.elspec.2010.12.001.

[234] J. Lai, B. Wang, Y. Gong, C. Sun, W. Wang, W. Yang, Synthesis of WO3@WS2 core-shell nanostructures via solution-based sulfurization for improved performance of water splitting, RSC Adv. 13 (2023) 4150–4155. https://doi.org/10.1039/d2ra06354a.

[235] A. Lippitz, T. Hu, XPS investigations of chromium nitride thin films, 200 (2005) 250–253. https://doi.org/10.1016/j.surfcoat.2005.02.091.

[236] D. Nugroho, R. Benchawattananon, J. Janshongsawang, N. Pimsin, P. Porrawatkul, R. Pimsen, P. Nuengmatcha, P. Nueangmatcha, S. Chanthai, Ultra-trace analysis of chromium ions (Cr3+/Cr6+) in water sample using selective fluorescence turn-off sensor with natural carbon dots mixed graphene quantum dots nanohybrid composite synthesis by pyrolysis, Arab. J. Chem. 17 (2024) 105443. https://doi.org/10.1016/j.arabjc.2023.105443.

[237] L.M. Bertus, C. Faure, A. Danine, C. Labrugere, G. Campet, A. Rougier, A.

Duta, Synthesis and characterization of WO3 thin films by surfactant assisted spray pyrolysis for electrochromic applications, Mater. Chem. Phys. 140 (2013) 49–59. https://doi.org/10.1016/j.matchemphys.2013.02.047.

[238] C. Te Hsieh, D.Y. Tzou, K.Y. Hsieh, K.M. Yin, Photoluminescence from amino functionalized graphene quantum dots prepared by electrochemical exfoliation method in the presence of ammonium ions, RSC Adv. 7 (2017) 18340–18346. https://doi.org/10.1039/c6ra28742e.

[239] G. Bhanjana, P. Rana, G.R. Chaudhary, N. Dilbaghi, K.H. Kim, S. Kumar, Manganese Oxide Nanochips as a Novel Electrocatalyst for Direct Redox Sensing of Hexavalent Chromium, Sci. Rep. 9 (2019) 1–10. https://doi.org/10.1038/s41598-019-44525-4.

[240] S.P. Stabler, Clinical practice. Vitamin B12 deficiency., N. Engl. J. Med. 368 (2013) 149–60. https://doi.org/10.1056/NEJMcp1113996.

[241] L. Randaccio, S. Geremia, N. Demitri, J. Wuerges, Vitamin B12: Unique Metalorganic Compounds and the Most Complex Vitamins, (2010) 3228–3259. https://doi.org/10.3390/molecules15053228.

[242] A. Sobczyńska-Malefora, A.D. Smith, Vitamin B-12, Adv. Nutr. 13 (2022) 2061–2063. https://doi.org/10.1093/advances/nmac030.

[243] J.F.H. Arendt, D.K. Farkas, L. Pedersen, E. Nexo, H.T. Sørensen, Elevated plasma vitamin B12 levels and cancer prognosis: A population-based cohort study, Cancer Epidemiol. 40 (2016) 158–165. https://doi.org/10.1016/j.canep.2015.12.007.

[244] F. Du, Z. Cheng, G. Wang, M. Li, W. Lu, S. Shuang, C. Dong, Detection of pH, (2021). https://doi.org/10.1021/acs.jafc.0c07019.

[245] E.A. Bulut, P. Soysal, A.E. Aydin, O. Dokuzlar, S.E. Kocyigit, A.T. Isik, Vitamin B12 deficiency might be related to sarcopenia in older adults, Exp. Gerontol. 95 (2017) 136–140. https://doi.org/10.1016/j.exger.2017.05.017.

[246] L.H. Allen, How common is vitamin B-12 deficiency? 1-3, Am. J. Clin. Nutr. 89 (2009) 693S-696S. https://doi.org/10.3945/ajcn.2008.26947A.

[247] J.F.B. Arendt, L. Pedersen, E. Nexo, H.T. Sørensen, Elevated plasma vitamin B12 levels as a marker for cancer: A population-based cohort study, J. Natl. Cancer Inst. 105 (2013) 1799–1805. https://doi.org/10.1093/jnci/djt315.

[248] J. Chen, C. Mao, H. Ye, X. Gao, L. Zhao, Natural biomass carbon Dots-Based fluorescence sensor for high precision detection of vitamin B12 in serum, Spectrochim. Acta - Part A Mol. Biomol. Spectrosc. 305 (2024) 123459. https://doi.org/10.1016/j.saa.2023.123459.

[249] M.A. El-Naka, M.R. Morgan, A. El-Dissouky, T.E. Khalil, A. El-Faham, D.S. El-Sayed, Synthesis and characterization of a novel fluorescent composite of triazine organic framework (TOF) and silicon quantum dots as a promising sensor of vitamin B12, Microchem. J. 218 (2025). https://doi.org/10.1016/j.microc.2025.115112.

[250] S. Pramanik, S. Roy, S. Bhandari, The quantum dot-FRET-based detection of vitamin B12 at a picomolar level, Nanoscale Adv. 2 (2020) 3809–3814. https://doi.org/10.1039/d0na00540a.

[251] K. Hencel, M. Sullivan, A. Akay, High-throughput detection and quantification of vitamin B 12 in microbiome isolates using Escherichia coli Key words, (2025).

[252] G. Tsiminis, E.P. Schartner, J.L. Brooks, M.R. Hutchinson, Measuring and tracking vitamin B12: A review of current methods with a focus on optical spectroscopy, Appl. Spectrosc. Rev. 52 (2017) 439–455. https://doi.org/10.1080/05704928.2016.1229325.

[253] Sweety, D. Kumar, Electrochemical immunosensor based on titanium dioxide grafted MXene for EpCAM antigen detection, J. Colloid Interface Sci. 652 (2023) 549–556. https://doi.org/10.1016/j.jcis.2023.08.099.

[254] C. Dalal, A.K. Garg, M. Mathur, S.K. Sonkar, Fluorescent Polymer Carbon Dots for the Sensitive-Selective Sensing of Fe3+Metal Ions and Cellular Imaging, ACS Appl. Nano Mater. 5 (2022) 12699–12710. https://doi.org/10.1021/acsanm.2c02544.

[255] P. Geissbühler, B. Mermillod, C.H. Rapin, Elevated serum vitamin B12 levels associated with CRP as a predictive factor of mortality in palliative care cancer patients: A prospective study over five years, J. Pain Symptom Manage. 20 (2000) 93–103. https://doi.org/10.1016/S0885-3924(00)00169-X.

[256] Aneesha, M.S. Mehata, Waterborne explosives: A rapid detection method using MoSe2 quantum dots, Mater. Res. Bull. 185 (2025) 113287.

https://doi.org/10.1016/j.materresbull.2024.113287.

[257] L. Hu, Q. Zhang, X. Gan, W. Yin, W. Fu, Switchable fluorescence of MoS2 quantum dots: a multifunctional probe for sensing of chromium(VI), ascorbic acid, and alkaline phosphatase activity, Anal. Bioanal. Chem. 410 (2018) 7551–7557. https://doi.org/10.1007/s00216-018-1374-2.

[258] P. Nagaraj, N. Aradhana, A. Shivakumar, A.K. Shrestha, A.K. Gowda, Spectrophotometric method for the determination of chromium (VI) in water samples, Environ. Monit. Assess. 157 (2009) 575–582. https://doi.org/10.1007/s10661-008-0557-2.

[259] N. Shao, Y. Zhang, S.M. Cheung, R.H. Yang, W.H. Chan, T. Mo, K.A. Li, F. Liu, Copper ion-selective fluorescent sensor based on the inner filter effect using a spiropyran derivative, Anal. Chem. 77 (2005) 7294–7303. https://doi.org/10.1021/ac051010r.

[260] D.F. Pereira, E.R. Santana, J. V. Piovesan, A. Spinelli, A novel electrochemical strategy for determination of vitamin B12 by Co(I/II) redox pair monitoring with boron-doped diamond electrode, Diam. Relat. Mater. 105 (2020) 107793. https://doi.org/10.1016/j.diamond.2020.107793.

[261] N. Pakeeza, M.U. Draz, A. Yaqub, A.T. Jafry, M. Khan, H. Ajab, Electrochemical sensing of B-complex vitamins: current challenges and future prospects with microfluidic integration, RSC Adv. 14 (2024) 10331–10347. https://doi.org/10.1039/d4ra00555d.

[262] S.A. Bhat, N. Rashid, M.A. Rather, S.A. Pandit, P.P. Ingole, M.A. Bhat, Vitamin B12 functionalized N-Doped graphene: A promising electro-catalyst for hydrogen evolution and electro-oxidative sensing of H2O2, Electrochim. Acta. 337 (2020) 135730. https://doi.org/10.1016/j.electacta.2020.135730.

[263] A. Kumari, V. Vyas, S. Kumar, Advances in electrochemical and optical sensing techniques for vitamins detection: a review, ISSS J. Micro Smart Syst. 11 (2022) 329–341. https://doi.org/10.1007/s41683-021-00084-3.

[264] S. Gopi, A. Thamilselvan, M. Il Kim, K. Yun, Enhanced vitamin B12 detection using a CxNixOyFeyOx+3 bimetal-organic framework: A comprehensive electrochemical study, Electrochim. Acta. 512 (2025) 145476. https://doi.org/10.1016/j.electacta.2024.145476.

[265] T. Mumcu, S. Oncuoglu, C.G. Hizliates, K. Ertekin, Emission-based sensing of cobalt (II) and vitamin B12 via a bis-indole derivative, Luminescence. 39 (2024) 1–13. https://doi.org/10.1002/bio.4863.

[266] H. Mittal, M. Raza, M. Khanuja, Liquid phase exfoliation of MoSe2: Effect of solvent on morphology, edge confinement, bandgap and number of layers study, MethodsX. 11 (2023). https://doi.org/10.1016/j.mex.2023.102409.

[267] Y. Qiu, S. Yu, L. Li, Research Progress in Fluorescent Probes for Arsenic Species, Molecules. 27 (2022) 1–18. https://doi.org/10.3390/molecules27238497.

[268] N. Bhatt, M.S. Mehata, WSe 2 quantum dots : A fluorescent probe for ultra-sensitive detection of, Mater. Res. Bull. 192 (2025) 113633. https://doi.org/10.1016/j.materresbull.2025.113633.

[269] B. Anchan, S.D. Kulkarni, A. Patil, Chemical and biological sensors Vitamin B12 Detection in Aqueous Media Using MPA-CdTe Quantum Dots, IEEE Sensors Lett. 8 (2024) 1–4. https://doi.org/10.1109/LSENS.2024.3495512.

[270] L. Zhang, H. Wang, Q. Hu, X. Guo, L. Li, S. Shuang, X. Gong, Carbon quantum dots doped with phosphorus and nitrogen are a viable fluorescent nanoprobe for determination and cellular imaging of vitamin B 12 and cobalt (II), (2019).

[271] S. Dadkhah, A. Mehdinia, A. Jabbari, A. Manbohi, Nicotinamide - Functionalized Carbon Quantum Dot as New Sensing Platform for Portable Quantification of Vitamin B12 in Fluorescence , UV – Vis and Smartphone Triple Mode, J. Fluoresc. (2022) 681–689. https://doi.org/10.1007/s10895-021-02863-5.

[272] M. Wang, Y. Liu, G. Ren, W. Wang, S. Wu, Analytica Chimica Acta Bioinspired carbon quantum dots for sensitive fl uorescent detection of vitamin B12 in cell system, Anal. Chim. Acta. 1032 (2018) 154–162. https://doi.org/10.1016/j.aca.2018.05.057.

[273] S. Beytu, S. Essiz, O. Bengu, Investigation of Structural and Antibacterial Properties of WS 2 - Doped ZnO Nanoparticles, (2024). https://doi.org/10.1021/acsomega.3c09041.

[274] G.B. Kolekar, RSC Advances A novel FRET probe for selective and sensitive

determination of vitamin B 12 by functionalized CdS QDs in aqueous media : applications to pharmaceutical and biomedical analysis, RSC Adv. 4 (2014) 683–692. https://doi.org/10.1039/c3ra42553c.

[275] Y. Li, Y. Jia, Q. Zeng, X. Jiang, Z. Cheng, A multifunctional sensor for selective and sensitive detection of vitamin B12 and tartrazine by Förster resonance energy transfer, Spectrochim. Acta Part A Mol. Biomol. Spectrosc. 211 (2019) 178–188. https://doi.org/10.1016/j.saa.2018.12.002.

[276] V. Sant, R. Cela-dablanca, A. Barreiro, L.R. L, E. Alvarez-rodríguez, M. Arias-est, A. Nú, M.J. Fern, Potential of low-cost bio-adsorbents to retain amoxicillin in contaminated water, 213 (2022). https://doi.org/10.1016/j.envres.2022.113621.

[277] K. Kaur, M. Kumar, D. Kumar, Journal of Water Process Engineering Insight into the amoxicillin resistance , ecotoxicity , and remediation strategies, J. Water Process Eng. 39 (2021) 101858. https://doi.org/10.1016/j.jwpe.2020.101858.

[278] P.K. Mutiyar, A.K. Mittal, Occurrences and fate of an antibiotic amoxicillin in extended aeration-based sewage treatment plant in Delhi , India : a case study of emerging pollutant, Desalin. Water Treat. 51 (2013) 6158–6164. https://doi.org/10.1080/19443994.2013.770199.

[279] S.I. Polianciuc, A.E. Gurzău, B. Kiss, M.G. Ștefan, F. Loghin, Antibiotics in the environment : causes and consequences, 93 (2020) 231–240. https://doi.org/10.15386/mpr-1742.

[280] S.R. Spectroscopy, Z. Yao, G. Chen, B. Zhang, J. Lin, Q. Luo, Retracted : A Review of Detection of Antibiotic Residues in Food by, 2021 (2024). https://doi.org/10.1155/2021/8180154.

[281] C. Monahan, R. Nag, D. Morris, E. Cummins, Toxic / Hazardous Substances and Environmental Engineering Antibiotic residues in the aquatic environment – current perspective and risk considerations, J. Environ. Sci. Heal. Part A. 56 (2021) 733–751. https://doi.org/10.1080/10934529.2021.1923311.

[282] M. Imran, S. Ahmed, A.Z. Abdullah, H.A. Rudayni, Nanostructured material-based optical and electrochemical detection of amoxicillin antibiotic, (2023) 1064–1086. https://doi.org/10.1002/bio.4408.

[283] V. Safran, M. Bakhshpour, A. Denizli, Development of Molecularly Imprinted Polymer-Based Optical Sensor for the Sensitive Penicillin G Detection in, (2021) 11865–11875. https://doi.org/10.1002/slct.202103058.

[284] A.Y. Khrushchev, E.R. Akmaev, I. V Kis, A.Y. Gulyaeva, V.O. Bondarenko, Vibrational Spectroscopy Combination of HPLC and SERS detection applied to the analysis of the trace content of amoxicillin in milk, Vib. Spectrosc. 123 (2022) 103473. https://doi.org/10.1016/j.vibspec.2022.103473.

[285] X. Chang, J. Cui, G. Wang, S. Meng, L. Chen, Environmental Science and Ecotechnology Emerging technologies for detecting antibiotics in aquaculture wastewater : A critical review, Environ. Sci. Ecotechnology. 25 (2025) 100572. https://doi.org/10.1016/j.ese.2025.100572.

[286] M. Frigoli, M.P. Krupa, G. Hooyberghs, H. Diliën, K. Eersels, B. Van Grinsven, J.W. Lowdon, T.J. Cleij, Electrochemical Sensors for Antibiotic Detection : A Focused Review with a Brief Overview of Commercial Technologies, (2024).

[287] J. Hong, M. Su, K. Zhao, Y. Zhou, J. Wang, S. Zhou, X. Lin, A Minireview for Recent Development of Nanomaterial-Based Detection of Antibiotics, (2023).

[288] J. Liang, Q. Wu, R. Xiao, R. Yu, H. Chen, Molecularly imprinted polymer / CdTe quantum dots-decorated polymer optic fi ber microprobes for Amoxicillin detection, (2025) 1–9. https://doi.org/10.3389/fbioe.2025.1700654.

[289] V. Divya, P. Battula, S. Pulipati, M.R. Veena, A. Rasool, G. Bhuvanesh, M. Khalid, S. Wahab, Ecotoxicity assessment and detection of antimicrobial compounds in urban environments and AMR hotspots, (2025) 1–11.

[290] A. Yadav, P. Sagar, M. Srivastava, A. Srivastava, R. Kumar, Spectrochimica Acta Part A : Molecular and Biomolecular Spectroscopy A smartphone-enabled colorimetric sensor based on VS 2 quantum dots for Rapid and on-site detection of ferric ions, Spectrochim. Acta Part A Mol. Biomol. Spectrosc. 329 (2025) 125609. https://doi.org/10.1016/j.saa.2024.125609.

[291] K. Wang, Q. Ji, J. Xu, H. Li, D. Zhang, X. Liu, Y. Wu, H. Fan, Highly Sensitive and Selective Detection of Amoxicillin Using Carbon Quantum Dots

Derived from Beet, (2018) 759–765.

[292] Y. Dong, F. Li, Y. Wang, Y. Wang, Low-Dimension Nanomaterial-Based Sensing Matrices for Antibiotics Detection : A Mini Review, 8 (2020) 1–7. https://doi.org/10.3389/fchem.2020.00551.

[293] A. Bayat, E. Saievar-iranizad, Synthesis of blue photoluminescent WS 2 quantum dots via ultrasonic cavitation, J. Lumin. 185 (2017) 236–240. https://doi.org/10.1016/j.jlumin.2017.01.024.

[294] K. Parto, S.I. Azzam, K. Banerjee, Defect and strain engineering of monolayer WSe2 enables site-controlled single-photon emission up to 150â€‰K, Nat. Commun. (n.d.) 1–8. https://doi.org/10.1038/s41467-021-23709-5.

[295] Y. Zhu, J. Lim, Z. Zhang, Y. Wang, S. Sarkar, H. Ramsden, Y. Li, H. Yan, D. Phuyal, N. Gauriot, A. Rao, R.L.Z. Hoye, G. Eda, M. Chhowalla, Room-Temperature Photoluminescence Mediated by Sulfur Vacancies in 2D Molybdenum Disulfide, (2023). https://doi.org/10.1021/acsnano.3c02103.

[296] M.S. Mehata, Reusable fluorescent WS 2 QDs sensor for ultralow-level detection of Cr 6 + in real water samples, Mater. Today Commun. 49 (2025) 114183. https://doi.org/10.1016/j.mtcomm.2025.114183.

[297] L. Ye, F. Chen, Y. Tang, W. Sun, Y. Song, Journal of Water Process Engineering Highly selective and sensitive detection of trace amoxicillin with a novel fluorescent nanoprobe N , S-CDs @ MIP based on S / N co-doped carbon quantum dots combined with molecularly imprinted polymer, J. Water Process Eng. 71 (2025) 107291. https://doi.org/10.1016/j.jwpe.2025.107291.

[298] M.O. Valappil, A. Anil, M. Shaijumon, V.K. Pillai, S. Alwarappan, A Single-Step Electrochemical Synthesis of Luminescent WS2 Quantum Dots, Chem. - A Eur. J. 23 (2017) 9144–9148. https://doi.org/10.1002/chem.201701277.

[299] S. Sharma, S. Bhagat, J. Singh, M. Ahmad, S. Sharma, Temperature dependent photoluminescence from - WS 2 nanostructures, J. Mater. Sci. Mater. Electron. 29 (2018) 20064–20070. https://doi.org/10.1007/s10854-018-0137-3.

[300] S.E. Laouini, A. Bouafia, M. Azzi, I. Laib, Synthesis and Characterization of Functionalized Ag / AgCl Nanoparticles : A Promising Multifunctional Platform for Next- - Generation Nanomedicine, (2025).

https://doi.org/10.1002/jbm.b.35661.

[301] L. David, A. Bebu, L. Szabó, N. Leopold, IR , Raman , SERS and DFT study of amoxicillin, 993 (2011) 52–56. https://doi.org/10.1016/j.molstruc.2010.11.067.

[302] Y.M. Soliman, M. Mabrouk, H. Hanan, K.M. Tohamy, Preparation and Characterization of Amoxicillin Loaded Bismuth Oxide as Drug Delivery System for Biomedical Applications, 63 (2024) 57–63.

[303] M.S. Mehata, Aneesha, Selectively probing ferric ions in aqueous environments using protonated and neutral forms of 7-azaindole as a multiparametric chemosensor, Photochem. Photobiol. Sci. 22 (2023) 1505–1516. https://doi.org/10.1007/s43630-023-00393-6.

[304] X. Zhang, Y. Ren, Z. Ji, J. Fan, Sensitive detection of amoxicillin in aqueous solution with novel fl uorescent probes containing boron-doped carbon quantum dots, J. Mol. Liq. 311 (2020) 113278. https://doi.org/10.1016/j.molliq.2020.113278.

[305] K. Chullasat, P. Nurerk, P. Kanatharana, F. Davis, Sensors and Actuators B : Chemical A facile optosensing protocol based on molecularly imprinted polymer coated on CdTe quantum dots for highly sensitive and selective amoxicillin detection, Sensors Actuators B. Chem. 254 (2018) 255–263. https://doi.org/10.1016/j.snb.2017.07.062.

[306] A.H. Gore, G.B. Kolekar, Fluorescence - based sensor for selective and sensitive detection of amoxicillin (Amox) in aqueous medium : Application to pharmaceutical and biomedical analysis, (2017) 1–6. https://doi.org/10.1002/bio.3271.

[307] A.M. Mahmoud, M.M. El, W. Ramadan, A. Hany, A.B. Reem, Double - signal quantification of amoxicillin based on interaction with 4 - aminoantipyrine at copper and nitrogen co - doped carbon quantum dots as an artificial nanozyme, Microchim. Acta. (2022). https://doi.org/10.1007/s00604-022-05253-1.

[308] B. Gangopadhyay, J. Subash, N. Saha, S. Hussain, S. Pal, S. Mukherjee, R. Hawaldar, S. Hazra, D. Chattopadhyay, Low-Temperature Base-Catalyzed Si-Capped ZnO Quantum Dots for pH-Switchable Dual Sensing of Amoxicillin

and Cr 3 +, (2024). https://doi.org/10.1021/acsanm.4c03682.

[309] C. Li, Y. Ma, C. Fan, C. He, S. Ma, Highly sensitive and selective detection of amoxicillin using molecularly imprinted ratiometric fluorescent nanosensor based on quantum dots, Microchim. Acta. (2024). https://doi.org/10.1007/s00604-024-06593-w.

[310] F. Zu, F. Yan, Z. Bai, J. Xu, Y. Wang, Y. Huang, X. Zhou, The quenching of the fluorescence of carbon dots: A review on mechanisms and applications, Microchim. Acta. 184 (2017) 1899–1914. https://doi.org/10.1007/s00604-017-2318-9.